Universidad Autónoma de Madrid

FACULTAD DE CIENCIAS

Departamento de Física Aplicada

Study of nanostructured hard ferrites and their coupling with a soft layer

Memoria presentada para optar al grado de Doctora en Ciencias Físicas por

Guiomar Delgado Soria

Directores:

Dr. Juan de la Figuera Bayón

Dr. Adrián Quesada Michelena

Madrid, Junio 2021

iqfr CSIC

Acknowledgements

Comenzando esta tesis doctoral quiero agradecer a todas las personas que me han acompañado a lo largo de este bonito camino.

En primer lugar me gustaría dar las gracias a mis directores de tesis Juan y Adrián. Gracias por confiar en mí para realizar esta investigación, ofrecerme vuestra ayuda incondicional, motivarme en los momentos más duros y sobre todo, por transmitirme tantos conocimientos. Ha sido un placer aprender de vosotros durante todos estos años. Quisiera expresar también mi gratitud a mi tutora Pilar por su apoyo y disponibilidad cada vez que lo he necesitado.

En segundo lugar y no por ello menos importante, quisiera dar las gracias a Pepe. Ha sido un orgullo trabajar con un investigador que me ha aportado tanta sabiduría, conocimientos, templanza, valores, confianza... En definitiva "mi padre científico". No quisiera olvidarme de Jose Emilio, quien además de enseñarme, siempre ha tenido buenas palabras hacia mí.

Doy las gracias a todos los compañeros del grupo "Surfmoss" con los que he tenido la suerte de trabajar y con los que he compartido muy buenos ratos: María, Ania, Miguel, Eva, Edu, Victor, Fernando, Guille y Alejandro. En especial quiero destacar a Ania y a María, quienes comenzaron ayudándome y alegrando mi día a día en el laboratorio y acabaron formando parte de mi vida.

Dentro del Instituto Rocasolano me gustaría agradecer al grupo de Láseres por su simpatía y colaboración con nuestro grupo así como a Juan Dávalos por su ayuda con el manejo del sputtering y su apreciado sentido del humor.

Quisiera también mencionar a mis compañeros del Instituto Cerámica y Vidrio, Ceci y Jesús. Gracias por la predisposición siempre a colaborar con cualquier estudio y vuestra acogida en mis visitas por allí. A Cesar y Jorge del Instituto de Ciencias de Materiales y a Santiago del Instituto de la Materia por su valiosa contribución a esta investigación. A Sandra por nuestro viaje en coche a Barcelona y las horas de análisis en el Sincrotrón ALBA. En este punto quisiera destacar la inestimable ayuda de Lucia y Michael en la línea de luz CIRCE de ALBA, sin los cuales no hubiera sido posible la adquisición de muchos de los resultados de esta tesis.

I want to thank all people who support me in my stay at Jerzy Haber Institute of catalysis and surface chemistry in Krakow. I felt really comfortable in your research group. Thank you again for bringing me the opportunity to amplify my goals in another country.

Un agradecimiento muy especial para mí es el dirigido a mi familia. A mis padres, a mis hermanos y a mis primos. A todos vosotros muchísimas gracias por estar conmigo en cada etapa que he afrontado, reforzarme en mis decisiones y darme vuestro animo. Me siento muy afortunada de pertenecer a la familia que tengo.

Doy las gracias a mis amigas que han estado junto a mí desde mi más tierna juventud: Mari Vega, Sandra, Cristina, Nerea, Elsa y Alba. Gracias a todas por brindarme con vuestra amistad, vuestras risas y comprensión y vuestra capacidad por hacer que cualquier momento sea inolvidable. Y también quisiera agradecer a aquellas amigas que conocí en la facultad y que desde entonces no se han separado de mi lado: Mónica, Marina e Isa. Gracias por tanto chicas.

Y a ti Fran, gracias por vivir conmigo cada momento, haber compartido mis alegrías y haber sido mi inquebrantable apoyo ante las dificultades. Gracias por ser mi vaso medio lleno.

Resumen

En los últimos 100 años, los imanes permanentes han desempeñado un papel fundamental en el desarrollo de múltiples campos de innovación tecnológica. Dichos materiales han sido utilizados principalmente para su aplicación en motores y generadores ya que permiten transformar la energía eléctrica en mecánica y viceversa. Además otros usos a destacar son como medios de grabación, componentes de dispositivos de microondas, radiofrecuencias y magneto-ópticos. Sin embargo, en la actualidad, los mejores imanes permanentes están compuestos por una considerable proporción de tierras raras. Las tierras raras presentan dos grandes problemas: su extracción provoca una elevado daño para el medio ambiente y tanto dicha extracción como su separación es controlada por China. Para evitar estos inconvenientes, se están dedicando esfuerzos a desarrollar nuevos imanes permanentes que no contengan tierras raras. En este contexto, esta investigación estudia óxidos magnéticamente duros que puedan sustituir a los imanes que incluyen tierras raras. Concretamente, el oxido estudiado en profundidad en la tesis ha sido la hexaferrita de estroncio ($SrFe_{12}O_{19}$, SFO). Esta ferrita hexagonal se ha convertido desde su descubrimiento a mediados del siglo XX en un material de gran importancia comercial y tecnológica gracias primordialmente a su alta anisotropía magnetocristalina unido a su bajo coste.

No obstante, la hexaferrita de estroncio pese a su alto campo coercitivo presenta unos valores de imanación remanente moderados, lo que provoca unos valores del producto energético por debajo de los alcanzados en imanes permanentes con tierras raras. Una estrategia para mejorar las propiedades magnéticas de este material será su acoplamiento con un material magnéticamente blando. Esta combinación posibilita, en las condiciones apropiadas, que el blando aumente la imanación sin disminuir de forma significativa el campo coercitivo aportado por el material magnéticamente duro. De esta forma se obtiene un mayor producto energético. Por lo tanto, un punto importante en esta investigación será comprender el acoplamiento magnético en la interfaz de dos materiales con coercitividades sustancialmente diferentes. Este es un problema científico continuo y sutil subyacente al desarrollo de futuros dispositivos espintrónicos/nanomagnéticos e imanes permanentes avanzados. Es importante señalar que estos materiales constituyen, además, sistemas muy interesantes para comprender la inversión de imanación colectiva e individual. Su comportamiento colectivo depende de las propiedades magnéticas de las capas individuales, así como de las interacciones dominantes entre ellas: acoplamiento de intercambio directo y/o interacciones magnetostáticas.

La primera etapa de la tesis se centra en entender las propiedades estructurales y magnéticas de $SrFe_{12}O_{19}$ y expone la caracterización de plaquetas de este compuesto mediante distintas técnicas microscópicas y espectroscópicas. Un resultado novedoso de esta sección fue obtener por primera vez su espectro de absorción de rayos X. Buscando mejorar sus propiedades magnéticas, se investigó su acoplamiento magnético con un material magnéticamente blando (cobalto) crecido por epitaxia de haces moleculares (MBE). Dicho estudio fue llevado a cabo en el microscopio de fotoemisión de electrones (PEEM) por medio de

dicroismo magnético circular de rayos X (XMCD) en el sincrotrón ALBA. Esta técnica permitió la determinación de los dominios magnéticos de cada capa. Paralelamente, simulaciones de micromagnetismo fueron realizadas para entender el comportamiento magnético observado en los resultados experimentales. Los análisis evidenciaron plaquetas de SFO de cientos de nanómetros con imanación prefencial perpendicular al plano. El acoplamiento en el sistema plaqueta-metal reveló una falta de acoplo magnético proveniente de la competición entre la anisotropía magnetocristalina de la plaqueta con la anisotropía de forma de la capa de cobalto.

Para evitar dicha competición y promover el acoplamiento magnético entre ambos compuestos, la segunda etapa de la tesis consiste en el crecimiento de láminas delgadas de SFO por pulverización catódica con la orientación magnética preferencialmente en el plano para la posterior deposición del metal por MBE. Inicialmente se comprobó el efecto del calentamiento en la formación de la fase cristalina de las láminas delgadas y se determinaron los parámetros involucrados en modificar el eje de fácil imanación de cada muestra. Para ello se estudió la composición, estructura y magnetismo de estas láminas en base a distintas técnicas de caracterización como la difracción de rayos X, espectroscopía Raman y Mössbauer. Nuevamente el estudio del acoplamiento magnético con la capa magnéticamente blanda fue analizado por PEEM-XMCD. En este experimento se apreció un acoplo estructural en el sistema bicapa.

Completando esta investigación, se ha estudiado la ferrita de cobalto ($CoFe_2O_4$, CFO) debido a sus notables propiedades como una alta constante de anisotropía magnetocristalina y una gran constante de magnetostricción. Al igual que la ferrita anteriormente comentada, este compuesto es magnéticamente duro. En esta tercera sección se han presentado y discutido láminas delgadas de CFO crecidas mediante MBE. Estas muestras se han caracterizado en un sistema de ultra-alto vacío con técnicas de microscopía y espectroscopía *in-situ* con especial énfasis en la discusión de la espectroscopia Mössbauer. La variación en el espesor y el calentamiento con y sin oxígeno promueve cambios en la estequiometría de la fase crecida y en consecuencia en sus propiedades.

Finalmente, para comprender el origen del acoplamiento tipo "muelle", observado en un sistema experimental formado por una lámina fina de $CoFe_2O_4$ y una capa de aleación Fe-Co, se llevaron a cabo simulaciones micromagnéticas. Estas simulaciones apoyaron como mecanismo dominante en el comportamiento magnético de la bicapa, la propagación de paredes de dominios en la fase blanda en contraste con lo predicho por los modelos teóricos, los cuales no tienen en cuenta este efecto.

Abstract

In the last 100 years, permanent magnets have played a key role in advancing many fields of technological innovation. These materials have been used mainly for their application in motors and generators since they allow the transformation of electrical energy into mechanical energy and vice versa. Other uses include recording media, microwave, radiofrequency and magneto-optical device components. However, at present, the best permanent magnets are composed of a considerable proportion of rare earths. Rare earths present two significant problems: their extraction causes great environmental damage, and China controls both extraction and separation. To avoid these handicaps, efforts are devoted to develop new permanent magnets that do not contain rare earths. In this context, these research studies magnetic materials based on hard oxides that can replace magnets that include rare earths. Specifically, the oxide studied in depth in the thesis has been strontium hexaferrite ($SrFe_{12}O_{19}$, SFO). Since its discovery in the mid-twentieth century, this hexagonal ferrite has become a material of great commercial and technological importance thanks primarily to its high magnetocrystalline anisotropy coupled with its low cost.

However, despite its high coercive field, strontium hexaferrite presents a moderate remanent magnetization, which results in energy product values below those achieved in rare earth permanent magnets. A strategy to improve the material magnetic properties would be coupling it with a magnetically soft material. Under the appropriate conditions, this combination allows the soft material to increase the magnetization of the system without significantly reducing the coercive field provided by the magnetically hard material. Thus, a higher energy product is obtained. Hence, an important point in this research will be to understand the magnetic coupling at the interphase of two materials with substantially different coercivities. This is an ongoing and subtle scientific problem underlying the development of future spintronic/nanomagnetic devices and advanced permanent magnets. Importantly, these materials are also very interesting systems for understanding collective and individual magnetization reversal. Their collective behaviour depends on the magnetic properties of the individual layers and the dominant interactions between them: direct exchange coupling and/or magnetostatic interactions.

The first stage of the thesis focuses on understanding the structural and magnetic properties of $SrFe_{12}O_{19}$ and exposes the characterization of this compound in platelets form by different microscopic and spectroscopic techniques. A novel result of this section was to obtain for the first time its X-ray absorption spectrum. The magnetic coupling with a magnetically soft material (cobalt) grown by molecular beam epitaxy (MBE) was investigated. This study was carried out in the photoemission electron microscope (PEEM) by means of X-ray circular magnetic dichroism (XMCD) on the ALBA synchrotron. This technique allowed the determination of the magnetic domains of each layer. In parallel, micromagnetism simulations were performed to understand the magnetic behavior observed in the experimental results. The analysis revealed SFO platelets of hundreds of nanometers in size with magnetization preferential normal to the platelet plane. The platelet-metal system

revealed a lack of magnetic coupling due to competition between the magnetocrystalline anisotropy of the platelet with the shape anisotropy of the cobalt layer.

To avoid such competition and promote magnetic coupling between the two compounds, the second stage of the thesis consists of growing SFO thin films by sputtering with the magnetic orientation preferentially in-plane for subsequent metal deposition by MBE. Initially, the annealing effect on the formation of the crystalline phase of the thin films was tested, and the parameters involved in modifying the easy axis magnetization of each sample were determined. The composition, structure and magnetism of these films were studied using different characterization techniques such as X-ray diffraction, Raman and Mössbauer spectroscopy. Again the study of the magnetic coupling with the magnetically soft layer was analyzed by PEEM-XMCD. In this experiment, a structural coupling was observed in the bilayer system.

Completing this research, cobalt ferrite ($CoFe_2O_4$, CFO) has been studied due to its remarkable properties such as a high magnetocrystalline anisotropy and large magnetostriction constant. Like the ferrite discussed above, this compound is magnetically hard and is used in permanent magnet applications. In this third section, MBE-grown CFO thin films have been presented and discussed. These samples have been characterized in an ultra-high vacuum system with microscopy and *in-situ* spectroscopy techniques with particular emphasis on the discussion of Mössbauer spectroscopy. The variation in thickness and heating with and without oxygen promotes changes in the stoichiometry of the grown phase and consequently to its properties.

Finally, to comprehend the origin of the spring-magnet coupling observed in an experimental system consisting of a $CoFe_2O_4$ thin film and a iron-cobalt alloy layer, micromagnetic simulations were carried out. These simulations supported the propagation of domain walls in the soft phase as the dominant mechanism for the bilayer magnetic behaviour of the bilayer, in contrast to theoretical models, which do not take into account this effect.

Contents

List of Figures

List of Tables

1 Preface

Permanent magnets are materials that have fascinated humankind for millennia. Although it will not be until the last century when they will be used industrially. Nowadays, many of these are used in motors, actuators and other magneto-mechanical devices, and for instance, stereos, laptop computers and cordless power tools - could not exist without permanent magnets [1, 2, 3]. These materials remain in a thermodynamically metastable magnetized state by their intrinsic properties [4, 5, 6]. Over the years, the development of magnets has improved by comprehending their material properties. The coercive field H_c is defined as the applied magnetic field required to remove the permanent magnetization and is related to the resistance of the magnet against demagnetizing fields. The product of the coercive field and the flux density that remains after removal of the magnetizing field, the remanence magnetization B_r, is the energy product BH_{Max} [7, 8]. This factor, which indicates the magnetic energy stored for each material, is shown in figure 1.1.

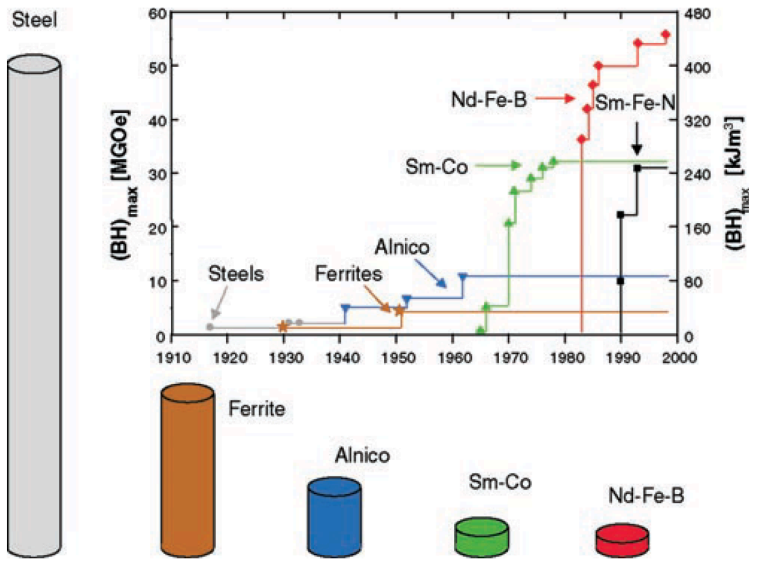

Figure 1.1: Evolution in the energy density $(BH)_{Max}$ of hard magnetic materials through the 20th century. Reprint from reference [9].

Rare earth (RE) permanent magnets were a revolution for the permanent magnet market in the 1970s. This was due to the high energy product presented by this type of materials, such as SmCo (240 kJ/m^3) and especially NdFeB (400 kJ/m^3) magnets. However, the extraction of these materials is very polluting [10, 11, 12]. As a consequence of this and of China industrial policy in this area, China is currently the main source of rare earth elements. According to this situation, the manufacturing and development of new materials as an alternative to RE magnets are sought.

One of the most popular permanent magnetic materials nowadays are ferrites: iron oxide compounds family that usually have one or more metallic elements such as nickel, barium, cobalt, strontium Etc. In general terms, ferrites can be divided into two groups following the difference in their magnetic properties as a criterion: hard and soft. We will focus on the first group, which corresponds to the ferrites with high coercivity. This makes these materials suitable as permanent magnets. The most important hard ferrites are the hexaferrites or M-type ferrites (strontium hexaferrite $SrFe_{12}O_{19}$, barium hexaferrite $BaFe_{12}O_{19}$, lead hexaferrite $PbFe_{12}O_{19}$) [13, 14] and some spinels such as cobalt ferrite are also considered ($CoFe_2O_4$) [15]. In fact, the first useful ferrite produced was $CoFe_2O_4$ by Kato and Takei in 1933, and the first commercial hard ferrite materials were the M-type ferrites manufactured by Phillips laboratory (1952) under the name of Ferroxdures [14, 16]. These ferrites share a high magnetocrystalline anisotropy leading to an elevated coercive field. The study of these properties depending on the shape of the material (nanoparticles, thin films, powders, targets, platelets) has enhanced the coercivity [17].

It is important to mention that in spite of the elevated coercivity shown by these hard ferrites, these compounds also have a moderate remanence. Thus, the combination of both results in an energy product with values BH_{Max} = 50-100 kJ/m^3[18]. Due to the problems of rare earths and the moderate energy product of hard ferrite materials, there exists the need to improve the remanence of the latter. Several strategies can be used for this purpose. One of the most promising one is the development of composite materials. This approach combines a magnetically hard phase (ferrite) with a magnetically soft one [19]. The soft magnetic materials are characterized by high permeability (B_r) albeit with low coercivity [20]. This fact makes the material easy to magnetize but also to demagnetize. The transition metals (Fe, Ni, Co) are found in this group due to their high saturation magnetization [21]. The improvement in the hard-soft system's magnetic properties occurs as a consequence of the magnetic coupling (exchange or magneto-dipolar interactions) between both phases, which seeks to align the magnetization direction of the soft phase with that of the hard phase. In this case, we might combine the high remanence of the soft phase and the coercivity from the hard phase. As a result of both contributions, the energy product would be enhanced (figure 1.2). These hard-soft material combination have been studied in the literature for different system such as nanocomposites [22, 23], core/shell nanoparticles [24, 25] and bilayers [26, 27]. In this thesis we study bilayer systems.

An underlying theme of these systems is the coupling regime that facilitates such magnetic interaction. The interaction by robust exchange coupling requires the overlap of orbitals between both phases, and thus, atomically coherent soft-hard interfaces [28, 29]. Further, the soft layer thickness has to be below a certain threshold, indicated by the hard phase exchange length, i.e., the Bloch wall width, which is usually of the order of a few nanometers [30, 31]. As will be seen throughout this thesis, producing a rigid exchange coupling is an arduous task to accomplish. Indeed, the exchange-coupling strength at the interface of the two layers can promote different magnetic behaviour in bilayers: rigid coupling, partial coupling (spring magnet) and decoupling [30, 32, 33, 34, 35].

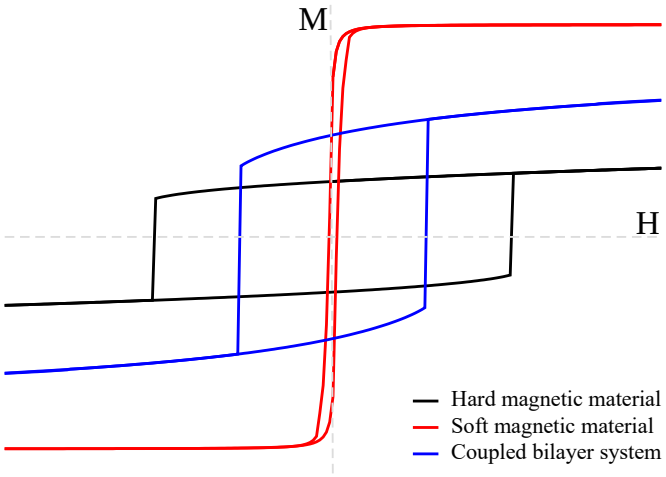

Figure 1.2: Magnetization curve vs applied magnetic field ("hysteresis loop") corresponding to a hard magnetic material (black curve), soft magnetic material (red curve) and rigid coupling between both (blue curve).

In the rigid coupling regime, both layers are fully exchange-coupled, and the spins of the magnetically soft layer are aligned with those of the hard layer. The magnetization reversal co-occurs for the whole system. Bilayer magnetic properties arise from averaging the magnetic properties provided by both materials.

The regime of a partial coupling or spring-magnet refers to a rigid exchange-coupling of the soft phase spins with those of the hard one at the interface, but those soft spins that are further from the interface are not coupled. This causes that for small magnetic fields, the uncoupled spins of the soft layer reverse their magnetization, while the spins that are coupled to those of the hard layer will need greater magnetic fields for reversing them, figure 1.3. This type of coupling also implies an improvement in the bilayer's magnetic properties since the partially coupled soft phase enables an increase in the system magnetization in the remanent state.

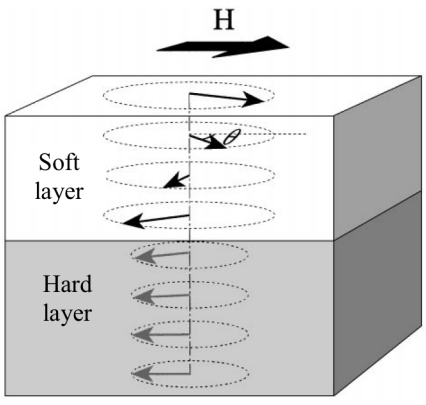

Figure 1.3: Illustration of an exchange-spring state in a hard-magnetic/soft-magnetic bilayer. Image modified from Ref. [30].

In the third regime, we consider that the bilayer is not exchange-coupled. In this case, the magnetization reversal is independent in each layer. However, dipole interactions might promote the alignment of the spins between both layers and, thus, might improve the system magnetic properties.

Therefore, in the context of the use of ferrites as an alternative to permanent magnets composed of rare earths as well as the magnetization improvement of these oxides by coupling magnetically soft layers, this thesis tries to address the following points:

- To determine the structural and magnetic properties of several hard ferrites (strontium hexaferrite and cobalt ferrite) in platelets and thin films form.

- To explore the magnetic nature of the coupling established between a hard ferrite layer and magnetically soft layer (cobalt and iron-cobalt).

To achieve these objectives, I present below the outline followed during the thesis.

Chapter 2. This chapter includes the growth and characterization techniques used through the thesis with a description of the systems where these techniques were employed.

Chapter 3. Here, the structure of strontium hexaferrite and its magnetic properties are discussed to provide context for the following chapters.

Chapter 4. This part is dedicated to the characterization of the structural and magnetic properties of SFO platelets grown through hydrothermal synthesis. Different microscopic and spectroscopic techniques with emphasis on Mössbauer spectroscopy and X-ray soft absorption were used.
Chapter 5. This chapter focuses on the growth of a soft cobalt layer on the SFO platelets and their magnetic interaction. The study was carried out by X-ray absorption techniques together with micromagnetic simulations.

Chapter 6. In this chapter, strontium hexaferrite thin films are grown on Si(100) by radio frequency magnetron sputtering followed by annealing. The growth is optimized to provide for in-plane magnetization in the films. Finally, the coupling with a magnetic cobalt layer is studied.

Chapter 7. Here, cobalt ferrite ultra-thin films on Pt(111) are grown by molecular beam epitaxy. The characterization of the films was carried out in-situ by several methods, including Mössbauer spectroscopy.

Chapter 8. In this part, micromagnetic simulations are performed to understand the experiments on the coupling between a cobalt ferrite thin film with a thin cobalt-iron layer.

Chapter 9. This chapter summarizes the main results obtained in this thesis.

2 Experimental details

This chapter presents the deposition techniques employed to grow the oxide films and metal layers studies in this thesis, followed by some of the most relevant characterization techniques applied to them. These growth and characterization techniques were carried out mainly in the laboratory "Ramón-Gancedo" at the Instituto de Química Física "Rocasolano" (CSIC), located in Madrid (Spain) and the LEEM-PEEM system at the CIRCE beamline of the ALBA Synchrotron Light Facility, located in Barcelona (Spain). Additionally, the cobalt ferrite ultrathin films growth and characterization experiments were performed at the Jerzy Haber Institute of Catalysis and Surface Chemistry located in Krakow (Poland). The sample preparation for each experiment has been described in each corresponding chapter. Further, micromagnetics simulations have been performed to understand the magnetic behaviour of the experimental systems.

2.1 Deposition techniques

The deposition techniques used in this research have been radio-frequency magnetron sputtering and molecular beam epitaxy. Both have been used to grow oxide or metal films on substrates or films. These techniques are included in the so-called physical vapour deposition processes (PVD). PVD comprises atomistic deposition processes in which a material of interest in solid form evaporates to atoms and is transported in the form of vapour through a vacuum or low-pressure gaseous (or plasma) environment to the substrate, where it condenses [36].

2.1.1 Radio-frequency Magnetron Sputtering

The radio-frequency (RF) magnetron sputtering technique is a type of deposition technique widely used for the growth of thin films, coatings, and multilayers [37, 38, 39]. This technique is performed in a high vacuum chamber. The growth is based on stripping atoms from a target material by charged particles bombardment and the subsequent deposition of the ejected atoms on a substrate.

The experimental system consists of vacuum pumps (rotary and turbomolecular pumps), vacuum chamber, gas trigger/gas supply subsystem, cathode with a built-in magnetron, target, a power source and substrate. The deposition process is described as follow:

Initially, we must start from a vacuum in the chamber. The vacuum pumps reach a pressure of 10^{-6} mbar. Next, gas is introduced into the chamber. Typically, the gasses used are inert as argon since they do not react chemically with the deposition material and thus

do not affect the deposited film's composition. This is called *non-reactive sputtering*. The material's target to grow is located in the cathode, where a negative electronic potential is applied, causing a plasma or glow discharge. This creates positive ions in the gas, which sputter the surface of the film negatively biased. Due to the exchange of momentum between the gas ions and the atoms on the target surface, the latter's extraction occurs. A magnet (magnetron) behind the cathode creates a transversal magnetic field that traps the secondary electrons generated in the target to avoid possible effects to the substrate as an increase of temperature or damage radiation. The magnetron also allows for faster deposition rates because an increase of negative charge in the target promotes the collision with the gas atoms. Finally, the atoms that arise from the target are deposited on the substrate located in the anode forming a film.

Radiofrequency in sputtering is used as the source of electrical potential, mainly for the growth of insulating materials and oxides. Unlike the growth using direct current (DC), RF allows to avoid the charge build-up on the target surface and continue the process for this type of materials [40, 41].

A schematic cycle illustration of the process is shown in figure 2.1.

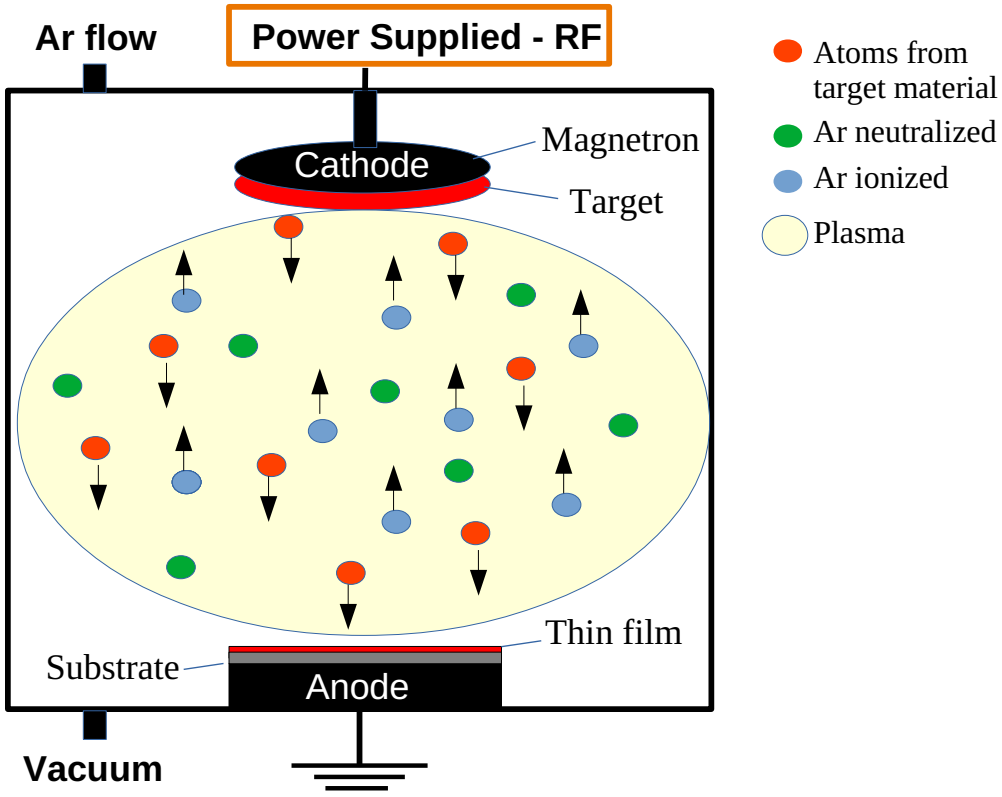

Figure 2.1: Diagram of the RF magnetron sputtering process.

Furthermore, in other cases, the deposition process can be carried out in the presence of gases such as N_2 and O_2 either in place of or in addition to argon or other inert gas. The non-inert gas can interact chemically with the target giving rise to other subspecies such as nitrides and oxides in the deposited samples (*reactive sputtering*). Commonly, a reactive gas is usually combined with inert gas to obtain a given stoichiometry in the case of oxides.

It also influences the characteristics of the deposited film, such as providing a preferential orientation.

Many sputtering systems allow the substrate to be heated to facilitate the diffusion of the deposited atoms and promote the crystalline phase's growth.

RF magnetron sputtering deposition was used for the growth of thin films of SFO. It is important to mention that although a target with the stoichiometric composition ($SrFe_{12}O_{19}$) was used, the deposited thin films do not present the same stoichiometry as the target. In our case, to achieve thin films of SFO, a post-annealing step in air was required.

In RF magnetron sputtering deposition, the deposited thin film is influenced by the deposition parameters such as oxygen flow ratio, sputtering power, base pressure, working pressure, deposition time, substrate-target distance, and substrate temperature [42]. In chapter 6, we will observe how the change in the sputtering power and post-annealing treatment affects the magnetic and structural properties of the strontium hexaferrite thin films, keeping the rest of the parameters fixed. The deposition rate for this method changes according to the values set in each parameter involved. As an example, for the SFO thin film grown with sputtering power of 140 W at room temperature, with a base pressure of 1×10^{-6} mbar, working pressure of 7×10^{-3} mbar, a target-substrate distance 60 mm, Ar/O_2 ratio of 2%, the deposition rate is 5.3 nm per minute.

The magnetron sputtering system used in the laboratory is shown in figure 2.2. To achieve the vacuum conditions, a rotary device is required to reach a pressure of 10^{-2} mbar, and a turbopump then works to reach 10^{-6} mbar. The argon and oxygen flow are computer-controlled, and the source settings are programmed in an 1500 W power supply.

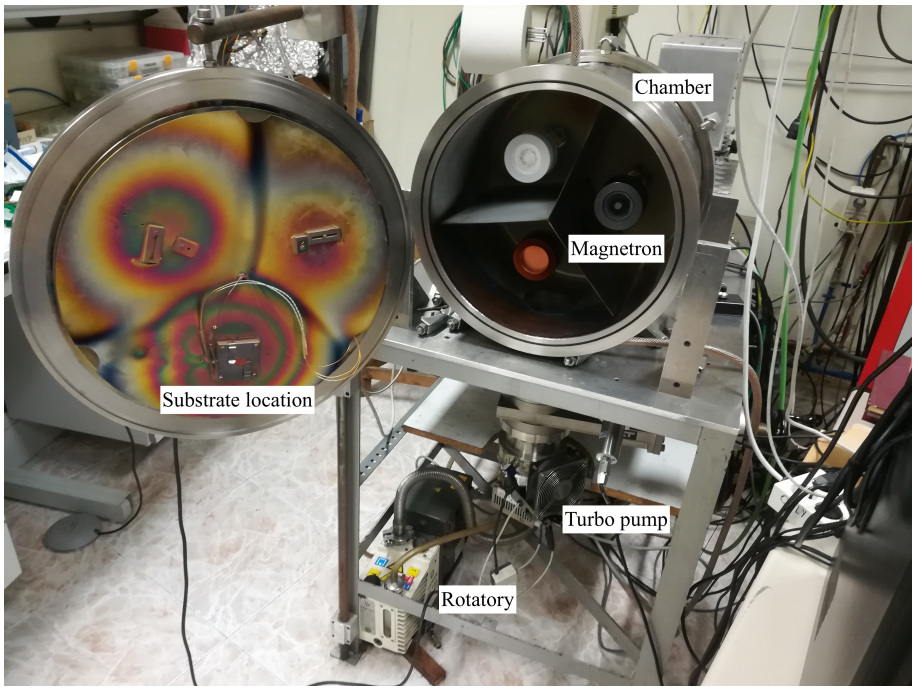

Figure 2.2: Magnetron sputtering system.

2.1.2 Molecular Beam Epitaxy

Molecular beam epitaxy (MBE) is a technique that consists of the evaporation of atoms of a certain element (cobalt, nickel, iron) that are deposited onto a substrate. In many cases, the substrate's sample holder allows heating to increase the diffusion of the atoms on the substrate surface. The deposition process begins with the heating of a tungsten (W) filament, in which electrons are generated. Applying a high voltage (HV), these electrons from the W filament are accelerated against a rod of the desired metal (electron bombardment). This produces a heating of the rod, causing the evaporation of the atoms. Finally, the atoms encounter a substrate on which they are deposited [43, 44].

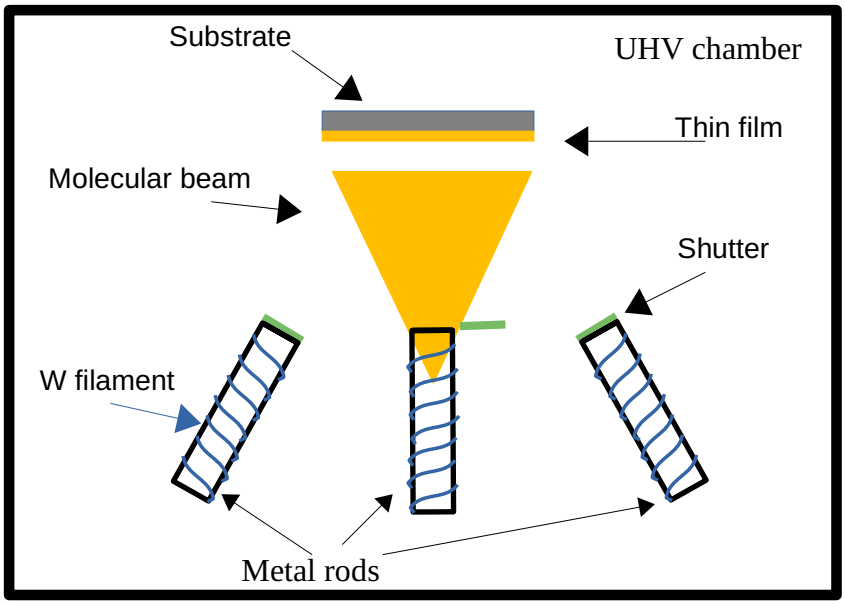

Figure 2.3: Diagram of the molecular beam epitaxy.

MBE technology is used for the growth of single-crystal thin films, quantum wells, superlattices and similar structures. This is a deposition method that allows a precise growth of the samples and that in addition to producing high-quality layers, good control of the thickness, doping, and composition of the samples is achieved [45, 41].

In order to deposit a particular element, the deposition rate of such element is previously calibrated by adjusting the heating power. It should be noted that this method is carried out in an ultra-high vacuum to avoid contamination from residual gas in the growth chamber.

This deposition technique was applied for the experiments of cobalt metal overlayers on oxide SFO films (Chapter 5 and 6). For this purpose, an evaporator with a cobalt metallic rod was used and the settings established were HV = 2 kV, (I_{Fil}) = 2.45 A and (I_{emiss}) = 14 mA. These parameters values typically give one monolayer's growth rate per four minutes (0.06 nm/min).

In comparison with RF magnetron sputtering, the deposition rates for this technique are much lower. This provides precise control of the growth process by MBE. Moreover, we are able to observe using the LEEM/PEEM microscope at CIRCE beamline in ALBA synchrotron how the metal film grows, while in the RF magnetron sputtering system, it is not possible to monitor the growth. Also, another difference between both techniques is that the previous one is performed in a high vacuum (pressure close to 10^{-6}) while molecular beam epitaxy is carried out in an ultra-high vacuum (pressure close to 10^{-9}).

Furthermore, the MBE technique can be used to grow oxides by depositing the metal atoms in an oxidizing background gas. This combination is called oxygen assisted-MBE (O-MBE). O-MBE will be used in cobalt ferrite growth (chapter 7), where the typical oxygen pressure is 10^{-6} mbar.

The molecular beam epitaxy technique was carried out in the ultra-high vacuum system of the CIRCE light line, ALBA Synchrotron, and the Jerzy Haber institute's ultra-high vacuum system.

2.2 Characterization methods

Throughout the thesis, different analysis techniques have been applied that have helped characterize the samples under study, determining their morphology, chemical composition, structural and magnetic properties. All characterization techniques used in this research, the location where they were performed and the personnel involved in each of them are described below:

- Transmission electron microscopy (TEM) [46] was performed at Josef Stephan Institute (Ljubljana, Slovenia), at the latter location in collaboration with Dra. Petra Jenus.

- Transmission X-ray Microscopy (TXM) [47] was performed at the MISTRAL beamline of the ALBA Synchrotron Light Facility in collaboration with Dra. Eva Pereiro.

- X-ray diffraction (XRD) [48] was performed at Instituto de Ciencia y Tecnología de Polímeros (CSIC) in collaboration with Pedro Gonzalez.

- X-ray photoelectron spectroscopy (XPS) [49] was performed at the Instituto de Química Física "Rocasolano" (CSIC).

- Mössbauer spectroscopy was performed at the Instituto de Química Física "Rocasolano" (CSIC) and Jerzy Haber Institute of Catalysis and Surface Chemistry (Krakow, Poland), at the latter location in collaboration with Dra. Nika Spiridis and Dr. Jozef Korecki.

- Vibrating-sample magnetometer (VSM) [50, 51] was performed at the Instituto de Química Física "Rocasolano" (CSIC) and at Josef Stephan Institute (Ljubljana, Slovenia), in collaboration with Dra. Petra Jenus.

- X-ray absorption spectroscopy (XAS), X-ray magnetic circular dichroism (XMCD) and Photoemission electron microscopy (PEEM) were performed at the CIRCE beamline of the ALBA Synchrotron Light Facility in collaboration with Dra. Lucia Aballe and Dr. Michael Foerster.

- Rutherford backscattering spectrometry (RBS) [52] was performed at the Centre for Micro Analysis of Materials (CMAM, Universidad autónoma de Madrid) in collaboration with Patricia Galán.

- Raman spectroscopy [53, 54] was performed at Instituto de Estructura de la Materia (CSIC) in collaboration with Dr. Santiago Sánchez.

- Atomic force microscopy (AFM) [55, 56] was performed at the Instituto de Química Física "Rocasolano" (CSIC).

- Auger spectroscopy (AES) [57] was performed at Jerzy Haber Institute of Catalysis and Surface Chemistry (Krakow, Poland) in collaboration with Dra. Nika Spiridis and Dr. Jozef Korecki.

- Low-energy electron diffraction (LEED) [58] was performed at Jerzy Haber Institute of Catalysis and Surface Chemistry (Krakow, Poland) in collaboration with Dra. Nika Spiridis and Dr. Jozef Korecki.

- Scanning Tunneling Microscopy (STM) [59, 52] was performed at Jerzy Haber Institute of Catalysis and Surface Chemistry (Krakow, Poland) in collaboration with Dra. Nika Spiridis and Dr. Jozef Korecki.

In particular, the following section will explain in detail the characterization techniques most relevant in this thesis: Mössbauer spectroscopy, XAS, XMCD and PEEM. As we will see in later chapters, these techniques have been crucial in understanding the results obtained in this thesis.

2.2.1 Mössbauer spectroscopy

Mössbauer spectroscopy is a powerful technique that has been used throughout this research for the characterization of both SFO platelets and thin films of cobalt ferrite and SFO. The main reason is that it allows us to characterize iron compounds providing information about the chemical, structural and magnetic state of the iron cations in a particular phase.

This spectroscopy is based on the Mössbauer effect, that is, on recoilless resonant absorption of a γ quanta by atomic nuclei [60, 61, 62, 63, 64]. Let us assume that a nucleus in an excited state emits a γ ray to return to its ground state. If the nucleus is isolated, it will recoil to maintain the momentum and energy conservation, therefore the gamma ray will have an energy given by:

$$E = E_\gamma - E_R \tag{2.1}$$

where E_γ is the energy of the nuclear transition and E_R is the recoil energy,

$$E_R = \frac{E_\gamma^2}{2Mc^2} \tag{2.2}$$

being M is the mass of the nucleus and c the speed of light. If in the vicinity of that nucleus there is a second isolated one of the same type, the nuclear resonant absorption will not occur since (i) the emitted γ ray will not have the required energy and (ii) this absorber nucleus will also recoil. Thus, in the case of isolated nuclei, the emission and absorption bands are separated by twice the recoil energy, and the overlap of the bands is not possible. In the case of ^{57}Fe, the recoil energy for the 14.4 keV nuclear transition is about 10^6 times higher than the linewidth of the emission and absorption bands what is really a huge amount.

However, if the nuclei belong to solids, the recoil energy will be shared by all the other atoms in the crystal, and the recoil energy will be negligible, providing the emission of the gamma ray will not affect the vibrational state of the atoms in the lattice significantly. The fraction of γ rays that are emitted and absorbed without energy loss by nuclear recoil is called **recoilless free fraction** (or f factor). This factor that defines the probability of observing a Mössbauer event can be written, within the Debye model of the solid, can be written as:

$$f = \exp\left\{-\frac{3}{2}\frac{E_R}{K_B\theta_B}\left[1 + \frac{2\pi^2}{3}\left(\frac{T}{\theta_B}\right)^2\right]\right\} \tag{2.3}$$

where θ_B is Debye temperature, T corresponds to sample temperature and K_B is the Boltzmann constant.

Therefore, having a large f value implies having moderate energy of the nuclear transition and a large Debye temperature compared with the temperature of the nucleus. Additionally, a favourable isotopic abundance is also needed. As a consequence of this, only a few transitions of a small number of isotopes are appropriate to observe the Mössbauer effect. In practical terms, observing the Mössbauer effect at room temperature is only feasible for ^{57}Fe, ^{119}Sn, ^{121}Sb and ^{151}Eu.

As far as this work is concerned, we will consider in the following only the 14.4 keV transition of ^{57}Fe. The parent radioactive nucleus of ^{57}Fe is ^{57}Co (figure 2.4). ^{57}Co decays by electron capture into a metastable ^{57}Fe state (I = 5/2). As the deexcitation scheme indicates, the I = 5/2 excited state can decay directly to the ground state (I = 1/2) by emitting a γ quantum of 136.3 KeV or indirectly through an intermediate excited state (I = 3/2) by emitting a γ quantum of 122 KeV that in its turn decays to the ground state through the emission of γ radiation of 14.4 KeV which is the adequate to observe Mössbauer effect.

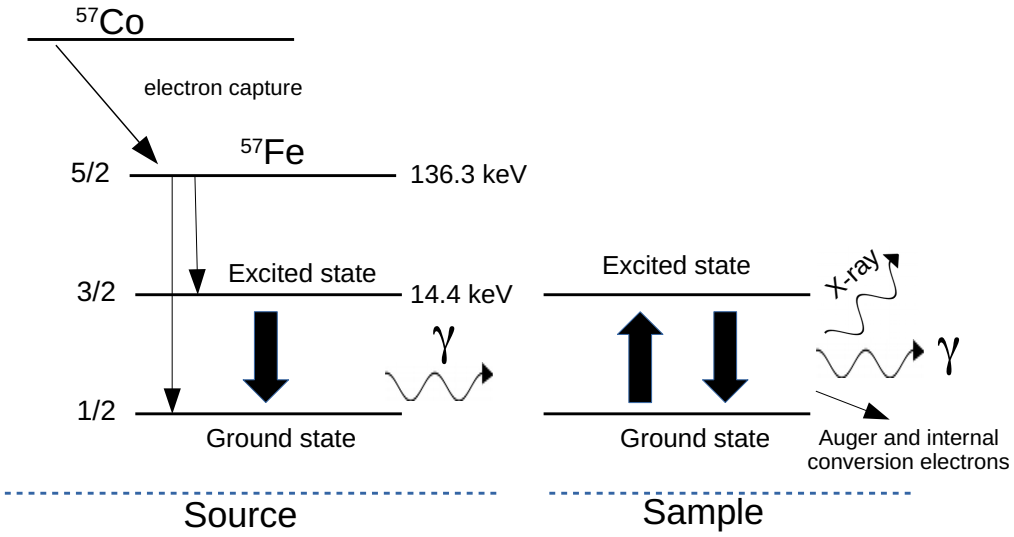

Figure 2.4: Symbolic illustration of the source (decay of ^{57}Co to ^{57}Fe) and the absorber in a Mössbauer experiment.

However, even if the conditions mentioned above to observe the Mössbauer effect are fulfilled, this does not guarantee its occurrence. The reason is that the interaction of the atoms in the solid with its environment (**hyperfine interactions**) modifies the nuclear levels. Therefore if the Mössbauer nuclei in the emitter and the absorber are not in identical environments, the resonance will be destroyed. In Mössbauer spectroscopy, in order to reestablish the resonant absorption, the source is moved with respect to the absorber, which remains stationary. In this way, the frequency (energy) of the emitted photons is modified by the Doppler effect to match the difference in energy of the nuclear levels in the emitter and the absorber and achieve the nuclear resonant absorption. Therefore, a Mössbauer spectrum is the representation of the number of counts collected in a detector as a function of the velocity applied to the emitter (source) with respect to the absorber (sample).
Mössbauer spectroscopy allows the quantification of the hyperfine interactions through the determination of several hyperfine parameters. The main hyperfine interactions that can be observed in the Mössbauer spectrum are the electric monopole, the electric quadrupole

and the magnetic dipole interactions, which are characterized by the hyperfine parameters isomer shift, quadrupole splitting and hyperfine magnetic field, respectively (figure 2.5).

Electric monopole interaction: it originates from the Coulomb interaction between the nuclear charge distributed over a finite, spherical nuclear volume and the charge density of the *s* electrons which can penetrate within this nuclear volume. As this monopolar interaction does not depend on the angular momentum, instead of level splitting, a shift of the nuclear energy levels occurs (figure 2.5a). Hence, the isomer shift (δ) is the doppler velocity supplied to the source in order to overcome the difference in energy between the nuclear levels of the emitter and the absorbed originated by the differences in s electron density in both nuclei. Mathematically it can be expressed as:

$$\delta = \frac{2\pi}{5} Ze^2 \left\{ |\Psi(0)|_a^2 - |\Psi(0)|_{em}^2 \right\} \left(\langle R_e^2 \ - \ R_g^2 \rangle \right) \tag{2.4}$$

where Ze is the nuclear charge, $\langle R^2 \rangle$ the average squared nuclear radius, $|\Psi_0|^2$ the electron density at the nucleus. Additionally, *a* refers to the absorber, *em* to the emissor, *e* to the excited and *g* to the ground state.

Usually, the isomer shift value of the sample under study is referred to the centroid of the spectrum of a standard compound. The most common reference material used is α-iron measured at room temperature. It follows from the above that any circumstance that affects the *s* electron density within the absorber nuclei will be reflected in the isomer shift: oxidation state, spin state, coordination, the electronegativity of the ligands, etc. The isomer shift is therefore used to obtain information on the chemical state of the absorber.

Electric quadrupole interaction: it arises from the interaction between the electric quadrupole moment of the nucleus, which presents a deviation of the charge density from the spherical symmetry and an electric field gradient (EFG) that can be acting in the nuclear site. This interaction partially breaks the 2I + 1 degeneracy of the nuclear spin levels $I > -\frac{1}{2}$. In the ^{57}Fe, the original degenerate excited state is split into two states with $m_I = \pm\frac{3}{2}$ and $m_I = \pm\frac{1}{2}$ (figure 2.5b). This is shown in the Mösbauer spectrum by the occurrence of two lines (doublet). The separation between the lines of the doublet is the quadrupole splitting (ΔE_Q), and it is defined by:

$$\Delta E_Q = \frac{e^2 qQ}{2} (1 + \frac{\eta^2}{3})^{1/2} \tag{2.5}$$

where Q is the principal component of the quadrupole electric moment, eq is the component z of the electric field gradient tensor, EFG, (V_{zz}) and η is the asymmetry parameter, a magnitude that depends on the EFG tensor being η=(V_{xx}-V_{yy})/V_{zz}.

The EFG can be originated by an asymmetric distribution of the lattice charges around the Mössbauer atom or by an asymmetric distribution of its valence electrons. Therefore, the quadrupole splitting can provide information about the oxidation state, molecular symmetry, spin state and coordination of the Mössbauer atom.

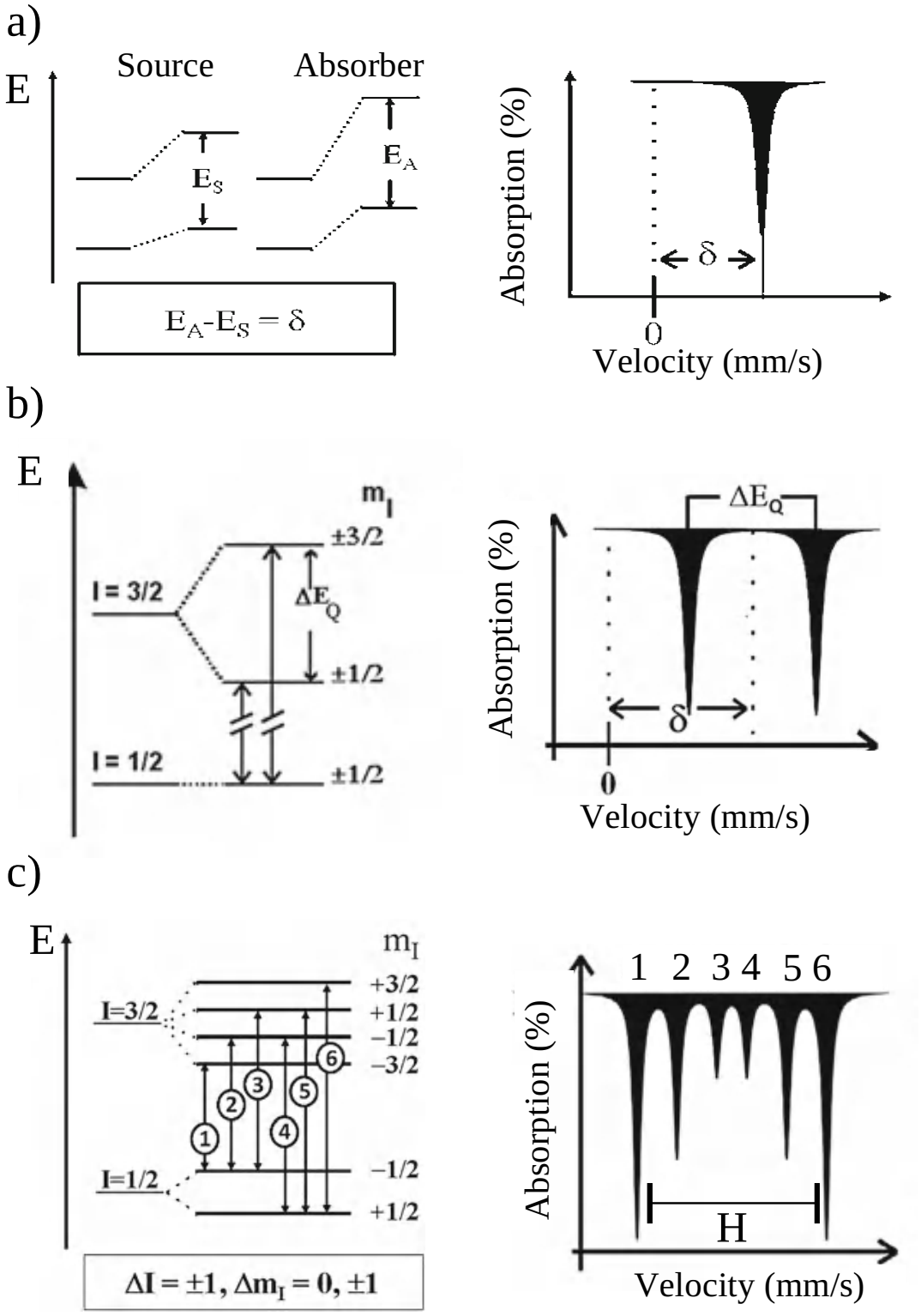

Figure 2.5: Left: schematic diagram showing the effect of the various hyperfine interactions on the nuclear energy levels a) electric monopole interaction, b) quadrupole electric interaction, c) magnetic dipole interaction. Right: corresponding Mössbauer spectra and hyperfine parameters. Illustration reprinted from Ref. [63].

Magnetic dipole interaction: this occurs as a result of the interaction between the magnetic moment associated to the nuclear spin and the net magnetic field that can exist at the nuclear site, producing the so-called Zeeman splitting. The variation of energy levels is described as:

$$E_m = -g_N \mu_B H_0 m_I \tag{2.6}$$

where g_N is the Landé nuclear factor, μ_B is the Bohr magnetron, H_0 is the hyperfine magnetic field and m_I is the component nuclear spin. The magnetic interaction breaks the degeneracy of the nuclear spin levels I $\neq$ 0 and splits each level into 2I+1 equally spaced sublevels. The permitted transitions between these sublevels are governed by the selection rules $m_I = 0,\pm 1$ and $\Delta I = 1$. This gives place to six allowed transitions reflected in six peaks ("sextet") observed in the experimental spectra as illustrated in figure 2.5c. The hyperfine field H is proportional to the separation between the first and the sixth peaks of the sextet. This last hyperfine parameter indicates if the sample is or not magnetically ordered and quantifies the magnetic field magnitude felt by the Mössbauer nucleus.

Further, the relative intensity of the sextet absorption lines indicates the average direction of the magnetization in the sample respect to the γ rays direction. The spectral areas follow the ratio 3:x:1:1:x:3 where x is a function of θ (the angle between the direction of the incoming γ-rays and the average direction of the magnetic hyperfine field), $x = 4\sin^2\theta/1+\cos^2\theta$ [60, 61]. A value x = 0 corresponds to a perpendicular orientation of the magnetization respect to the sample plane ($\theta = 0°$) while a value x = 4 indicates an in-plane orientation ($\theta = 90°$).

Experimentally, a Mössbauer spectrometer is composed of a Doppler velocity transducer, the γ ray source, the sample, a radiation detector, a usual chain of nuclear electronics (preamplifier, spectroscopic amplifier and HV power units), a single channel analyzer or discriminator and a multichannel analyzer which is synchronized with the transducer.

In the transmission mode, the γ rays from the source pass through the sample and are collected in a detector, usually a proportional counter (figure 2.6a). A Mössbauer spectrum, then, is a collection of negative peaks appearing at the velocities (energies) at which the nuclear absorption has taken place in the sample. **Transmission Mössbauer spectroscopy** is used for the study of compounds in bulk, and in this thesis, it has been employed for the characterization of SFO commercial powders, platelets and films thicker than 1 μm. All these samples have been measured at room temperature, and 22 K using a He-closed cycle cryorefrigerator [65].

Other variants of this spectroscopy, based on the detection of conversion and Auger electrons, can be used for surface studies. After the nuclear resonant absorption, the nucleus left in an excited state can decay to the ground state by means of the emission of a γ quanta or via an alternative process called **Internal Conversion** which results in the direct ejection of electrons from various atomic shells (predominantly, from the K shell). Since the electrons can travel a limited range within the solid, they contain mainly surface information. In the case of ^{57}Fe, the probability of decaying via an Internal Conversion process is approximately nine times higher than by the emission of a 14.4 keV γ ray. The most abundant conversion electrons come from the K shell and have an energy of 7.3 keV.

After the nuclear relaxation, which gives place to the emission of conversion electrons, an atomic relaxation process takes place, which results in the emission of Auger electrons of different energies as well as fluorescent X-rays [66]. The Mössbauer technique based on the detection of all the electrons emitted by the sample irrespectively of their energy is called **Integral Conversion Electron Spectroscopy (ICEMS)**. This mode provides information up to a depth of 300 nm, although more weighted to the uppermost 50 nm.

In this thesis, we have used ICEMS for the characterization of SFO films (Chapter 6). Given the limited range of the electrons, in ICEMS, the sample is placed inside the detector, figure 2.6b. In our case, the detector used is a parallel plate avalanche counter that works with acetone gas at a pressure of about 50-60 mmHg [67]. The sample is one of the electrodes (ground), while the other electrode is a plastic plate covered by graphite to which an HV in the range 1000-1600 V is applied. In this detector, the electrons emitted from the sample ionize the gas and the charge generated is collected in the front electrode. Since we have collected the electrons emitted from the sample and not the photon transmitted through it, the resultant spectrum consists of positive peaks.

It can be shown that the surface sensitivity of Mössbauer spectroscopy in the electron detection mode can be enhanced by using a channeltron as an electron detector. A channeltron presents the maximum detection efficiency for electrons with energies around 1 KeV. In Mössbauer spectroscopy, we have a large number of resonant Auger and shake off electrons [68] of low energies, and therefore with an inelastic mean free path of a few nanometers. Therefore, if a small positive voltage is applied to the entrance cone of the channeltron we can enhance the detection efficiency of these low energy electrons making the technique more surface sensitive. This mode is known as **Integral Low Energy Electron Mössbauer Spectroscopy (ILEEMS)**. Since this technique implies the use of a channeltron, a high or ultra-high vacuum system is required (figure 2.6c). We have also used ILEEMS for the characterization of SFO films.

The three Mössbauer spectroscopy modes explained above are available in the laboratory "Ramón-Gancedo" at the Instituto de Química Física "Rocasolano" (CSIC). The laboratory's room where is performed the Mössbauer measurements is shown in the image 2.7a. Lead plates are used to block the radiation coming from the source. Behind these plates are the source attached to the transducer, the sample, the detector and the preamplifier. Figure 2.7b shows the alignment of the source, sample and detector for the Mössbauer experiment carried out in transmission mode. The rack mounts the electronic devices corresponding to the spectroscopic amplifier, the wave function generator, which is responsible for the movement of the source (transducer), HV power units, discriminator and multichannel analyzer. The wave function generator, HV and amplifier modules are presented respectively in figure 2.7c. The data acquisition is obtained by computer software, which allows the selection of the pulses/energies from the multichannel analyzer corresponding to the spectrum.

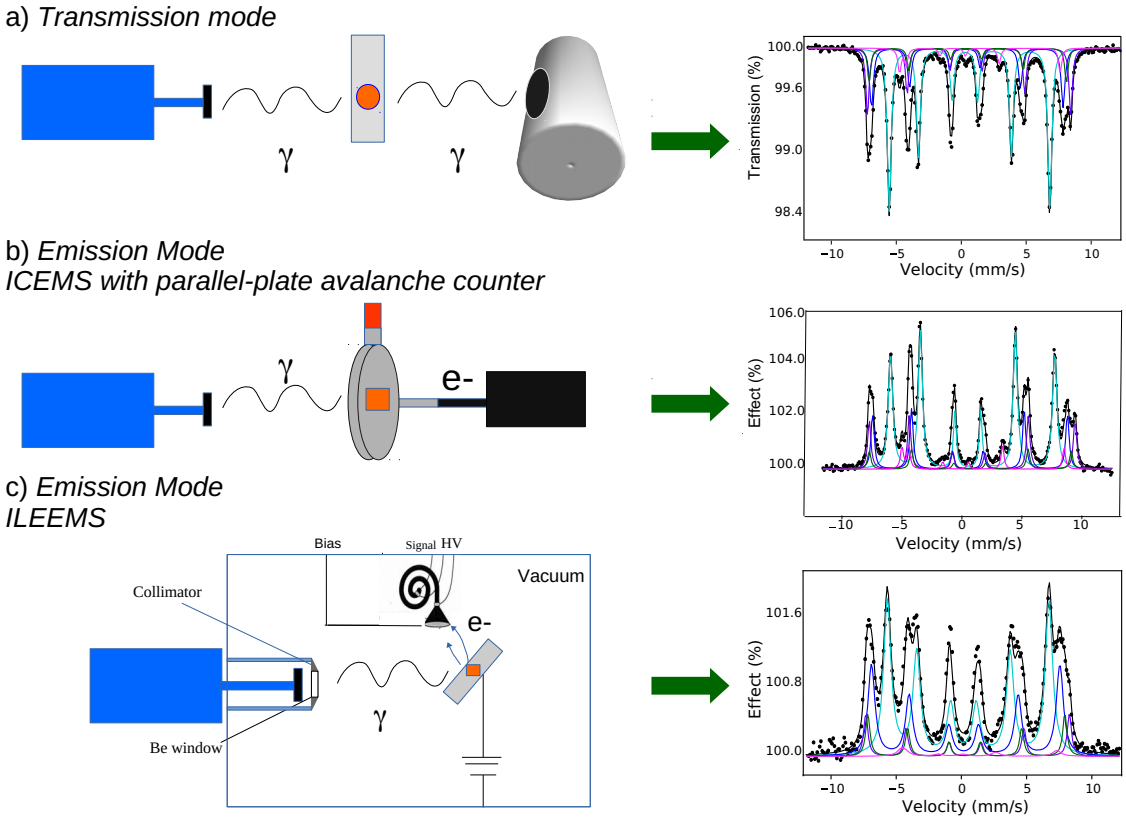

Figure 2.6: Schematic illustration of the configuration of different spectrometers and an example of the Mössbauer spectrum obtained from each one. a) Transmission mode detects the γ-rays that have passed through the sample. The spectrum extracted from the technique corresponds to SFO commercial powders. b) Emission mode, the electrons from the sample are collected using an avalanche counter. The spectrum obtained is referred to a SFO thin film. c) ILEEMS also collects electrons from a sample being a much more superficial analysis. The spectrum corresponds to SFO platelets.

This spectroscopy was also carried out at the laboratory from Jerzy Haber Institute of Catalysis and Surface Chemistry, located in Krakow. The laboratory presents a multi-chamber ultra-high vacuum system to prepare and characterize *in-situ* samples. In such multi-chamber between different characterization techniques is include an CEMS spectrometer (figure 2.8). This fact provides a complete characterization of iron compound films grown *in-situ* and avoid atmosphere contamination or oxidation. Indeed, there are not many systems that allow measuring Mössbauer *in-situ*. The CEMS spectrometer, composed of a channeltron to detect electrons emitted from the sample, and a Mössbauer ^{57}Co(Rh) γ-ray source outside the vacuum system, has been described in detail Ref. [69]. A liquid nitrogen bottle can be installed in the circuit in order to perform experiments at low temperatures. This system has been used for the characterization of cobalt ferrite ultrathin films (chapter 7).

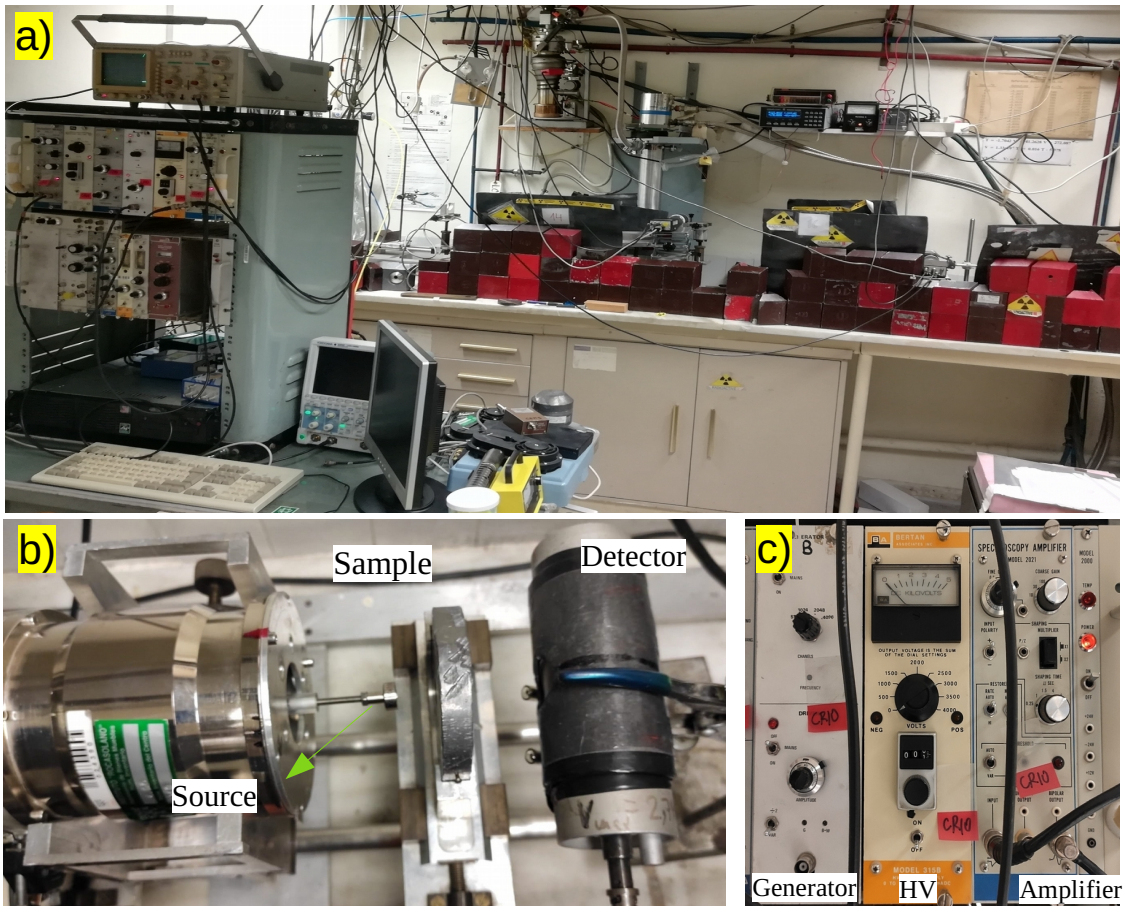

Figure 2.7: a) Room of Mössbauer spectroscopy experiments. b) Mössbauer measurement in a transmission configuration. c) Electronic devices: waves function generator, HV source and the amplifier module.

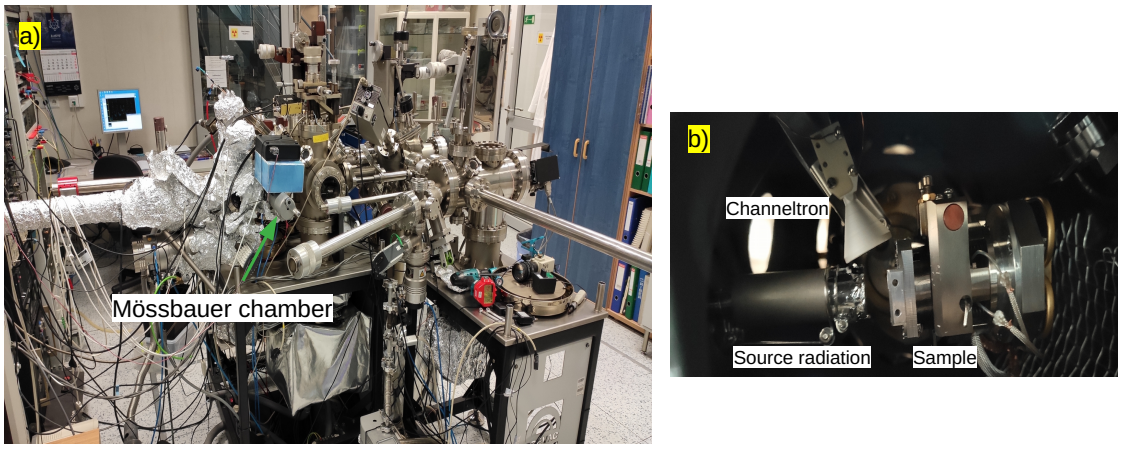

Figure 2.8: a) Multi-chamber UHV system from Jerzy Haber Institute of Catalysis and Surface Chemistry. The green arrow points to the chamber where Mössbauer measurement is performed. b) Sample position with respect to the source (γ radiation) and to the channeltron (detector) in the Mössbauer experiment.

2.2.2 X-ray absorption spectroscopy (XAS)

This spectroscopy allows obtaining information about the crystal structure and chemical composition of the sample. This technique has been used to characterize SFO platelets, thin films and the metallic layers on top of them (chapter 4, 5 and 6).

When an atom absorbs an X-ray photon, an electron from the inner atomic shell (K, L or M) absorbs the photon's energy and is excited to an unoccupied valence state. This electron leaves a hole in the inner shell that is filled with another electron from another upper shell, which can be de-excited by photon emission or by the escape of an electron of the outer shell. This electron is called Auger. Figure 2.9 depicts the process. On the way of the Auger electron to the surface, it causes a cascade of secondary electrons to escape from the sample [70].

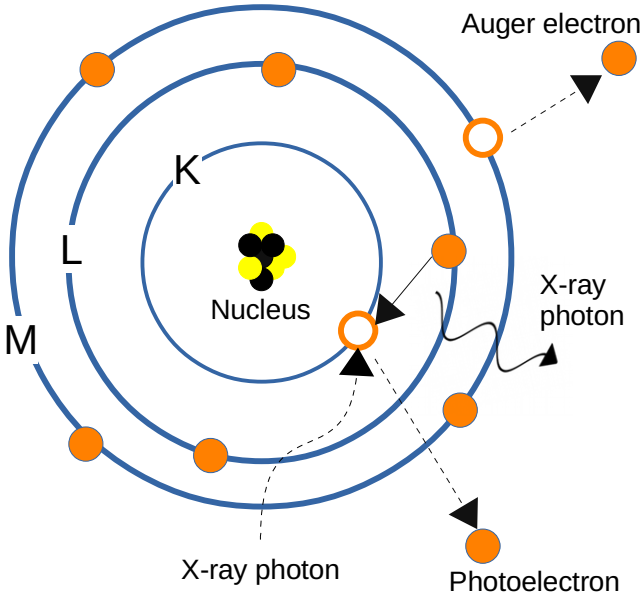

Figure 2.9: Interaction process when a photon illuminates an atom and the processes it triggers.

Thus, the spectrum resulting from the technique corresponds to the photons or electrons emitted from the sample when the X-ray beam interacts with the matter vs the incident beam energy. This spectrum identifies the electronic transitions of a particular element. The electronic transitions provide information about the atom, such as its oxidation state or its crystalline field. Typically, the method used to measure X-ray absorption is the total electron yield detection (TEY). This mode is based on collecting all the electrons that escape from the sample, both those produced by photoemission as well as Auger electrons and secondary ones being these latter electrons that contribute the most to the signal [71].

It should be noted that for an electron spectroscopy to work, the electrons have to exit the sample. The average distance an electron can travel in a solid between inelastic collisions is called the inelastic mean free path of electrons (IMFP). The "universal curve" represents the trend of IMPF in function of the energy for many elements (figure 2.10) [72]. The XAS TEY signal corresponds mostly to the secondary electrons, which correspond to those

with low kinetic energy. So, this technique supports the sample's characterization with high surface sensitivity (order to nanometers of depth), although this surface sensitivity is typically lower than for XPS.

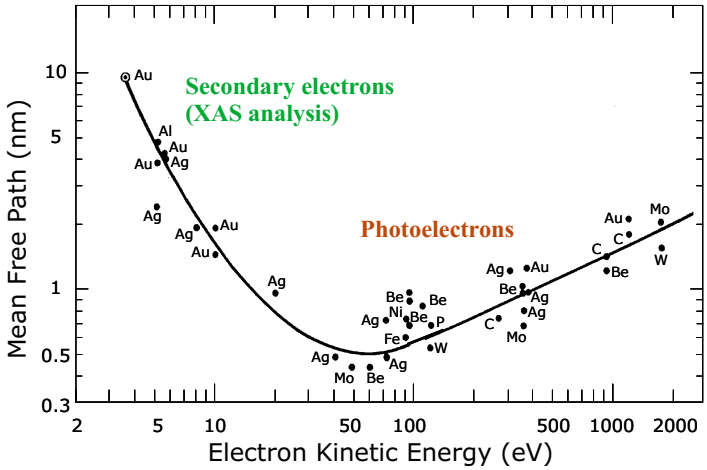

Figure 2.10: Universal curve plot of electron ineslatic mean free path of various elements. Reprinted from Ref [72].

Specifically, in this thesis, we have studied XAS spectra at the $L_{2,3}$ edge transitions to characterize the iron and cobalt atoms' properties in our samples.

These transitions correspond to electrons excited from the 2p core levels to the unoccupied 3d electronic states (holes). Due to the spin-orbit splitting produced in the 2p core shells, the spectrum recorded shows two characteristic absorption peaks, L_3 and L_2, which correspond to the initial states $2p_{3/2}$ and $2p_{1/2}$ core shells electrons, respectively. In addition, the XAS spectrum intensity is directly correlated with the number of holes in the 3d core shell. Figure 2.11 shows typical XAS spectra for iron at the edge $L_{2,3}$ in different compounds.

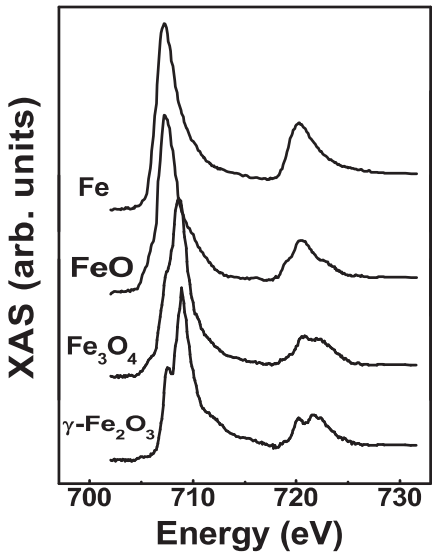

Figure 2.11: XAS spectra at the Fe $L_{2,3}$ edges of metal iron and iron oxides reference compounds. Extracted from Ref. [73]

2.2.3 X-ray magnetic circular dichroism (XMCD)

X-ray magnetic circular dichroism (XMCD) is the difference in absorption that a ferro or ferrimagnetic material undergoes when irradiated with X-rays with left- and right-circularly-polarized light [70, 74]. This absorption provides detailed information on the electronic and magnetic structure of an element. For example, the oxidation state, the crystal symmetry and the spin and orbital magnetic moments can be determined. As we will see throughout the thesis, the elements characterized by XMCD have been iron and cobalt.

It is well known that the magnetic properties of 3d transition metals are mainly determined by their "d" valence electrons [75, 76]. The spin magnetic moment arises from the difference between the number of spin-up and spin-down electrons. This imbalance is equivalent to the difference in the spin-up and spin-down holes states. Considering that the intensity of the XAS spectra is proportional to the 3d holes, the magnetic moment of spin can be obtained as a result of the XAS spectra with different polarizations. This is the principle of XMCD phenomenon, which can explain as:

1. We have an atom of a transition metal whose 2p core-shell is divided into two levels, j = 3/2 (L_3 edge) and j = 1/2 (L_2 edge), where spin and orbit are coupled parallel and antiparallel, respectively.

2. Electrons are excited with a preferential direction of spin up (or down) depending on the circular polarization of the illuminating X-ray beam. As the light is polarized in two opposite directions, photoelectrons with opposite spin directions are obtained (figure 2.12a). Note that from the $2p_{3/2}$ level X-rays with positive helicity (μ^+) excite 62.5% spin up electrons and those with negative helicity (μ^-) excite 37.5% spin up electrons, while from the $2p_{1/2}$ level the opposite happens.

3. These spin polarized excited photoelectrons are directed to the unoccupied states of the 3d valence band. As it is not possible to change the spin direction in an electric dipole transition, polarized excited electrons from the 2p shell (for instance, with spin-up configuration) can only occupy spin-up 3d hole bands. The spin-split valence shell acts as a detector for the spin of the excited photoelectron. Thus, the XMCD effect depends on the relative orientation between the photons' helicity and the sample magnetization direction. The XMCD signal scales with the scalar product between those two quantities [77, 78, 79]. For maximum dichroism effect, the photon spin direction needs to be aligned with the sample magnetization direction (figure 2.12b).

Conventionally, the XMCD spectrum is obtained as the difference between the two XAS spectra with the circular polarization vector parallel and antiparallel to the external magnetic field applied to the sample. Specifically, XAS spectra are measured in total electron yield using a positive (μ^+) and negative (μ^-) helicity light and for both magnetic fields applied (M^+, M^-), normalizing by the incoming X-ray beam intensity. The resulting XMCD spectra are thus:

$$XMCD(M^+) = XAS(M^+, \mu^+) - XAS(M^+, \mu^-)$$
$$XMCD(M^-) = XAS(M^-, \mu^-) - XAS(M^-, \mu^+)$$

The final XMCD spectrum is the average of the XMCD (M^+) and XMCD (M^-) spectra in order to remove the non-magnetic interaction [80]. This method was used in the SFO platelets spectra acquired in the BOREAS beamline [81] at the ALBA synchrotron (chapter 4).

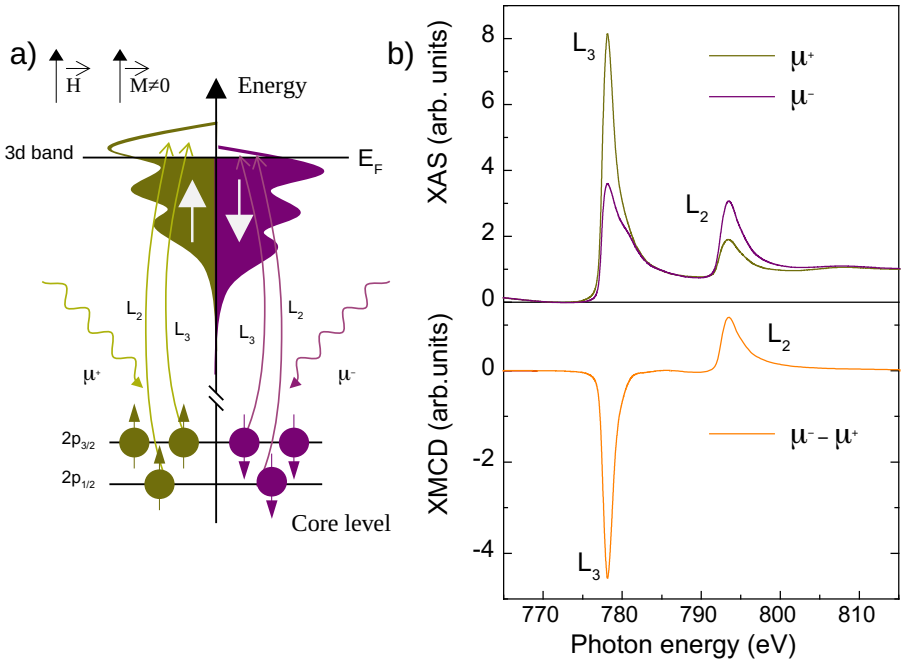

Figure 2.12: a)The XMCD effect illustrated for the L-edge absorption in cobalt metaL. b) Top: XAS spectra at Co L-edge at different X-ray polarization. Botton: XMCD spectrum from the difference between the XAS spectra. Figure reprinted from Ref. [71].

Another method used to acquire XAS and XMCD spectra in this research has been using the X-PEEM microscope at CIRCE beamline. This method will be explained in the LEEM-PEEM microscope section.

Sum Rules

An important aspect of the XAS and XMCD spectra is that they can be used to estimate the spin and the orbital part of the magnetic moment. The sum rules [82] relates the integrated intensities on the absorption edges of these spectra with the spin and orbital moments. The sum rules correspond to the following equations:

$$m_{orb} = -\frac{4q}{3r} N_h \tag{2.7}$$

$$m_{spin} = -\frac{6p - 4q}{r} N_h \left(1 + \left(\frac{7\langle T_z \rangle}{2\langle S_z \rangle}\right)\right) \tag{2.8}$$

where m_{orb} and m_{spin} are the orbital and spin magnetic moments in units of μ_B/atom, respectively. N_h in the number of empty 3d states (holes) of the specific transition metal. $\langle T_z \rangle$ is the expectation value of the magnetic dipole operator, and $\langle S_z \rangle$ is the half of m_{spin} in Hartree (atomic units). It has to be assumed that $\langle T_z \rangle$ is zero or must be known from other experiments or theoretically approximated [70]. The values of p, q and r are the integrals of the absorption edges intensities:

$$p = \int_{L_3} \left(\mu^+ - \mu^-\right) dw \tag{2.9}$$

$$q = \int_{L_3+L_2} \left(\mu^+ - \mu-\right) dw \tag{2.10}$$

$$r = \frac{1}{2} \int_{L_3+L_2} \left(\mu^+ + \mu^-\right) dw \tag{2.11}$$

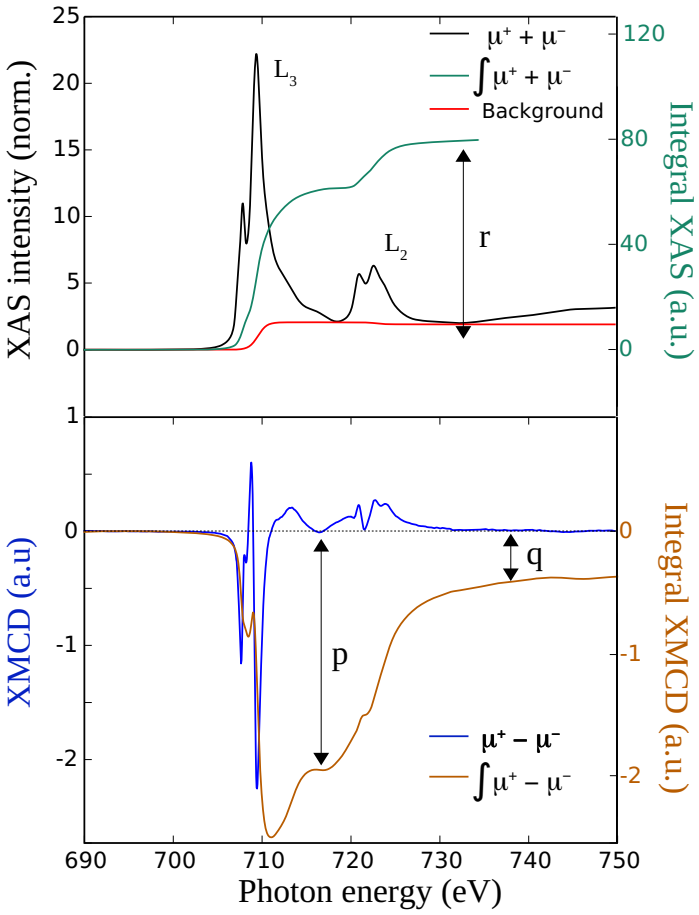

Figure 2.13: $L_{2,3}$ XAS (upper panel) and XMCD (lower panel) spectra of Fe from strontium ferrite platelets sample. The integrals from XAS and XMCD spectra are shown indicating p, q and r.

2.2.4 LEEM/PEEM microscope

Many of the experiments performed during the research presented in this thesis have been carried out at the ALBA synchrotron. A synchrotron is a powerful X-ray source that, together with the analysis techniques available in the beamline[1], it has made possible a complete characterization of the samples.

Synchrotron light is electromagnetic radiation emitted by charged particles, moving at a relativistic speed in an accelerator when their trajectory deviates on a single curved trajectory. The three types of magnet structures carry out the generation and deflection of the charged particles: bending magnets, undulators, and wigglers [83, 84].

The CIRCE beamline allows doing low-energy electron microscopy (LEEM), and photoemission electron microscopy (PEEM) [74]. The latter, combined with X-rays from synchrotron light (X-PEEM) and X-ray absorption and dichroism techniques (XAS and XMCD, respectively), are the methods used in this thesis. The system works at ultra-high vacuum (pressure $\sim 10^{-9}$ mbar). Figure 2.14 represents the LEEM-PEEM instrument located in the CIRCE beamline.

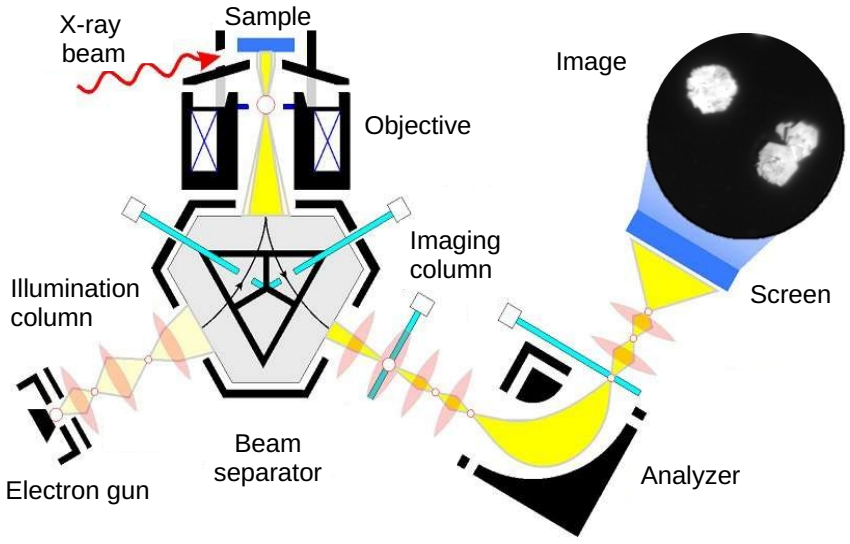

Figure 2.14: Schematic representation of the LEEM-PEEM instrument of the CIRCE beamline. Modified image of the poster displayed on the ALBA synchrotron website. The image shown corresponds to the characterization of SFO platelets by photoemission electron microscopy.

A LEEM provides images of the sample surface at a field of view of several microns with 10 nm lateral resolution in real-time imaging the electrons reflected from the sample [85, 77]. For this, the following mechanism occurs:

- First, a high-energy electron beam (up to 20 keV) is generated in the illumination

[1] It is an experimental area of the synchrotron, which is made up of a set of equipment that directs the X-rays to the sample and allows analysis through different characterization techniques according to the incorporated instrumentation.

column. The beam enters into a beam separator or splitter, which turns the beam towards the sample. This is generated by a magnetic field in a prism deflector.

- The electrons are decelerated before reaching the sample due to an electrical potential applied between the objective lens and the sample. The energy at which they reach the sample is between 1-100 eV. The objective lens again accelerates the electrons reflected from the sample. Also, a diffraction pattern from the surface forms at the back focal plane of the objective lens.

- The electron beam passes back through the separator that directs it to the imaging column. This part is composed of a set of lenses that magnifies either a real space image formed by the reflected electrons or their diffraction pattern.

- Finally, the electron beam hits a multi-channel plate detector (MCP). This multi-channel plates amplifies the signal and retransmits it to a fluorescent screen to obtain images in real-time on a CCD camera.

PEEM also provides high spatial resolution (20 nm) real-time surface images and works similarly to LEEM. The difference between both is that the resulting image, instead of being formed with the electrons reflected in the sample, is formed by the photoelectrons from the sample surface due to the interaction with ultraviolet radiation or X-rays (X-PEEM). The synchrotron supplies this radiation.

The mechanism by which the image is obtained follows the same steps as for LEEM except that since an electron source is not used, the illumination column is not necessary. The sample illuminated with X-ray radiation produces photoelectrons. These photoelectrons are accelerated in the objective lens to form an image. The electron beam will pass through different electromagnetic lenses (image column) being finally detected on a CCD camera. In addition, there is an energy analyser that can select the energy of the electrons that form the final image. This is done to reduce chromatic aberrations in the image as well as to select an energy range for performing photoemission spectroscopy.

The LEEM microscope can provide information on the morphology of the sample surface as well as its structure. However, as it depends on the reflection of electrons at the surface, a sample that is crystalline and not rough is required. This drawback does not affect PEEM.

Further, as it has been previously advanced, most of the absorption and dichroism spectra in this thesis have been obtained using X-PEEM. Following this method, it is essential to mention that the spectra's measurement is performed in remanence. This fact is because in PEEM, applying a magnetic field to magnetize the sample in a specific direction affects the electrons' path emitted from the sample.

Likewise, for the XAS and XMCD spectra obtention, a pair of XAS images were acquired with opposing X-ray helicities, measuring the spatially resolved emission of secondary electrons at low kinetic energy. The two images are then added and subtracted pixel by pixel to provide the averaged XAS image and the XMCD image, respectively. When the full spectrum is required, a stack of images is made for each energy. Thus, the XAS spectrum is obtained from the averaged intensities of the pair of XAS images as a function of the

photon energy and the XMCD spectrum of the difference of intensities of the pair of XAS images scanning the photon energy.
XMCD images show an asymmetry contrast according to the maximum or minimum intensity recorded in the XMCD spectrum at a specific energy. Such contrast reveals the magnetic signal in the sample. Indeed, the dichroic contrast is proportional to the local magnetization along the x-ray beam direction. So, to determine the easy axis of magnetization in the sample or the vector magnetization pattern of its magnetic domains, three XMCD images corresponding to the sample rotated with respect to the direction of the X-ray beam at different azimuthal angles are compared. For instance, see figure 4.12 from chapter 4, where the magnetization direction was determined of magnetic domains from SFO platelets following the procedure described above.

Therefore, the XMCD-PEEM combination makes it possible to determine specific element magnetic information in acquiring images at the submicron scale. This method allows observing the magnetic contrast in a particular area of the surface [78, 79]. This dichroic effect will be seen in the following chapters of the thesis about the SFO platelets, SFO thin films and bilayer systems.

Figure 2.15 shows the LEEM-PEEM system of the CIRCE beamline. It consists of an entrance chamber (blue box), a preparation chamber (green box) and the main chamber (red box) where the microscope is located. The entrance chamber incorporates a parking to store samples that allow a quick transfer without losing the samples' vacuum conditions. The preparation chamber is equipped with different evaporators for MBE growth and gas inlet and ion gun to prepare the sample surface. In addition to the LEEM-PEEM microscope, the main chamber allows monitoring of *in-situ* growth also with the inclusion of evaporators. The sample inside the main chamber can be rotated with respect to the X-ray beam. In addition, the sample holder used allows the sample to be heated up to 2000 K in both the preparation and main chamber. The temperature is measured by a W/Re thermocouple attached to the sample holder.

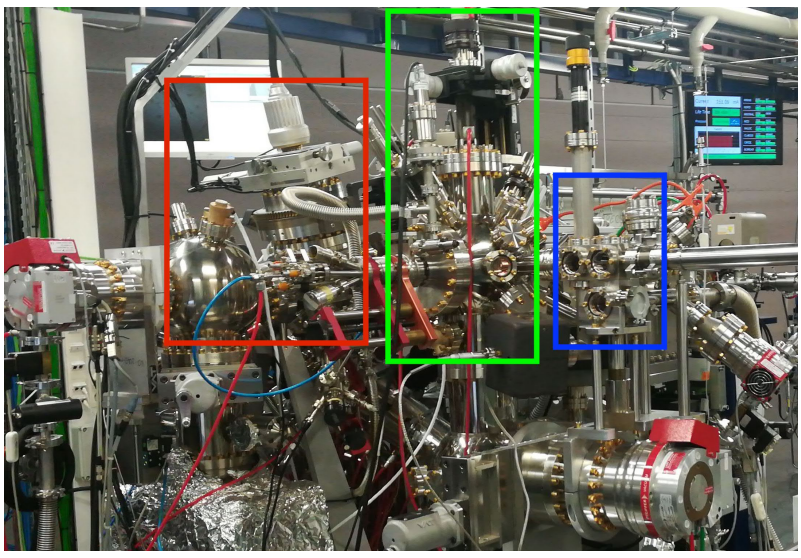

Figure 2.15: CIRCE beamline.

2.3 Micromagnetic simulations

Throughout this thesis, a tool that has been frequently used to understand experimental systems has been micromagnetics simulation. These simulations have been used to reproduce and predict the magnetic behaviour observed in SFO platelets and films, as well as the SFO/Co and CFO/FeCo bilayer systems also introduced in this research.

The program used to perform these simulations is MuMax3 [86]. It calculates the space and time-dependent magnetization dynamics in nano to micro-sized ferromagnets using a finite difference discretization. Thus, the sample is divided into a 2D or 3D grid of orthorhombic cells. The simulation cell dimensions are established in function to reproduce the magnetic features accurately. The parameters involved in the simulation are: saturation magnetization (M_s), exchange stiffness constant (A_s) and uniaxial and cubic magnetocrystalline anisotropy constant(K_u and K_c, respectively). All of them are characteristic factors of the material under study. It is important to keep in mind that volumetric quantities such as magnetization and effective field are referenced within each cell, while coupling parameters such as exchange strength are referenced at the interface between two cells. Therefore, a simulation represents the magnetization moment evolution per cell and its interaction with the magnetization moment from neighboring cells according to the parameters set.

The micromagnetic simulations that give rise to these magnetization changes are defined by the Landau-Lifshitz-Gilbert (LLG) equation [87]. The LLG equation gives temporal evolution of the magnetization towards to system's equilibrium state, and it is expressed as:

$$\frac{d\vec{M}}{dt} = \frac{-\gamma}{1+\alpha^2}\vec{M} \times \vec{H}_{eff} - \frac{\gamma\alpha}{M_s(1+\alpha^2)}\vec{M} \times (\vec{M} \times \vec{H}_{eff}) \tag{2.12}$$

where α is the dimensionless damping coefficient, γ is the electron gyromagnetic ratio, $\vec{H}_{eff}$ is the effective magnetic field and $\vec{M}$ is the magnetization. The LLG equation is composed of two terms:

- The first term $\sim -\vec{M} \times \vec{H}_{eff}$ is related to the magnetic precession around the effective magnetic field.
- The second term $\sim -\vec{M} \times (\vec{M} \times \vec{H}_{eff})$ is refers to the damping torque which induces the transverse relaxation towards to effective field direction. It causes minimizing energy, driving the system into an equilibrium state. This state is reached when magnetic moment and applied field are aligned corresponding to the condition $\vec{M} \times \vec{H}_{eff} = 0$ [88].

The figure 2.16 represents the torques involving in the movement of the magnetization respect with a $\vec{H}_{eff}$ and depicts the magnetization dynamics.

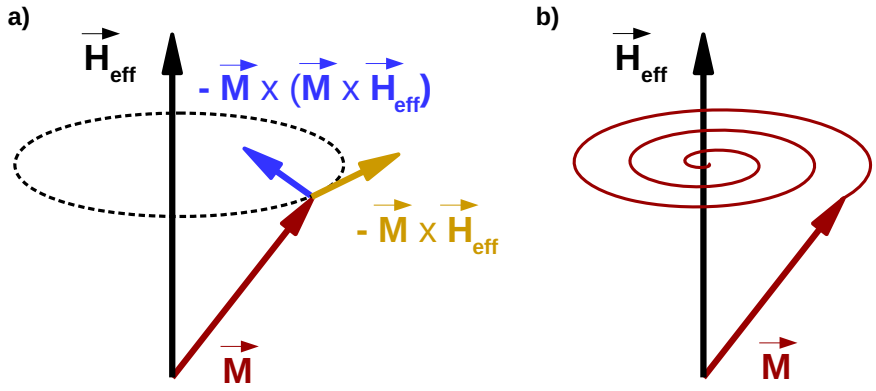

Figure 2.16: Time evolution of a single magnetic moment as described by the LLG equation. (a) Torques affecting the magnetization vector $\vec{M}$ (precessional and damped motions). (b) Resulting motion due to the precessional and damping torques.

Furthermore, it should be noted that the effective magnetic field is made up of several contributions which the most important are:

Externally applied field ($\mathbf{H}_{ext}$): this contribution arises from the interaction between the applied magnetic field with the magnetic moments from the sample. This is also known as Zeeman term. The applied field drives the magnetization motion, trying to orient the latter to the same direction as H_{ext}.

Magnetostatic or demagnetization field ($\mathbf{H}_{demag}$): this term is the field created by the magnetization from itself material, and it corresponds to dipole-dipole interactions. The demagnetization field is responsible for the magnetic domain formation since that reduces the energy associated with the sample magnetization.

Exchange field ($\mathbf{H}_{exch}$): this is due to the exchange interaction between the magnetic moments. Such interaction produces the alignment of the magnetic moments of the neighbouring atoms. As it will be seen in the following chapters, when considering different materials, we can rescale the exchange interaction with a factor to parametrise the coupling between them.

Magneto-crystalline anisotropy field ($\mathbf{H}_{anis}$): this field describes the preference of the magnetization to point along a crystallographic direction depending on the crystalline structure of the material. That is, it is easier to align the magnetization parallelly to particular crystallographic axes. This contribution occurs as a result of the spin-orbit interaction.

In the micromagnetic simulations presented in this thesis, we have performed energy minimization of each initial configuration. In some cases, the initial configuration has been obtained directly from the experiment, while in others, either a uniform or a random magnetization was used. MuMax3 performs the energy minimization disabling the precession term so that the effective field points towards decreasing energy. As a final step, it minimizes the magnitude of the torque instead of the energy since close to equilibrium; the torque should decrease monotonically and is less noisy than the energy.

3 $SrFe_{12}O_{19}$

3.1 Strontium ferrite structure

Strontium hexaferrite belongs to the group M-type ferrites. The M-structure borrows its name from the lead-containing magnetic mineral magnetoplumbite ($PbFeMn_{12}O_{19}$), on which this structure is based. Adelsköld in 1938 determined the crystal structures of BFO ($BaFe_{12}O_{19}$), SFO ($SrFe_{12}O_{19}$) and PFO ($PbFe_{12}O_{19}$), prepared by heating co-precipitated mixtures from nitrates solutions [89].

SFO crystallizes in a hexagonal structure with space group P63/mmc, and two chemical formula units $SrFe_{12}O_{19}$ in the unit cell. The structure shows a hexagonal close-packing of O ions, where 2 of the 40 sites are occupied by Sr ions; Fe^{3+} ions are in interstitial sites. Wyckoff's notations are adopted for every site in the crystal. The 24 Fe^{3+} ions are distributed on five different chemical environments: three octahedral (12k, 4f2, 2a), one tetrahedral (4f1) and one bipyramidal (2b). The strontium hexaferrite structure can be considered a sequence of alternating spinel blocks S and rocksalt blocks R (figure 3.1). Each block is explained as follows:

Block S: It consists of two spinel units (face-centered cubic structure) and, therefore, has the unit formula unit $(Fe_6O_8)^{+2}$. The S block comprises two packed layers of oxygen anions with three metal atoms between each layer, four octahedral sites (2a and 12k) where the cation is surrounded by six oxygen anions and two tetrahedral sites (4f1) where four oxygen anions surround the cation.

Block R: It consists of three hexagonally packed layers of four oxygen atoms each, but one of the oxygen atoms in the centre layer is replaced by a heavy cation (Sr^{2+}). Due to the presence of strontium atoms in the R block, the Fe^{3+} cations sites are distorted. This generates five octahedral sites (12k and 4f1) and one bipyramidal site (2b) in which the cation is surrounded by five oxygen anions, a unique position only found in the R block. The R block has the composition $(SrFe_6O_{11})^{-2}$.

Hence, the R blocks due to their -2e charge must be combined with the blocks S with +2e, giving neutral-M units. The basal plane containing the barium atom is a mirror plane of the R block, and consequently, the blocks preceding and succeeding the R block (S and S*) must be rotated over 180^{o} around to c-axis with respect to each other. Again, a mirror R plane is necessary for the structure. Only after a second R block is passed is the original situation found again. The SFO crystal structure can thus be symbolically described as a RSR*S* c-stacked sequence where the asterisk indicates a 180^{o}-rotation of the corresponding block around the hexagonal axis [13, 90, 91, 92]. The lattice parameters of SFO are 23.031 Å for c and 5.864 Å for a [89].

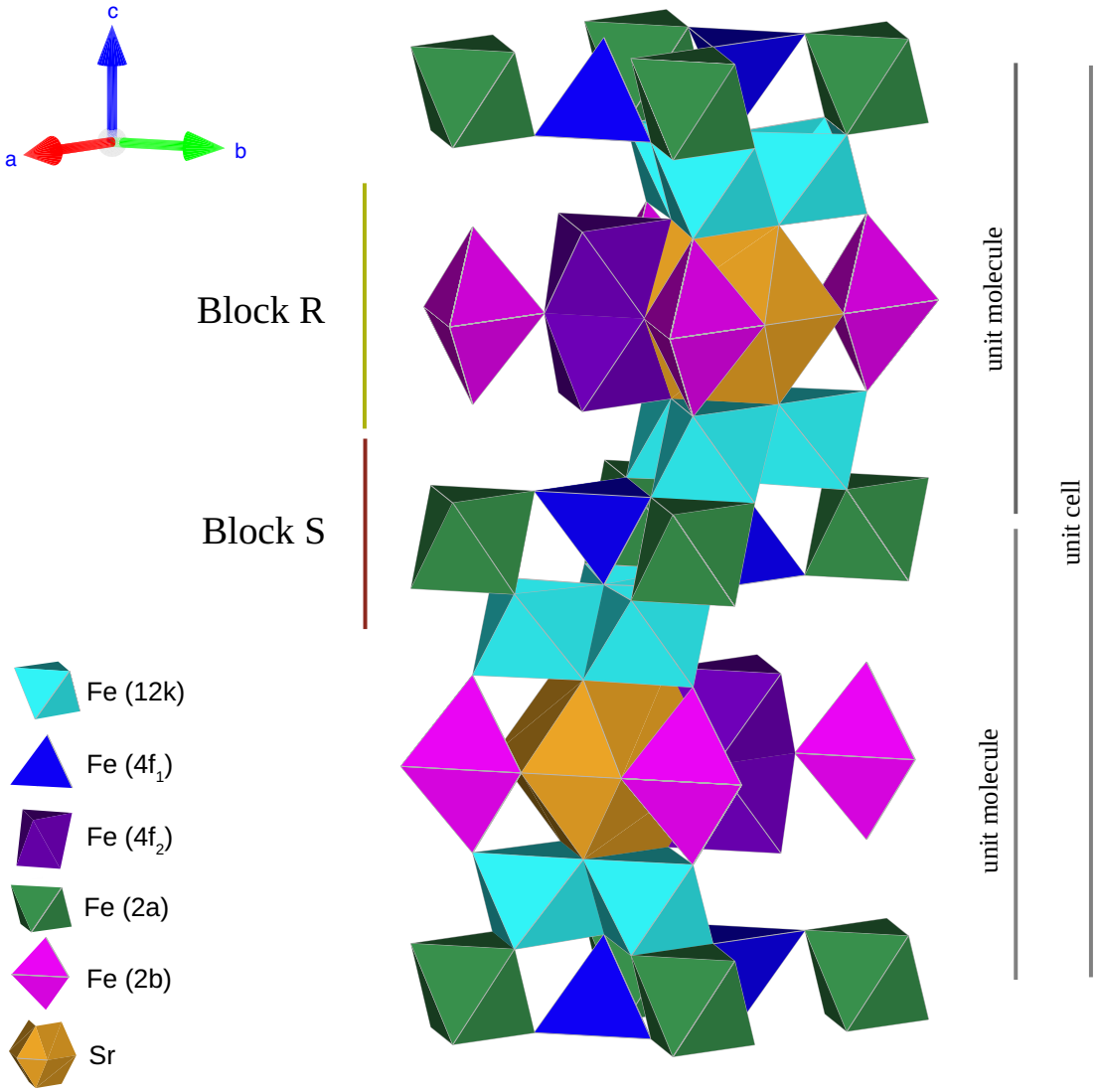

Figure 3.1: Polyhedral model of the $SrFe_{12}O_{19}$ structure. The drawing shows the S- and R-blocks and the various iron and strontium sites in different colors. (Figure generated by VESTA [93])

3.2 Magnetic order in strontium ferrite

Type M ferrites have a complex structure, as mentioned above, made up of alternating spinel and rock salt blocks. This peculiar structure results in interesting magnetic properties. These hexagonal ferrites are ferrimagnetic, and for the understanding of this property, the magnetic interaction of the cations within and between each block needs to be considered in detail.

Spinel magnetism was one of the examples used by Neel to explain his theory of ferrimagnetism as an extension of antiferromagnetism [13]. Ferromagnetism and antiferromagnetism are physical phenomena related to a strong interaction between the atoms, determined by the parallel or antiparallel orientation of their spins (magnetic moments) in the crystal below the Curie (T_c) and Néel (T_N) temperatures, respectively. Above these temperatures, the spins are randomly oriented, and they only align in the presence of an external magnetic field (paramagnetism). In ferrimagnetic materials, the simplest model assumes the existence of two sublattices whose moments are antiparallel, although, within each sublattice, the interaction is ferromagnetic. As the moment is different for each sublattice, the resulting coupling will result in net magnetization, figure 3.2.

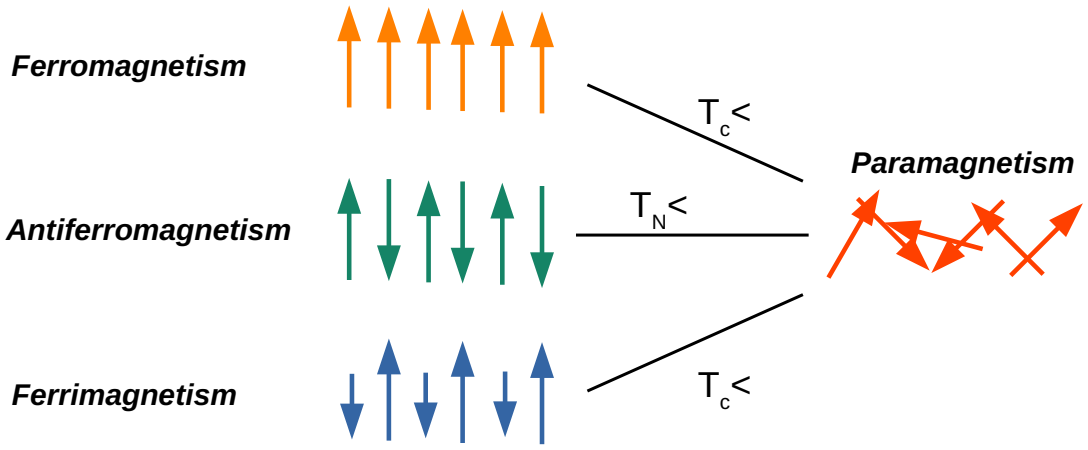

Figure 3.2: Orientation of the atomic magnetic moments in different types of magnetic materials.

The interaction that promotes the magnetic order between neighboring atoms is called the **exchange interaction**, proposed by Heisenberg and Dirac [94, 95]. Such interaction occurs between the unpaired spins of adjacent atoms and reflects the effectiveness of the overlapping of electron wave functions. The exchange energy (U_{ij}) of two atoms (i, j) is defined by the equation:

$$U_{ij} = -2J_{ij}S_iS_j \tag{3.1}$$

where J_{ij} is the exchange integral that is related to the overlap of the electron wave functions, and S_i and S_j are the spins of the unpaired electrons of the two atoms. Depending

on the sign of J the magnetic order will be ferromagnetic ($J>0$) or antiferromagnetic ($J<0$).

For metals, the spins are linked by exchange interactions between the magnetic moments of neighbouring atoms. This short-range interaction is negligible over longer distances. In the case of ferrimagnetic ferrites, the spin interaction mechanism occurs indirectly because the metal cations are too far away to interact directly. Therefore, the indirect exchange mechanism involves the non-magnetic oxygen atoms between the cations. The indirect interaction is known as **super-exchange interaction**. It consists on the connection between the unpaired 3d electrons of the metal ions and the 2p of the O^{2-} anions. Since the oxygen anion has its 2p orbitals completely filled, the oxygen anion does not contribute to the magnetic moment. However, the metal ions can disturb the state of oxygen anion, leading to an interaction between the spins of the electrons in the oxygen p orbital with the electrons in the d orbitals of the neighbour cations (Fe–O–Fe'), figure 3.3. The magnitude of the exchange energies between two magnetic cations Fe^{3+} and Fe^{3+} and therefore, the orientation of the spin moments, depend upon the distances from these ions to the oxygen ion O, and on the angle between the three atoms Fe–O–Fe'. It has been shown [13, 91, 96, 14] that the maximum exchange energy occurs for an Fe–O–Fe' angle of 180° (antiparallel spins) while the minimum exchange energy is obtained when this angle is 90° (parallel spins). It has been also demonstrated that the exchange energy decreases rapidly with increasing distance Fe-O distance.

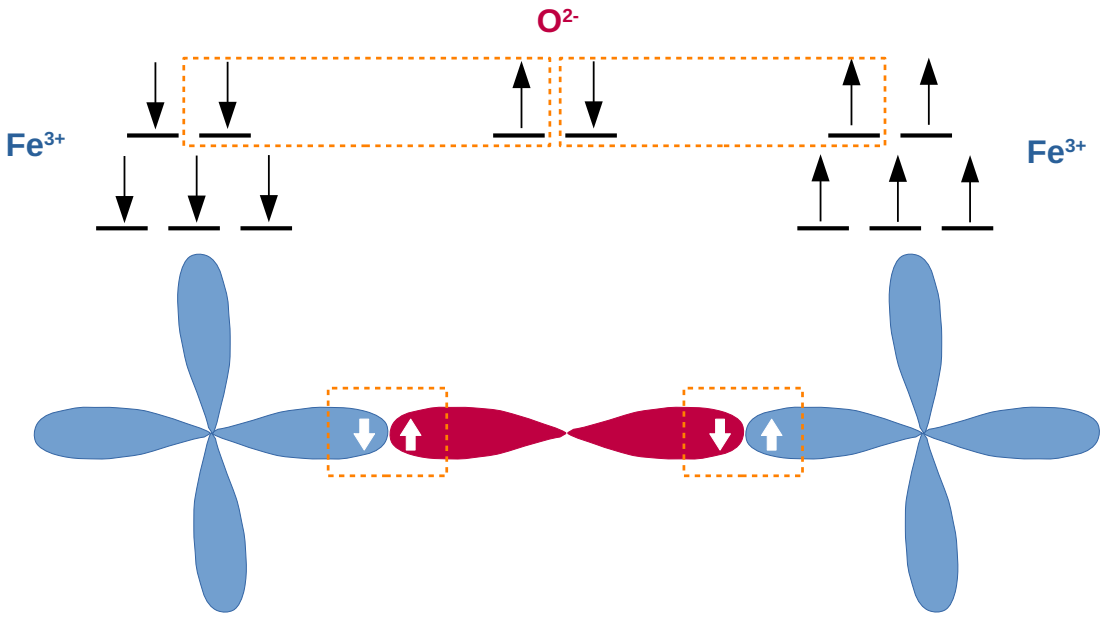

Figure 3.3: Schematic representation of the O 2p and metal 3d orbitals in a super-exchange interaction.

Focusing on the structure (SFO), the magnetic moment in each block can be estimated as follows:

- For the S block, the iron cations are found in tetrahedral (A) and octahedral sites (B). Gorter [96] calculated the super-exchange interactions as a function of the Fe-O distances and the Fe–O–Fe' angle for different configurations within the spinel structure (figure 3.4).

He found a larger contribution from A-O-B interactions where A indicates the cation in a tetrahedral site and B in an octahedral site. This is due to the small distance between the atoms ($d_{AOB} \sim 3.9$ Å) as well as the angle of 126°. The value for exchange constant strength, J_{AOB} is -8.3 MeV [97, 98]. The B-O-B configuration has an angle close to 90° ($J_{BOB} \sim 1.0$ MeV), and the A-O-A has the lowest exchange interaction with an angle of 80° and a large distance ($d_{AOA} \sim 4.1$ Å) corresponding to J_{AOA} close to 1 MeV. This distribution produces the magnetic order in the iron cations. Therefore, the Fe_A^{3+} (4f1) have their moments oriented antiparallel to the Fe_B^{3+} moments (12K and 2a) which are coupled ferromagnetically among them.

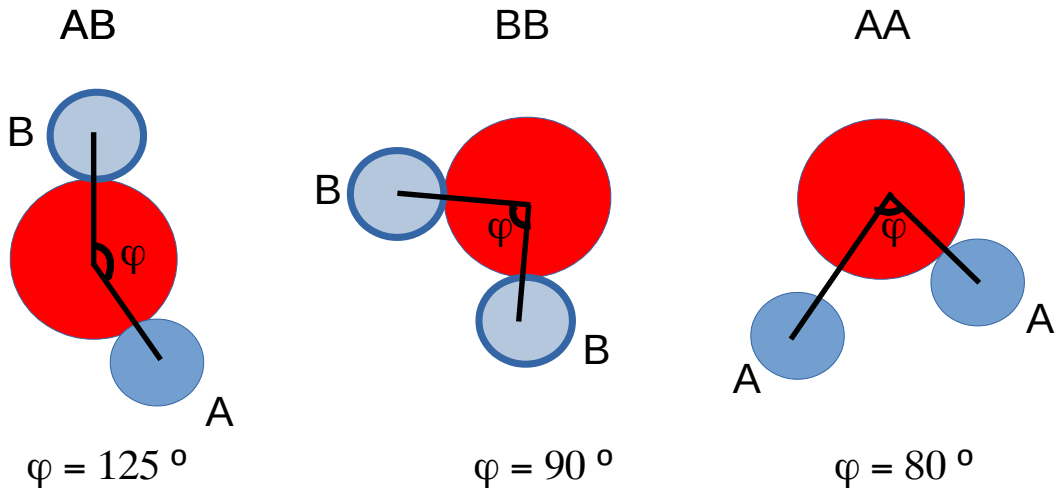

Figure 3.4: Some of the configurations of ion pair which probably make the greatest contributions to the exchange energy in the spinel lattice. Image adapted from literature [13].

- For the R block, a representative image of the spin moments orientation has been added for each iron in order to understand the super-exchange interaction between them (figure 3.5). The Fe site named (1) is the trigonal bipyramidal one which forms an angle of 140° with the iron (2), which is in an octahedral site. Due to the large angle, the exchange interaction is large too (J_{12} = -10.4 MeV), and the spins are aligned antiferromagnetically. The Fe(3)-O-Fe(2) interaction between octahedral sites presents an angle of 80° indicating a ferromagnetic coupling being the exchange constant value equal to 1 MeV. The coupling with the S layer is produced by the interaction between octahedral ions Fe(3) and Fe(4). The angle for this interaction is 130º, and its J_{34} -10.2 MeV. Therefore, the moments are coupled antiparallel [13, 14, 97].

To sum up the orientations of spins: at the spinel block, four octahedral iron cations (2a and 12k) point towards the net magnetization direction, while two tetrahedral (4f1) ones point in the opposite direction. In the R block, the presence of Sr^{2+} distorts the neighbouring octahedral iron sites, giving rise to two distorted octahedral sites (4f2), which are antiferromagnetically coupled to the rest of the octahedral sites (12k). It also has an unusual bipyramidal Fe site (2b), coupled ferromagnetically to the majority of octahedral sites.

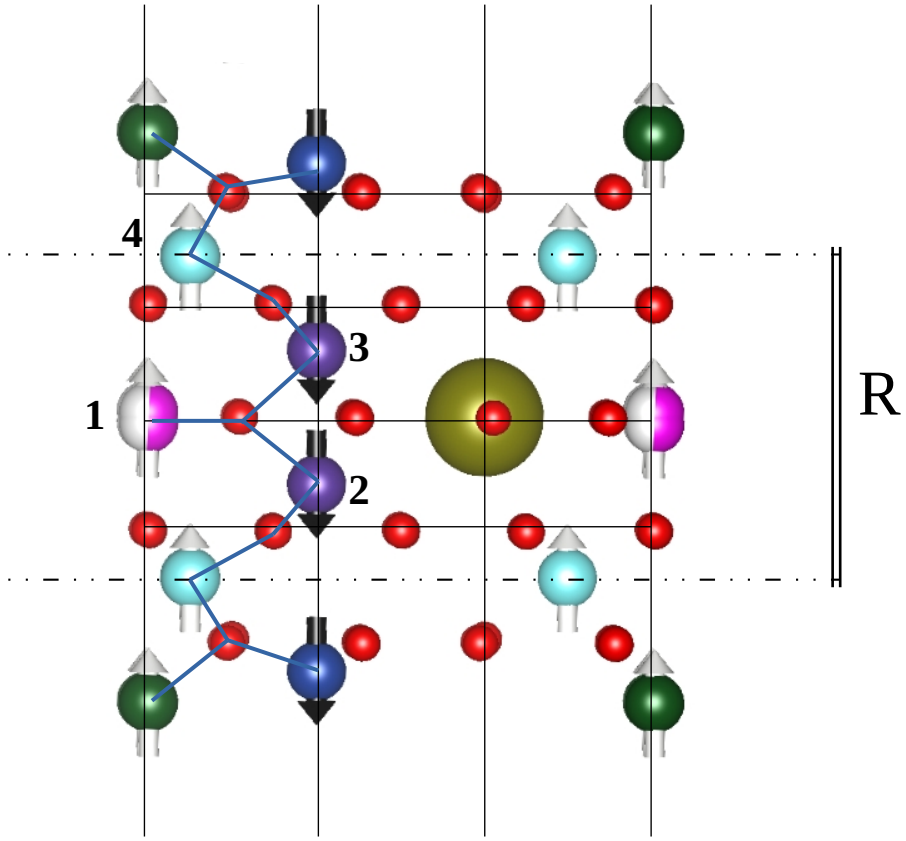

Figure 3.5: The superexchange (Fe–O–Fe') spin interactions in the R blocks. Image adapted from the reference [13].

Table 5.1 summarizes the spin magnetic moments configuration for each block.

Blocks	Tetrahedral ions	Octhaedral ions	Bipyramidal ions	Total magnetic moments
S	2 ↓	4 ↑	-	2 ↑
R	-	3 ↑ 2 ↓	1 ↑	2 ↑

Table 3.1: Number of metal ions on the various sites in the R and S blocks. The relative direction of their magnetic moments is indicated by arrows.

All magnetic ions have a magnetic moment of 5 Bohr magnetons (μ_B), so that the magnetization per formula unit is equal to (1 + 7 - 2 - 2)×5 = 20 μ_B [91]. M-type structure depicting the spin magnetic moments is presented in figure 3.6.

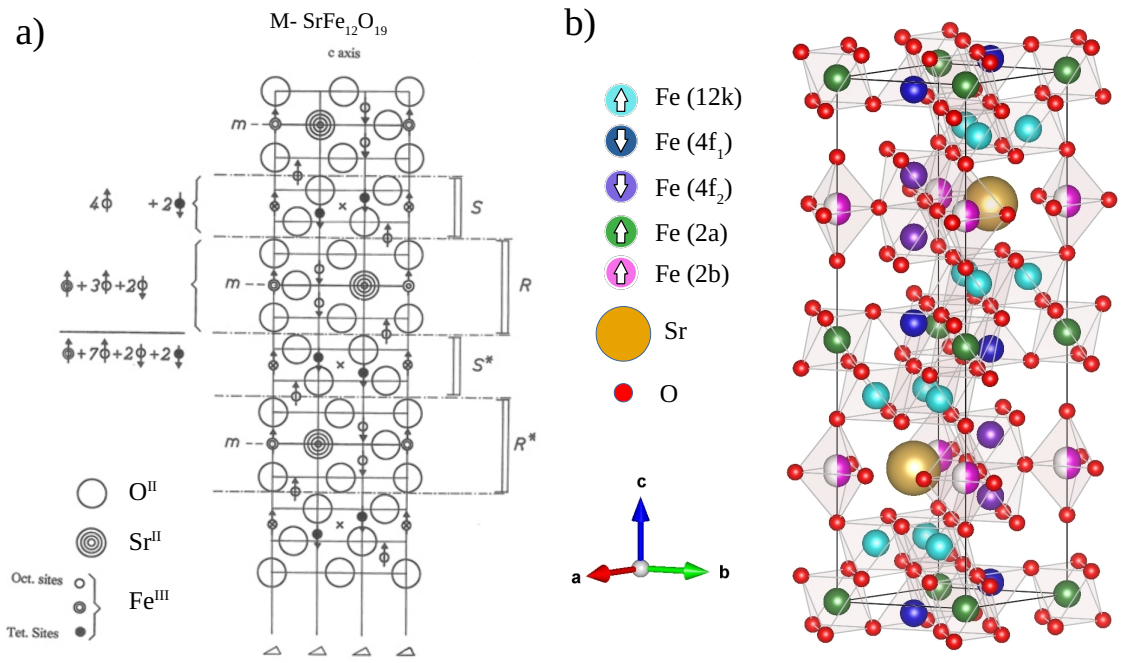

Figure 3.6: a) Cross section view of the M ferrite ($SrFe_{12}O_{19}$) structure in which the vertical lines are threefold symmetry axes. Picture modificated from [13]. b) 3D view of the M unit cell.

3.2.1 Intrinsic magnetic properties

It is the magnetic structure in terms of sublattices and their mutual orientation that governs magnetic behavior, which in turn is described in terms of intrinsic and material properties (saturation magnetization, magnetocrystalline anisotropy and coercive force [99, 100, 101, 102, 78, 103]).

- **Saturation magnetization, M_s**: it is the maximum magnetic moment per unit of volume. As it was studied in the previous section, the M_s value for strontium hexaferrite is derived from the spin configuration of the sublattices contributing with 20 μ_B per unit formula. However, this value ideally only occurs in a compound with its fully ordered magnetic moments, high crystallinity, and a temperature of 0 K. The temperature increase reduces the saturation magnetization of the compound (figure 3.7). For instance, for barium hexaferrite (isostructural compound), the theoretical approximation (20 μ_B) was reached in a polycrystalline sample at liquid hydrogen temperature (20 K), and an external magnetic field of 26000 Oe [13]. The data reported in the literature for the saturation magnetization of strontium ferrite single crystal range between 20.4 μ_B and 16.8 μ_B [91, 104].

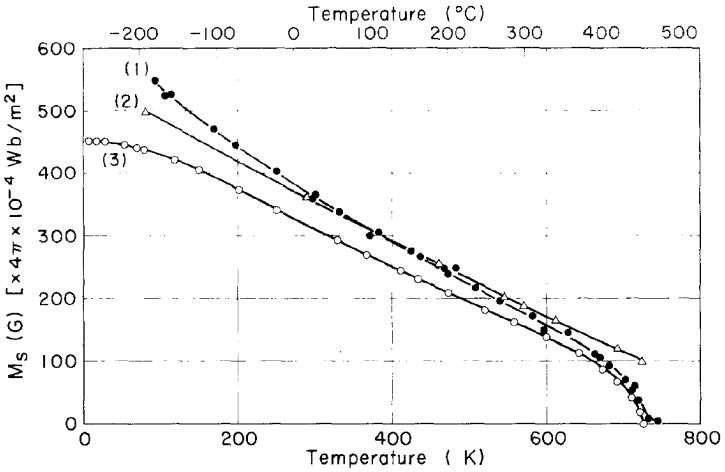

Figure 3.7: Saturation magnetization of BFO (1), SFO (2) and PFO (3) as a function of temperature. Reprinted from Ref [90].

Saturation magnetization is the governing parameter of the **magnetostatic energy, $\mathbf{E}_m$**. This energy defines the conventional dipole-dipole interaction between magnetic moments, located at the atomic positions in the lattice:

$$E_m = \frac{1}{2}\mu_0 V N M_s^2 \tag{3.2}$$

where μ_0 is the permeability of the vacuum, N is the demagnetizing factor for the easy axis and V the sample volume. This energy is directly related to the shape of the sample (*shape anisotropy*).

- **Magnetocrystalline anisotropy**: it describes the preference for magnetization to be oriented in a certain crystallographic direction. Specifically, for M-type ferrites, it corresponds to an uniaxial anisotropy with preferential magnetization along the hexagonal c-axis. The mathematical expression for the energy, $\boldsymbol{E}_a$, is given by:

$$E_a = K_1 \sin^2\phi + K_2 \sin^4\phi + K_3 \sin^6\phi ... \tag{3.3}$$

where ϕ is the angle between the magnetization and the crystallographic easy axis and K_1 is the so-called first order anisotropy constant. Higher order constants (K_2, K_3) are negligibly small. The value of this constant for SFO is $K_1 = 3.5 \times 10^5$ Jm^{-3} [105]. Also, the temperature affects this parameter. This fact can be understood in terms of dependence upon spontaneous magnetization. The K_1 should change with the temperature proportionally to $\sim M_s^3$. The reason is that thermal agitation can produce local variations of the direction magnetization vector and hence, changes in the energy [106].

An important factor related to the previous ones is the anisotropy field strength, $\boldsymbol{H}_A$. This parameter corresponds to the maximum internal reverse field needed to switch the magnetization in the direction perpendicular to the preferred axis:

$$H_a = 2K_1/M_s \tag{3.4}$$

It represents the upper limit for the coercive force (see below).

- **Coercive force**: it can be defined as the external field necessary to demagnetise a magnet completely. In general terms, it can be said that in the case of ferrite magnets, such as sintered or bonded compacts of SFO powders, this parameter arises from the magnetic behaviour of single domain particles with uniaxial magnetocrystalline anisotropy. To understand this, we need to take into account several considerations involved in the coercive force value.

  Critical diameter: It is the size of a particle below which a single domain state can be energetically achieved, and thus, the magnetization reversal proceeds by coherent rotation:

$$D_c = \frac{9}{2\pi}\frac{\sigma_w}{M_s^2} \tag{3.5}$$

  where σ_w is the specific domain wall energy. Inside this wall, the spin direction gradually changes from one preferred direction to another one. σ_w can be expressed as:

$$\sigma_w = 4(AK)^{1/2} \tag{3.6}$$

  being A the exchange stiffness coefficient which correspond to the energy associated with the (anti)parallel coupling of the ionic moments, **exchange energy ($\mathbf{E}_e$)**. A is an intrinsic parameter for each material ($\mathrm{A}_{SFO} = 6 \times 10^{-12}\mathrm{Jm}^{-1}$).

  The critical diameter for strontium hexaferrite is close to 1 μm, so the coercive force for a particle of smaller diameter than this D_c can be written as:

$$H_c = H_a - NM_s \tag{3.7}$$

  It is important to note that depending on the shape of the particle, the demagnetizing factor changes. The latter ranges from 0 (for needles) to 1 (for thin plates). For platelet-shaped M ferrite crystals, N ranges from 0.6 to 0.9. The coercivity values are high, and, as we have seen, they are a function of shape and size. For particles with a higher size than D_c, coercitivity values become smaller due to the formation of transient domains and magnetostatic interactions. The presence of domain walls facilitates the reversal of magnetization compared to the coherent rotation process, and this causes the coercive field to drop [22, 28, 107].

4 $SrFe_{12}O_{19}$ platelets

4.1 Introduction

Strontium hexaferrite has been a highly studied compound since its discovery. This is due to its magnetic properties [91, 108] that make it a good material to manufacture permanent magnets [109, 7, 28]. It has been grown by several methods: chemical co-precipitation [110, 111], solid-state synthesis [112], conventional ceramic process [113], sol-gel [114, 115], ball milling [116] and hydrothermal route [117, 118, 119, 120, 121, 122]. Among them, hydrothermally synthesis method has provided very homogeneous and high purity powders. Such powders in most of the cases presented platelet-shaped particles which have their crystal c-axis perpendicular to platelet plane. This phenomenon can be explained by the fact that the crystal growth rate for M-type ferrites is much faster in the basal plane than in the c-axis direction [13]. SFO single crystal platelets are of great scientific interest because the magnetocrystalline anisotropy is located in the c-axis, producing an anisotropic magnetic material. As it will be studied in this section, the intrinsic properties of the material, both morphological and magnetic, can be affected to a large extent by the shape and size of the material particles.

The results presented in this chapter have been published in:

- G. D. Soria, P. Jenus, J. F. Marco, A. Mandziak, M. Sanchez-Arenillas, F. Moutinho, J. E. Prieto, P. Prieto, J. Cerdá, C. Tejera-Centeno, S. Gallego, M. Foerster, L. Aballe, M. Valvidares, H. B. Vasili, E. Pereiro, A. Quesada, and J. de la Figuera, "Strontium hexaferrite platelets: a comprehensive soft X-ray absorption and Mössbauer spectroscopy study", Scientific Reports, vol. 9, no. 1, p. 11777, 2019.

4.2 Synthesis by hydrothermal method

The platelets were provided by Dr. Petra Jenus from the Josef Stephan Institute in Ljubljana, Slovenia, and they were grown by hydrothermal synthesis. In this method aqueous solutions containing the appropriate metal ions prepared from strontium (II) nitrate ($Sr(NO_3)_2$, 99% +, Across Organics) and iron (III) nitrate nonahydrate ($Fe(NO_3)_3 \times 9H_2O$, 98%, Carlo Erba Reagents) salts are mixed. The exact metal concentration of the reagents is determined by inductively coupled plasma atomic emission spectroscopy (ICP-AES) [123, 124]. To the aqueous Sr^{2+} and Fe^{3+} containing solution with a Sr^{2+}/Fe^{3+} ratio of 1/6, a sodium hydroxide (NaOH, Alfa Aesar, 98%) aqueous solution is added at room temperature so that the final NO_3^-/OH^- ratio is $\frac{1}{2}$. The mixture is then put into a stainless-steel autoclave and keeps in an oven until a temperature of 503 K is reached for a holding

time of 15 min, and immediately after that, the heating is turned off, and the autoclave is cooled to room temperature.

4.3 Morphological, structural and compositional characterization

In order to check the morphology and crystallinity of the powders, they were first examined by transmission electron microscopy (TEM). This technique generates an image of the sample using a beam of high-energy electrons transmitted through it. TEM images of the SFO powders (figure 4.1) revealed a few small particles, below 100 nm, and a majority of platelets with lateral dimensions around 1 μm and thickness of a few tens of nanometers. The platelets present a hexagonal shape [91] and observable lattice fringes at higher magnifications, which suggests good crystallinity. The high degree of crystallinity was supported by selected area electron diffraction (SAED) measurements. This method provides diffraction patterns acquired from a zone of a single platelet. For the identification of the SAED pattern, the reference diffraction pattern for $SrFe_{12}O_{19}$, simulated with SingleCrystalTM using the 69022 ICSD file, was used [125]. The SAED pattern is compatible with the $SrFe_{12}O_{19}$ crystal planes being oriented in the [001] direction. I.e., the single particle has its basal plane up (figure 4.1 in the upper right panel).

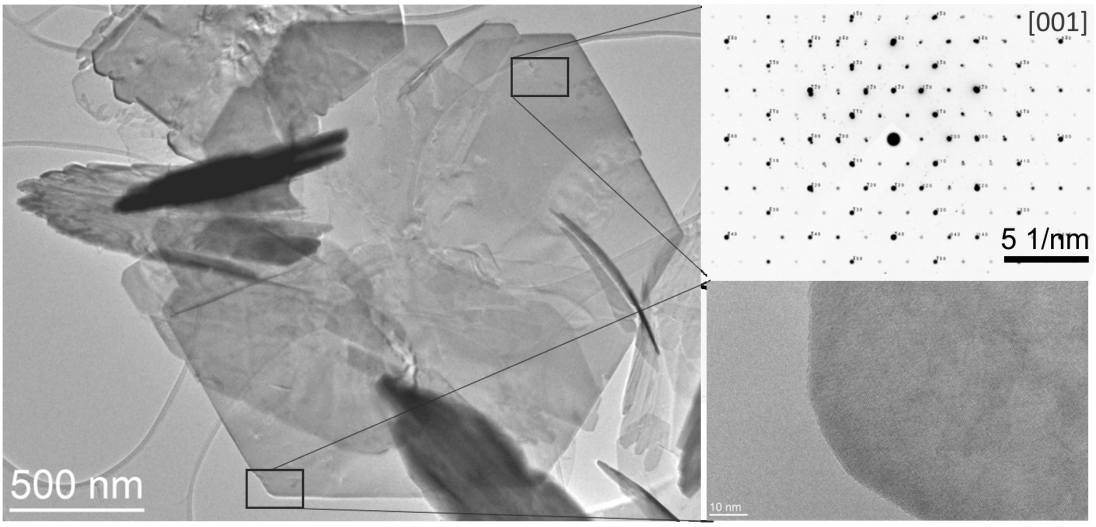

Figure 4.1: Left: TEM image of platelets. Bottom right: TEM image corresponding to a zoom of the selected area. Top right: diffraction pattern from SAED analysis. The structure has an orientation in the [001] plane.

Continuing with the morphological characterization of platelets, images were taken from Transmission X-ray Microscopy (TXM). In this case, the image is acquired by measuring the transmitted X-rays through the sample. The microscope is composed of both condenser and objective lenses. X-ray radiation comes to the elliptical glass capillary condenser, which focuses the light on the sample. An objective Fresnel Zone plate (FZP) collects the transmitted signal. This FZP is rotationally symmetric diffractive grating, composed of radially decreasing width rings. This lens is used to form an image of the field of view on the detector (direct illumination CCD camera) [47, 126]. The measurements were

carried out at the MISTRAL beamline of the ALBA synchrotron [127]. They were taken with a Fresnel zone plate of 25 nm. TXM images were acquired in absorption contrast mode at the Fe L_3 and L_2 edges, figure 4.2. Each panel corresponds to the same region rotated with respect to the Y-axis. The images were taken at -50°, -30°, 0°, 30° and 50°. Again, platelets present a hexagonal shape with lateral sizes several orders of magnitude higher than the thickness. Furthermore, platelets appear to form aggregates, and they are randomly oriented with respect to each other within the aggregates.
Additionally, this technique allows determining the magnetic contrast of the platelets by the difference in the absorbance signal obtained at the Fe L_3 and L_2 edges. However, platelet stacking complicates correctly distinguish the magnetic signal from each one.

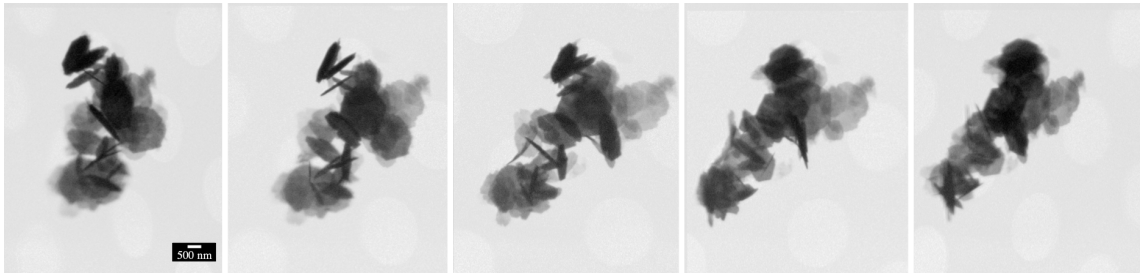

Figure 4.2: TXM images show the absorption contrast of the same cluster of SFO particles, at the angles: -50°, -30°, 0°, 30°, 50°, respectively. Effective pixel size = 10 nm.

The structural analysis of the sample was also performed by X-ray diffraction. Figure 4.3 shows the XRD diffraction pattern of the SFO platelets and the reference diffraction pattern for $SrFe_{12}O_{19}$ simulated with Crystal DiffractTM using the 69022 ICSD file (reference from [125]). All the reflections found on the platelet are indexed to crystallographic planes belonging to the reference hexagonal structure of $SrFe_{12}O_{19}$. Different families of planes are detected due to the random orientation of the platelets relative to the incident X-ray beam. No additional peaks were observed, indicating the absence of other phases. However, the width of the peaks indicates that the crystallite size is not too large. The average size of crystallites can be estimated using the Scherrer formula [128]. The value obtained was 50 ± 2 nm. This crystallite size is much smaller than that revealed by the TEM and TXM images which are often hundreds of nanometers wide. The most likely explanation could be that the platelets appear at different orientations relative to the X-ray beam, so even for large micron sized platelets, most of them would appear much smaller. The unit cell lattice parameters were calculated, obtaining a = 0.588 nm and c = 2.308 nm. Both are in good agreement with values reported in literature [91, 125].

X-ray photoelectron spectroscopy (XPS) was used to confirm the presence of strontium and iron species expected for the SFO structure. The energy scale was referenced to the binding energy (BE) of the C 1s core level of the adventitious contamination layer, which was set at 284.6 eV. The Sr 3d spectrum (BE Sr $3d_{5/2}$ = 132.5 eV and $3d_{3/2}$ = 134.3 eV) revealed the existence of Sr^{2+} cations, figure 4.4a. Figure 4.4b presents the corresponding Fe 2p spectrum. The binding energy of the Fe $2p_{3/2}$ core level is 710.0 eV, and the presence of a weak shake up satellite at 8.9 eV above the main Fe $2p_{3/2}$ line indicates that Fe is in the Fe^{3+} oxidation state as expected for the SFO structure.

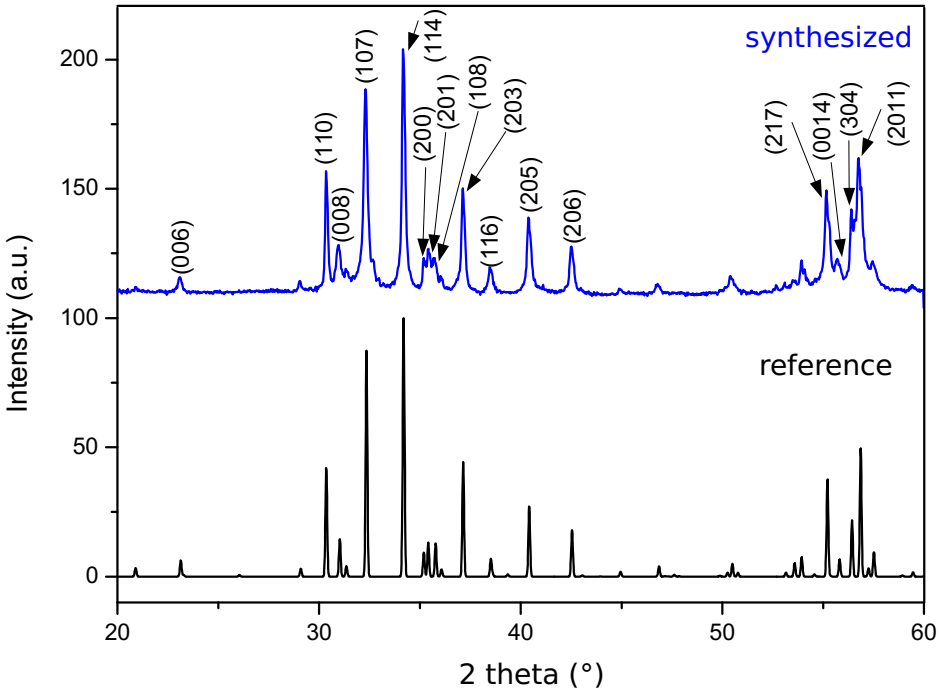

Figure 4.3: XRD diffraction patterns from the SFO powder, together with the reference pattern (bottom one).

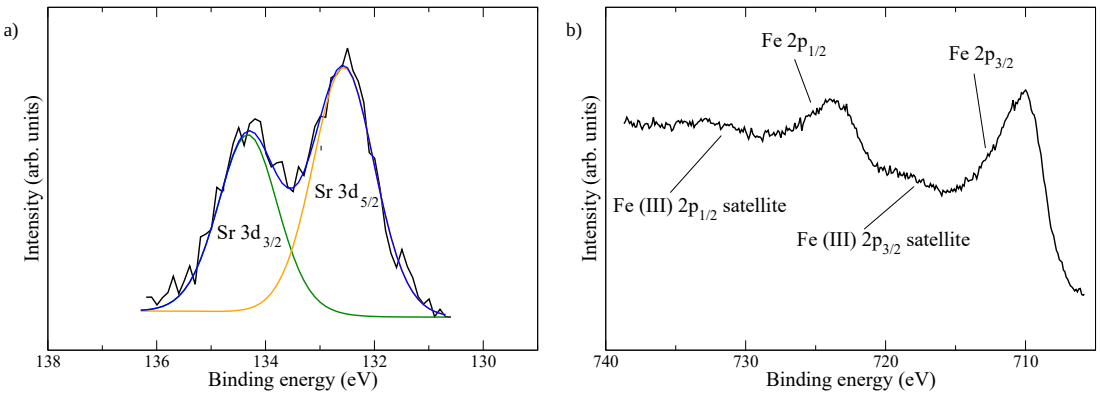

Figure 4.4: Sr 3d and Fe 2p core level X-ray photoelectron spectra recorded from $SrFe_{12}O_{19}$ platelets.

Mössbauer spectroscopy, as it has been explained in the techniques section, can provide information about the oxidation state and coordination of the iron cations. The room temperature Mössbauer spectrum of strontium hexaferrite is quite complex as it contains five overlapping sextets each one associated to a specific Fe^{3+} site within the SFO structure. Because of this complexity, there is some dispersion in the hyperfine parameters which characterize these sextets [129]. In this section, we have measured Mössbauer data at 298 K (RT) and 26 K (LT) from a commercial pure powder of SFO in order to have a reference to guide the fit of the data recorded from the platelets. These two reference spectra are shown in figure 4.5a and 4.5b, respectively. The corresponding hyperfine parameters obtained from the fit to a sum of sextets having Lorentzian-shaped lines are collected in Table 7.4. The obtained hyperfine parameters and spectral areas for the RT measurement are all in reasonable agreement with those reported previously for this material [130, 131, 132]. The 26 K spectrum has a very different shape resulting from the increase in both the hyperfine magnetic field values (whose temperature variation is not the same for each of the different sites [132]) and the isomer shifts of the various contributions. Similarly to that described in Ref. [132], this spectrum has been fitted to five sextets (Figure 4.5b), the results being also in reasonable agreement with these literature values.

The RT Mössbauer spectrum recorded from the SFO platelets is depicted in figure 4.5d. Compared to that of the standard sample, this spectrum shows much broader lines (about twice broader than in the SFO reference) and resembles other spectra recorded from SFO samples made by hydrothermal synthesis [131, 132]. This might be related to the occurrence of disorder, or structural inhomogeneities in the material [130]. The broadening of some of the lines in the X-ray diffraction data (see figure 4.3) is compatible with this interpretation. An explanation of the line broadening considering the occurrence of superparamagnetic effects could be discarded as the lateral dimensions of the platelets are in the micrometer range. The spectrum fits well considering a 3:2:1:1:2:3 area ratio for the lines of all the sextets, indicating that the platelets in the sample are randomly oriented. In any case, the hyperfine parameters obtained from the fit are very similar to those of the SFO standard sample (Table 7.4).

It is interesting to compare this spectrum with the RT ILEEMS spectrum recorded from the platelets (figure 4.5c). In an ILEEMS spectrum, the surface contributions are enhanced [68], therefore the differences, if any, between the ILEEMS and transmission spectra have to be due to structural/compositional changes in the surface with respect to the bulk. Inspection of figures 4.5c and 4.5d shows clear differences between these two spectra, particularly in the outermost lines. The fit to the ILEEMS spectra shows a considerable increase of the intensity of the area of the sextet corresponding to the tetrahedral 4f1 sites, which almost doubles respect to that shown in the transmission spectrum (Table 7.4). Therefore, the results point out a higher concentration of tetrahedral sites at the surface. In this respect is also very interesting to compare the 26K spectrum recorded from the platelets (figure 4.5e) with that recorded at that temperature from the SFO standard (figure 4.5b). Again, there is a large difference between these two spectra: the spectrum of the platelets is less asymmetric, and the outer lines are broader. It must be recalled that there is no unique fit to this low temperature platelets spectrum. It is clear that the lines are much narrower than in the RT spectrum and, therefore, that the strong overlap between the different contributions complicates the fit. In the case of the spectrum of the SFO standard, this difficulty is mitigated at some extent because the outer sextets are relatively well distinguished from that corresponding to the most populated 12k site (see

outer lines of the spectrum in figure 4.5b). According to this and due to the difficulty for providing a unique fitting for the spectrum measured in platelets at 26 K, a qualitative analysis of the spectrum was done. When trying to fit this spectrum various trends were observed: (i) there is a strong tendency to obtain as the most intense sextet the one having hyperfine parameters close to tetrahedral coordination; depending on the parameters fixed, the intensity of the sextet corresponding to site 2a increases noticeably but its isomer shift goes to very low values, again compatible with a coordination lower than the octahedral one which is the one expected (it is known that the hyperfine parameters of sites 4f1 and 2a are strongly correlated [129]) and (ii) the area of the sextet corresponding to the octahedral site 12k has a tendency to decrease; in some of the fitting models tried the area goes down to a half of the expected value. The large increase of the contribution corresponding to "tetrahedral/lower than octahedral coordination sites" at the 26 K spectrum of the platelets might be understood on the basis of their recoil free fraction. Since, as the ILEEMS data have suggested, these sites are preferentially located at the surface of the platelets, it could be assumed that their recoil free fraction at room temperature is low [133] and that it increases dramatically at low temperature.

Taken together the results seem to indicate that the platelets contain a large amount of "tetrahedral/lower than octahedral coordination sites" which are mainly located at the surface. It must be taken into account that given the shape of the platelets, whose lateral dimensions are several orders of magnitude larger than their thickness, the amount of sites unsaturated in oxygen which are located at the surface has to be larger than the number of these sites in the bulk. It would follow that the broadening observed in the XRD data, and at some extent in the RT Mössbauer data, would reflect then the various configurations arising from the distribution of iron ions which cannot complete their octahedral coordination and that can show either tetrahedral- or penta-oxygen coordination. As the low temperature data have suggested, this situation would imply, consequently, a reduction in the number of well-defined 12k sites existing in the platelets. This should be reflected in the magnetic moment measured in these particles (see below).

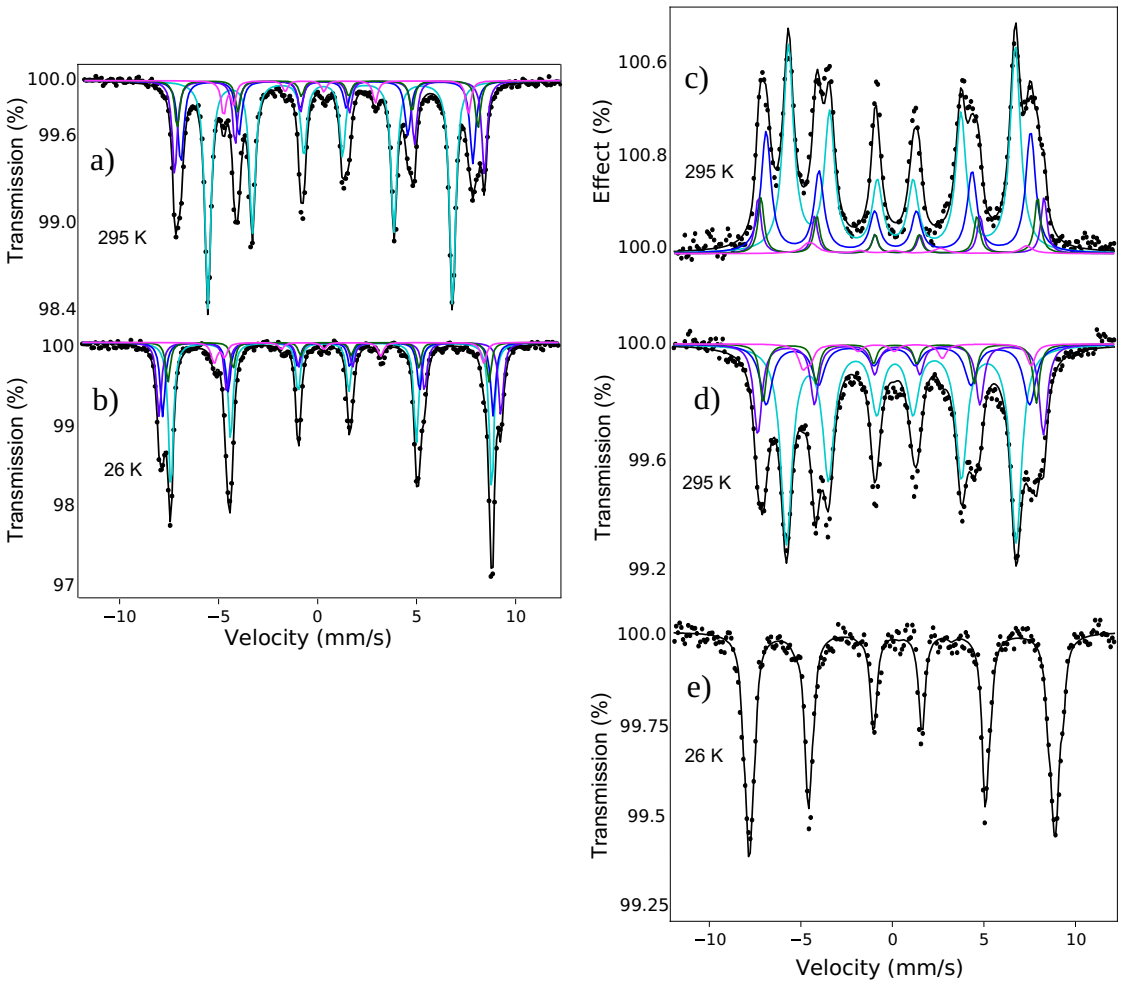

Figure 4.5: a) and b) Mössbauer spectrum of the SFO commercial powder recorded in transmission mode at 295 K and at 26K, respectively. c), d) and e) Mössbauer spectrum of the SFO platelets in electron detection mode at 295 K and transmission mode at 295 K and at 26 K, respectively. The five sextets in each spectrum correspond to the sites where the iron cations are positioned. The color for each sextet was selected according to the SFO structure image depicted in the $SrFe_{12}O_{19}$ structure section.

Sample	Site	δ ($\pm$ 0.03 mms^{-1})	2ε ($\pm$ 0.05 mms^{-1})	H ($\pm$ 0.01T)	Γ ($\pm$ 0.03 mms^{-1})	Area %
C - 295K	12k	0.35	0.38	40.5	0.38	49
	4f1	0.26	0.18	48.3	0.38	18
	4f2	0.38	0.26	51.3	0.32	18
	2a	0.33	0.14	49.8	0.32	9
	2b	0.27	2.22	40.5	0.32	6
C - 26K	12k	0.47	0.40	51.6	0.30	42
	4f1	0.39	0.20	53.2	0.30	21
	4f2	0.49	0.22	55.0	0.30	21
	2a	0.46	0.14	51.7	0.28	10
	2b	0.38	2.40	43.4	0.32	6
P - 295K	12k	0.35	0.38	40.6	0.78	53
	4f1	0.25	0.22	46.9	0.66	17
	4f2	0.39	0.26	50.3	0.68	17
	2a	0.31	0.14	49.3	0.52	9
	2b	0.26	2.32	40.2	0.56	4
P - ILEEMS	12k	0.35	0.38	40.8	0.72	53
	4f1	0.26	0.16	47.5	0.70	29
	4f2	0.40	0.22	51.4	0.42	8
	2a	0.33	0.14	49.7	0.42	8
	2b	0.26	2.32	39.3	0.80	2

Table 4.1: ^{57}Fe Mössbauer parameters obtained from the fit of the spectra recorded in figure 4.5 at 295K and 26 K, being SFO commercial (C), SFO platelets (P) and SFO platelets measured by ILEEMS (P - ILEEMS). The symbols δ, 2ε, H, Γ correspond to isomer shift, quadrupole shift, magnetic field and linewidth, respectively.

4.4 Magnetic characterization

The hysteresis cycle recorded from the platelets at room temperature is shown in figure 4.6. The measurements were carried out by VSM. At first glance, it can be seen that the 1.5 T applied magnetic field fails to fully saturate the sample since a constant magnetization value has not yet been reached at this field. Therefore, this cycle is a *"minor loop"*. The saturation magnetization (M_s) and remanent magnetization (M_r) for this magnetic field (1.5 T) gave values of 44.4 Am^2/kg and 20.4 Am^2/kg, respectively. Generally, the ratio between both parameters (M_r/M_s) indicates the preferential magnetic orientation of the sample. As this measurement is in a minor loop, the ratio obtained is a rough approximation. The value M_r/M_s reached was 0.46, so the net magnetization does not present a preferential orientation. This evidence is consistent with the fact that platelets are randomly oriented in clusters.

In any case, inspection of figure 4.6 suggests a M_s close to 50 (Am^2/kg) which is below that expected for bulk $SrFe_{12}O_{19}$ (72-90 Am^2/kg). This can be explained considering the results obtained in the Mössbauer spectra. The spectra indicated an increase in iron cations at the tetrahedral sites (4f1) involving a decrease in cations at octahedral sites (12k). Knowing that the cations in tetrahedral environment have their magnetization direction oriented antiparallel to the net magnetization, a decrease in saturation magnetization is expected.

The coercivity of the as-synthesized platelets is 0.13 T, as estimated from the loop in figure 4.6. This is also lower than the bulk coercivity of $SrFe_{12}O_{19}$. This evidence, again, might be a consequence of the low applied magnetic field (1.5 T) employed since the anisotropy field of SFO is of the order of 1.8 T [91]. The coercitivity could also be affected by the crystallinity of the platelets, which present different cationic distribution on the surface, as mentioned above.

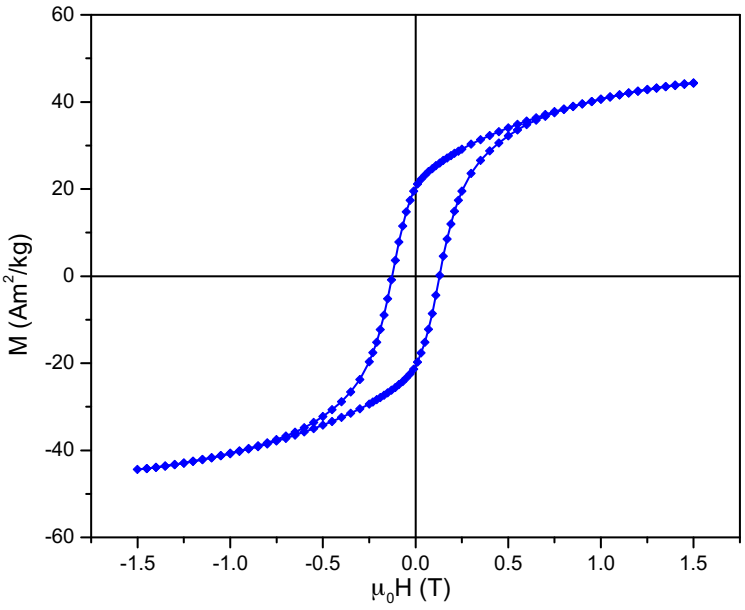

Figure 4.6: The M-H minor hysteresis loop of as-synthesized SFO particles at room temperature.

The XAS measurements were carried out at the BOREAS [81] and CIRCE [74] beamlines of ALBA synchrotron. It is important to highlight that this research involves three different ALBA beamlines (the latter two and MISTRAL). In fact, the use of the characterization techniques from these facilities has allowed a full characterization of the platelets and, therefore, are crucial tools for this research.

Hence, to increase the understanding of the structure and magnetic properties of $SrFe_{12}O_{19}$ platelets, we acquired X-ray absorption and magnetic circular dichroism spectra and images. Spectra were obtained under a 6 T magnetic field to saturate the magnetization of the sample, both at room temperature and 2 K, and scanning the photon energy through the iron L_3 and L_2 edges. Additionally, spectra were measured from the SFO commercial powdeR [134]. As it was anticipated in the introduction section, one of the novel results of this investigation was to collect reference XAS and XMCD spectra from $SrFe_{12}O_{19}$ for the first time in the literature, to the best of our knowledge. The X-ray iron absorption spectra, presented in figure 4.7a, show at both L_3 and L_2 edges the typical double peak structure characteristic of Fe^{3+}. Further information can be obtained from the X-ray magnetic circular dichroism spectra (figure 4.7b). The spectra from the commercial powder and that of the hydrothermal samples are similar. The iron XMCD spectra present several characteristic features, of which the most prominent at the L_3 edge is an initial large valley (707.5 eV), then a small peak (708.0 eV) and valley structure followed by a peak (709.0 eV) and a large valley (709.5 eV), depicted in the inset of figure 4.7b. The main peak at 709.0 eV arises mostly from Fe^{3+} in tetrahedral positions, while the last, deepest, valley originates mostly from Fe^{3+} in octahedral positions [135]. However, all the $SrFe_{12}O_{19}$ spectra recorded also show the first valley (707.5 eV), which in iron oxides can be attributed to Fe^{2+} in octahedral positions [136, 137, 138] or to Fe^{3+} in octahedral sites [139, 140]. Taking into account that there is no Fe^{2+} in our material, as shown by X-ray photoelectron and Mössbauer spectroscopies, we performed a multiplet calculation of the contributions of the different cation environments for Fe^{3+} in order to understand the origin of this valley [70].

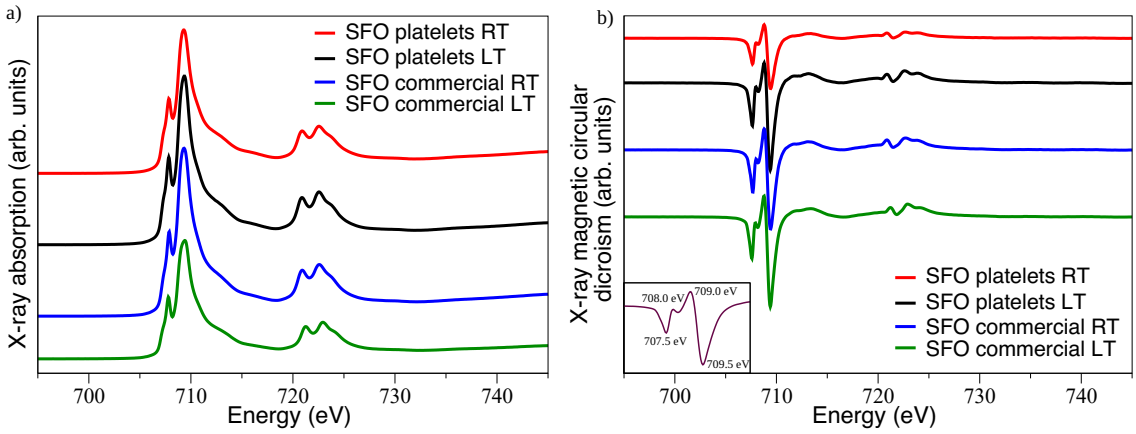

Figure 4.7: a) X-ray absorption spectra at the Fe $L_{2,3}$ absorption edges recorded from the platelets and the commercial powder at room temperature, RT (297 K) and low temperature, LT (2 K). They were acquired under an applied field of 6 T and averaged for both light helicities. b) X-ray magnetic circular dichroism spectra for both samples at RT and LT obtained by subtracting the spectra acquired with opposite light helicities. Inset: Energy positions for each of the peaks observed in the Fe $L_{2,3}$ edge XMCD spectra.

Calculations were carried out with the Crispy+Quanty code [141, 142] which is able to calculate core-level spectra using the multiplet approach, including the splitting values of the crystal field for several symmetries. So, this method allows simulating the absorption spectrum from the 2p to 3d electronic dipole transitions for Fe^{3+} cations. A combination of contributions to simulate the Fe cation sites in SFO was used: an octahedral crystal field (Oh symmetry), a tetrahedral one (Td symmetry) and for the trigonal bipyramidal site, C3v crystal field symmetry. The differences in the oxygen-cation distances [143] for the different octahedral environments are not expected to change significantly the crystal field splitting. Thus, the same 10Dq parameter (1.1 eV) has been used for all octahedral sites (2a, $4f_2$, 12k). In addition, the tetrahedral sites($4f_1$) has been modeled with 10Dq = -0.5 eV, and the bipyramidal one (2b) with 10Dq = 0.8 eV, Dτ = -0.08 eV and Dσ = 0.01 eV using literature values [144]. The Slater parameters were reduced to 72% of the Hartree Fock values following [144]. The Gaussian broadening value used for each peak in the simulated spectrum was 0.09 eV, in order to match the experimental resolution. Each component, as well as the complete fit, are shown in figure 4.8.

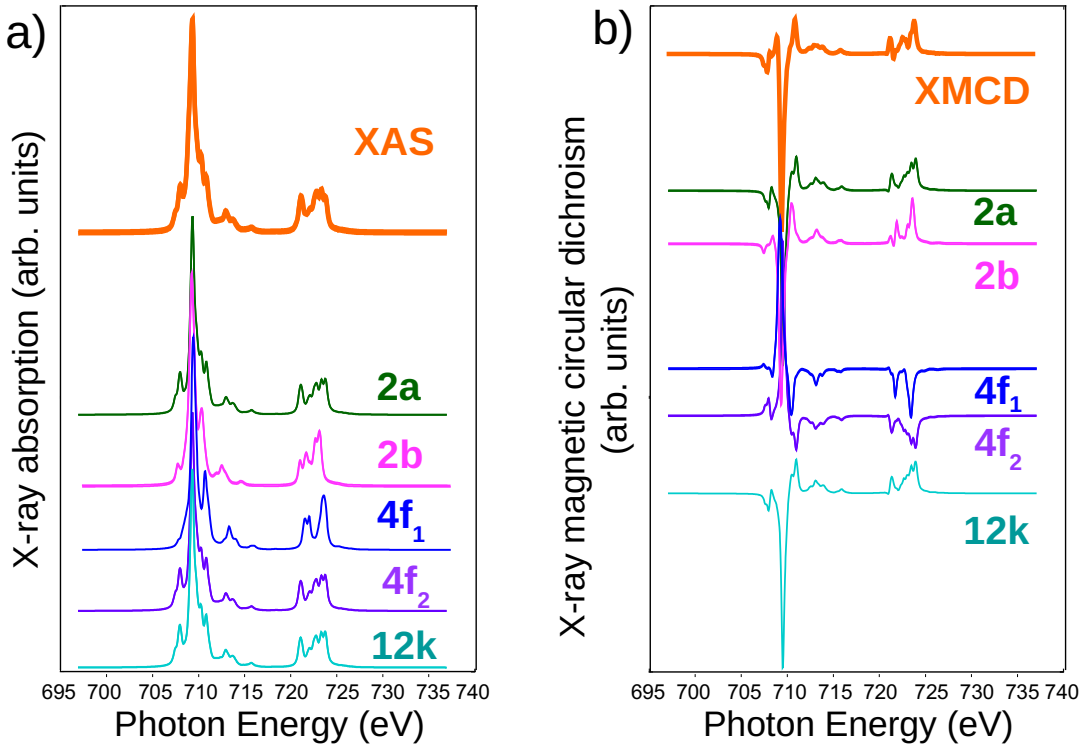

Figure 4.8: Atomic multiplet calculations used to simulate the XAS and XMCD spectra at the Fe $L_{2,3}$ absorption edges using Crispy+Quanty [142]. For each iron cation, the XAS and XMCD spectra are calculated, while on the top of each figure, the sum of the sublattice contribution is shown, as discussed in the text.

Figure 4.8a shows that the XAS spectrum shape seems to arise primarily to the contribution of the iron cations in 3+ oxidation state in octahedral positions (12k, 4f2 and 2a). However, looking closely at the dichroism spectrum (figure 4.8b) it is observed that its features come from the sum of Fe^{3+} in different chemical environments. In order to understand the shape of the XMCD spectrum of SFO, it is worth comparing it with that of the Fe^{3+} containing oxide maghemite (γ-Fe_2O_3) which has a spinel-related structure. Its absorption spectrum turned out to have an appearance similar to that of our material but without the characteristic peak at 708.0 eV [145]. Since the difference between the position of the irons in maghemite and SFO is that the latter contains one in a bipyramidal site, initially it was thought that this peak at 708.0 eV could belong to the contribution of the irons at that site. Nevertheless, this fact is unlikely given that there is only one Fe in this position per formula unit and, as Mossbauer spectroscopy advanced, it is a small contribution. In fact, if we do not take into account the bipyramidal contribution in the sum of the XMCD simulation spectra from various chemical sites, the peak would still emerge at 708.0 eV. Looking again at the literature, it was found that both maghemite and ferrihydrite (a Fe^{3+} oxyhydroxide) show this peak in high-resolution experiments [139, 140]. Therefore, the Fe^{3+} cations in octahedral and tetrahedral environments are responsible for the observed characteristics of the XMCD spectra. This analysis highlights the need to acquire spectra with high resolution.

To estimate the spin and orbital contributions to the magnetic moment of the iron cations from the XMCD spectra (figure 4.7), the sum rules were applied [82]. It is necessary to take into account that the dipolar operator has a value negligible for Fe^{3+} (d^5) [70]. In addition, the number of d-holes for the cations set was 4.7 following Ref.[146]. The spin and orbital magnetic moments for the platelets and commercial powder obtained are collected in table 4.2 for room temperature and 2 K.

Sample	Temperature (K)	Spin MM (μ_B)	Orbital MM (μ_B)
Platelets	297	0.61	0.03
	2	0.84	0.01
Commercial Powder	297	0.86	0.01
	2	1.23	0.04

Table 4.2: Magnetic momens per Fe cation in both samples at RT and LT.

The difference found between the platelets and the commercial powder can be understood with the information provided by the Mössbauer spectra (see figure 4.5c,d,e), as it was discussed for the VSM measurements. They show (as it has discussed previously) that the platelets have more iron cations in either tetrahedral or lower-than-octahedral coordination sites. While the 12k octahedral sites point in the net magnetization direction of the SFO, the 4f1 tetrahedral cations point in the opposite direction. Therefore, the variation of the cation population found by Mössbauer suggested a lower spin magnetic moment in the platelets. Furthermore, the magnetic moment per cation for both the platelets and the commercial powder decreases with temperature. The decrease is compatible with a critical exponent β of 0.33 for the magnetization *vs* temperature dependence $(T_c - T)^{\beta}$. This comparison is shown in figure 4.9. This critical exponent is expected from the 3D Ising model [147, 148], where the magnetization vector can only lay along two directions in the structure (up and down). This is reasonable in view of the strongly uniaxial character of the strontium hexaferrite structure along the c-axis plane where the spins of iron cations

are aligned anti- and ferromagnetically. This issue will be discussed in detail below through the vector analysis from XMCD-PEEM images.

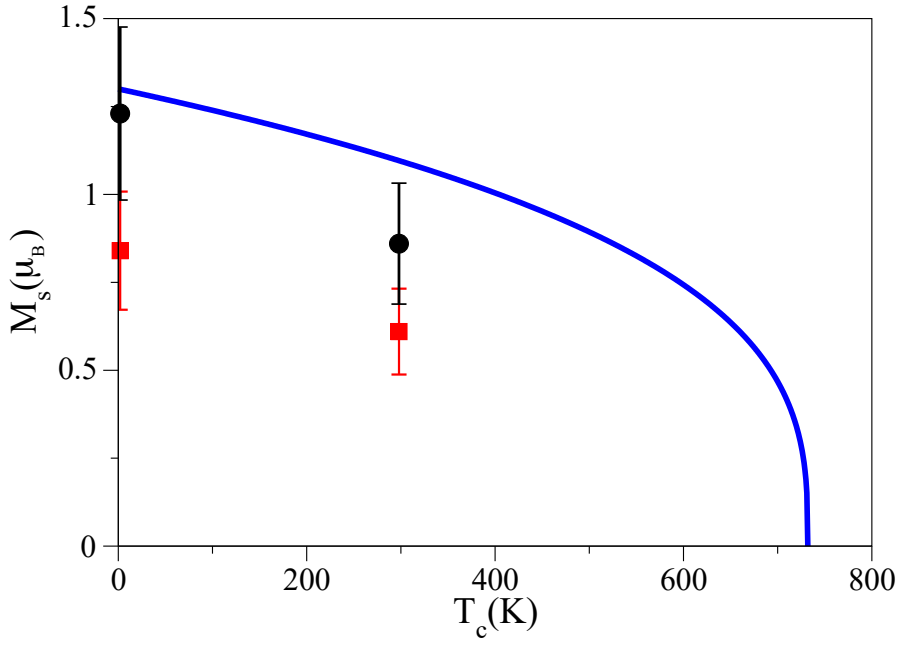

Figure 4.9: Total magnetic moment per Fe cation for the platelets (red squares) and from the commercial SFO powder (black circles) for two temperatures. An error of 20% in the sum rules was considered for the calculation of the spin orbital moment [149]. The continuous line is the expected change of the magnetization from the bulk magnetic moment with a critical exponent 0.33, which corresponds to a 3D Ising model [147].

Delving into the magnetic moment of the SFO structure, the density functional theory (DFT) calculations done by Dr. Jorge Cerdá from "Instituto de Ciencia de Materiales de Madrid" (ICMM), gave a total magnetic moment per formula unit of 20.00 μ_B. This result is in close agreement with previous calculations [150]. The Bader charges and magnetic moments projected on the different Fe cations are given in Table 4.3. The Bader charge is one of several ways to calculate the atomic charge in molecules or crystals. Basically, it calculates the charge density, ρ(r), in real space, and around each atom, it seeks the surface along which the density gradient, $\nabla\ \rho$(r), is zero. So, the integral of the charge contained in that surface is assigned to the atom [151]. For all the iron cations, the calculated magnetic moment is close to 4.0 μ_B. Neglecting the magnetic moments (MMs) induced in the oxygen anions, the total magnetic moment per f.u. is 17.2 μ_B, giving an average of 1.39 μ_B per Fe cation. This calculated value is in reasonable agreement with the experimental one obtained from the commercial powder.

Following the study of the Fe $L_{2,3}$ edges, we acquired the XAS spectrum at the O K edge. The O K-edge corresponds to transitions from the oxygen 1s to the oxygen unoccupied states, which are 2p orbitals strongly hybridized with the iron ones. The spectrum, shown in figure 4.10 (blue line), presents several well-defined peaks which can be compared against equivalent data measured for different iron oxides [152, 153]. To interpret the O-K XAS spectra, it is common to disregard the influence of the core hole on the unoccupied bands, as these have most weight on the metal sites [154]. This allows considering the peaks directly as arising from the unoccupied density of states of the oxygen. Following Ref.[152, 154],

Site	Charge (e)	MM (μ_B)
12k	6.37	4.07
4f1	6.41	-3.96
4f2	6.29	-3.93
2a	6.32	4.08
2b	6.46	3.99
TOTAL	220.00	20.00

Table 4.3: Bader charge and magnetic moment of each Fe site and total values per formula unit including also the oxygen and Sr ions.

the double peak at 532 eV is explained by the hybridization of 2p antibonding oxygen states with iron 3d states. The separation between the two peaks that compose it is related to the splitting between the t2g and eg orbitals in the iron cations due to the crystal field [154]. However, as is the case for maghemite and magnetite [153], the presence of three different iron environments (tetrahedral, octahedral, and trigonal bipyramidal) smears out the clear double peak detected in hematite. The peaks at higher energies (536-576 eV) reflected transitions into oxygen p-states hybridized with extended 4p and 4s iron states. Their particular origin has been assigned by means of multiple scattering cluster calculations in Ref. [152], to intrashell multiple scattering (peak at 545 eV) and single scattering between the absorber and consecutive oxygen shells (peaks at 563 and 550 eV). In figure 4.10 the XAS spectrum was compared with the density of unoccupied states projected (PDOS) on the O 2p state directly calculated by DFT (dark line). Most of these peaks are correctly reproduced both in shape and energy location within the expected accuracy of the DFT formalism. Therefore, a reasonable overall correlation was attained. Furthermore, comparison versus the DOS projected on the Sr atoms and the Fe -*s*, -*p* and -*d* states revealed that the influence of the former on the oxygen p-states is negligible compared with the latter and that, particularly at higher energies, there is certain correlation between the O-*p* and Fe-*p* PDOS.

The study of the XAS spectra by DFT calculations was only carried out for the oxygen at the K edge since the excitations are calculated from the 1s core level being much simpler computationally than for the excitations of the principal quantum number n = 2 (L edge). The first-principles calculations at the L edge must take into account more electronic transitions as well as the peak-splittings emerging from the presence of a strong spin-orbit coupling in the 2p orbitals.

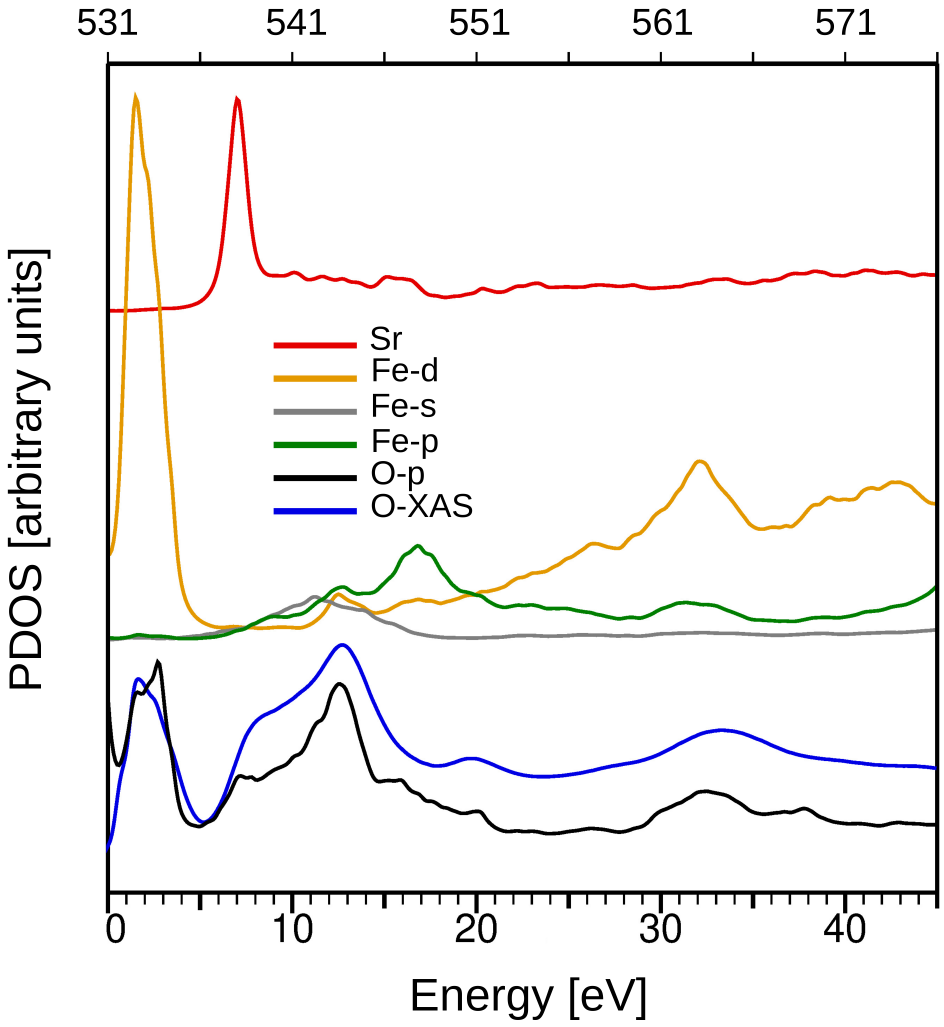

Figure 4.10: Blue line: X-ray absorption spectrum at the O K absorption edge, recorded at 2 K and an applied magnetic field of 6 T from the SFO platelets and averaged for both light helicities. Rest of lines: Calculated density of states projected on the Sr atoms, Fe-*d*, *p* and *s* and the O-*p* states (see legend). The PDOS curves for each species have been vertically shifted and rescaled for visual inspection.

The measurements of X-ray spectroscopy shown above (figure 4.7) correspond to the signal associated to a macroscopic quantity of powder, as it was seen in figures 4.1 and 4.2. In order to determine the XAS-XMCD images and spectra on a single platelet, we used photoemission electron (PEEM) microscopy [74]. For this analysis, the powder was dispersed in ethanol, diluted several times, sonicated, and then deposited on a Si(100) wafer covered with its native oxide. Once introduced the sample into the chamber, we searched the surface for platelets lying on the plane. The XAS average image (figure 4.11b) was taken at maximum energy of the XAS at the Fe L_3 edge spectrum (figure 4.11a) while the dichroism image (figure 4.11c) was acquired at the most intense energy peak of the dichroic signal of the XMCD spectrum (figure 4.11a). The XAS spectrum resembled those shown in figure 4.7 and the XMCD spectrum is somewhat noisier than those determined above since it is obtained from a sub-micron area at room temperature. Nonetheless, the features

resemble what is seen in the high-quality dichroism spectra acquired with a macroscopic amount of powder. The averaged XAS image shows platelets that appear partially stacked on top of each other. In addition, there is a detectable shadow together to some particles edges due to the platelets height prevents the incident X-ray beam. So, knowing the incident X-ray beam angle and the shadow size, the platelet thickness can be determined. The thickness estimated for these platelets was 18 nm. The XMCD image shows several domains (black and white regions) on the platelet. It is well-known that the asymmetry contrast is proportional to the local magnetization along the X-ray beam direction [155]. Hence, this platelet presents magnetic domains.

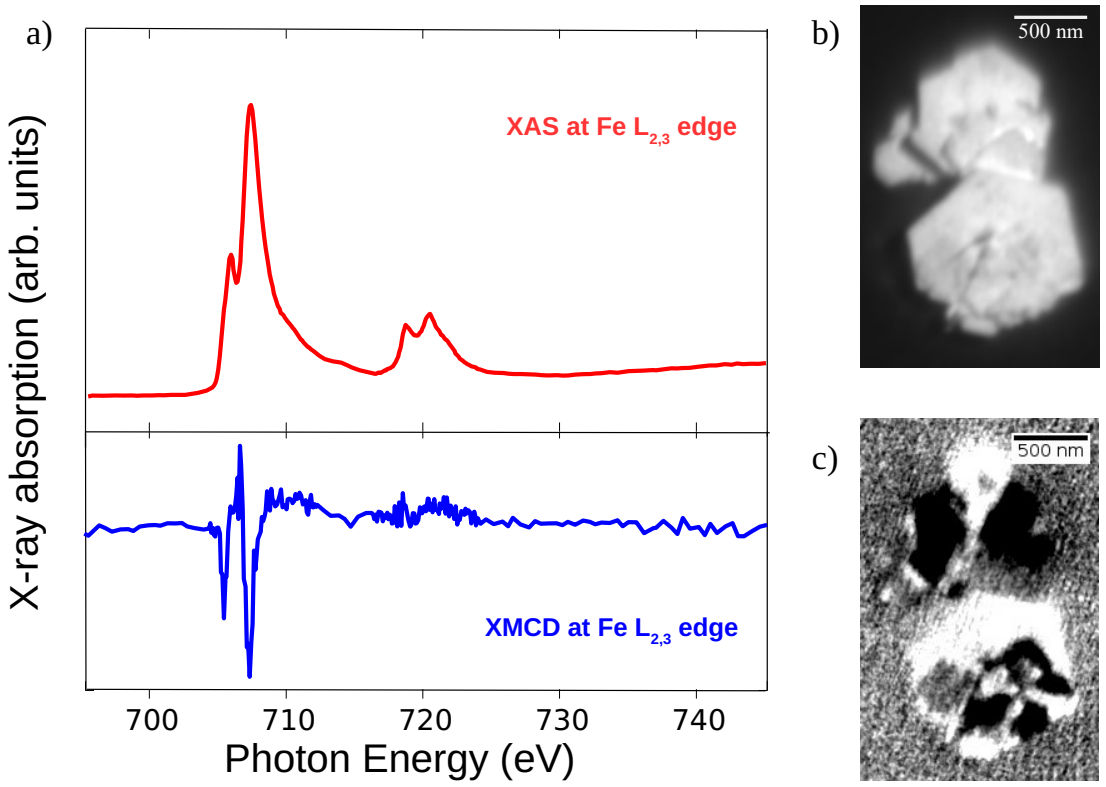

Figure 4.11: a) XAS and XMCD spectra acquired at the Fe $L_{2,3}$-edge on the platelet by PEEM. b) X-ray absorption image collected at the Fe L_3 maximum and c) dichroism image extracted from the most intense peak in the XMCD signal as a result of the difference between both X-ray helicities.

Proceeding with the characterization of the vector magnetization pattern, we measured XMCD images with three non-coplanar orientations [156] of the X-ray beam relative to the sample (figure 4.12). For the three images, the same magnetic domains are observed on the same areas in the platelet. So, it can be concluded that the magnetization orientation in the platelet is mostly out-of-plane. The result was expected since this material presents a large anisotropy and the crystallographic c-axis is perpendicular to the platelet, and thus also the magnetic easy axis.

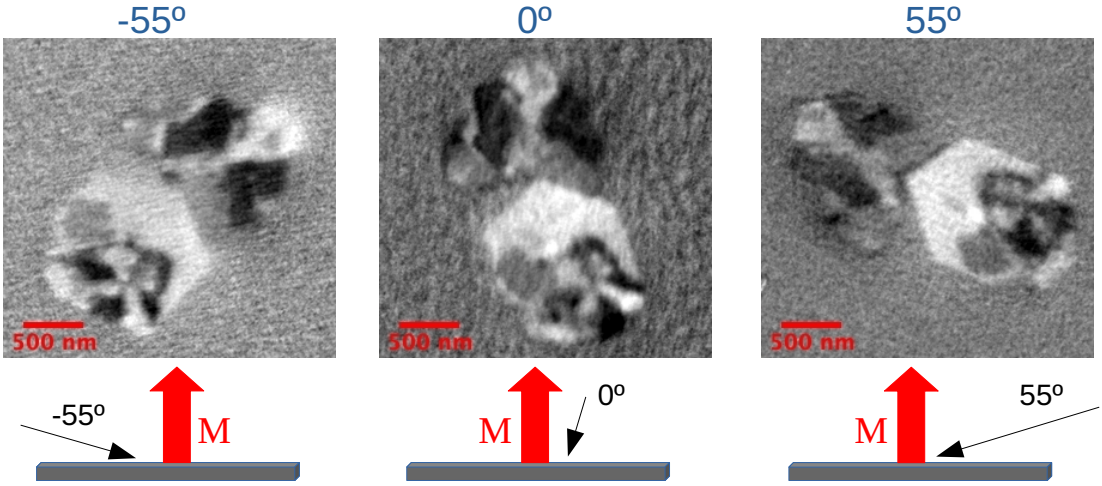

Figure 4.12: Top: XMCD images acquired at different angles respect to the X-ray beam. Botton: Magnetization orientation in the sample (out-of-plane) at each angle.

From the combination of this XMCD three images, the pixel-by-pixel magnetization vector can be determined, as shown with a color map in figure 4.13a. The platelets in the image are multidomain, with their magnetization vector mostly in and out-of-plane (black and white areas) with 180° domain walls between them. Using the 3D rendering software "Muview" the magnetization was depicted with arrows that pointed in the local magnetization direction (figure 4.13b). The green and pink colors correspond to domain walls (DWs) between black and white areas and also, to a lesser extent, to the noise in the determination of the magnetization vector. It is important to consider that the polar angle of incidence of the X-ray beam is fixed at 74° with respect to the normal to the sample, where 90° indicates the in-plane direction. Therefore, the out-of-plane magnetization sensitivity is reduced. Additionally, the domain walls observed were quite sharp. In fact, their width is likely smaller than the experimental resolution. Their expected width is $\pi\sqrt{A/K} = 13$ nm, where A is the exchange stiffness and K the uniaxial anisotropy constant [157]. A cut across a domain wall is shown in figure 4.13e, confirming this prediction. The pixel width in the images is 8.5 nm, and the overall experimental lateral resolution is around 20 nm [74]. To better understand the observed magnetic domain distributions in the platelet, micromagnetic simulations have been carried out with the Mumax software [86]. For this purpose, we have used the experimental magnetization map as the initial configuration of a micromagnetic simulation for an object with a shape similar to the one experimentally determined.

The voxel size in the simulation was 4.23 nm, to reproduce accurately the domain walls. The material constants employed for the saturation magnetization, exchange stiffness and magnetocrystalline hexagonal anisotropy were $M_s = 3.8 \times 10^5$ Am^{-1}, $A_s = 6 \times 10^{-12} Jm^{-1}$ and $K_u = 3.6 \times 10^5$ Jm^{-3}, respectively [91, 158, 108]. When the energy is minimized, the initial configuration gives rise to the magnetization pattern shown in figure 4.13c. The domains closely resemble the experimental ones, with a similar curvature of the domain walls. A cut across the domain walls gives the magnetization profile in figure 4.13e. Another simulation was performed using instead the maximum magnetization measured for the platelets by VSM. The resultant simulation is presented in figure 4.13d. An important observation is that the magnetic domain distribution relaxes to a different one (compared to the experimental image shown in Fig. 4.13a) if the measured Ms-value is used. Specifi-

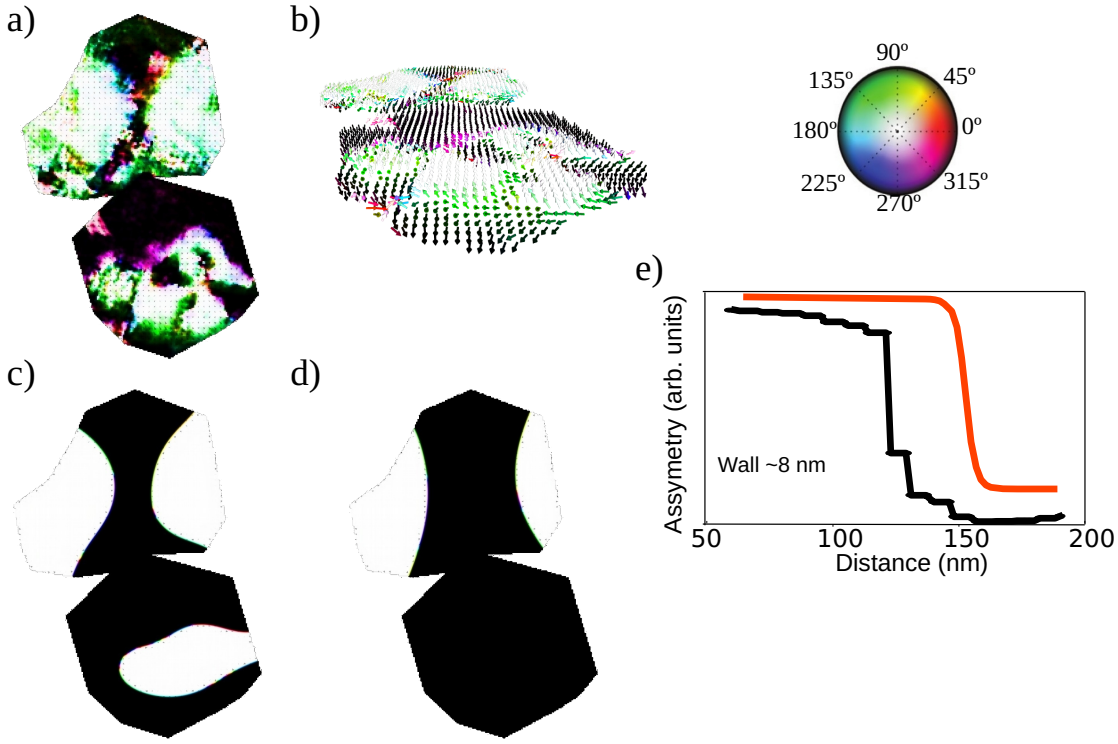

Figure 4.13: a) Reconstructed magnetic state of the $SrFe_{12}O_{19}$ platelet pixel by pixel. b) 3D projection of the magnetization vector in the platelet represented by arrows. c) Relaxed simulation of the initial configuration using the reported bulk magnetization saturation of $SrFe_{12}O_{19}$. d) Relaxed simulation of the initial configuration using a reduced magnetization saturation measured experimentally on the $SrFe_{12}O_{19}$ platelets by VSM. e) comparison between domains wall width of the experiment and simulations. Note that the color palette in the right corner represents the spin direction in the magnetic domains.

cally, the domain walls have less curvature and reproduce worse the experimental results. Probably, the main reason for the change in the magnetic domain distribution at the latter simulation could be due to that the VSM magnetization measured at 1.5 T underestimates the saturation magnetization.

In summary, in this chapter, a full characterization of strontium hexaferrite platelets grown by hydrothermal synthesis has been carried out. For this purpose, several experimental techniques have been used. For the morphological, compositional and structural characterization, microscopies (TEM and TXM), diffraction (XRD) and spectroscopies (XPS and Mössbauer) have been applied. The magnetic properties have been determined using VSM and X-ray absorption techniques and have been understood according to the cationic distribution discussion done in the Mössbauer spectroscopy section. Furthermore, calculations (DFT and multiplet approach) and micromagnetic simulations have been supported the results obtained.

4.5 Conclusions

- Strontium hexaferrite platelets have been synthesized by the hydrothermal method. The particles have a hexagonal shape with lateral sizes of micrometres and tens of nanometers thickness and are found forming aggregates.

- In addition to confirming the presence of Fe^{3+} species and the existence of the pure SFO phase observed by XPS and XRD, Mössbauer spectroscopy provided information on the cationic distribution. Platelets show an increase of iron cations in tetrahedral sites with respect to octahedral sites in the region near the surface. This fact plays an essential role in the understanding of the magnetic moments values.

- XAS and XMCD spectra of the $L_{2,3}$ iron absorption edges and oxygen K edge both for the platelets and for the reference commercial material have been presented. In order to understand the origin of each feature in the iron L edge spectra, multiplet calculations were carried out, taking into account the crystal field symmetry of each iron cation. It was determined that the contributions from Fe in octahedral and tetrahedral sites turned out to be responsible for the observed features showing the importance of performing the XAS measurement with high resolution.

- The sum rules applied to the XMCD spectra gave estimates for the net magnetic moments of Fe. The lower net magnetic moment of Fe in the platelets grown by the hydrothermal method compared to the value of the commercial SFO was attributed to the increase of the iron in tetrahedral positions in the former where the spin moments are aligned antiferromagnetically to the net magnetization. The O K edge spectrum was reproduced by the unoccupied density of states calculated by DFT by Jorge Cerda et al.

- XMCD-PEEM imaged the magnetic domains in platelets showing a magnetization mostly perpendicular to the platelet plane. Micromagnetics simulations using the bulk parameters for SFO reproduced the distribution of the magnetic domains.

5 Magnetic interactions in magnetic single domain platelet with cobalt overlayer

5.1 Introduction

The purpose of this chapter is to understand the magnetic coupling between a hard magnetic layer and a soft magnetic layer. Specifically, the experimental system corresponds to a magnetic single domain SFO platelet with a metallic cobalt layer on top. As explained in Chapter 1, this combination of soft-hard layers is a resource much studied and discussed during the last decades for the development of permanent magnets [159, 160]. By rigidly coupling both layers, an enhancement in its magnetic properties can be achieved. The magnetically soft material brings high magnetization while the hard material provides high coercivity. Nonetheless, several studies [161, 162, 163] reported a decrease in the coercive field in a robust rigid coupling. This decline is promoted by the propagation of unpinned domain walls generated at the soft phase, which facilitates the reversal magnetization [22].

Therefore, this chapter, with the analysis of the platelet/metal system by means of X-ray absorption techniques and micromagnetism simulations, addresses the question about the magnetic interaction conditions necessary to improve the magnetic properties of a bilayer system. In particular, we will research to what extent soft magnetization direction might align with that of hard by pure magnetodipolar interaction and/or in low exchange-coupling regime, which is the interaction that induces the domain wall propagation mechanism.

The results presented in this chapter have been published in:

- G. D. Soria, C. Granados-Miralles, A. Mandziak, P. Jenus, M. Saura-Múzquiz, M. Christensen, M. Foerster, L. Aballe, J. F. Fernández, J.d.l. Figuera, and A. Quesada, “Uncorrelated magnetic domains in decoupled $SrFe_{12}O_{19}$/Co hard/soft bilayers", Journal of Physics D: Applied Physics, vol. 54, no. 5, p. 054003, 2020.

5.2 Cobalt

Cobalt is a transition metal that crystallizes at room temperature in the hexagonal close-packed structure (hcp). Its lattice parameters are a = 2.5 Å and c/a = 1.632 Å. Since its magnetization easy axis is the c-axis, presenting a strong uniaxial anisotropy (4.1×10^5 Jm^{-3}) [164, 165, 166]. However, in thin film form, the packing can be modified by changing the particle size and the growth temperature. Above 725 K, the cobalt crystal structure is the face-centered cubic (fcc) one [167]. We selected this material for the coupling study because its high value of saturation magnetization (1.4×10^6 Am^{-1}) [168]. This property suggests that in a rigid or partial exchange-coupling composed of cobalt metal as a soft magnetic material and a hard ferrite, an enhancement in the energy product of the system might be found [169, 170]. In contrast, for instance, such improvement would not be so obvious using a soft phase such as nickel whose M_s is 4.8×10^5 Am^{-1} [168] (similar than to SFO ferrite).

5.3 XAS-XMCD characterization from a single domain platelet

In the previous chapter, we studied SFO platelets which presented a crystallographic structure with the c-axis oriented normal to the platelet plane. Thus, taking into account that the magnetocrystalline anisotropy is along the c-axis, the net magnetization was found to be perpendicular to the platelet-plane. These results are in agreement with other studies of strontium hexaferrite platelets reported in the literature [13, 91]. That particular platelet showed several magnetic domains.

For this study, a SFO platelet was selected, displaying only a single magnetic domain in order to avoid the possible effects of domain walls and internal demagnetizing fields associated with multidomain structures. The characterization of this platelet and the subsequent magnetic coupling experiment with a cobalt layer was performed at the ALBA synchrotron by means of X-ray absorption microscopy.

The platelets that were used for this study were synthesized by the same hydrothermal method explained previously. As a result, the obtained particles showed similar shape and dimensions to those previously synthesized. For their characterization, the platelets were dispersed in ethanol and sonicated. Subsequently, a drop of the dispersion was deposited onto a Si (100) substrate without removing the native Si oxide and left to dry. The sample was then introduced in the ultra-high vacuum (UHV) chamber of a PEEM microscope and degassed at 100 °C. Since photoemission electron microscopy allows the characterization of a single platelet by means of the collection of images in real-time, as it has already been done in chapter 4, an isolated platelet was selected.

Figures 5.1a and 5.1b present the Fe L_3 edge X-ray absorption and XMCD spectra measured on a single strontium hexaferrite platelet which are characteristic of this phase (see the previous chapter). As discussed, the peaks arise from the Fe^{3+} cations in different chemical environments in the SFO structure [102, 171]. The images shown in the right panel of figure 5.1 correspond to the image of the micron size platelet measured by PEEM

at the energy of maximum intensity of the absorption spectrum (a), the XMCD image obtained at an energy of 707.0 eV (b) and, the XMCD image acquired at an energy of 708.0 eV (c). From these pictures, it is interesting to comment on the change in the intensity (gray level) on the platelet between the different dichroism images. The XMCD contrast indicates the magnetization component along the X-ray direction. The first observation of the XMCD image is that the gray level in each image is the same through the platelet indicating the platelet has a single magnetic domain. The reversal of intensity, black in figure 5.1d and white in figure 5.1e, can be understood looking at the XMCD spectra (5.1b): the XMCD intensity is reversed at the two energies, 707 eV and 708 eV. This result is in agreement with the prediction that established that the SFO single domain threshold size is approximately 1 μm [91, 109].

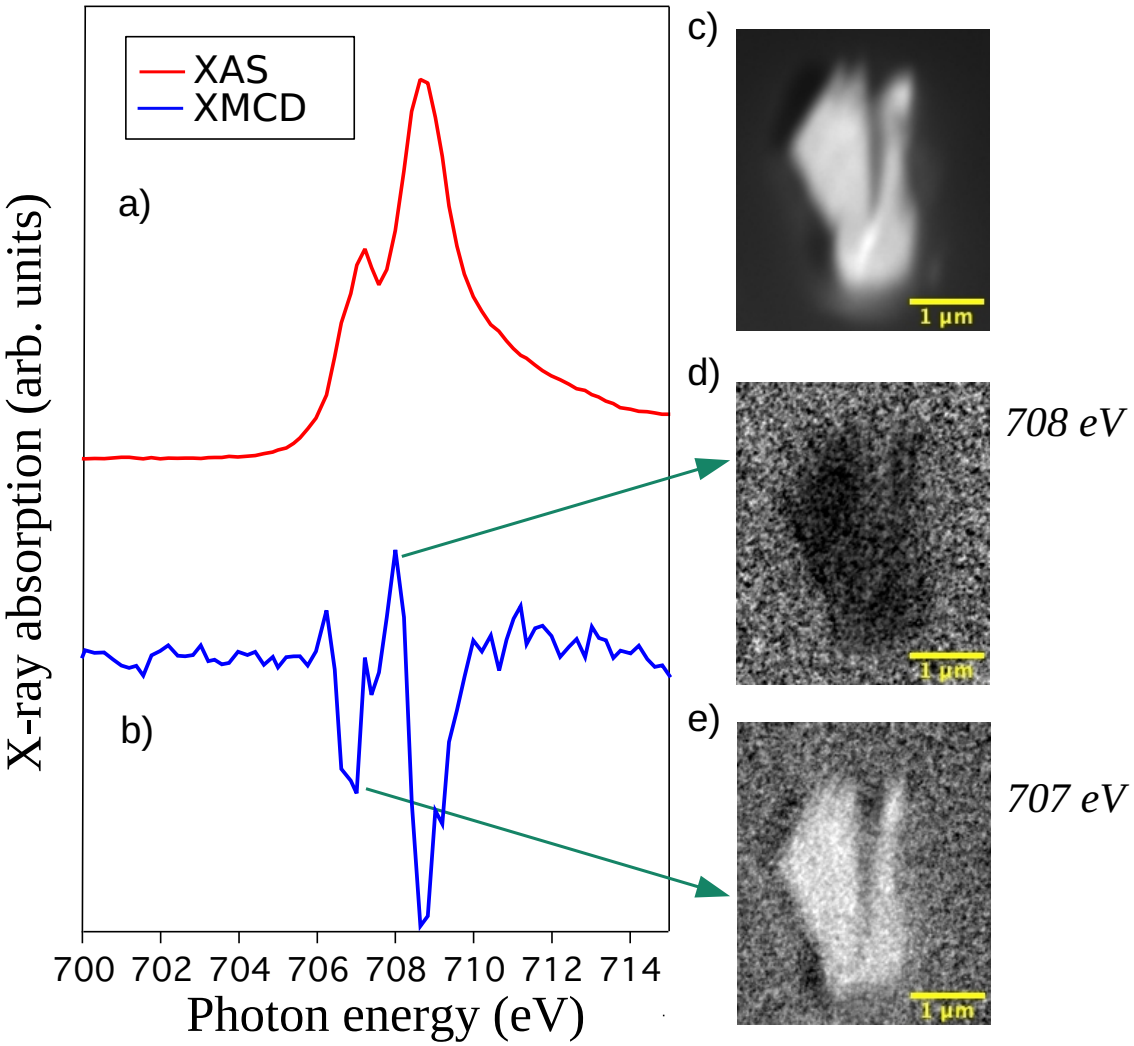

Figure 5.1: a) Fe L_3 edge XAS spectra of a SFO platelet before deposition of the cobalt layer. b) XMCD spectra associated to Fe L_3 edge XAS spectra of a SFO platelet before deposition of the cobalt layer. c) XAS-PEEM image recorded at the energy of the maximum in the Fe L_3 edge XAS spectrum. d) and e) corresponding XMCD-PEEM images obtained at the energies indicated by the arrows.

5.4 Growth and characterization of cobalt overlayer

Once the SFO platelet was analysed, a metallic cobalt overlayer was deposited on top of it by molecular beam epitaxy. The growth was carried out in the UHV PEEM chamber, where the XAS spectra and images are acquired. An electron bombardment doser was used to deposit cobalt from a cobalt metallic rod. A 2 kV difference voltage between the tungsten filament of the doser and the rod was used, and an emission current of 14 mA (corresponding to a heating power of 28 W) provided one cobalt layer for an evaporation time of 4 minutes. The evaporator calibration was carried out previously to the deposition on a ruthenium single crystal. The growth of cobalt was performed at room temperature. The total monolayers evaporated were 7, giving a thickness close to 1.2 nm [172].

The Co $L_{2,3}$ edge X-ray absorption and dichroism spectra are presented in figure 5.2a. The XAS spectrum of the cobalt layer is typical of metallic cobalt [70]. This indicates that cobalt has not been intercalated among the surface atoms of the strontium hexaferrite platelet or, if so, it has done to a minimal extent. Otherwise, the oxidized cobalt formed at the interface should be detected in the absorption spectrum giving distinctive XAS, and XMCD spectra [173]. Since atomic diffusion at room temperature is low, the formation of a metallic cobalt overlayer is not an unexpected result [174, 175]. Based on a comparable work by Kang et al. [26] on Fe/SFO bilayers and considering the growth was carried out at RT, one might expect the soft cobalt layer to be polycrystalline, although it has not been experimentally checked. In addition, the Co $L_{2,3}$ edge XMCD spectrum indicates a magnetic signal in the cobalt layer. The Fe $L_{2,3}$ edge XAS-XMCD spectra after cobalt evaporation is shown in figure 5.2b. It is similar to the iron spectra acquired before cobalt deposition.

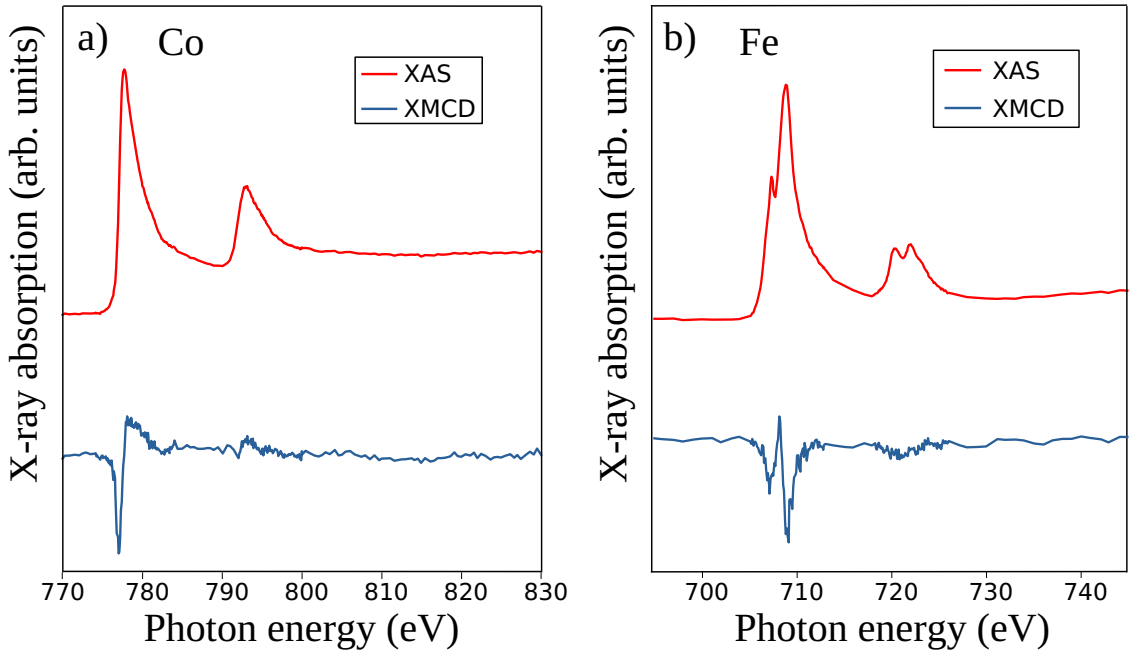

Figure 5.2: a) XAS and XMCD spectra at Co $L_{2,3}$ edge after cobalt deposition. b) XAS and XMCD spectra at Fe $L_{2,3}$ edge after cobalt evaporation.

5.5 Magnetic domains in the bilayer system

XMCD-PEEM images were obtained at three different azimuthal angles at the Co and Fe L_3-edges to characterize the magnetic domains emerging from each layer of the system and to determine the correlation between such domains, figure 5.3. The images acquired at the Co L_3-edge provided the magnetic domains from the cobalt metal layer, while the images obtained at the Fe L_3-edge revealed the magnetic domain in the underlying SFO platelet. In the cobalt layer (Fig. 5.3) several magnetic domains were observed across the platelet. The image acquired at an azimuthal angle of 120° presents reversed contrast when compared with the one acquired at 0°. For instance, the black spot in the middle of the platelet in the image recorded at 0°, appeared with colour white in the image taken at 120°. This fact indicates that the magnetization vector of the cobalt layer lies predominantly in the surface plane. Schematically, this situation is depicted in figure 5.3d. For the case of SFO domains (Fig. 5.3e-f-g), a completely different situation was appreciated. The change in the image acquisition angle did not affect the magnetic contrast of the platelet, remaining black in all the cases. This result indicates an out-of-plane magnetization for the strontium hexaferrite platelet. A schematic representation of this situation is depicted in figure 5.3h. Therefore, it can be concluded that the magnetic domains of the two layers appear to be uncorrelated, being their magnetization vectors orthogonal to each other.

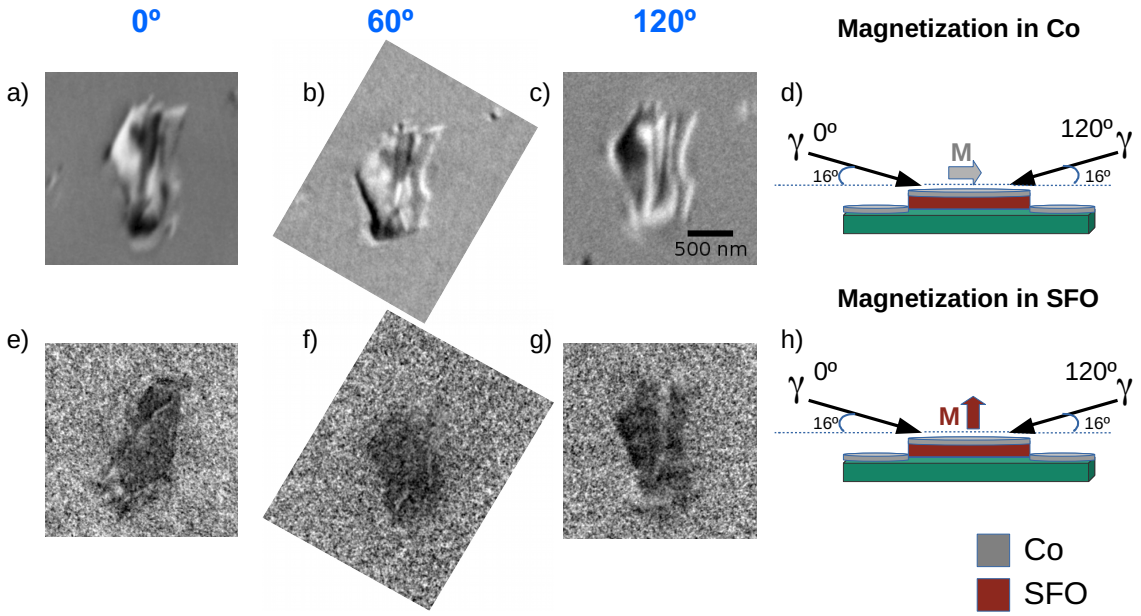

Figure 5.3: Upper row: Co L_3-edge (708 eV) XMCD-PEEM images taken at (a) 0°, (b) 60° and (c) 120° azimuthal angles. Lower row: Fe L_3-edge (777.5 eV) XMCD-PEEM images taken at (e) 0°, (f) 60° and (g) 120° azimuthal angles. On the right side, schematic representations of the magnetization of the cobalt layer d) and platelet h) at two different incoming photon azimuthal angles are presented.

Furthermore, by combining the three dichroism images at different azimuthal angles at the absorption edge of each element, the in-plane magnetization vector was determined for the platelet and for the cobalt layer. Figure 5.4a shows the resulting image for the magnetic signal in the plane of the SFO platelet. It is not easy to differentiate which area corresponds to the platelet with respect to the background. It can only be distinguished

with the platelet silhouette outlined. The SFO platelet exhibits only out-of-plane magnetization, thus the in-plane magnetization presents a similar noise signal that the background substrate. However, for in-plane magnetization in the cobalt layer (figure 5.4b), it is possible to distinguish within the area deposited on the platelet different magnetic domains, all of them in the sample plane. The magnetization orientation of the cobalt layer domains on the platelet is represented in the azimuthal angle, magnetization histogram graph (figure 5.4c). The magnetic domains in the soft layer are preferentially oriented along the directions 90° and 45° within the plane. The magnetization orientations determined in the cobalt layer might be generated due to the cobalt doser location used. I.e. the direction of metal deposition can induce certain magnetic anisotropy. This likely explanation can be supported by Park et al [176] work where an in-plane magnetic anisotropy for iron deposited on Mg(001) induced by the incidence direction of the growth method (MBE) was reported.

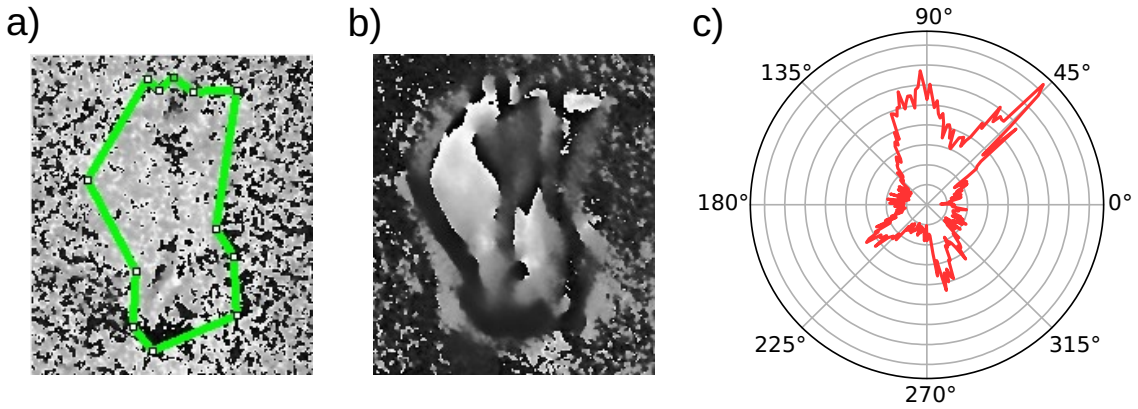

Figure 5.4: a) and b) correspond to the vector maps for the SFO platelet and cobalt layer, respectively. c) Magnetization histogram along the azimuthal angle for in-plane cobalt layer on top of the SFO platelet.

5.6 Energetic contributions to the magnetic response from cobalt domains

As it can be seen in the dichroism images, it seems that there is no coupling between the cobalt layer and the SFO platelet. Theoretically, the exchange length L_{ex} of strontium hexaferrite, which determines the soft phase (Co) thickness below which rigid coupling should occur, is approximately $L_{ex} = 21$ nm [91]. Specifically, in this case, the cobalt overlayer is 1.2 nm thick. This rigid coupling was not observed experimentally. It has been reported that without thermal activation of diffusion/reaction at the interfaces or structural match at the atomic scale [174, 175], exchange-coupling between hard and soft layers is not likely to occur since it requires chemical bonds and orbital overlap for the exchange interaction to be activated [177]. Assuming this lack of coupling, the interactions that govern the domain configuration from each layer are the magnetocrystalline anisotropy and the magnetodipolar interaction. A simplistic calculation has been made in response to the experimentally observed magnetization orientation in the cobalt layer to make a quantitative estimate of the energy terms specified in the bilayer system.

On one hand, the SFO platelet generates an external magnetic field $H_{ext} = M_{SFO}$, where M_{SFO} is the SFO magnetization per unit volume. This magnetic field is associated with an energy term, Zeeman energy (E_{Zeeman}), that also depends on the magnetization cobalt layer, involving all the sample volume [177, 99]. This energy can be expressed as:

$$E_{Zeeman} = -\mu_0 M_{Co} M_{SFO} cos\phi \tag{5.1}$$

ϕ being the angle between the cobalt magnetization and the direction of the external field stemming from the SFO magnetization, μ the vacuum permeability ($4\pi 10^{-7}$ Nm^{-2}) and M_{Co} and M_{SFO} the saturation magnetization values corresponding to each layer, which are taken as 1.4×10^6 Am^{-1} and 3.8×10^5 Am^{-1}, respectively [168, 108].

On the other hand, the shape anisotropy contribution (E_m) is described by the following equation:

$$E_m = \frac{1}{2}\mu_0 M_{s(Co)}^2 cos^2(\Theta) \tag{5.2}$$

Where Θ is the angle between the magnetization of the cobalt layer and the normal to the film plane [178].

Considering that the purpose was to align the magnetization of both layers out-of-plane and the experimental results show different magnetization direction of each layer, we determinate the total energy for two specific configurations: 1) the magnetization from the cobalt layer normal to the platelet such that the magnetic domain is aligned with the SFO magnetization, figure 5.5a. 2) The magnetization orientation in the cobalt layer is parallel to the sample plane (figure 5.5b). The results from the energy calculations for both scenarios are collected in table 5.1.

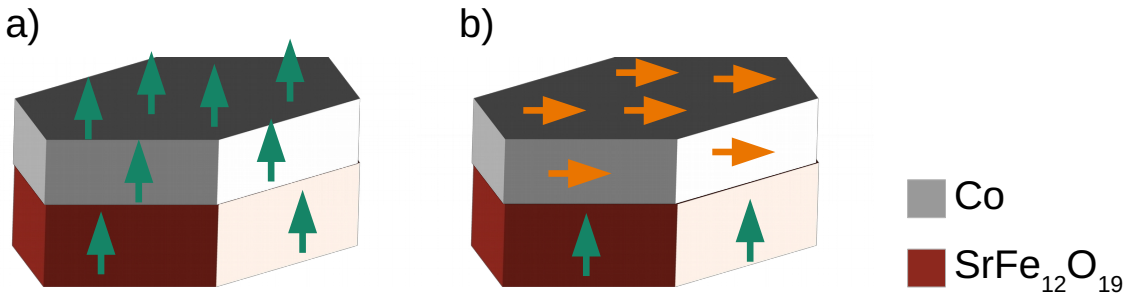

Figure 5.5: Schematic drawing showing the magnetization direction configurations in the bilayer system. a) Cobalt layer with out-of-plane magnetization and b) cobalt layer with in-plane magnetization. For both cases, the SFO presents a magnetization out-of-plane.

Configurations	Zeeman energy (kJ/m^3)	Shape anisotropy (kJ/m^3)	Total energy (kJ/m^3)
Out-of-plane	-669	1232	563
In-plane	0	0	0

Table 5.1: Results from considering the different energy contributions in the cobalt layer according to the magnetization orientation.

In the first configuration, the cobalt magnetization is aligned with the external magnetic field, so $\phi = 0°$ and $\Theta = 0°$. Thus, it minimizes E_{Zeeman} (-669 kJ/m^3) although it maximizes E_m (1232 kJ/m^3). In the second configuration, the cobalt spins are normal to the SFO layer magnetization, hence $\phi = 90°$ and $\Theta = 90°$. Here, the energy balance is the opposite of the previous one since, for both energy terms, the value is 0 kJ/m^3. According to these calculations, the out-of-plane configuration has a 563 kJ/m^3 higher energy than the in-plane configuration resulting in the latter to be most energetically favorable. Therefore, in the SFO/Co system, the soft overlay's preferred magnetization configuration is in-plane, which is in agreement with the experimental observations. In addition, this result points out that the shape anisotropy arising from the metal thin film (in-plane magnetization) overcomes the magnetocrystalline anisotropy emerging from the hexaferrite layer (out-of-plane magnetization).

5.7 Micromagnetic simulation

Micromagnetic simulations were performed to further understand the balance between the different contributions to the magnetic energy and domain structure. Such simulations represented the model of the studied bilayer system, i.e. SFO/Co. Thus a layer is characterized by the strontium hexaferrite parameters and another for cobalt ones. The values were, for SFO: exchange stiffness $A_s = 6 \times 10^{-12} Jm^{-1}$, uniaxial magnetocrystalline anisotropy $K_u = 3.6 \times 10^5$ Jm^{-3} (pointing out of the plane of the platelet), saturation magnetization $M_s = 3.8 \times 10^5$ Am^{-1}, thickness = 18 nm [91, 158, 108]. For cobalt: $A_s = 1.5 \times 10^{-11} Jm^{-1}$ [179], $M_s = 1.4 \times 10^6$ Am^{-1} [168], thickness = 1.2 nm. The magnetocrystalline anisotropy for cobalt was considered negligible, $K_u = 0$ Jm^{-3}, due to the fact that the cobalt layer is expected to be polycrystalline after being grown at room temperature (RT), which averages the effective anisotropy of the film to a lower value [180]. The cell size used is 4.2 x 4.2 x 1.2 nm, and the full simulation slab is 1.2 μm × 1.2 μm × 19.2 nm.

We used as starting configuration one in which the SFO platelet is considered to be a single domain, having an out-of-plane magnetization, and the cobalt layer is considered to have a random magnetization orientation, figure 5.6a. The palette in the corner in figure 5.6 shows the color corresponding to each magnetization azimuthal angle. Thus, in this initial distribution, the spins depicted with white color in the SFO platelet represent a magnetization orientation out-of-plane, and the spins depicted with multiple colors in the cobalt layer correspond to random magnetization orientation. Then, this configuration is relaxed [86] finding the systems' energy minimum [86]. The simulation was repeated for five different values of the interlayer exchange coupling strength (κ). The κ parameter is a scaling factor that is used to alter the exchange coupling between layers. This factor is parametrized between $0 < \kappa < 1$ [22], where 0 corresponds to complete absence of

exchange-coupling and 1 to rigid exchange coupling. For $\kappa \geq 0.25$ (figure 5.6b-d), it can be observed that the spins present color white for both the platelet and the cobalt layer. This indicates that the spins of the soft layer are perfectly aligned with those of SFO. In the case of $\kappa = 0.1$ (figure 5.6e), a mild "colouring" is detected in the cobalt spins, which points out that they are deviating slightly from the out-of-plane magnetization direction emerging from SFO spins (white color) and start to follow their multidomain configuration. Finally, in the absence of exchange coupling (a value of κ equal to zero), the spins from the cobalt layer show different colors corresponding to the in-plane magnetization showing a multidomain pattern. In this case, the soft layer does not experiment with any influence of the magnetization normal to plane arise from the platelet (figure 5.6f).

The micromagnetism simulations performed at different degrees of exchange-coupling suggested that a magnetic behavior similar to the experimental results of the bilayer (figure 5.3) is observed only when κ is zero. One possibility to consider is that the resolution of the dichroism images in small sections of the platelet is not capable of reflecting a slight turn of the spins of the cobalt layer influenced by the external field of the SFO layer. Likewise, with the data at hand, the simulated spin configuration suggests that there is no exchange coupling between the two phases: at κ couplings equal to or greater than 0.1, the cobalt spins should align to some extent with the hexaferrite strontium spins. This fact supports the hypothesis that the shape anisotropy of the cobalt layer overcomes the field generated by the SFO layer.

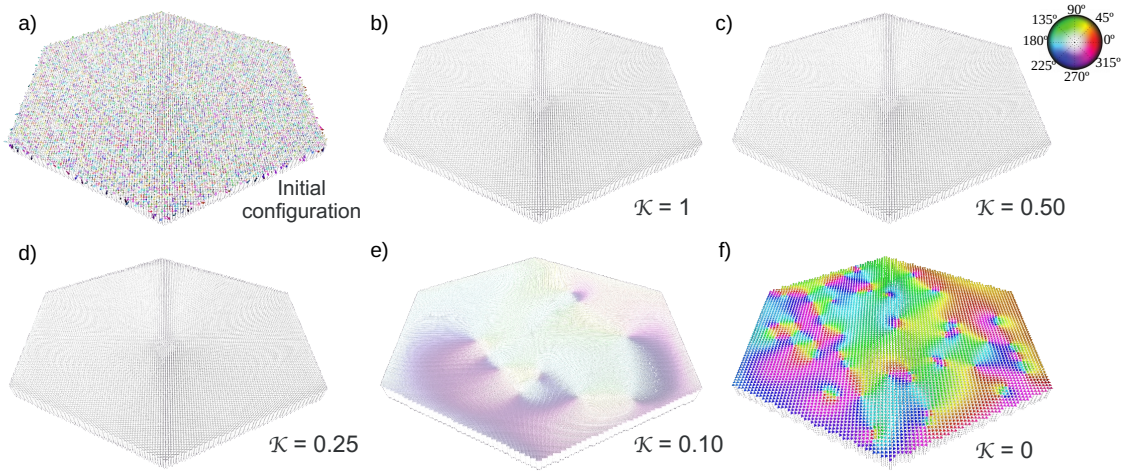

Figure 5.6: Micromagnetic simulation showing the configuration of spins of both a 18 nm thick SFO hexagonal platelet and a 1.2 nm thick cobalt film on top. Spins illustrated in white color are pointing up in an out-of-plane configuration, spins illustrated in rainbow colors correspond to different in-plane directions following the colour scheme on the upper right corner. Images (a) to (f) correspond to the micromagnetic pattern of the platelet and the metal overlayer with random initial configuration of spins and five different values of the exchange-coupling strength κ, from completely coupled ($\kappa = 1$) to completely uncoupled ($\kappa = 0$).

Hysteresis loops were simulated using the micromagnetic configuration described above to comprehend the bilayer system's exchange-coupling interaction further. Experimentally, it was not possible to measure the magnetic hysteresis loops in the PEEM instrument because the sample holder used for studying the platelet system was not suitable for applying a magnetic field. The loop simulations were performed at different strength of the exchange-

coupling κ between the platelet and the overlayer applying an external magnetic field of up to 2500 kA/m in the out-of-plane direction. The results are presented in figure 5.7a. A variation can be appreciated in the remanence magnetization (M_r) and the coercive field (H_c) of the bilayer system according to the coupling degree. An additional graph was done to show coercitivity as a function of exchange-coupling (figure 5.7b) to see the effect of the coupling better. Knowing that the magnetically soft phase is characterized by a small coercive field, it is not surprising that the coercive field of the bilayer system decreases compared to the isolated magnetically hard material as the strength of exchange coupling is increased. The soft layer acts as a source of domain walls and facilitates magnetization reversal and reducing then the coercivity. Likewise, the rise in κ involves a higher strength of alignment of the soft layer. The highest magnetization at remanence value is achieved for a perfectly rigid coupling ($\kappa = 1$).

Such simulations are a simplistic model of the experimental setup which do not include possible physical elements that may occur in practice, such as the formation of dislocations in the layers, changes in crystallinity of each phase, interlocation of atoms in the interface..., etc. Nevertheless, these micromagnetic simulations provide an approximation of the qualitative trends and underlying physical mechanisms of the experimental configuration.

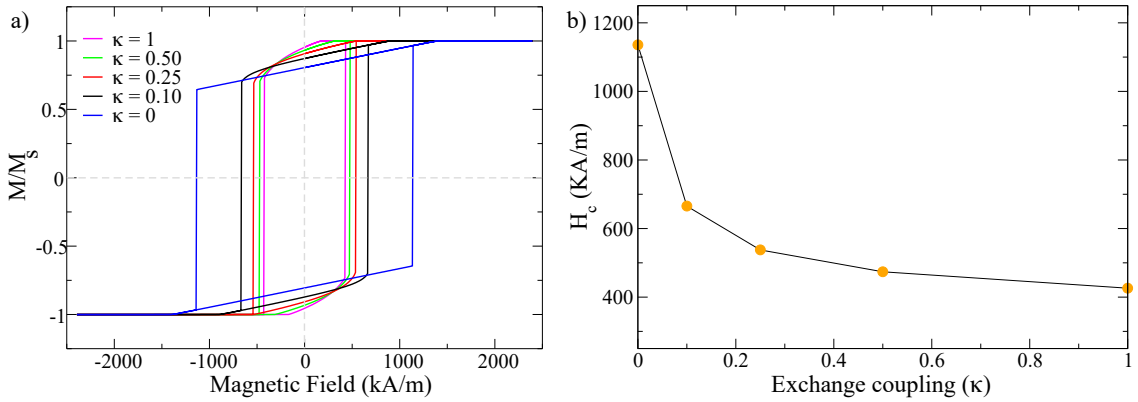

Figure 5.7: a) Simulated hysteresis loops for the $SrFe_{12}O_{19}$/Co hard/soft system portrayed in figure 5.6 with various strength of exchange coupling (κ).The magnetic field was applied perpendicular [001] to the bilayer. b) Coercive field (H_c) values as a function of exchange-coupling strength.

Hence, this result brings forward the fact that close interfacial contact and a soft phase thickness clearly below the threshold for rigid coupling are not sufficient to achieve exchange-coupling. The orbital overlap at the interface is required. As we have commented previously, this overlapping is favoured by different factors such as crystallinity, atomic coherence between both phases, and diffusion/reaction in the atoms of the interphase prompted by thermal energy. Studies carried out by Fullerton [19], and Sabet [181] for different hard/soft bilayer systems reported the need for controlled crystallinity, epitaxy and rearrangement of the atoms between both phases in order to tailor the extent of exchange coupling at the interphase. F. Casoli [182], and Y. Kang [26] works showed that annealing promotes the rearrangement of atoms at the interphase, increasing coupling.

However, although in this chapter, the objective of the magnetic coupling between both phases has not been achieved, a very promising result has been obtained. And this is that the micromagnetic simulations suggest that at low exchange couplings, the system's magnetic properties could be substantially improved, i.e., the hard-soft layers allow aligning the soft layer with the hard phase without facilitating massive domain wall propagation. This development would avoid a loss of coercivity as it was observed in previous works for fully rigid coupled systems [183, 163, 184, 185].

5.8 Conclusions

A bilayer system composed of a single magnetic domain SFO platelet and a cobalt metal layer has been studied by means of X-ray absorption techniques at the ALBA synchrotron in order to study the magnetic coupling between both layers. Cobalt metal layer 1.2 nm thick has been deposited by MBE on strontium hexaferrite platelet at room temperature. Dichroism images at the Co and the Fe L-edges at different azimuthal angles have determined that the magnetization is in the plane for the soft layer and perpendicular to the sample plane for the platelet. The lack of correlation between the magnetic domains of both phases indicated the absence of exchange coupling between them. Theoretically, this hypothesis was supported by a consideration of the energy contributions involved in the system. The shape anisotropy of the soft layer overcomes the external field created by the SFO layer. In addition, micromagnetic simulations were carried out that corroborate the absence of the interlayer exchange-coupling as it was seen in the experiment. Furthermore, these simulations provided a possible path for a substantial improvement in the energy product, $(BH)_{max}$, for hard-soft bilayer systems. It was shown that at low couplings between both layers ($\kappa < 0.25$), it is possible to maximize the magnetization without a high loss of the coercitivity of the system. For this exchange coupling range, the magnetization of both layers is aligned while, at the same time, the domain wall propagation activated in more rigid coupling conditions is avoided.

6 $SrFe_{12}O_{19}$ thin films

6.1 Introduction

In the previous chapter, we have studied and demonstrated that in the SFO/soft configuration, the shape anisotropy from the soft layer overcomes the out-of-plane magnetization from SFO layer. In addition, we have proved that there is no alignment between both without the occurrence of interlayer exchange-coupling. In this chapter, we present results on a SFO/Co bilayer system but with the peculiarities that the SFO layer is continuous (thin film) and presents magnetization within the plane. With this approach, we want to avoid the problem of shape anisotropy from the soft layer. Further, we seek the occurrence of some kind of magnetic coupling in this different bilayer system (again in the absence of exchange-coupling).

The main growth techniques used to prepare strontium hexaferrite films are pulsed laser deposition [186], chemical solution deposition [187], metal–organic chemical vapor deposition [188], spin coating sol–gel process [189] and RF magnetron sputtering [42]. The latter (and used in this study) can produce SFO films with magnetic easy axes distributed randomly in plane, or aligned perpendicularly, depending on the sputtering process [190]. This change in the easy axis orientation is attributed to the variation in the c-axis growth direction's orientation relative to the film plane. This c-axis orientation can depend on different deposition parameters such as: substrate temperature, sputtering power, oxygen pressure, annealing conditions [191, 192, 42, 193]. Also, the film thickness and the growth in an epitaxial intermediate layer are factors involved in the prefered c-axis direction [194, 195]. Here, the influence of several factors will be discussed in-depth, such as annealing treatment, sputtering power and thickness. The structure of this chapter follows the next points:

1. Growth of SFO thin films by RF magnetron sputtering and the annealing effect.

2. Magnetization orientation study of the thin films as a function of the growth parameters.

3. Understanding of the coupling with a Co overlayer in in-plane conditions.

Part of the results presented in this chapter has been published in:

- G. D. Soria, J. F. Marco, A. Mandziak, S. Sánchez-Cortés, M. Sánchez-Arenillas, J. E. Prieto, J. Dávalos, M. Foerster, L. Aballe, J. López-Sánchez, J. C. Guzmán-Mínguez, C. Granados-Miralles, J. d. l. Figuera, and A. Quesada, "Influence of the growth conditions on the magnetism of $SrFe_{12}O_{19}$ thin films and the behavior of

$Co/SrFe_{12}O_{19}$ bilayers", Journal of Physics D: Applied Physics, vol. 53, p. 344002, 2020.

6.2 SFO target

For the growth of the strontium hexaferrite thin films, we have used radiofrequency magnetron sputtering. As explained in the first chapter, a plasma is generated, which etches on the substrate, and the material is a target of the compound to be deposited, in our case, $SrFe_{12}O_{19}$. The target was sintered from commercial $SrFe_{12}O_{19}$ powders.

Initially, the commercial powders were sieved. These were compacted using a 7% by weight solution of 20% paraloid (resin-adhesive) and 80% acetone. Then they were pressed by an automatic pressing machine at 150 kg/cm^2. Finally, they were put in an oven whose temperature was ramped at 5°C/min from RT to 1250 °C and kept at that temperature for three hours. The organic part disappeared at 600 °C. The resulting target dimensions were 5.1 cm in diameter and 2.5 mm thickness.

In order to determine if the sintered sputter target presented a pure strontium hexaferrite phase and, in consequence, was a suitable target, transmission Mössbauer and Raman spectra were acquired at room temperature (figure 6.1). The Mössbauer spectrum was fitted to five sextets. Each sextet corresponds to Fe^{3+} in a different crystallographic site[143]. Table 6.1 collects the hyperfine parameters used for the fit. All parameters are characteristic of strontium hexaferrite [131]. Thus, the Mössbauer data indicates that the target is composed only by SFO. The Raman spectrum shows the expected vibration bands for strontium hexaferrite [196, 197, 198, 199]. Specifically, the Raman modes at 409, 469, 618, 688, and 729 cm^{-1} map vibration modes arising from different Fe^{3+} sites. The peak observed at 409 cm^{-1} is assigned to the octahedral site (dominated by 12k and 2a), the peak at 469 cm^{-1} is a mixture of octahedral sites (12k and 2a), 620 cm^{-1} corresponds to the octahedral sites (4f2), and the peaks at 688 and 734 cm^{-1} are due to the bipyramidal sites (2b) and tetrahedral sites (4f1) vibration modes, respectively. Hence, again it is confirmed that the target is entirely SFO.

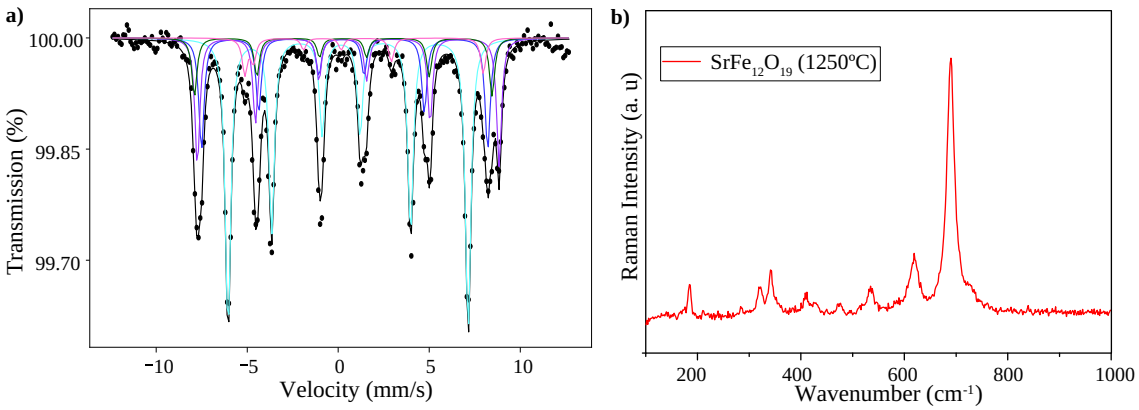

Figure 6.1: a) Mössbauer spectrum and b) Raman spectrum recorded at RT from the SFO target.

Site	δ ($\pm$ 0.03 mms^{-1})	2ε ($\pm$ 0.05 mms^{-1})	H ($\pm$ 0.05 T)	Γ ($\pm$ 0.05 mms^{-1})	Area (%)
12k	0.35	0.38	40.9	0.36	48
4f1	0.26	0.18	48.8	0.34	18
4f2	0.39	0.30	51.4	0.32	19
2a	0.29	0.02	50.7	0.34	9
2b	0.27	2.28	40.6	0.34	6

Table 6.1: ^{57}Fe Mössbauer parameters obtained from the fit of the spectra shown in Figure 6.1a. The symbols δ , 2ε, H, Γ correspond to isomer shift, quadrupole shift, hyperfine magnetic field and linewidth, respectively.

6.3 Annealing effect in SFO thin films formation

Once the purity of the phase in the target is confirmed, SFO thin film deposition can be carried out. It has been reported that the growth of the crystalline phase of SFO requires two steps: deposition and post-annealing treatment at high temperature (800°C - 900°C) [158, 192, 42]. Several works have demonstrated the need for the annealing step on the sample either *in-situ* or *ex-situ* of the deposition chamber [191, 200, 201]. Such studies pointed out, by X-ray diffraction analysis, that the as-grown sample is amorphous. However, only a few studies discuss the character of the as-grown film and how it is affected by the annealing step. Snyder et al. [202, 203, 204] reported the local structural anisotropy in the as-grown film before annealing for barium ferrite thin films (a compound which is isostructural to SFO) by EXAFS. The data suggested networks of iron atoms surrounded by their oxygen nearest neighbors, with barium atoms fitting into in between spaces. Apparently, this determines the final crystalline texture (and the resulting magnetic anisotropy), which forms upon annealing.

According to the phase diagram of SrO-Fe_2O_3 (figure 6.2), the formation of SFO appears at the composition of 10 % weight of strontium oxide together with iron oxide at elevated temperature [205, 100]. One might expect that the thin film without annealing step would be composed of the species mentioned (SrO, Fe_2O_3).

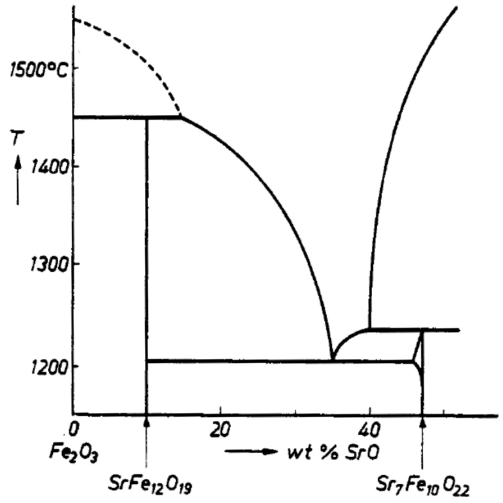

Figure 6.2: The binary phase diagram SrO-Fe_2O_3 reprinted from reference [205].

To understand the influence of annealing on the formation of the strontium hexaferrite structure in our thin films, two films were grown in identical conditions using the parameters collected in Table 6.2. Subsequently, one of them was annealed at 850°C in air for three hours.

Substrate Si (100)	Temperature 25°C	Target distance 60 mm	Base pressure $1x10^{-6}$mbar	Time pre-sputter 15 min
Working pressure 7×10^{-3} mbar	Ar pressure 1 mbar	Ar/O_2 ratio 2%	Power 260 W	Time deposition 5 hours

Table 6.2: Parameters used in the deposition process rf-magnetron sputtering.

6.3.1 Compositional and structural characterization

The composition and thickness of the different films were determined by Rutherford backscattering spectroscopy (RBS) in a 5 MV tandem accelerator using $^4He^+$ at 3.045 MeV, figure 6.3. This analysis was carried out in the Centre for Micro Analysis of Materials (CMAM). The RBS technique is based on elastic collision between atoms. The ion beam (He^+) hits the sample, and depending on the atom it collides with, the backscattered ions will have different energies. Hence, RBS provides elemental chemical identification since these energies are specific of the scattering atoms and, furthermore, the number of ions reaching the detector at these specific energies is proportional to the concentration of scattering atoms in the film examined, allowing for quantitative characterization. A energy of the incident He^+ beam of 3.045 MeV was chosen as it is the appropriate both to finger all the different atoms in this particular film as well as to enhance the oxygen cross section (resonant backscattering). The depth distribution and quantification of the various elements were determined with the SIMNRA simulation software package [206]. The ion fluence for the Rutherford backscattering and resonant backscattering experiments was set at 10 μC. A silicon barrier detector, at a scattering angle of 170.0 °, collected the backscattering ions while a three-axis goniometer was employed to control the crystal position.

First of all, a very similar composition was found for both samples. Both the non-annealed sample as well as the post-annealed film present the same elements in the spectra: O, Si, Fe, Sr and Ba (figure 6.3). These atoms come from the SFO film as well as from the substrate. The small amount of barium arises from a small Ba impurity in the commercial powder. The fit is done using the SIMRA program resulted in good agreement with the experimental spectra. The concentrations of the different elements are not too different between both samples. The atomic Fe/O ratio expected for pure SFO is 0.63. In the case of the non-annealed film, the Fe/O ratio is 0.66, while for the annealed film is 0.63. Thus, the missing O atoms during deposition are recovered after the annealing treatment.

The films thicknesses have also been determined. The concentration obtained for the annealed sample is 1.53×10^{19} atoms/cm^2. Assuming that this film is strontium hexaferrite and using a density of 5.14 g/cm^3 as corresponds to pure SFO [18], the calculated thickness is 1.62 μm. For the non-annealed sample, the concentration of the atoms is 1.75 x 10^{19} atoms/cm^2 what results, using the same density value, in a thickness of 1.86 μm. The difference in thickness (13%) between both films probably arises from the systematic error of the growth method. The results above are collected in table 6.3.

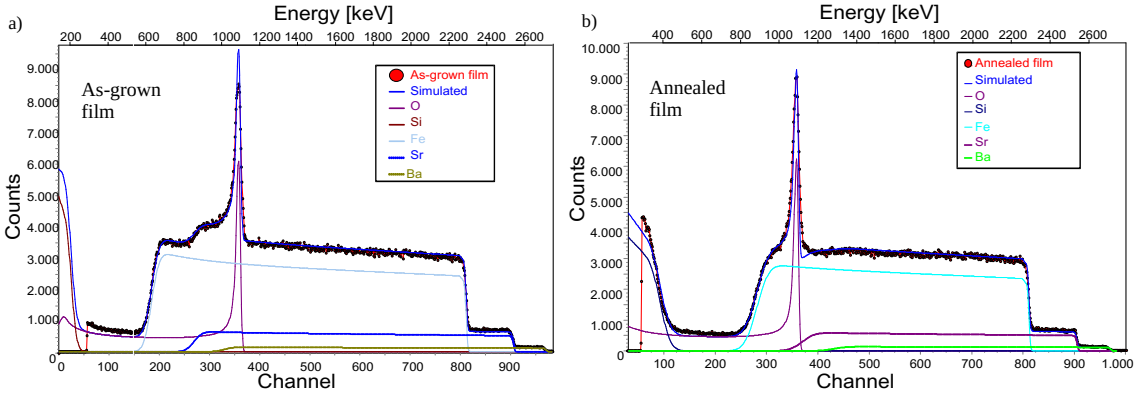

Figure 6.3: RBS experimental spectra (red circles) of SFO: a) as-grown film and b) annealed film. The simulationed spectrum obtained by the SIMRA code for each sample is defined by blue solid line. The signals corresponding to the diferent elements are depicted in the legend of each spectra.

Samples	Fe/O ratio	Concentration (at/cm^2)	Thickness (μm)
As-grown film	0.66	1.75×10^{19}	1.86
Annealed film	0.63	1.53×10^{19}	1.62

Table 6.3: Parameters calculated for the films from RBS spectra.

The crystal structure and texture of the films was analyzed by X-Ray Diffraction (XRD). Figure 6.4 presents the XRD patterns recorded from each sample. The XRD pattern of a commercial SFO powder has been included for comparison.
The annealed film (black pattern) presents all the diffraction peaks that correspond to a crystalline strontium hexaferrite structure, with the exception of the Si peaks arising from the Si substrate. The higher intensity peaks appear at 30.4°, 35.2°, 37.1°, 54.0° and 63.2° which match with the (110), (201), (203), (300), (220) Miller indices, respectively of SFO [112, 207]. Additionally, the most prominent peak is the one at 30.4°. This suggests a preferential growth of the structure with the c-axis of the SFO parallel to the film plane. The crystallite size was determined by the Scherrer formula [128], and the lattice parameters by the distance formula between adjacent planes in the set (hkl) for hexagonal crystal structure [48]. The value of particle size is 55 nm and the lattice parameters are a = 5.89 Å and c = 23.49 Å. The unit cell values are in good agreement with the literature [91, 207]. The non-annealed sample shows a few broad diffraction peaks indicating a low crystallinity of the film. As it was mentioned previously, some authors found the as-grown samples to be amorphous. Our as-grown film shows broad diffraction peaks which do not correspond to SFO. In fact, the diffraction peaks at 30.1° and 66.5°, could be associated to magnetite (Fe_3O_4) or maghemite (γ-Fe_2O_3) [208, 209, 210, 211, 212]. XRD does not allow to distinguish well between Fe_3O_4 and γ-Fe_2O_3, therefore we resort to Mössbauer spectroscopy to achieve a more confident identification (see section 6.3.2). The crystallite size of this film determined from the XRD data is 12 nm.

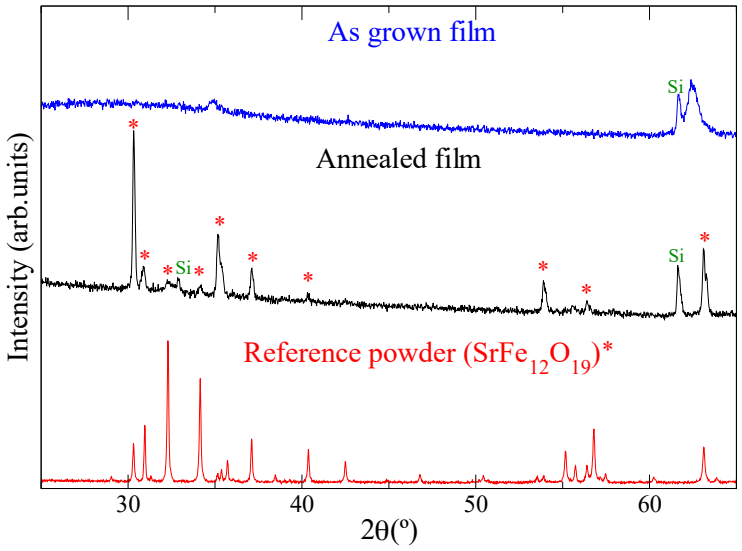

Figure 6.4: XRD diffraction patterns from the SFO films: as-grown (blue color) and post-annealed (black color), together with the reference powder (bottom one).

Raman spectroscopy was then used for the chemical characterization of the films (figure 6.5). A reference SFO powder pattern was used for identification purposes. The annealed sample shows the bands characteristic of strontium hexaferrite [213, 196, 197, 198, 199]. Such Raman modes were explained in a previous section as arising from the iron cations in different crystallographic sites of SFO. The as-grown sample shows a vibration mode with a broad peak at 690-700 cm^{-1}. According to the literature, the broad and most intense peak for maghemite is around 703 cm^{-1}, which could be assigned to the A1g vibration mode (O-Fe-O bridge) [214, 215, 216]. This correlates well with the XRD data in that the as-grown sample seems to have a maghemite-like structure.

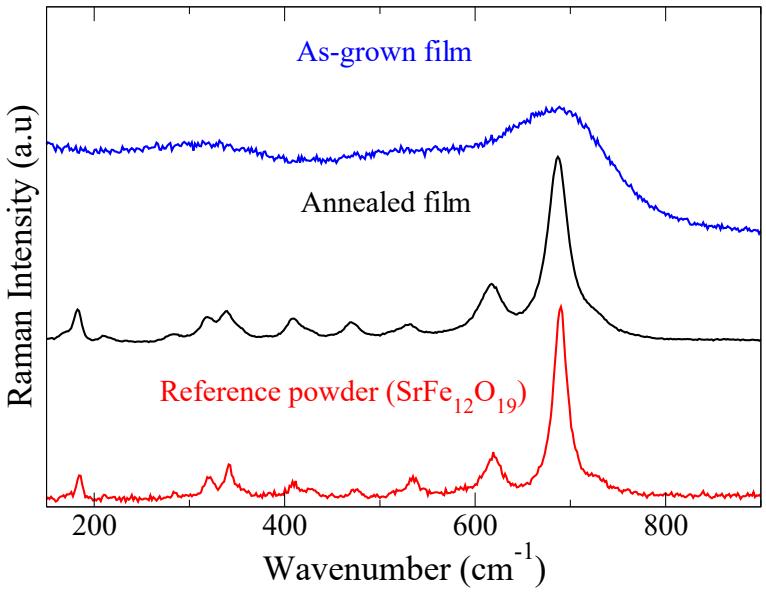

Figure 6.5: Raman spectra of $SrFe_{12}O_{19}$ recorded from the films and the reference powder.

6.3.2 Magnetic characterization

From a Mössbauer spectrum, information about the chemical, structural and magnetic state of a particular iron cation can be obtained. In figure 6.6a, the transmission Mössbauer spectra recorded from the as-grown SFO film at 298 K (RT) and 35 K are presented. In the spectrum recorded at RT, a paramagnetic doublet is observed instead of the usual five magnetic components expected for SFO [131]. This doublet presents an isomer shift ($\delta = 0.34$ mm/s) which is characteristic of Fe^{3+} [217]. The collapse of the magnetic interactions at room temperature is compatible with the poorly crystalline/superparamagnetic character of the as-deposited film and probably arises from the small size of the film grains. This assumption is in good agreement with the results observed by Raman and XRD. When the non-annealed sample was measured at 35 K, two magnetic contributions were observed, which can be associated to Fe^{3+} cations in octahedral and tetrahedral environments. The hyperfine parameters determined from the spectra of the non-annealed sample are collected in Table 6.4. The low temperature spectrum recorded from the non-annealed sample does not correspond, then, with that expected for SFO and resembles clearly that shown by many oxides having an spinel-related structure. In this particular case, the 35 K spectrum, and the corresponding hyperfine parameters, are very similar to those reported for 5 nm maghemite nanoparticles measured at comparable temperatures (40 K) [218]. Both the RT and 35 K Mössbauer spectra endorse the XRD and Raman results and confirm that the iron phase contained in the as-grown film is superparamagnetic maghemite. Opposite to this, the RT and 35 K spectra recorded from the annealed film (figure 6.6b) are fully characteristic of SFO [131], except by the small Fe^{3+} paramagnetic doublet (3%) observed at RT, which possibly arises from a very minor fraction of SFO/maghemite particles of nanometer dimensions.

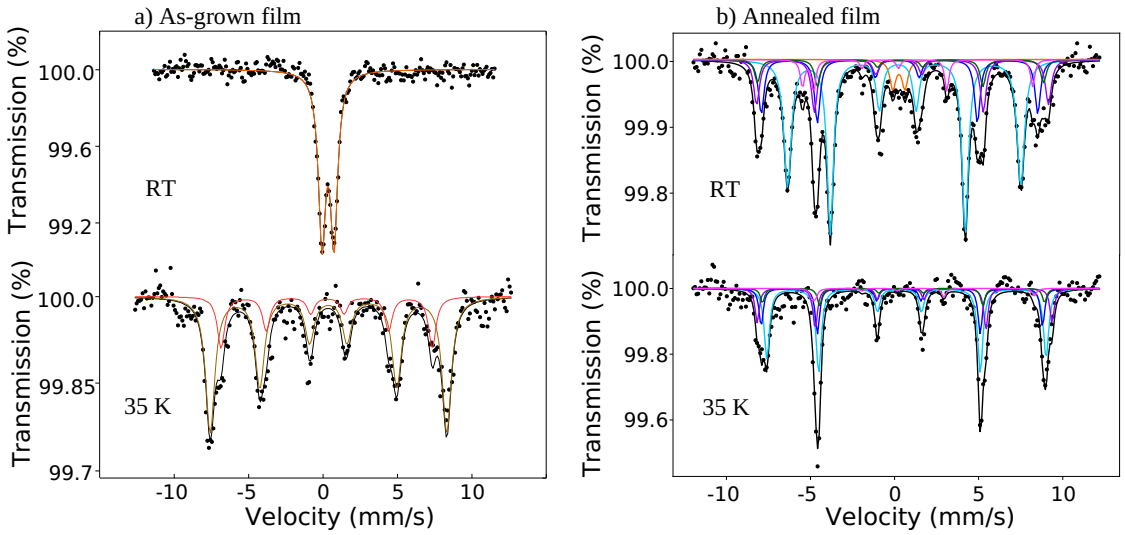

Figure 6.6: Transmision Mössbauer spectra recorded from both films at RT and 35 K. The as-grown spectrum at 35 K was fitted by 2 sextets corresponding to tetrahedral sites (red) and octahedral sites (yellow). The annealed spectra was fitted by five sextets in each spectrum corresponding to the sites occupied by the iron cations in the SFO structure.

The intensity ratio of the absorption lines of the sextets (3:x:1:1:x:3) can be used to determine the average orientation of the magnetization in each sample. The spectrum of the as-grown sample (6.6a) at 35 K is best-fitted using a value of x = 2, indicating a random orientation of the magnetization. For the annealed sample x = 3.5 correspondings to an average magnetization mostly within the plane (15°).

T (K)	Site ($\pm$ 0.03 mms^{-1})	δ ($\pm$ 0.05 mms^{-1})	2ε ($\pm$ 0.05 T)	H ($\pm$ 0.05 mms^{-1})	Γ (%)	Area
298	Fe^{3+}	0.34	0.80	-	0.40	100
35	Fe^{3+}_{Td}	0.39	-0.03	44.2	0.40	28
	Fe^{3+}_{Oh}	0.46	0.01	49.3	0.40	72

Table 6.4: ^{57}Fe Mössbauer parameters obtained from the fit of the spectra shown in figure 6.6a. The symbols δ , 2ε, H, Γ correspond to isomer shift, quadrupole shift, hyperfine magnetic field and linewidth, respectively.

Magnetization curves were measured from both samples under a maximum applied external field of 1.25 T. Figure 6.7 shows the RT hysteresis loops for the as-grown sample and for the annealed-sample, a and b, respectively. In the case of the sample without annealing treatment, no easy magnetic axis nor hysteresis cycles are observed. The noise of the hysteresis loops increases with the applied magnetic field due to the coupling of other signals resulting from the VSM setup. The shape of the curves can be interpreted in terms of a paramagnetic behavior of the film as already reported by Mössbauer spectroscopy at room temperature (figure 6.6), however, given the low quality of the data, it can not be discerned whether the coercive field is zero or not. The saturation magnetization calculated for this sample is approximately 20 emu/g. For the annealed film, a clear easy axis is appreciated within the sample plane. These results agree with a crystalline preference of the c-axis oriented parallel to the plane of the film as indicated by XRD, figure 6.4 since the magnetization is along that axis. Then data also confirm the in-plane magnetization orientation determined by Mössbauer spectroscopy at RT and 35 K (figure 6.6b). However, within the plane of the film, there is not preferential magnetic orientation (red, green and black curves). A possible explanation of this might be that the sample is polycrystalline, and each grain points its magnetization in a different in-plane direction. The saturation magnetization and the coercive field determined with the in-plane configurations were 63.1 emu/g and 0.49 T, respectively. These values are within the range of magnetization values reported for this compound [136, 91]. When the hysteresis cycle was recorded perpendicular to the sample plane, a different saturation magnetization value was found. This evidence results from the need for a higher applied field to reach the threshold value of magnetization seen previously in the in-plane measurements.

We conclude from the characterization of these thick films by different techniques that the annealing treatment is crucial for obtaining strontium hexaferrite. The results suggest a nanocrystalline maghemite phase for the as-grown film deposited by sputtering and probably with the presence of amorphous strontium oxide. The latter compound was presumed according to the phase diagram for SFO, and due to no crystalline phase was evidenced in the XRD data, we suggested an amorphous state for SrO.

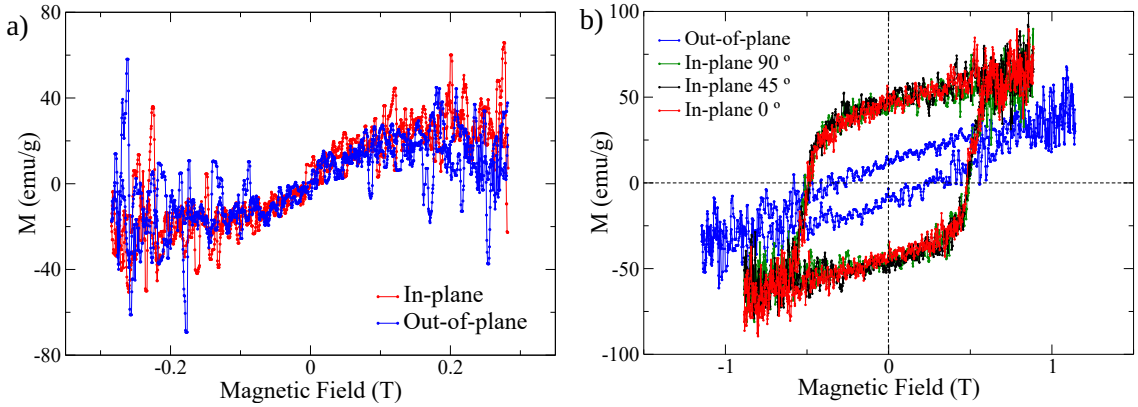

Figure 6.7: Room-temperature hysteresis loops recorded from as grown SFO film and post- after annealing treatment. The blue curve was recorded with a magnetic field applied perpendicular to the sample. Red, green and black curves were recorded with a magnetic field applied parallel to the sample.

6.4 Thin films

Knowing the importance of the annealing step for growing good quality SFO thin films, several strontium hexaferrite samples were deposited to achieve one of the goals of this work: create a thin film with a magnetization easy axis parallel to the sample plane. For this purpose, the samples were grown by RF magnetron sputtering using the parameters specified in the previous section 6.2. The only factor which was varied in the growth method of each thin film was the sputtering power (140 W, 180 W, 220 W and 260 W). The thin films were deposited for 30 minutes sputtering time. All samples were then annealed at 850 °C for three hours.

To determine their thickness, the step between the substrate and the film was measured by means of a profilometer. As it can be seen in the inset of figure 6.8, the amount of sample deposited in a certain deposition time increases linearly with the sputtering power.

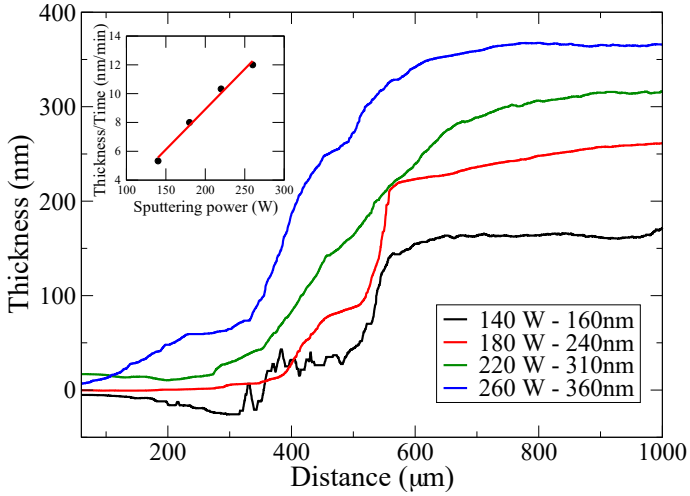

Figure 6.8: SFO films thicknesses measured by a profilometer. Inset: thickness-time ratio as a function of the sputtering power (sputtering time, 30 min).

6.4.1 Characterization of crystallinity and composition

To elucidate the composition, crystallinity, preferred crystal orientations (texture) and other structural parameters of our samples, spectroscopy and diffraction techniques were applied. The Raman spectra recorded from all samples grown at different sputtering powers are represented in figure 6.9. Additionally, the reference pattern of the SFO target is added for comparison purpose. For all the films, the spectra present the same peaks shown by the SFO target. No additional peaks that might belong to other phases were found in film, confirming a strontium hexaferrite structure for all of them [196, 197, 198, 199]. The main vibration modes expected for the different Fe^{3+} sites in the type M-ferrite structure are labelled.

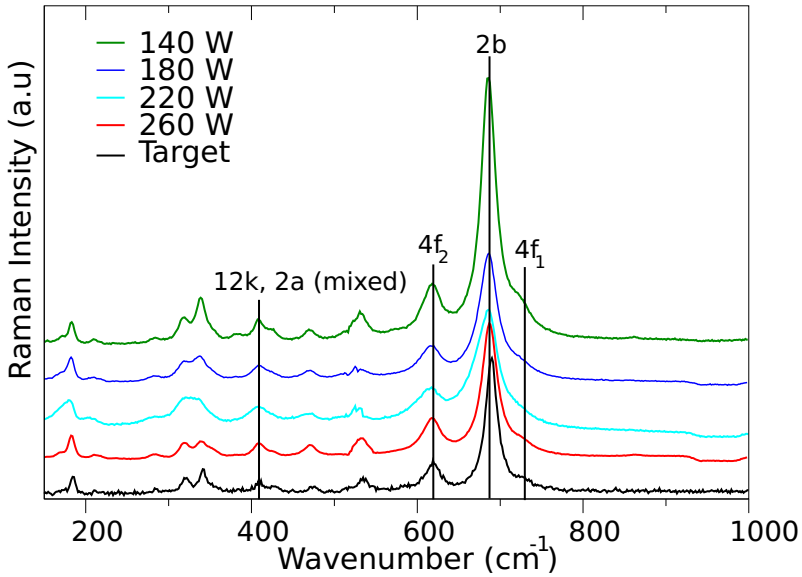

Figure 6.9: Raman spectra recorded from the SFO deposited thin films and a commercial sputter target.

The X-ray diffraction θ-2θ patterns taken from all the samples are shown in figure 6.10a, together with that of the SFO reference. On top of the panel, the indexed planes associated to the diffraction peaks are shown. Although all the XRD patterns are characteristic of SFO [112, 207], inspection of figure 6.10a clearly shows that the films have grown with different preferred crystalline orientations suggesting that these depend on the sputtering power (and, as we will show, below, on the thickness of the deposited film). As it can be observed in the figure, the film deposited at the lowest power shows prominent $(00l)$ peaks along [(004), (006), (008) and (0014)] with some other peaks of lower intensity, suggesting a preferential orientation in the c-axis normal to the film. The most intense reflections of the sample grown at 180 W also arise from the $(00l)$ family, although, to a lesser extent, it also has peaks corresponding to the (110) and (220) planes. So, the preferential c-axis orientation is established mostly out-of-plane, although a significant contribution of crystalline structures oriented in the plane of the film is also observed. The experiment carried out at 220 W, reverses the trend of the intensity in the crystalline planes. Hence, this sample displays preferential in-plane orientation, with some structures having their c-axis oriented perpendicular to the surface. Finally, for higher sputtering powers (260 W), the diffraction pattern shows that reflections (110) and (220) are considerably stronger than those expected for a randomly oriented sample, indicating that this film grows along

direction 110, i.e., it has its c-axis in-plane. In addition, to appreciate the change in the orientation of the c-axis in all of the films, a plot with the ratios intensity of the peaks (110) and (008) has been performed (figure 6.10b). Further, the particle size and lattice parameters for each film are listed in table 6.5.

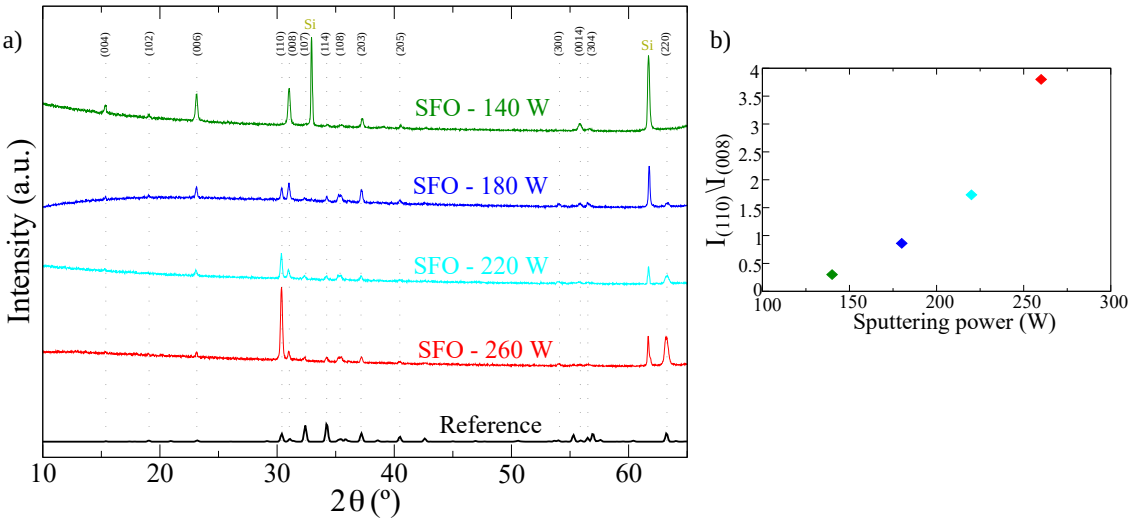

Figure 6.10: a) XRD diffraction patterns from the SFO films grown at different sputtering powers together with the reference pattern. b) Plot of the intensity ratio of the peaks (110) and (008) vs sputtering power.

Structural parameters	140 W	180 W	220 W	260 W
Particle size (nm)	39	43	48	44
Lattice parameter a (nm)	0.578	0.587	0.588	0.586
Lattice parameter c (nm)	2.358	2.356	2.354	2.351

Table 6.5: Particle sizes and lattice parameters calculated from the XRD data.

In order to check the morphology of the thin films that presented the greatest differences in their structural orientation, the samples deposited at the lowest and highest sputtering power (140 W and 260 W) were studied by atomic force microscopy (figure 6.11). Actually, we found in the literature several works which relate the orientation of the grains with the structural properties [219].

The film grown at 140 W has a surface that presents well-separated grains across the film (figure 6.11a). These grains protrude 73 nm from the surface, figure 6.11b with the root mean square roughness (rms) was 8 nm. In contrast, for the films grown at the highest power, a surface with grains up to 41 nm heigh for all the sample is obtained, figure 6.11c, thus columnar growth is still observed although without spaces between the grains (figure 6.11d). This sample presents a rms roughness of 12 nm. This film is also the thicker film grown (360 nm). Cho et al. had already reported in their study about barium ferrite thin films that an increase of thickness produces an increase in the surface roughness[1] [194].

[1]Surface roughness is a measurement of surface texture. It is defined as a vertical deviation of a real surface from its ideally smooth form.

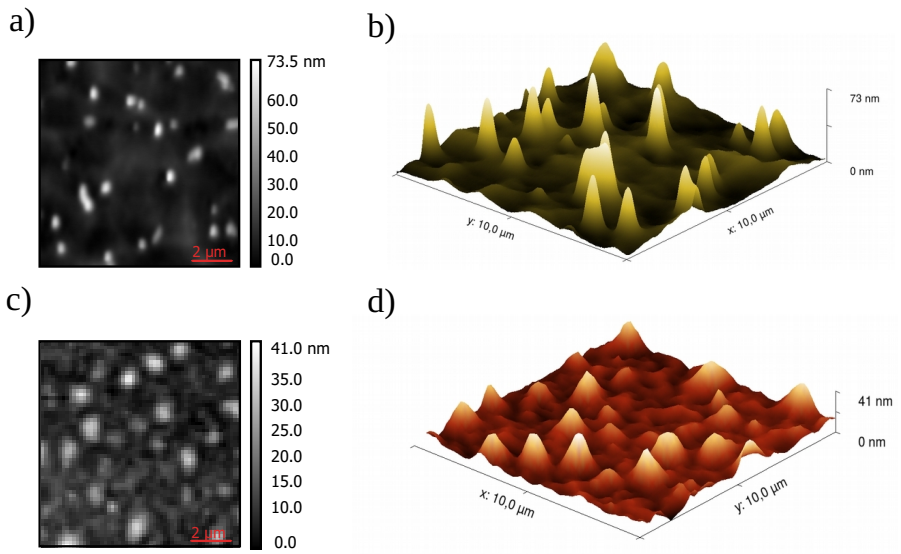

Figure 6.11: a) and b) surface and 3D map of the sample grown at 140 W, respectively. c) and d) surface and 3D map of the sample grown at 260 W, respectively.

These data seem to indicate that at low deposition power and thus, at smaller thickness, the grains in the sample grow preferentially with the c-axis perpendicular to the film plane. While for high power (and higher thickness), the higher roughness and smaller height of the isolated grains suggest grains oriented with the c-axis mostly parallel to the plane of the sample. This interpretation fits quite well with the crystallographic planes found in the diffraction patterns for the samples grown at 140 W and 260 W (figure 6.10).

6.4.2 Magnetic characterization

To determine the magnetization orientation of the samples, Mössbauer spectroscopy was used. Figure 6.12 shows the ICEMS spectra recorded from the films deposited at different sputtering powers. All the spectra were fitted to five sextets, with each sextet corresponding to Fe^{3+} in a different crystallographic site [143]. The values of the different hyperfine parameters are virtually the same for all films. Table 7.4 collects a representative set of hyperfine parameters which corresponds to the film grown at 260 W (Fig.6.12d). The parameters are all characteristic of strontium hexaferrite [131].

In the spectrum for the sample grown with 140 W (figure 6.12a), the absorption lines intensities indicate an average magnetization angle of 55°. As the deposition power is increased, the average magnetization orientation in the films changes (as shown in the schematic in the right corner in each spectrum from figure 6.12). Specifically, the film grown with the maximum sputtering power applied, 260 W, an almost in-plane magnetization (18°) is observed. Thus, the increase in sputtering power and thickness of the films tends to align the magnetization parallel to the sample plane. The XRD measurements indicated that for higher sputtering power (and film thickness) the c-axis is mostly oriented in the film plane. Since the Mössbauer results indicate that the magnetization is oriented within the film plane, the results, taken together, confirm that the c-axis is the magnetization easy axis, as expected.

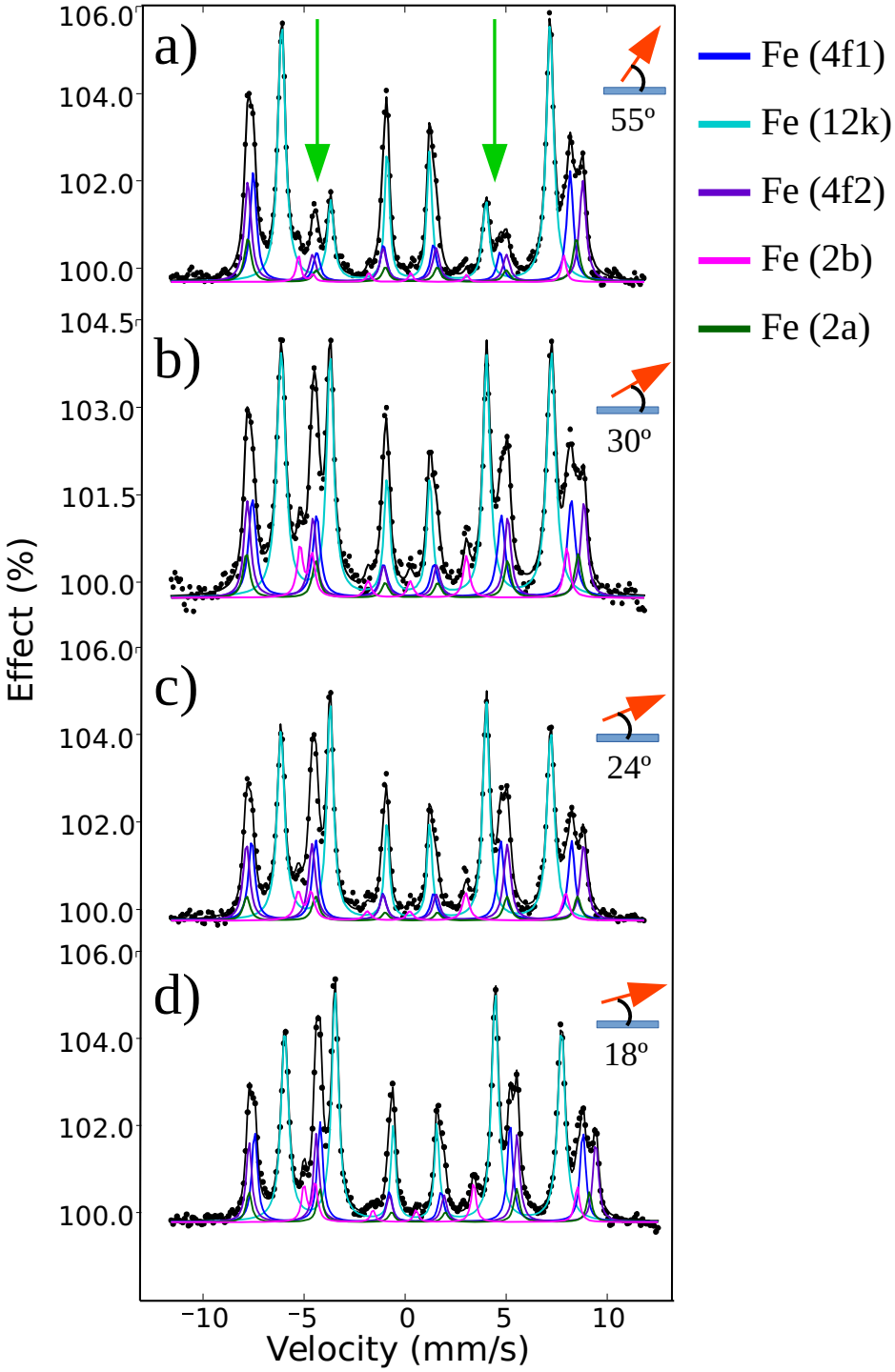

Figure 6.12: Room temperature ICEMS spectra recorded from SFO films deposited at different magnetron powers: a) 140 W, b) 180 W, c) 220 W, and d) 260 W. The five sextets in each spectrum correspond to the sites occupied by the iron cations in the SFO structure [131]. The green arrows point to the 2 and 5 lines of the sextets that undergo a change in intensity as the sputtering power increases. The arrows on the upper right side of each spectrum indicate the average angle of magnetization direction in each sample. Note that the angle depicted in the figure is that formed between the hyperfine magnetic field and the surface plane.

Site	δ ($\pm$ 0.03 mms^{-1})	2ε ($\pm$ 0.05 mms^{-1})	H ($\pm$ 0.05 T)	Γ ($\pm$ 0.05 mms^{-1})	Area (%)
12k	0.34	0.38	41.3	0.28	53
4f1	0.24	0.18	49.0	0.32	18
4f2	0.37	0.28	51.7	0.32	17
2a	0.33	0.04	50.7	0.32	6
2b	0.27	2.22	40.8	0.28	6

Table 6.6: ^{57}Fe Mössbauer parameters obtained from the fit of the spectrum shown in Figure 6.12d. The symbols δ , 2ε, H, Γ correspond to isomer shift, quadrupole shift, hyperfine magnetic field and linewidth, respectively.

Comparing these results with the literature, we found different data on the thickness/sputtering power effects in the thin films deposited by RF magnetron sputtering. On the one hand, works carried out by Acharya et al. [220, 192, 42, 190] had predicted long ago that the magnetization orientation can be tuned by the appropriate choice of the magnetron deposition power. These studies start from samples with identical thicknesses. On the other hand, Cho et al. [194] pointed out the dependence of the magnetization with the film thickness of barium ferrite, BFO (which is isostructural with SFO) on sapphire (001) using the same sputtering power for the growth of all the samples. In that study, they found that at thicknesses less than 100 nm, the BFO grains grew perpendicular to the substrate surface with the c-axis out-of-plane, while at larger thicknesses elongated grains grew at the top of the columnar grains parallel to the surface substrate, their c-axis lying also parallel to the surface plane. Like strontium ferrite, the magnetocrystalline anisotropy in barium ferrite makes the c-axis the magnetic easy axis. Thus the rise of elongated grains causes a change magnetization axis [194]. Also, several studies of Sui's group [221, 222] confirmed that the morphology and disposition of the grains affects to the c-axis orientation and, in consequence, the magnetic properties of thin films.

In the case of the samples reported here, it has been appreciated that, for a fixed deposition time, the thickness of the films increases with magnetron sputtering power (figure 6.8). I.e., both parameters vary and hence, both are correlated with the change in the magnetization orientation. Thus, the next section seeks to clarify which of the power and thickness parameters is the dominant one in determining the magnetization easy axis.

6.5 Influence of thickness and power sputtering on the magnetic behaviour of thin films

Two new samples have been prepared to disentangle the role of the parameters involved in the magnetization direction. These thin films were grown to compare with those grown at 140 W and 260 W from the previous section since they present the same thicknesses but have been produced at different sputtering powers. Specifically, a first sample was deposited at 140 W with a thickness of 360 nm (Sample A), and a second (Sample B) was grown at 260 W with a thickness of 160 nm. The rest of the parameters of the sputtering process were not changed. Subsequently, both samples were also subjected to an annealing treatment at 850°C for 3 hours.

The crystallinity of these films was determined by X-ray diffraction. Figure 6.13a shows the diffraction pattern of samples A and B together with that of the canonical strontium hexaferrite reference, and figure 6.13b shows the diffraction pattern of the sample grown at 140 W of 160 nm thick and the sample grown at 260 W of 360 nm thick from the previous section for comparison. First of all, figure 6.13a, shows that for both films, the indexed diffraction peaks correspond to strontium hexaferrite structure. Sample A presents significant ($ll0$) peaks compared to other reflections, indicating a preferential orientation of the c-axis within the sample plane. Sample B displays similar reflection intensities being the most prominent those arising from the ($00l$) family. Thus, this result suggests a crystalline growth with a substantial contribution of c-axis orientation normal to the thin film. In addition, both films have the same mean particle size (46 nm) as determined from the peak widths through the Scherrer formula. When these XRD results are compared with the diffraction patterns of the previous thin films 6.13b, we can conclude that the thinner films (green color in both graphs) tend to grow with the c-axis perpendicular to the sample plane while thicker films show a trend to grow with the c-axis parallel to the surface plane (red color in both graphs).

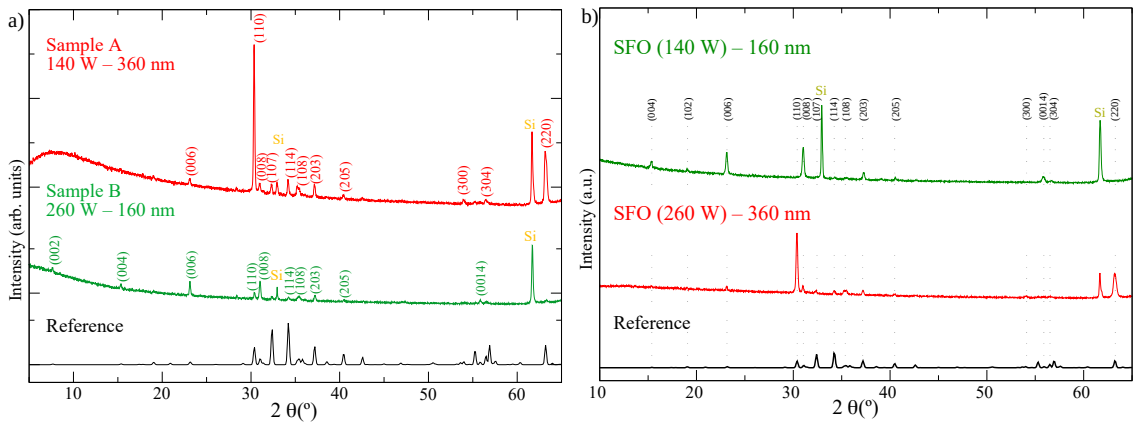

Figure 6.13: a) XRD diffraction patterns from the SFO films: Sample A and Sample B, together with the simulated pattern (bottom one). b) XRD diffraction patterns from the SFO films grown at 140 W and 260 W from previous section.

The surface morphology of the samples was measured by AFM. On the one hand, the thicker film deposited at 140 W, Fig.6.14a, presents a few protrusions of 129 nm while the rest of the surface keeps with similar morphology. The RMS roughness is 11 nm. On the

other hand, sample B show an increased density of columns (60 to 95 nm tall), Fig.6.14b. The RMS roughness in this film is 8 nm.

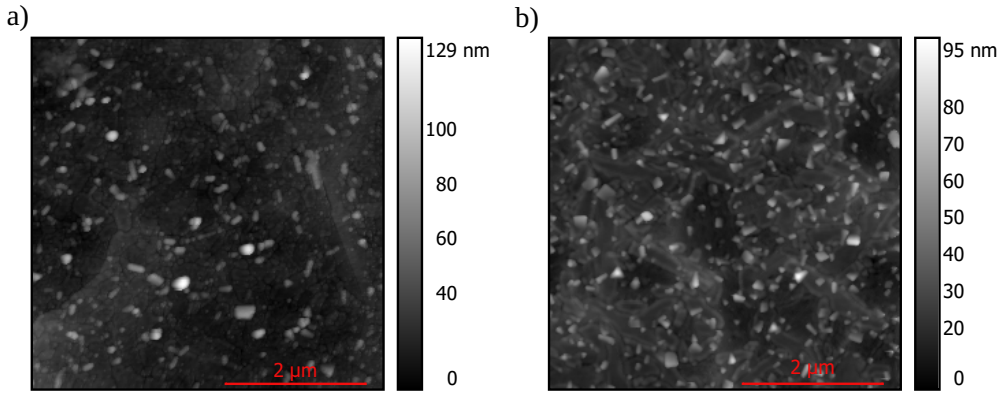

Figure 6.14: a) and b) surfaces of the samples A and B, respetively. The vertical sizes of the pictures are 5 $\times$5 μm.

Taking into account these AFM images with those from the previous section (images 6.11b and 6.11d), we have suggested how the protrusions distribution varies in function to sputtering power and thickness. According to Sui´s works [221, 222] this grain arrangement can be related to the c-axis orientation in the structure.
At low values of sputtering power, typically, the grains grow in a more pronounced and isolated columnar shape. When the film thickness is small, isolated tall grains are observed. As the thickness of the film increases, the grains tend to change their orientation within the plane. At high sputtering power values, a more homogeneous columnar growth, although of lower height, was found. For this case, at small thicknesses, we suspect that part of the grains tends to grow perpendicular to the plane while another part parallels it. The film thickness increase causes the majority of the grains to be oriented in the sample plane. Assuming that grain preferential orientation determines, to some extent, the change of the average c-axis orientation of SFO films, the thickness and sputtering power are parameters involved in such change.

The magnetic behaviour in this new set of samples was also studied by Mössbauer spectroscopy. Figures 6.15a and 6.15b show the CEMS spectra recorded from Sample A and Sample B, respectively, which are both characteristics of strontium hexaferrite [131]. The area ratio of the spectral lines obtained from the fit of the spectrum recorded from Sample A was 3:3.5:1:1:3.5:3. This implies that the sample shows a magnetization practically in the film plane (magnetization/surface angle of 15 °). This is remarkable comparing this result with that shown in figure 6.15c, which corresponds to a film produced with the same sputtering power but having a much smaller thickness, a significant difference is observed in the averaged orientation of the magnetization. However, correlating the sample A spectrum with that from the film with the same thickness (360 nm) but different sputtering power (figure 6.15d), a similar average magnetization orientation is detected (18 °). In the case of Sample B (figure 6.15b), an area ratio of 3:2.2:1:1:2.2:3 was obtained, which corresponds to a magnetization having a significant out-of-plane magnetization component (average 33°). In comparison with a film grown with the same sputtering power (260 W) but thicker, we can observe the difference in the average magnetization orientation between both (figure 6.15d). A difference in the magnetization direction is also seen when comparing sample B spectrum with the film grown at lower sputtering power with the identical

thickness (figure 6.15c).
So, despite the low sputtering power used, a thicker film makes the magnetization practically in-plane (Sample A). In contrast, a larger sputtering power but a smaller thickness (Sample B) gives place to an intermediate situation in magnetic behaviour, implying that the thinner film contains a significant out-of-plane magnetization component. Again, considering that the net magnetization is along the c-axis, Mössbauer spectra present the same behaviour as the diffraction data, figure 6.13.

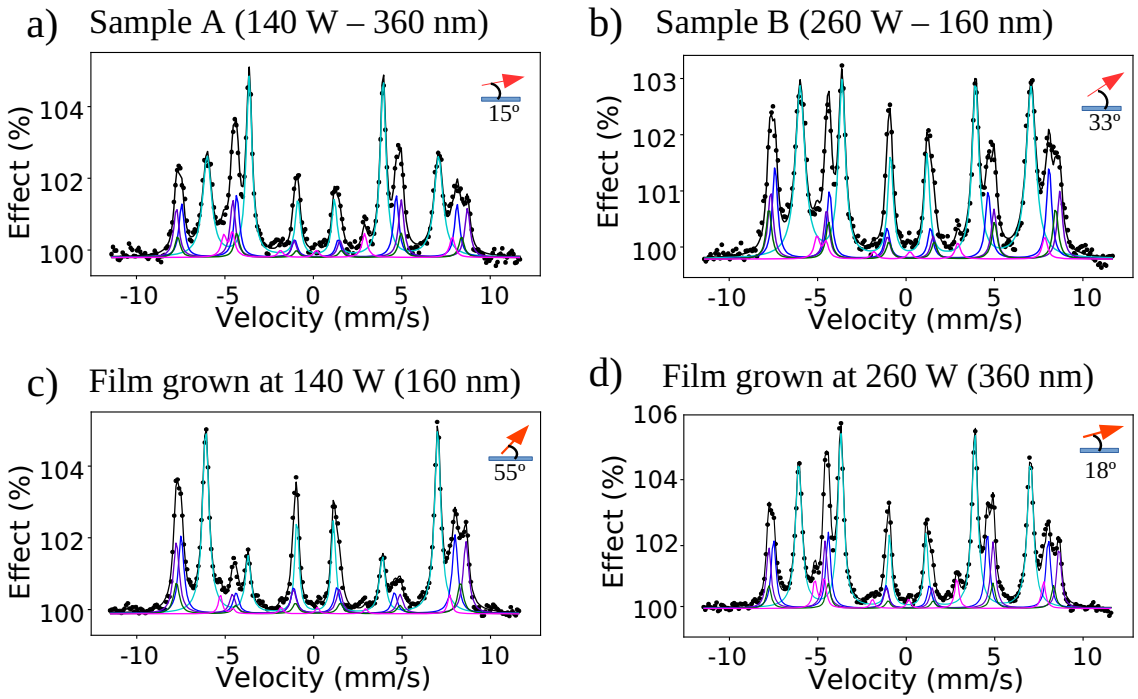

Figure 6.15: Mössbauer spectra for SFO films: a) Sample A, b) Sample B, c) film grown at 140 W (160 nm) and d) film grown at 260 W (360 nm).

Therefore, the present results indicate that the sputtering power used during deposition is not, by itself, the main factor that determines the magnetization orientation and that the thickness and consequently the morphology of the sample are also crucial. The magnetization orientation in thin films depends on the interplay among the shape anisotropy of the grains, the shape anisotropy of the overall deposited film and the magnetocrystalline anisotropy of the SFO films, the latter term being most probably the dominant one. In any case, within the context of these experiments in which we are using sputtering powers between 140 W and 260 W and thicknesses between 160 nm and 360 nm, the results indicate that:

i At low sputtering powers, the thickness is the determining parameter since the magnetization orientation can be tuned by an appropriate choice of the film thickness.

ii At high thicknesses, the sputtering power does not influence the magnetization due to this is oriented in the sample plane for both cases.

iii At low thicknesses, the sputtering power affects moderate the magnetization direction of the sample.

6.6 Interaction between strontium hexaferrite thin film with cobalt overlayer

In this section, we will consider the sample deposited at 260 W and having a thickness of 360 nm, which has its magnetization oriented within the film plane. As mentioned previously, one of the stated objectives of this research is to obtain a $SrFe_{12}O_{19}$ sample with magnetization in the plane to study its magnetic coupling with a magnetically soft layer specifically with a thin cobalt layer deposited on top. This coupling experiment was decided in order to avoid the competition between the shape anisotropy arise cobalt layer and magnetocrystalline anisotropy from SFO platelet observed in the previous chapter. Therefore, the sample grown at 260 W is a suitable candidate for such experiment. Hysteresis loops were measured by VSM to confirm the magnetic orientation determined from the CEMS spectrum, figure 6.16. The black curve was measured by applying a magnetic field parallel to the sample plane, while the red curve was recorded by applying a magnetic field perpendicular to the sample plane. For the black curve, the measured coercive field is 0.42 T, and the saturation magnetization is achieved for an applied field of 1.8 T. From the red curve, a smaller coercive field (0.37 T) is measured while the saturation magnetization is reached at a slightly larger applied field (2.3 T). Figure 6.16 also shows a larger remanence magnetization in the black curve than in the red one. These observations confirmed that the film has its magnetic easy axis, mainly in the sample plane.

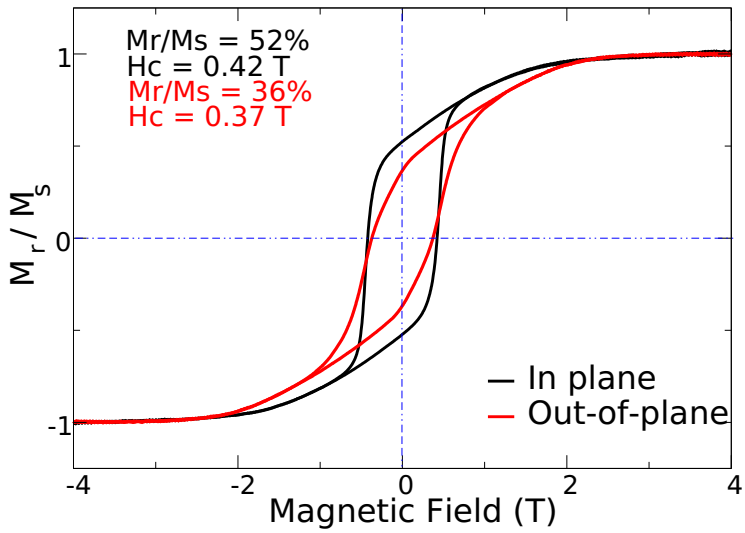

Figure 6.16: Room-temperature hysteresis loops recorded from a 360 nm thick SFO film deposited at 260 W after annealing. The black curve was recorded with the magnetic field applied within the plane. Red curve recorded with a magnetic field applied perpendicular to the sample.

Then, a cobalt layer two nm thick was evaporated using MBE in the UHV chamber of CIRCE beamline ALBA Synchrotron (Barcelona). Firstly, the characterization of the bilayer system was carried out by X-ray absorption analysis.

XAS and XMCD spectra and images were measured at Fe $L_{2,3}$ edge on the strontium hexaferrite thin film before and after deposition of the cobalt layer (figure 6.17a). The upper left image from figure 6.17a corresponds to XMCD image acquired at the Fe $L_{2,3}$ edge before depositing the cobalt overlayer and the upper right image once the cobalt was

grown. Both images show a magnetic contrast as expected from XMCD spectra signal (figure 6.17a lower panel). It should be noted that XAS spectra recorded at Fe $L_{2,3}$ before and after cobalt growth are slightly different. An additional feature is observed at a lower photon energy (706.9 eV) in the spectra of the Co-covered SFO films. In figure 6.17b XAS and XMCD spectra and XMCD image acquired at the Co $L_{2,3}$ edge are shown. XAS spectrum is quite similar to that shown by metallic cobalt [172]. However, the spectrum shows minor peaks at 776.0 eV and 778.5 eV, which are compatible with the presence of some Co^{2+} arising from the oxidation of a fraction of metallic cobalt during deposition. This evidence, together with the XAS spectrum obtained in the SFO film once cobalt is deposited, suggests the following: the cobalt evaporated on the strontium hexaferrite film interacts with oxygen atoms from the SFO film producing oxidation of part of cobalt atoms and consequently a reduction of some Fe^{3+} of the SFO to Fe^{2+} at the interphase. Note also the two peaks appearing beyond the Co L_3 (784.0 eV) and L_2 edges (797.5 eV). They correspond to a residual barium contamination [172, 223, 224] stemming from the SFO target used in the magnetron sputtering system.

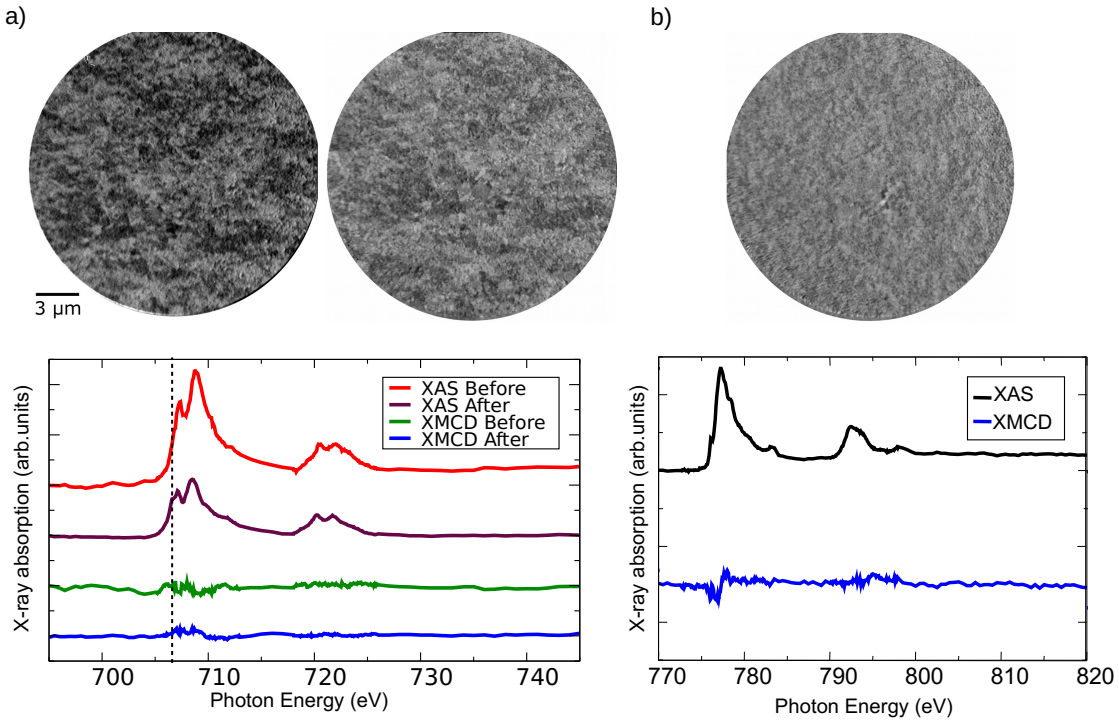

Figure 6.17: a) Upper: X-ray magnetic circular dichroism images at Fe L_3 edge before(left) and after(right) cobalt deposition. Lower: XAS and XMCD spectra at Fe $L_{2,3}$ edge before and after cobalt exposition. b) Top: X-ray magnetic circular dichroism images at Co L_3. Botton: XAS and XMCD spectra at Co $L_{2,3}$ edge.

In order to find whether the addition of a cobalt overlayer influences at some extent the average magnetization orientation and the magnetic properties of the SFO films, Mössbauer spectroscopy (ICEMS) and hysteresis loop data were recorded from the Co/SFO bilayer. The ICEMS spectrum recorded at room temperature is found in figure 6.18a. As well as for the other strontium hexaferrite samples studied, the spectrum was fitted to the five sextets (figure 6.12). Similar spectral areas were obtained for the different components to

those of the sample without the cobalt coating. The area ratio of the sextet lines is 3: 3.4: 1 in all cases, which corresponds to an average magnetization orientation virtually within the plane (16°). This magnetization orientation is comparable to that registered for the SFO sample without cobalt. The recorded hysteresis loop of this bilayer, figure 6.18b, also suggests a magnetization lying preferably in the sample plane. Furthermore, the values of the different magnetic film properties (remanent magnetization/saturation magnetization ratio, M_r/M_s, and the coercive field, H_c) are comparable with those acquired from the single strontium hexaferrite for both in-plane and out-of-plane hysteresis loops (figure 6.16). In the in-plane data, the coercive field is 0.42 T, and the magnetization is saturated under an applied field of 1.8 T, while in the out-of-plane configuration, the coercive field is 0.33 T, and a larger magnetic field is required to magnetize the sample completely (2.2 T).
Both results indicate no significant change in magnetization with the deposition of the metal layer. This fact is not surprising given the small thickness of the cobalt layer (2 nm) compared to the SFO thin film (360 nm).

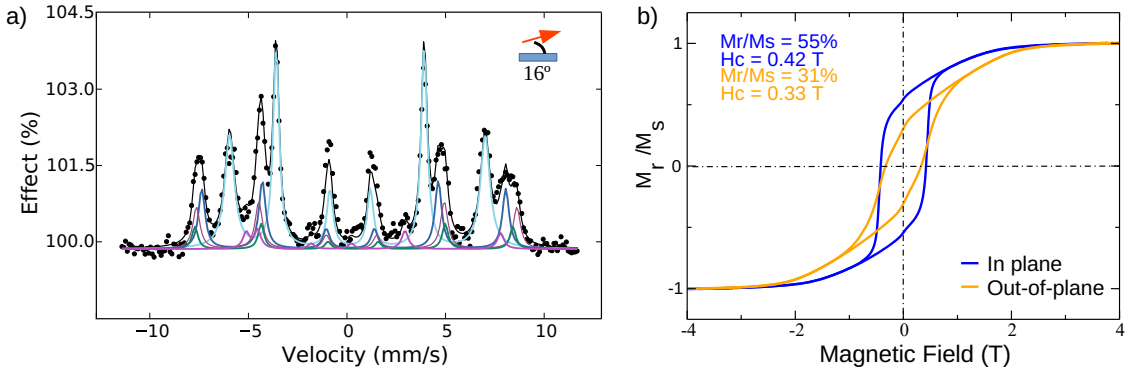

Figure 6.18: a) Room temperature ICEMS spectrum recorded from the Co/SFO bilayer. The arrow in the upper right side represents the average angle of the magnetization direction respect to the sample surface. b) Room temperature hysteresis loops recorded the from Co/SFO bilayer system. The blue curve was recorded with a magnetic field applied within the sample surface plane, while the yellow curve was recorded with a magnetic field applied perpendicular to the sample.

To elucidate the nature of the coupling between the soft magnetic layer (cobalt) and the hard magnetic thin film (SFO), a vector magnetization map was measured at the Fe-L_3 X-ray absorption edge before cobalt deposition (figure 6.19a) and at the Fe-L_3 (figure 6.19b) and Co-L_3 X-ray absorption edges (figure 6.19c) after cobalt deposition. The vector magnetization is proportional to the magnetization in each layer, and it can be obtained by combining three XMCD images along three non-coplanar directions with azimuthal angles of 0°, 60° and 120°, and a polar angle of 16° [156]. There was no significant change in the SFO domains upon cobalt deposition: figure 6.19f shows a comparison between the Fe L_3 X-ray absorption edge of SFO figure 6.19b shown in f as a color pattern and figure 6.19a shown in f as the contour. The most prominent result is that the SFO film shows a uniaxial anisotropy large enough as to show a magnetization vector preferentially aligned in the directions (160° and 340°) within the film plane, figure 6.19d. No correlation is apparent between the cobalt domains and the SFO ones (figure 6.19c). Hence, the magnetic domains of the hexaferrite layer are not imposed on the cobalt layer. This strongly suggests a lack of exchange-coupling between the hard and soft layers. Nonetheless, it has been determined that the easy axis of the cobalt layer is the same as the in-plane easy axis of the hexaferrite layer (figure 6.19e). This is evidenced by the same colors (green and red) in figures 6.19b

and 6.19c, with the magnetic domains of cobalt pointing either parallel or antiparallel sense to the underlying hard domains. Thus, the point to be debated in this context is: in the absence of interchange coupling between both layers, what mechanism intervened so that an alignment of the easy axes occurs. First, let us consider the hexaferrite structure in the [110] direction, which is the film growth direction. Strontium hexaferrite is a ferrimagnet, with iron cations in some crystallographic sites pointing along the net magnetization direction and others pointing in the opposite direction. Along (110), there are planes within the unit cell with different populations of each iron cation. Thus the net surface magnetization is opposite along different planes. If some grains of the hexaferrite film present such different terminations, a dipolar magnetic coupling with the cobalt layer should give rise to grains where the magnetization of the cobalt, coupled to the net surface magnetization of the hexaferrite, has opposite directions between different grains.

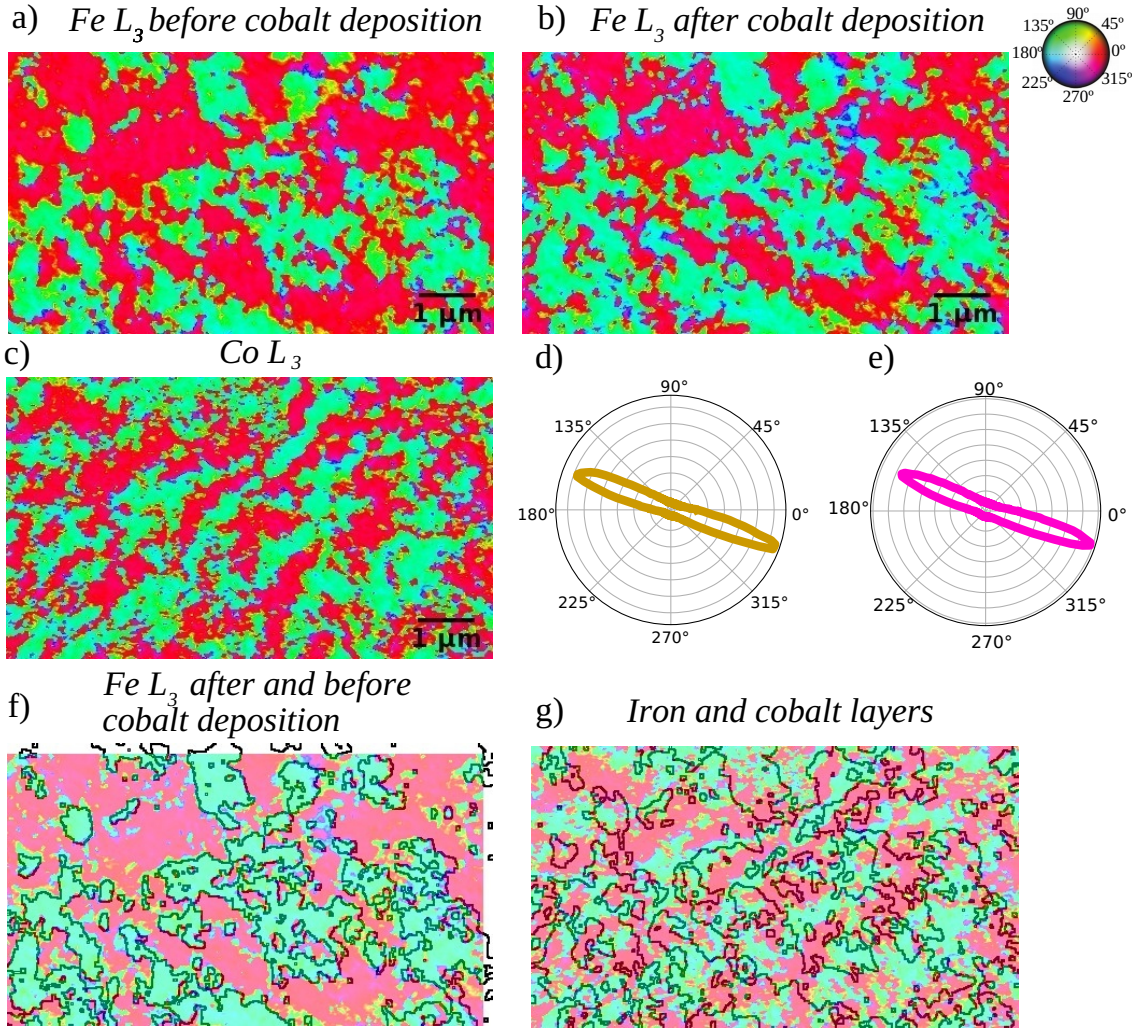

Figure 6.19: Vector magnetization maps for: the Fe L_3 X-ray absorption edge before a), after b) cobalt deposition and c) the Co L_3 X-ray absorption edge. d) and e) polar plots representing the magnetization distribution in the surface plane extracted from a) and c) images, respectively. f) Overlay images at Fe L_3 X-ray absorption edge before and after cobalt deposition. g) Overlay images at Fe L_3 and Co L_3 X-ray absorption edges after cobalt deposition. Note that the color palette in the upper corner represents the spin direction in the magnetic domains.

Figure 6.20 shows a scheme of the situation discussed above. The iron cations corresponding to the different chemical environments have been represented in blue or yellow spheres according to the direction of their spins. Assuming different terminations in the surface grains, the cobalt deposited on top should have the same magnetic orientation as the termination where it is found due to the magnetostatic interaction. Thus, for the lowest terrace (to the right), the iron cations (blue) present their spin oriented in one direction, so the upper cobalt should also be oriented in the same direction. For the middle terrace, the iron cations (yellow) have their spin in the opposite direction, and consequently, the coupling promotes such magnetization orientation in the cobalt layer. However, this scenario is considered unlikely for several reasons. On the one hand, the film needs to present a substantial number of grains with different terminations, although the crystal termination is often determined by the lowest surface energy. On the other hand, this situation would require a correlation between the domain walls in the cobalt overlayer and the hexaferrite layer, even if the magnetization were coupled either ferromagnetically or antiferromagnetically (depending on the underlying termination). No such correlation is observed in figure 6.19g.

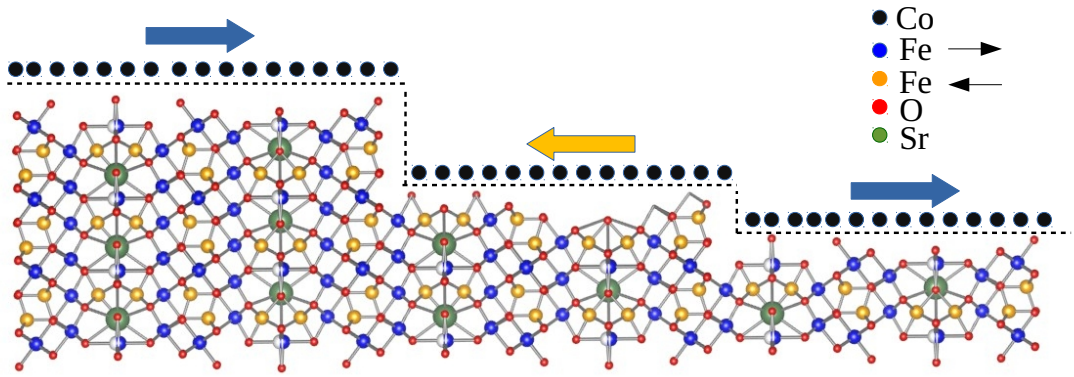

Figure 6.20: Strontium hexaferrite structure with different terminations. The elements are depicted in the legend. The arrows on top of Co atoms represent the magnetization direction in the soft layer.

The explanation we propose is that both directions (but not sense) of the magnetization in the two layers are coupled structurally. This could happen in two ways. On one side, the strain imposed at the interface by the ferrite layer could favor a specific growth direction of the cobalt layer that leads to the alignment of the easy axes. On the other, the epitaxial relationship alone could explain this alignment as well. Given the very low thickness of the cobalt layer, our data, especially XRD, are not able to confirm the epitaxial relationship.

Thus, it was suggested that the coupling between the two layers is structural instead of magnetic. This result is not entirely surprising, as, for instance, growth of cobalt on W(110) always produces some uniaxial anisotropy of the cobalt layer [225, 226] and this does not require different surface terminations. A consequence of this interpretation, already suggested by the lack of correlation between domain patterns in the two layers, is that in the absence of exchange-coupling, dipolar interactions alone do not lead to the alignment of the spins of the soft layer with the magnetization of the hard one.

In order to further understand the magnetic behavior observed in the bilayer PEEM images, micromagnetic simulations have been performed [86] in a simplified system. Such system

consists of a strontium hexaferrite slab having a well-defined in-plane magnetization easy axis (100) covered by a layer of cobalt on top. The cobalt overlayer has its easy axis of magnetization oriented along the same direction (100) as the easy-axis of the hexaferrite layers. The thickness of the two layers was set to that shown by the experimental sample studied in PEEM (SFO thin film 360 nm thick with a 2 nm cobalt overlayer). The following set of magnetic parameters was thus used as input in the simulations: exchange stiffness of hard and soft phases: $A_s(SFO) = 6 \times 10^{-12} Jm^{-1}$ and $A_s(Co) = 1.5 \times 10^{-11} Jm^{-1}$ from ref.[91, 179]; saturation magnetization $M_s(SFO) = 3.8 \times 10^5$ Am^{-1} and $M_s(Co) = 1.4 \times 10^6$ Am^{-1} from ref. [108, 168] and magnetocrystalline uniaxial anisotropy $K_u(SFO) = 3.6 \times 10^5$ Jm^{-3} and $K_u(Co) = 4.1 \times 10^5$ Jm^{-3} from ref. [158, 227, 166]. A random multi-domain structure for the cobalt layer and a single domain configuration for the hexaferrite layer was used. Then, the configuration was relaxed. The first simulation was carried out, considering no exchange coupling between the two layers. It was observed that the magnetic domains in the soft and the hard magnetic layers are indeed not correlated (figure 6.21a). The hard magnetic layer (SFO) shows only one magnetic domain (color red in the figure) that corresponds to the orientation of the magnetization at 0°, while in the soft magnetic layer (cobalt), there are two magnetic domains (blue and red) that represent the spin in the same directions but in the opposite sense, 180° and 0°, respectively. The second simulation was performed, incorporating a 25 % interlayer coupling. In this case, the domains in the cobalt and ferrite layers are totally aligned (figure 6.21b). For both layers, a single magnetic domain (red color) can be seen. For the third case, no magnetocrystalline anisotropy direction in the cobalt layer was set and the simulation running in the absence of exchange coupling with the SFO layer. This micromagnetic simulation showed that the soft layer presents magnetic domains within the plane in all directions irrespectively of the orientation of the magnetic domain of the hard ferrite layer (figure 6.21c) if there is no exchange coupling between both layers. Specifically, the strontium hexaferrite layer has a single magnetic domain (red color), while the cobalt layer exhibits different magnetic domains representing the distinct magnetizations (rainbow). The simulations thus support that the dipolar coupling is unable to impose the magnetization domain pattern of the hard layer onto the soft layer in the thickness range investigated in the absence of a correlation between the easy axis of both layers.

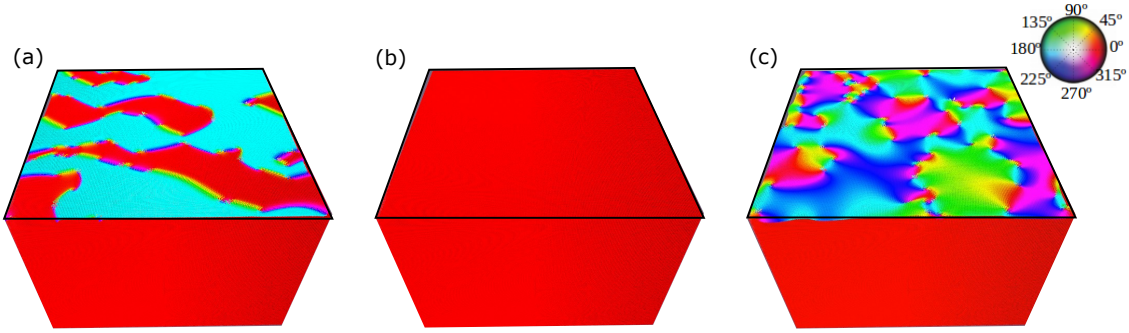

Figure 6.21: Micromagnetic simulations of bilayer SFO/Co: a) without exchange coupling, b) with 25 % exchange coupling and c) cobalt without magnetocrystalline anisotropy and without exchange coupling. Note that the color palette in the upper corner represents the spin direction in the magnetic domains.

6.7 Conclusions

First, we have determined that the annealing step after growing SFO results crucial for obtaining a genuine SFO film having the right composition and crystal structure. To this end, two samples with and without annealing treatment were characterized by different spectroscopic and microscopic techniques. The results for the sample as-grown indicate that it is composed of nanosized maghemite. Strontium is presumed to be present forming part of SrO amorphous oxide.

Subsequently, SFO thin films were deposited at several sputtering powers with constant deposition times (and thus different thickness) in order to adjust the net magnetization orientation. XRD data have shown that the films are textured and that their structural orientation changes with the sputtering power and thickness. Mössbauer spectroscopy was used to determine the average magnetic easy axis in each thin film. Taken together, the Mössbauer and XRD data suggest that the magnetization of the SFO films is oriented along the c-axis growth direction. SFO films grown at the highest power used (260 W) showed preferential in-plane magnetization.

Trying to understand the role of thickness and sputtering power in the magnetization easy axis orientation from the samples studied, two new thin films were grown. AFM images, x-ray diffractions and Mössbauer spectra for the new samples pointed out that both factors were involved in the c-axis direction of SFO films and then the magnetization orientation of them.

To obtain a hard-soft bilayer system, a cobalt layer was deposited on an SFO film grown at a power of 260 W (360 nm thickness) by molecular beam epitaxy. The characterization of the bilayer was performed using synchrotron PEEM. The XAS spectra at the Co and Fe-$L_{2,3}$ edges revealed the presence of a small amount of Fe^{2+} and Co^{2+} likely due to the interaction of the deposited cobalt with oxygen atoms from the SFO surface. Acquiring XMCD images at Co and Fe-$L_{2,3}$ edges, we obtain vector magnetization maps showing the magnetic domains associated with each layer. The polar graphs calculated from 3D magnetization images indicated the same uniaxial easy axis for both the SFO film and cobalt layer. However, the magnetic domains in the cobalt overlayer are not correlated with the magnetic domains in the SFO surface. This result suggests a lack of exchange-coupling between the layers. We suggest the coincidence in the direction of the uniaxial easy axis arises from a structural coupling. This is further supported by micromagnetic simulations, which confirmed that dipolar interactions alone do not lead to an alignment of the soft spins with the hard layer magnetization.

7 $CoFe_2O_4$ ultra-thin films

7.1 Introduction

Cobalt ferrite, $CoFe_2O_4$ (CFO), has attracted much interest since it shows a variety of electronic and magnetic properties such as the magnetoelectric effect, the magneto-optical effect, and others, resulting in its prospective application for data storage and switching devices, actuator and transducers, hyperthermia applications and magnetic field [15, 228, 229, 17, 230, 231, 232, 233]. $CoFe_2O_4$ leads to the applications mentioned above mainly due to its high magnetocrystalline anisotropy constant, which is larger by over an order of magnitude than other spinel ferrites (K_1 in the range of 2-4$\times 10^5$ J/m^3), its large magnetostriction constant among all iron magnetic oxides, its high Curie temperature and its large saturation magnetization for a ferrite [234, 235, 15]. Much of the research has centered upon the magnetic properties of polycrystalline and monocrystalline bulk or thin film materials [236, 237, 238, 239]. Specifically, in this chapter, we will focus on CFO films.

CFO films have been grown by many different methods, such as by the sol-gel process [240, 241], by dual ion beam sputtering [242, 243], by pulsed laser deposition [244, 245, 246], by magnetron sputtering [247, 248, 244], and by molecular beam epitaxy, to cite a few. The latter has been employed by depositing cobalt and iron in atomic oxygen [249, 250] or molecular oxygen [251, 252], using post-oxidation steps of metal layers [253], depositing cobalt on magnetite [254] or even annealing oxide layers [255, 256]. In the present chapter, CFO thin films have been deposited by oxygen assisted molecular beam epitaxy on Pt(111) at 523 K and subsequently annealed up to 723 K.

Many of the studies about cobalt ferrite thin films have been carried out using oxides or insulator as substrates. Unlike for other spinel ferrites, only a few works, such as that carried out by Santis et al. [253], report the growth of CFO on a metallic substrate, in their case on Ag (100). Thus, the use of a metallic substrate (platinum) for the growth of thin layers is something relative unexplored and important to consider as it opens the door for spintronics applications. Also, the growth and annealing temperatures were chosen in order to prevent the formation of multiphasic films, island growth, or dewetting phenomena [251, 252]. The dependence of the magnetic properties with the growth conditions and subsequent annealing treatments has been already reported [257]. As we will see in the following section, cobalt ferrite displays a spinel structure in which the cation distribution depends on the growth method and particular growth conditions.

Therefore, the main purpose of this work is to understand the structural and magnetic properties of CFO samples with different thicknesses (5 nm and 20 nm) grown by MBE on platinum metallic substrates and determine the effect on these properties of different

heating treatments. Importantly, both the growth and the characterization of the films were performed *in-situ*, i.e., in the same ultra-high vacuum chamber. This fact provided samples without possible external atmosphere contamination.

7.2 Cobalt ferrite: Structure and magnetic properties

Structurally, CFO is a spinel crystal (AB_2O_4) with space group $Fd\bar{3}m$. The spinel structure is based on an oxygen face-centered cubic (fcc) sublattice with the cations occupying interstitial sites: 1/3 of the cations are located in 1/8 of the available tetrahedral sites, and 2/3 of the cations are located in 1/2 of the available octahedral sites. I.e., of the 64 available tetrahedral holes, 8 are occupied by cations, and of the 32 available octahedral holes, 16 are occupied by cations. The normal cation distribution in spinel ferrites presents the divalent cations on tetrahedral sites (A) and the trivalent cations on octahedral sites (B). However, cobalt ferrite shows an inverse spinel structure in which cobalt cations (Co_B^{2+}) together with half of the iron cations (Fe_B^{3+}) occupy octahedral sites, while the other half of iron cations (Fe_A^{3+}) are located at tetrahedral sites, resulting in the chemical formula ($Fe_A^{3+}Fe_B^{3+}Co_B^{2+}O_4$) [13, 102, 258, 259]. The cubic lattice parameter a is 8.392 Å [260]. The CFO structure is depicted in figure 7.1.

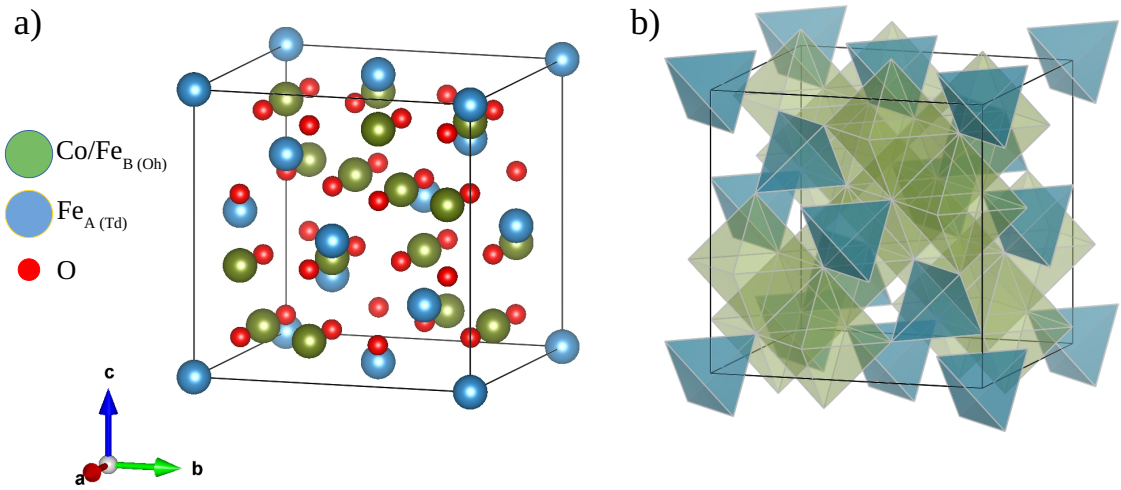

Figure 7.1: Inverse spinel structure of cobalt ferrite. Perspective illustration showing atoms (a) and polyhedra (b).

It should be noted that cobalt ferrite usually presents a partial Co^{2+} occupation of the tetrahedral sites, and the inversion degree γ, defined as the fraction of divalent ions in octahedral sites, is lower than 1. So, CFO usually is a partial inverse spinel. This cation distribution depends on the preparation method and the sample thermal history [257, 261, 262, 263, 264, 253].

In the spinel structure, the magnetic moments of each cation align in sublattices as a consequence of the super-exchange interaction with other cations (the magnetic interactions are produced through the oxygen atoms). In cobalt ferrite, the two magnetic subnets corresponding to cations in the octahedral and tetrahedral sites show antiferromagnetic coupling between them, and both subnetworks present a ferromagnetic order. The most relevant

exchange coupling configuration and the responsibility for the ferrimagnetic character in the CFO is the interaction between the Fe in tetrahedral sites with the iron and cobalt of the octahedral sites with an angle of 125° and a short distance [13]. Their exchange constants are J_{FeFe} = -2.89 meV/μ_B^2 and J_{FeCo} = -2.23 meV/μ_B^2 [265]. The Fe^{3+}-O-Fe^{3+} interaction is stronger than the Fe^{3+}-O-Co^{2+} interaction due to the electronic configuration of Fe^{3+} cations [266]. The ferromagnetic ordering of the lattice composed of atoms at octahedral sites is induced by the super-exchange interaction between the cobalt and iron cations J_{FeCo} = 0.36 meV/μ_B^2. A brief summary of the moments in each sublattice is presented in the table 7.1.

	Metal ions on lattice sites				
	A (Td sites)		B (Oh sites)		Resultant
Compound	Ions	Moment	Ions	Moment	Moment
$CoFe_2O_4$	Fe^{3+}	5 $\mu_B \Downarrow$	Fe^{3+}	5 $\mu_B \Uparrow$	
			Co^{2+}	3 $\mu_B \uparrow$	3 $\mu_B \uparrow$

Table 7.1: Metal ion distribution in cobalt ferrite (Inverse spinel).

The net magnetic moment per formula unit can be calculated from the distribution of the cations over these sites. Fe^{3+} and Co^{2+} have five and three unpaired electrons, respectively. Thus, the A-site sublattice has a spin magnetic moment of 5 μ_B and the B-site sublattice has a 5 μ_B + 3 μ_B = 8 μ_B. The opposite alignment of the two sublattice yields a net magnetic moment of 3 μ_B per formula unit. The resulting moment is contributed by the Co^{2+} cations. Experimentally, the saturation magnetization measured at 0 K is 3.7 μ_B [13]. The saturation magnetization for bulk values is 0.45 MA/m [99]. This parameter decreases with increasing temperature (see figure 7.2). The Curie temperature is 793K.

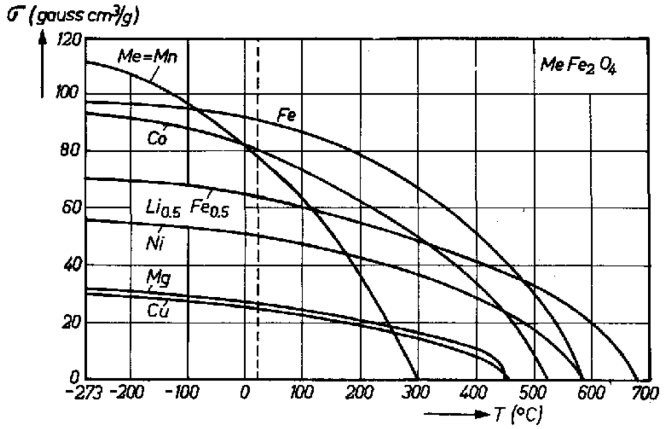

Figure 7.2: Saturation magnetization for different ferrites as a function of temperature. Reprinted from Ref. [13].

The magnetocrystalline anisotropy energy for $CoFe_2O_4$ which belongs to a cubic symmetry group is defined as:

$$E_a = K_1(\alpha_1^2\alpha_2^2 + \alpha_2^2\alpha_3^2 + \alpha_3^2\alpha_1^2) + K_2(\alpha_1^2\alpha_2^2\alpha_3^2) + ... \tag{7.1}$$

where K_1 and K_2 are constants for the material, dependent on temperature, and α_i are

direction cosines of the magnetization with respect to the three principal crystal axes. K_2 is generally very small in comparison with K_1.

The easy axis of magnetization of cobalt ferrite lies in the [100] directions (positive value of K_1 390 kJ/m^3). CFO presents the highest magnetocrystalline anisotropy of the cubic ferrites, resulting in a high coercivity of 3000 Oe [15, 243, 267]. This is attributed to a spin-orbit stabilized ground state (with unquenched orbital momentum $l_{orb} = \pm 1$) caused by a trigonal crystal field on the Co^{2+} octahedral cations [268].

An important property is its large *magnetostriction* constant, λ_s -110×10^{-6}, in contrast to M-type hexaferrites[1]. Magnetostriction refers to how a change in the distance between atoms of a crystalline compound modifies its magnetic properties. Vice-versa, magnetization along specific directions can deform the material. The magnetostrictions or strains are defined along each of the principal axes of the crystal [99, 179, 269]. The magnetostriction constant in a cubic material can be defined as:

$$\lambda_s = \frac{3}{2}\lambda_{100}\left(\alpha_1^2\beta_1^2 + \alpha_2^2\beta_2^2 + \alpha_3^2\beta_3^2 - \frac{1}{3}\right) + 3\lambda_{111}\left(\alpha_1\alpha_2\beta_1\beta_2 + \alpha_2\alpha_3\beta_2\beta_3 + \alpha_3\alpha_1\beta_3\beta_1\right) \tag{7.2}$$

where λ_{100} λ_{111} are the saturation magnetostriction constants measured along the (100) and (111) directions, respectively. β_i and α_i represent the direction cosines in which the magnetostriction is measured and the axis along which the magnetic moment is saturated, respectively.

7.3 Growth of the cobalt ferrite thin films

The substrate on which the films were grown is a Pt (111) single crystal. This substrate was cleaned by cycles of sputtering with argon ion bombardment (500 eV, 5μA, for 35 min), flashing in UHV at 1200 K, and annealing in oxygen atmosphere (1×10^{-7} mbar, 10 min, 825 K). Its temperature was controlled by a PtRh-Pt thermocouple pressed against the back of the crystal. The cycles were repeated until a sharp (1×1) Pt(111) low-energy electron diffraction (LEED) pattern was obtained. Nonetheless, some residual iron contamination could be detected by Mössbauer spectroscopy after numerous preparation cycles due to iron impurities diluted deeper in the substrate.

The cobalt ferrite films were grown by co-deposition of iron, enriched to 95% ^{57}Fe, and cobalt in an oxygen atmosphere (oxygen assisted-MBE) on the heated platinum substrate. The reason for using iron with a high ratio of ^{57}Fe is for increasing the Mössbauer signal intensity. For the 20 nm CFO thin film the preparation parameters consisted of:

- An oxygen partial pressure of 8×10^{-6} mbar and a substrate temperature of 523 K.

[1] The uniaxial magnetocrystalline anisotropy for strontium hexaferrite is strong enough to dominate all the other sources of anisotropy and to keep the magnetic easy axis unchanged.

- A growth rate of 0.28 nm/min for iron and 0.14 nm/min for cobalt while keeping the nominal iron flux double than that of cobalt, so that the nominal film composition was $CoFe_2O_4$.

- An annealing treatment in UHV at 673 K and 773 K. Each treatment time was 15 min.

In the case of the 5 nm CFO thin film, the preparation parameters were the following:

- An oxygen partial pressure of 8×10^{-6} mbar and a substrate temperature of 523 K.

- A growth rate of 0.16 nm/min for iron and 0.08 nm/min for cobalt, while keeping the nominal iron flux double than that of cobalt, so that the nominal film composition was $CoFe_2O_4$.

- An annealing treatment in UHV at 673 K and 773 K. Each treatment time was 15 min.

- An annealing treatment in oxygen (pressure $\sim 1 \times 10^{-6}$ mbar) at 773 K for 15 min.

With the aim of determining the structural and magnetic modifications that occur in each film after each treatment as well as the effect produced by the variation in film thickness on these, the chapter has been structured in a section commenting on the 20 nm thin film and another section discussing the 5 nm thin film and comparing it with the first one.

7.4 20 nm thin film

7.4.1 Compositional, structural and morphological characterization

For the characterization of the 20 nm thin film after each preparation step (growth and annealing in UHV), Auger spectroscopy (AES), low-energy electron diffraction (LEED), and scanning tunnelling microscopy (STM) have been used.

AES allows identifying the sample atomic composition by measuring the Auger electrons energy. Auger electrons are emitted as a consequence of internal electronic transitions after an atom has been ionised in a core level (see chapter 2). The Auger electron's energy is characteristic of a particular transition of a specific element. Moreover, the signal intensity in the spectrum is proportional to the number of atoms of the element under study [270].

Figure 7.3 shows the AES spectra recorded from the as-grown film, as well as after annealing to 673 and 773 K. The Auger spectra have been acquired using a four-grid LEED spectrometer (i.e. using it as a Retarding Field Analyzer, RFA). The incoming electron beam used for excitation is 1.7 keV.
All the spectra show the expected O KLL, Fe LMM, and Co LMM lines that refer to the electronic transitions in each element. Due to the overlap of several of the Co and Fe LMM lines, we use the peaks at 598 and 775 eV, which are well isolated, from iron and

cobalt, respectively, to monitor changes in the composition. We have determined the ratio between both peaks without taking into account any atomic sensitivity factor. Accurate sensitivity factors are not available since the values reported in "Handbook of auger electron spectroscopy" [57] are acquired with a different analyzer (cylindrical mirror analyzer) and are tabulated for other energies of the primary electron beam (3 keV, 5 keV, 10 keV). Since we are interested in the relative variation of the Fe/Co ratio among the samples, the use of atomic sensitivity factors for quantification is not really necessary. The data show an increase in the intensity of the Co LMM lines relative to the Fe LMM lines upon annealing, going from a ratio of Fe(598 eV)/Co(775 eV) 0.95 to 0.81 (673 K) and 0.60 (773 K). Assuming that the nominal composition for the as-prepared film is $CoFe_2O_4$, this intensity evolution implies the change of the Fe/Co ratio from 2:1 to 4:3. We note that the electron beam energy used to acquire the AES spectra is rather low, 1.7 keV. Under these conditions, AES is very surface sensitive. The inelastic mean free path for Auger electrons at I_P of 600 eV is close to 1 nm, so here we are collecting electrons coming from surface layer 2-3 nm thick[271]. Therefore, the annealing treatment causes an increase in the ratio of cobalt atoms to iron atoms near the surface. This increase in cobalt atoms or decrease in iron atoms on the surface with the annealing step is also reflected in the oxygen peak (512 eV). On the one hand, the ratios between the intensity of the O KLL lines with respect to the Fe LMM intensity line, Fe(598 eV)/O(512 eV), after growth, and after the annealing treatments at 673 K and 773 K are 0.115, 0.110, and 0.095, respectively. On the other hand, if we compare the intensity in the oxygen KLL lines with respect to the intensity of the cobalt LMM lines, Co(775 eV)/O(512 eV) for all the treatments, we obtain the following values: 0.130 (growth), 0.145 (673 K) and 0.175 (773 K). These data trends from Fe/O and Co/O ratios confirm the decrease in the number of iron atoms on the surface upon annealing.

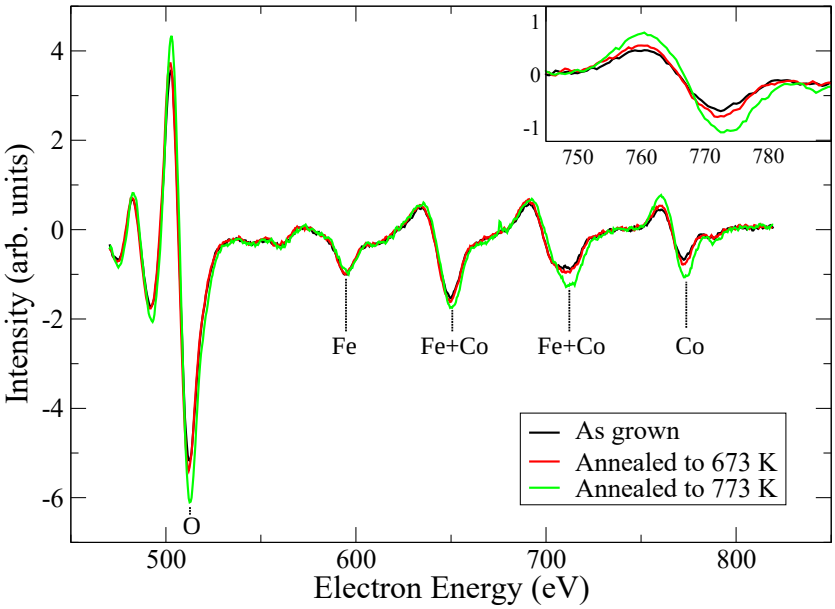

Figure 7.3: Auger spectra recorded from the 20 nm film. The spectra were normalized to the intensity of the Fe peak at 598 eV.

Continuing with the structural characterization of the thin film, LEED patterns were acquired. The images show diffraction spots of the elastically backscattered electrons from the surface when an electron beam (with a given primary energy of 66 eV) is directed

towards the sample. The diffraction pattern reveals the structural order of the CFO thin film. The LEED images of the 20 nm thick CFO sample after each step are shown in figure 7.4. In the first panel (a), the pattern from the substrate is presented, showing the Pt(111) first-order spots. The as-grown film shows also a 1×1 pattern (figure 7.4b), with the same symmetry as the substrate and somewhat smaller spacing which corresponds to a larger surface unit cell of 0.30 nm as compared to 0.277 nm for Pt(111). No significant changes are observed in the pattern upon annealing (figure 7.4c,d). These hexagonal patterns observed after the different treatments should correspond to the (111) orientation of a cubic structure. Misha and Thomas [272] have already explained that the closed-packed (111) planes of spinel ferrites are the lowest surface energy ones. However, the bulk unit cell of cobalt ferrite spinel along the (111) direction is close to twice the unit cell of Pt(111), i.e. 0.59 nm. Experimentally, we observe that the position of the diffracted beams is close to the Pt ones.

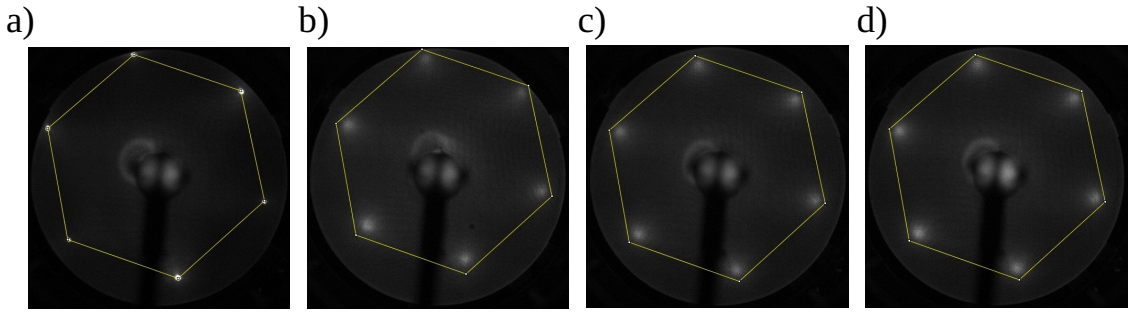

Figure 7.4: Diffraction patterns for: a) Platinum substrate, b) as-grown 20 nm CFO film, annealed to 673 K c), and to 773 K, d). The LEED patterns were acquired at an energy of 66 eV.

The expected diffraction pattern for the cobalt ferrite film should correspond to a periodicity close to a 2×2 pattern relative to the Pt one. This 2×2 diffraction pattern has already been observed for other spinels (i.e. magnetite) grown on Pt(111) [273, 274, 275, 69], or in the structure of highly perfect but non-stoichiometric cobalt ferrite grown on Ru(0001) at higher temperatures [251]. A possible explanation of the lack of the 2×2 pattern might be due to structural disorder at the cationic level in the films. This would indicate that the diffraction pattern is attributed to the oxygen-oxygen in-plane unit cell of the film, which corresponds to half the unit cell size of the spinel. A similar effect was seen in the evaporation of cobalt on Fe(100) where at some point only the oxygen unit cell was shown in the LEED pattern [254]. However, we consider that this explanation is unlikely since annealing up to 773 K, the LEED pattern does not change into the 2×2 one as expected for a more ordered film.

The second explanation is that the LEED patterns correspond to a near-surface region of the films with a rocksalt structure and thus with a $Fe_xCo_{1-x}O$ composition. There are a few reported results in support of this explanation. First, in the growth of magnetite on Pt(111) and Ru(0001) a surface reconstruction, the so-called bi-phase reconstruction, has often been observed upon molecular oxygen growth. It has been explained by a FeO-terminated spinel phase [69]. A similar reconstruction has been observed in cobalt ferrite grown at high temperature on Ru(0001) [251]. Furthermore, annealing of CoO/Fe_3O_4 has also reported on the surface segregation of a CoO layer [255], where it was suggested that the origin is the lower surface energy of CoO. This would explain the Co surface enrichment

shown in the Auger spectra which could be readily accommodated in such a $Fe_xCo_{1-x}O$ termination. We hence suggest that our conditions are such as to promote a rocksalt termination of the film.

The surface morphology of the as-grown and post-annealed treatment at (673 K and 773 K) ferrite films were observed by scanning tunneling microscopy. A direct real-space image of a surface is achieved by moving a tiny metal tip across the sample surface and recording the electron tunnel current between tip and sample as a function of position [52]. Figure 7.5a shows an STM image recorded from the as-grown film. The image shows the presence of aggregates/particles with a size around 15–20 nm, with surface root mean square (RMS) roughness of 0.3 nm. Figure 7.5b, which corresponds to the previous sample after annealing up to 773 K in UHV, shows a film with somewhat larger clusters of 20–25 nm and slightly larger 0.4 nm RMS roughness. These results indicate that with increasing temperature, the particle size and roughness on the surface of the films increases. A previous study by Lee et al [241] had already addressed the dependence of surface roughness on annealing temperatures. This work pointed out that the surface roughness increases linearly with increasing annealing temperature. Furthermore, Oujja et al. [245] reported increasing particle size with increasing temperature in good agreement with our results.

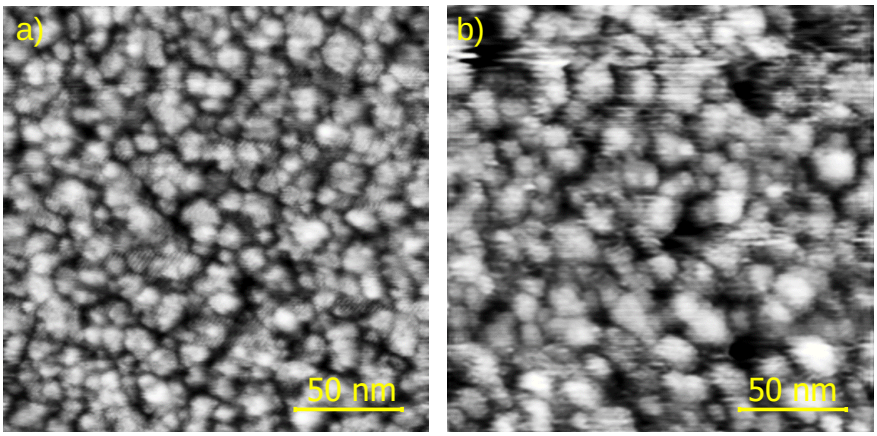

Figure 7.5: STM images of the 20 nm CFO thin film: a) as grown and b) annealed to 773 K.

7.4.2 Magnetic characterization

To determine the change in the magnetic behavior experimented in the 20 nm CFO thin film after the different treatments, Mössbauer spectroscopy has been used. However, the interpretation of the Mössbauer spectra is complicated as the data can be fitted in various reasonable ways. In fact, we will show how the Mössbauer spectrum recorded from the as-grown sample at room temperature can be fitted using different models, presented in figure 7.6. The spectra were fitted using the Recoil program with Lorentzian multiple analysis (a) and Voigt-based fitting (VBF) (b)[2]. The second fit model was proposed by

[2]The Lorentzian multiple analysis is taking into account the analysis with Gaussian singlets, doublets or sextets according to paramagnetic components with or without quadrupole splitting and magnetic components with magnetic hyperfine fields. The Voigt-based fitting allows the use of a distribution of hyperfine parameters. This corresponds to the Gaussian sum for representing a quadrupole splitting distribution in paramagnetic sites or magnetic hyperfine distribution in magnetic sites.

our collaborators from "Jerzy Haber Institute of Catalysis and Surface Chemistry" for the discussion of the research results. The values of the hyperfine parameters for the various components obtained from each fit are collected in table 7.2.

Fit *a*, figure 7.6a, shows strong paramagnetic signals (one singlet and two doublets) in its central part and a magnetic component with broader lines. The paramagnetic singlet corresponds to residual metallic iron contamination present in the platinum substrate. Such contribution will be constant in the spectra studied hereinafter. The hyperfine values of the doublets point out to Fe^{3+} in distorted octahedral coordination and Fe^{2+} also in octahedral environment. The magnetic contribution exhibits hyperfine parameters characteristic of Fe^{3+}. In fit *b*, figure 7.6b, a doublet and two contributions associated with magnetic components are obtained. On the one hand, the doublet corresponds to Fe^{3+} taking into account a quadrupole splitting distribution. On the other hand, the high-contribution magnetic component presents a very low hyperfine magnetic field distribution to be able to adjust the asymmetric peak the central part while another magnetic component adjusts the broad magnetic pattern. Both magnetic components present an isomer shift value compatible with $Fe^{2.5+}$. Thus, like the previous fitting model, this fit shows Fe^{3+} and a certain concentration of iron in 2+ oxidation state.

Despite the differences in the two fits, it can be deduced from both fits that the spectrum presents a paramagnetic part together with magnetic contributions, caused probably by a lack of structural cationic order/small size particle distribution. This is supported by the STM image for the as-grown thin film, where very small diameter particles (sizes between 10 and 15 nm) are observed. To understand the discussion raised in the Mössbauer spectra, we will briefly explain what superparamagnetism consists of.

The particle size, as well as the temperature, are factors that can modify the magnetic behavior of the system. A ferromagnetic compound that must be magnetically oriented at a certain temperature, due to the small volume of the particles, exhibits a paramagnetic state (**superparamagnetism**). However, when it is measured at lower temperatures, it does present ferromagnetic behavior. The threshold temperature in which both states coexist is called the blocking temperature (T_B). Above T_B, thermal excitations cause continuous changes in the orientation of the magnetization for individual particles, and therefore, there is a distribution of magnetic orientations. Below T_B, the magnetic moments are frozen.

In the Mössbauer spectra, this change in magnetic behavior for small particles is reflected by a transition from a doublet (superparamagnetic) to a sextet (ferromagnetic/antiferromagnetic) with the temperature decrease. In addition, the particle size distribution causes line broadening since the moment alignment for all particles does not occur at the same temperature.

One of the first works about superparamagnetic effect in nanoparticles was carried out by Schuele et al [276] where $CoFe_2O_4$ and $NiFe_2O_4$ ultrafine particles (30 to 200 Å) were studied. In the literature, we found many publications on this topic [62, 277].

In the case of thin films, different authors have pointed out this superparamagnetism behaviour associated with the small size of the grains in their samples. J.G. S. Duque [240] reported this phenomenon for CFO films with particle sizes between 10-20 nm. Also, López et al. [278] commented on the influence of the grain size with an average size of

10-40 nm in their $CoFe_2O_4$ films. In addition, Yanagihara´s group [279] working on 13 nm thick cobalt ferrite films on α-Al_2O_3 (0001) reported the occurrence of a broad magnetic component which was interpreted as a result of a thermally fluctuating magnetic order near the critical temperature or the blocking temperature associated to a superparamagnetic character of the films.

In any case, the type of fitting model chosen for the as-grown spectrum has been (a) because the second one might contribute to a more complicated interpretation associated with magnetite formation and possible electron hopping processes.

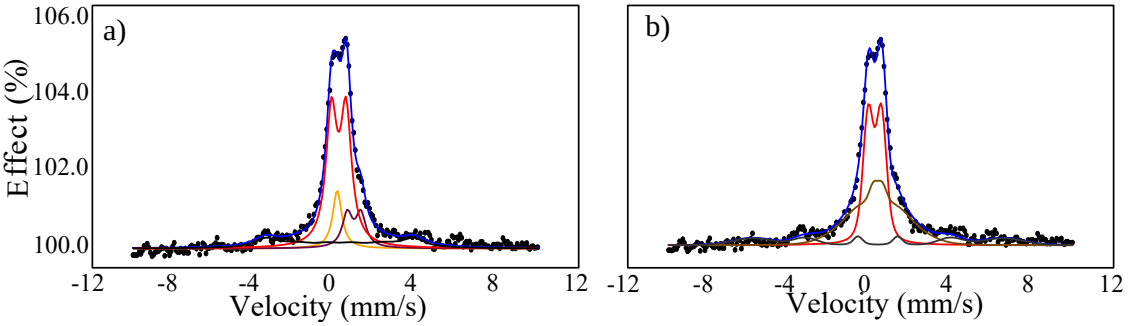

Figure 7.6: Mössbauer spectrum from as-grown sample measured at RT resolved for two different models fit: a) Lorentzian multiple analysis and b) Voigt-based fitting.

Spectrum	Site	δ ($\pm$ 0.03 mms^{-1})	2ε ($\pm$ 0.05 mms^{-1})	H ($\pm$ 0.05 T)	Area (%)
As grown a)	Fe^{0}	0.33	-	-	11
	Fe^{2+}	1.25	0.75	-	14
	Fe^{3+}	0.41	0.80	-	58
	Fe^{3+}	0.43	0.02	25.1	17
As grown b)	Fe^{3+}	0.35	0.75 (δ 0.414)	-	41.2
	$Fe^{2.5+}$	0.56	0	9.3 (δ 7.0)	43
	$Fe^{2.5+}$	0.53	0	42.8 (δ 6.5)	15.8

Table 7.2: ^{57}Fe Mössbauer parameters obtained from both fits of the as-grown sample spectrum measured at RT from figure 7.6. The symbols δ, 2ε, H, and δ correspond to isomer shift, quadrupole shift, hyperfine magnetic field, and distribution of the hyperfine parameter, respectively. The isomer shift values are quoted relative to α-Fe at room temperature.

Figure 7.7 shows the Mossbauer spectra measured at RT and 125 K after the sample has been heated to 673 K and 773 K in UHV.
In the spectrum measured at RT (figure 7.7a), a notable difference is observed as compared with the spectrum of the as-grown spectrum. The annealing treatment causes a rearrangement and short distance diffusion of nearby atoms promoting the crystallization as well an increase of the aggregates sizes in the thin film. This is reflected in the spectrum as defined magnetic components, although some magnetic relaxation is still observed in the sample responsible for broadening the lines. For this reason, it is necessary to fit the spectrum using, in addition to discrete components, a hyperfine magnetic field distribution. Therefore, for this type of fitting, code NORMOS [280] is used.

In this spectrum, two discrete sextets corresponding to Fe^{3+} in tetrahedral sites and Fe^{3+} in octahedral sites can be seen as well as broad magnetic component fitted by a hyperfine

magnetic field distribution of Fe^{3+} cations. Furthermore, the spectrum also presents the paramagnetic components already previously observed in the as-grown sample from fit (a): a singlet that refers to Pt metallic and the two doublets that correspond to Fe^{3+} and Fe^{2+}. It should be noted that the Fe^{3+} doublet is less intense here in comparison with that of the as-grown sample. This can be understood by the increase in particle size upon annealing. In addition, the presence of a Fe^{2+} contribution supports the possible explanation of rock salt terminations suggested by the LEED pattern.

Discrete sextets can be associated with the expected sites for oxides with a spinel-like structure [60]. However, the cobalt ferrite presents a ratio between iron in tetrahedral and in octahedral sites Fe_A^{3+}/Fe_B^{3+} equal to 1, while for this spectrum, it was obtained a value of 3. It is well-known that the cation distribution of cobalt ferrite cannot be precisely determined from its RT Mössbauer spectrum. In general, the tetra/octa site ratio is usually overestimated from a such type of measurement. Several publications from our group have discussed this issue in detail [246, 243, 264, 281]. This is mainly due to the strong overlap of the sextets corresponding to Fe^{3+} in both sites, the result being very much dependent on the constraints imposed to the linewidths of both sextets during fitting. In general, the tetrahedral sextet tends to be broader, and this appears to be related with the occurrence of supertransferred magnetic fields in the spinel structure [282]. Due to the supertransfer mechanism, a significant percentage of the Fe^{3+} at the octahedral sites experience hyperfine magnetic fields, which can be very similar and even smaller than the average hyperfine field felt by the tetrahedral Fe^{3+} cations. This broadens the tetrahedral sextet, and, thus, it results in an area that is larger than that expected.

The spectrum of the sample measured at 125 K (figure 7.7b) was fitted using NORMOS program too. This spectrum shows less superparamagnetic relaxation because the sextets appear to be much better resolved and the contribution of the hyperfine magnetic fields distribution is reduced. However, the measurement temperature should be lowered further to completely remove superparamagnetic effects. The singlet associated with the substrate is still observed, but the paramagnetic doublets have dissapeared. If we compare this spectrum with respect to the spectrum measured at RT, the central part do not allow the doublets to be included in the fit.

Likewise, the values of the hyperfine parameters for the sextets are compatible with those expected for cobalt ferrite [246]. The obtained Fe_A^{3+}/Fe_B^{3+} ratio (1.6) is still much higher than that expected for a canonical cobalt ferrite. Certainly, although recording data at low temperatures usually helps in determining the cation distribution, in the present case there still exists a significant contribution of the hyperfine magnetic field distribution at 125 K which complicates such determination. However, the isomer shift which characterizes this distribution has character markedly octahedral which indicates that most of the cations contributing.

In addition, it should be noted that the intensity of the sextet lines in the spectrum reveals the average magnetization orientation in the sample. Considering that the area ratio of the magnetic lines is 3:3.5:1:1:3.5:3, the average magnetization direction of the CFO thin film is practically within the sample plane (14°).

The values of the hyperfine parameters used in the fits of spectra measured at RT and at 125 K are found in the table 7.3.

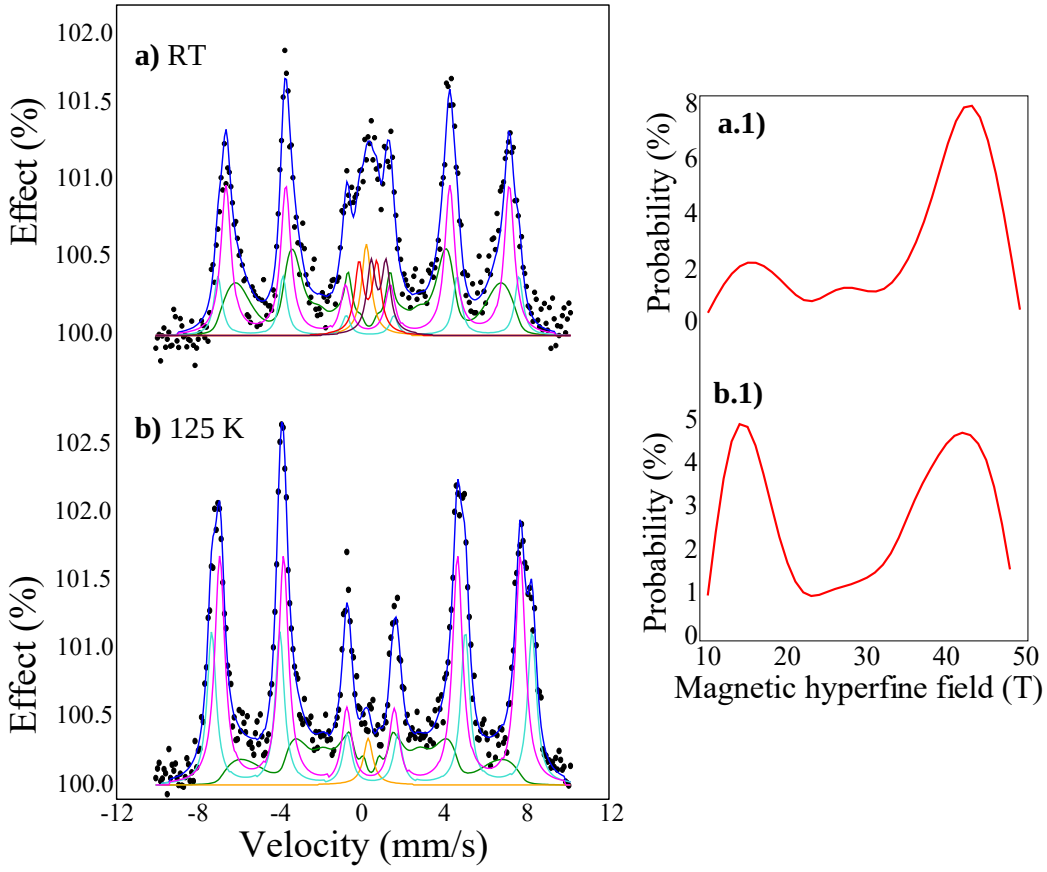

Figure 7.7: Left: Mössbauer spectra obtained for the 20 nm cobalt ferrite thin film after post-annealed treatment: a) measured at RT and b) measured at 125 K. Right: Hyperfine magnetic field distribution used to fit of the broad magnetic component in the spectra on the left.

Spectrum	Site	δ ($\pm$ 0.03 mms^{-1})	2ε ($\pm$ 0.05 mms^{-1})	H ($\pm$ 0.05 T)	Area (%)
Annealed, RT	Fe^{0}	0.23	-	-	5
	Fe^{3+}_{B}	0.38	-0.09	49.3	12
	Fe^{3+}_{A}	0.30	-0.01	46.4	37
	Fe^{3+}	0.31	0.93	-	6
	Fe^{2+}	0.87	0.78	-	6
	Fe^{3+}	0.35	-0.04	44.0 (H_{AVG} - 37.1)[a]	34
Annealed, 125 K	Fe^{0}	0.30	-	-	2
	Fe^{3+}_{B}	0.51	-0.04	52.5	29
	Fe^{3+}_{A}	0.41	-0.03	49.2	47
	Fe^{3+}	0.47	0.02	43.0 (H_{AVG} - 31.2)[a]	22

[a] In the case of the distribution component, H corresponds to the maximum of the distribution while H_{AVG} refers to the average field of distribution.

Table 7.3: ^{57}Fe Mössbauer parameters obtained from the fit of the spectra shown in figure 7.7 measured at room temperature and 125 K. The symbols δ , 2ε, H, H_{AVG} correspond to isomer shift, quadrupole shift, hyperfine magnetic field and average magnetic field, respectively. The isomer shift values are quoted relative to α-Fe at room temperature.

7.5 5 nm thin film

7.5.1 Compositional, structural and morphological characterization

The AES spectra recorded from the as-grown 5 nm thick CFO film as well as from the annealed films both in vacuum and in oxygen are shown in figure 7.8. Again, the O KLL, Fe LMM and Co LMM lines are observed. However, unlike for the 20 nm sample that showed an increase in the cobalt to iron ratio near the surface region after the heating treatments, the Auger peaks intensities of the three elements for all the treatments are very similar or practically the same suggesting that a surface cobalt enrichment does not occur here.

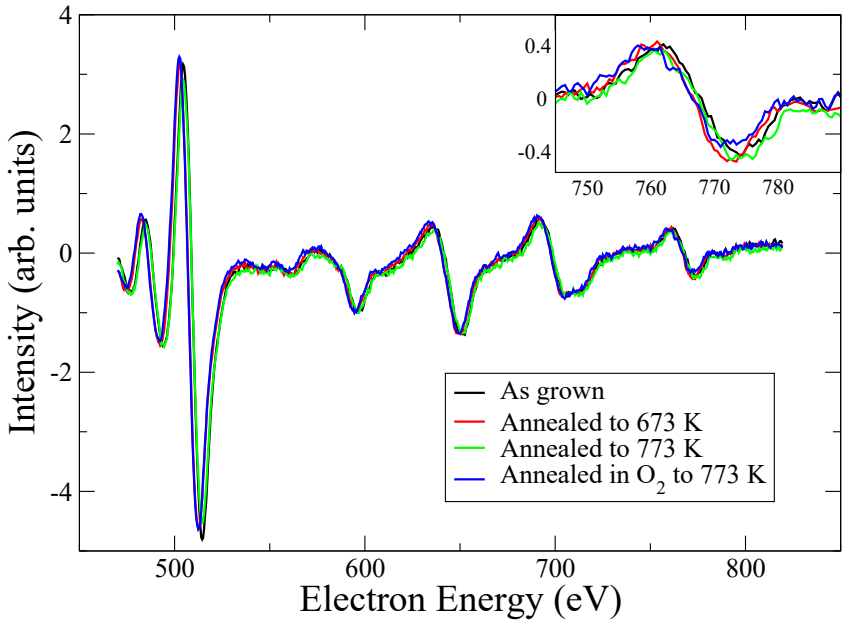

Figure 7.8: Auger spectra of the 5 nm film for each process performed. The spectra were normalized to the intensity of the Fe peak at 598 eV.

The LEED diffraction patterns from the as-grown and annealed films are shown in figure 7.9. The diffraction pattern of the substrate, Pt(111), is shown first (figure 7.9a). As for the thicker film, all the patterns are hexagonal with the same symmetry and orientation as the substrate (1×1 diffraction pattern). The LEED pattern for the as-grown sample presents a slightly smaller spacing compared to the Pt pattern, implicating a higher distance between lines of atoms in-plane and more diffuse spots, suggesting the occurrence of structural disorder in the thin film, figure 7.9b. As the sample is annealed, the spots become sharper, indicating a better crystallinity of the film (figure 7.9c,d). This feature is more evident in the annealing step with oxygen (figure 7.9e). In addition, the spots show atoms planes separation that approaches those of the substrate. Considering that the distance between planes of atoms is proportional to the distance between atoms within the plane, a graph has been made showing the in-plane lattice parameter of the 5 nm thick film after each treatment, taking as a reference the Pt in-plane lattice parameter (a = 0.28 nm), figure 7.9f. After annealing in oxygen, the lattice parameter for the sample is practically the same as the platinum lattice parameter. Regarding the observation of a

1×1 LEED diffraction pattern, instead of expected 2×2, we suggest the same explanation put forward for the thicker sample.

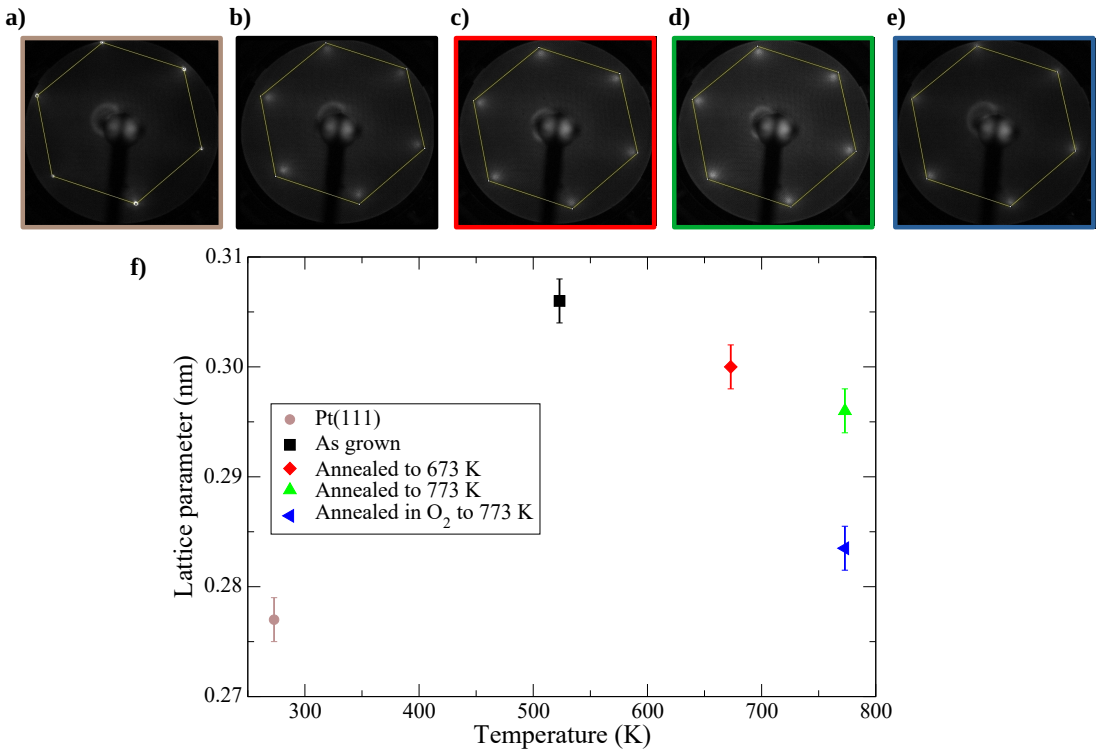

Figure 7.9: Top panel: LEED diffraction patterns for: a) platinum substrate, b) As grown 5 nm film, b) annealed in UHV to 673 K, d) annealed in UHV to 773 K e) annealed in O_2 to 773 K. Botton panel: f) lattice parameter from LEED for each processing step.

STM images from the as-grown film as well as from the film annealed at 773 K both in vacuum and in oxygen, are shown in figure 7.10. They show aggregates of particles 10-15 nm in size with an rms roughness of 0.3 nm, 15-18 nm and a rms roughness value of 0.4 nm and 20-25 nm with an rms roughness of 0.5 nm, respectively. As we have seen for the 20 nm film, annealing in an ultra-high vacuum and in an oxygen atmosphere favors the increase in the size of the aggregates.

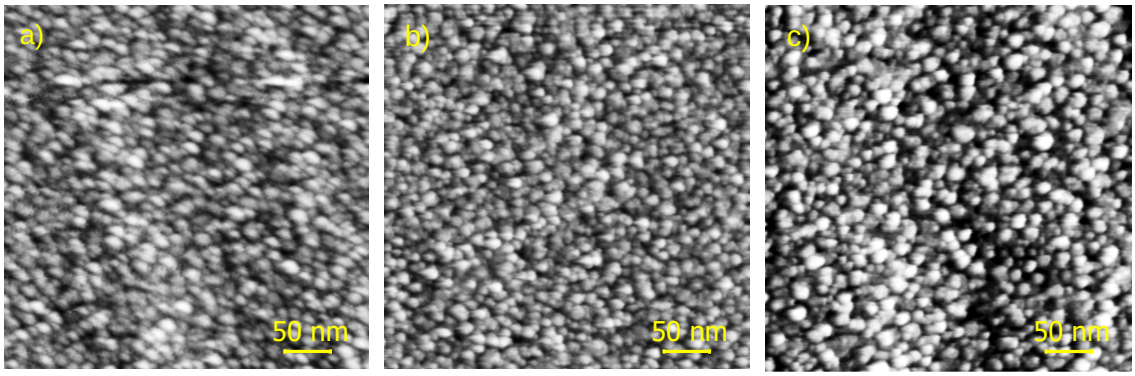

Figure 7.10: STM images for CFO thin film 5 nm thick: a) as-grown, b) annealed to 773 K in vacuum, and c) annealed to 773 K in oxygen.

7.5.2 Magnetic characterization

Figure 7.11 shows the Mössbauer data recorded from the as-grown sample at RT, the annealed film in vacuum both at RT and 115 K and the film annealed in oxygen also both at RT and 125 K. These spectra were fitted using the NORMOS code. Table 7.4 collects the values of the corresponding hyperfine parameters.

The spectrum for the as-grown sample was fitted to a singlet arising from Fe^0, a Fe^{3+} doublet and a broad magnetic component fitted with a hyperfine magnetic field distribution. This spectrum differs from the one of the 20 nm thin film mainly in its magnetic component. In this case, it is much more significant (81 %) so it seems that this sample is more magnetically ordered than the previous one. This is remarkable since one might expect that the increase in thickness would confer the sample magnetic properties closer to those observed in the bulk. Moreover, the average grain size shows an similar value from both films, figure 7.5a and 7.10a.
Several studies on magnetite, a spinel-type iron oxide, reported similarly shaped Mössbauer spectra for low thickness thin films. These have attributed their spectrum shape to possible effects produced by antiphase domain boundaries, resulting in frustration of the interdomain interactions [283, 284]. However, this explanation is unlikely since these works indicate the total elimination of the superparamagnetic component upon increasing the thickness of the sample, unlike what was obtained in the present investigation.

From our point of view, as explained in the previous sample, the spectrum is compatible with a distribution of aggregate sizes with a range of sizes that includes those grains small enough to be in a paramagnetic state at room temperature (superparamagnetic behaviour), as well as some grains that exhibit magnetic state. Nonetheless, the grains' atomic structuring might be the causative factor of this different magnetic behaviour between both as-grown films. I.e., we assumed that both samples present a poor crystallinity; however, the increase magnetic contribution shown in the thinner film appears to point out a higher atomic order compared with 20 nm film. This fact might be explained as a consequence of the deposition rates used for each sample. Deposition rates for the 5 nm film have been slower than for the thicker film in a factor of almost two. Considering that the temperature growth was relatively low (523 K), slower deposition rates favour an arrangement of the atoms more orderly way in the structure. So, we suggest that the deposition rate difference between both samples has led to the atomic order variation, and thus, the change in the magnetic behaviour.

As in the case of the thicker film, the annealing treatments induce significant changes in the nature of the deposited film. The RT spectra recorded from the annealed film both in vacuum and in the presence of oxygen are very similar and they are also similar to the RT spectrum recorded from the annealed 20 nm CFO film: they show much better defined magnetic components and significantly less intense paramagnetic contributions. Although, a priori, the as-grown samples for both thicknesses start from different crystalline states within the grains, the increase in temperature up to 773 K produces the atomic reorganization to a spinel-like structure [241]. Therefore, spectra have been all fitted using the same procedure. Thus, the same considerations mentioned in the case of the annealed 20 nm-thick film are of application here. From the results, compiled in table 7.4 for the RT Mössbauer data of the annealing in UHV and oxygen atmosphere, we cannot detect a significant change in the structural and magnetic properties with the thickness of the films.

At LT the spectra show much narrower sextet lines although some magnetic relaxation is still present, hence the need of including a low-intensity hyperfine magnetic distribution. Contrarily to the LT spectrum of the thick film, the 125 K spectra of these films continues to show a Fe^{2+} contribution. The appearance of Fe^{2+} cations can be fitted again.

Important information to consider when comparing the spectra at LT of the 5 nm thick sample with that of the 20 nm film is the Fe_A^{3+}/Fe_B^{3+} area ratio. For the thicker film, we observed a ratio of 1.6, while for the thinner film they are 1.9 and 1.1 for those films annealed in vacuum and oxygen, respectively. It seems that annealing in oxygen favors the formation of a inverse cobalt ferrite structure [243, 240]. Certainly, these ratios are overestimated since for all the spectra we have a certain magnetic relaxation. To eliminate this contribution, the temperatures should be lowered even further. However, these temperatures cannot be reached with the present experimental setup.

Further, for the 5 nm-thick film the area of the sextet lines follow the ratio 3:3.1:1:1:3.1:3 which corresponds to an average angle of the magnetization to the sample surface of 20°. Thus, in the present film, the magnetization is slightly more out-of-plane than in the 20 nm-thick film. Hence, the thickness increase promotes the orientation of the magnetization within the film plane, in line with the results of Khodaei et al [235].

In any case, the results indicate that the film thickness does not play a crucial role in the characteristics of the film, and that the annealing treatment helps to achieve a cation distribution close to that expected for cobalt ferrite. Additionally, the thinner film has shown an improvement of the cationic order after annealing in oxygen.

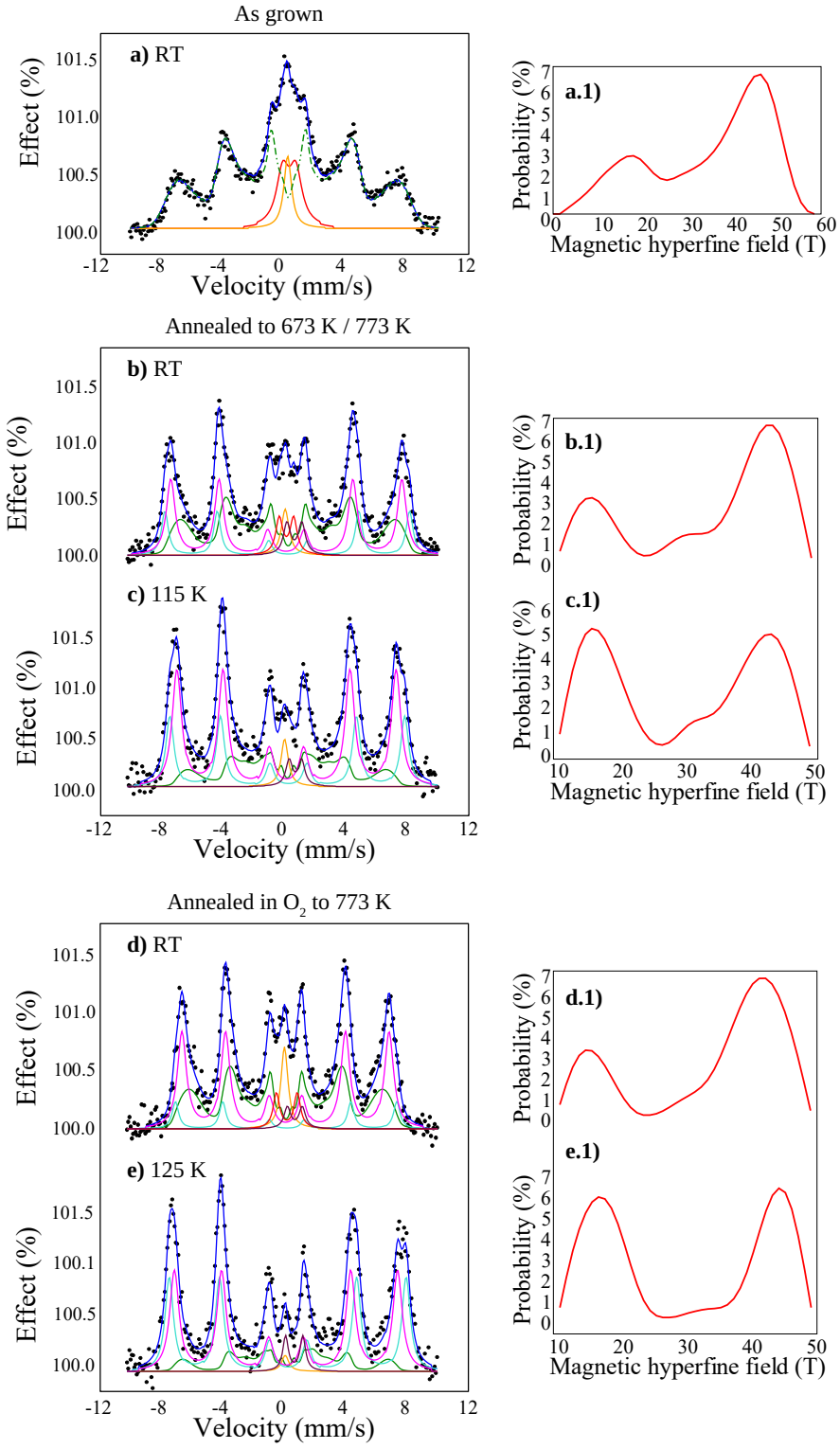

Figure 7.11: Left: Mössbauer spectra obtained for the 5 nm cobalt ferrite thin film for the different stages: a) as-grown measured at RT, b) and c) annealed to 673 K and 773 K measured at RT and 115 K, respectively, d) and e) annealed in oxygen atmosphere to 773 K measured at RT and 125 K, respectively. Right: Hyperfine magnetic field distribution used in the fit of the broad magnetic component from the spectrum on the left.

Spectrum	Site	δ ($\pm$ 0.03 mms^{-1})	2ε ($\pm$ 0.05 mms^{-1})	H ($\pm$ 0.05 T)	Area (%)
As grown	Fe^{0}	0.30	-	-	6
	Fe^{3+}	0.40	0.85	-	13
	Fe^{3+}	0.34	-0.03	46.5 (H_{AVG} - 33.7)[a]	81
Annealed, RT	Fe^{0}	0.23	-	-	4
	Fe^{3+}_{B}	0.39	-0.05	49.4	14
	Fe^{3+}_{A}	0.29	0.02	46.7	31
	Fe^{3+}	0.31	0.93	-	5
	Fe^{2+}	0.82	0.97	-	5
	Fe^{3+}	0.41	-0.03	43.5 (H_{AVG} - 34.9)[a]	41
Annealed, 115 K	Fe^{0}	0.30	-	-	3
	Fe^{3+}_{B}	0.46	-0.08	51.4	24
	Fe^{3+}_{A}	0.36	0.00	48.0	47
	Fe^{2+}	0.99	0.88	-	3
	Fe^{3+}	0.41	-0.04	44.0 (H_{AVG} - 30.5)[a]	23
Annealed in O_2, RT	Fe^{0}	0.23	-	-	6
	Fe^{3+}_{B}	0.37	-0.05	48.5	8
	Fe^{3+}_{A}	0.31	0.01	45.4	39
	Fe^{3+}	0.39	1.47	-	4
	Fe^{2+}	0.86	1.05	-	3
	Fe^{3+}	0.33	-0.02	43.0 (H_{AVG} - 35.3)[a]	40
Annealed in O_2, 125 K	Fe^{0}	0.30	-	-	1
	Fe^{3+}_{B}	0.49	-0.03	51.9	37
	Fe^{3+}_{A}	0.36	-0.01	48.9	43
	Fe^{2+}	0.93	1.21	-	4
	Fe^{3+}	0.40	-0.16	45.2 (H_{AVG} - 30.5)[a]	15

[a] In the case of the distribution component, H corresponds to the maximum of the distribution while H_{AVG} refers to the average field of distribution.

Table 7.4: ^{57}Fe Mössbauer parameters obtained from the fit of the spectra shown in figure 7.11 measured at room temperature and low temperature (115 K and 125 K). The symbols δ , 2ε, H, H_{AVG} correspond to isomer shift, quadrupole shift, hyperfine magnetic field and average magnetic field, respectively. The isomer shift values are quoted relative to α-Fe at room temperature.

7.6 Conclusions

Cobalt ferrite thin films of different thicknesses (5 and 20 nm) have been synthesized by molecular beam epitaxy on Pt(111) and characterized *in-situ* under UHV conditions. Deposition at 523 K gives rise to superparamagnetic/poorly crystalline thin films composed of a distribution of Fe^{3+} containing-aggregates of different sizes in the nanometer scale. The results show that together with the deposition of these Fe^{3+}-containing aggregates, a minor Fe^{2+} phase develops. The 1×1 LEED pattern observed in these films suggests a $Fe_xCo_{1-x}O$ termination of the films. The thinner film presents higher cationic ordering than the thicker sample, explained by the lower deposition rate employed. This atomic distribution change is reflected in the intensity of the magnetically ordered components in the Mössbauer of the spectra as-grown. Annealing in vacuum at 773 K promotes an increase in the size of the Fe^{3+} aggregates resulting in the development of magnetic ordering at RT, although the annealing treatment has not been able to remove the superparamagnetic contribution completely. Annealing of the films also produces a cobalt enrichment of the thicker film's surface, probably associated with the segregation of CoO. The low-temperature Mössbauer spectra recorded from the various films point out differences in the cation distribution of the deposited CFO films. The Fe_A^{3+}/Fe_B^{3+} ratios reveal the formation of cobalt ferrite after annealing treatment achieving for the thinner film a cation distribution close to that expected for a CFO inverse spinel after annealing in oxygen.
Therefore, we have shown that cobalt ferrite thin films on a platinum substrate can be obtained at the growth and annealing conditions established in this research. This fact represents an advantage with respect to other CFO thin film studies reported in the literature since it is not necessary to heat the substrate at high-temperature what might hinder a continuous film's deposition. Further, The O-MBE deposition method has provided precise control of the growth of the deposited layers, and the deposition on the metallic substrate brings an interesting system for spintronic applications.

8 Magnetic interactions in $CoFe_2O_4$/FeCo bilayer thin films

8.1 Introduction

As already seen in chapters 5 and 6, rigid coupling magnetically two materials with substantially different coercivities in order to improve the combined magnetic properties is challenging. This is, in part, because the complete exchange coupling is influenced by different factors such as the thickness of the soft phase, the atomic coherence at the interface, the crystallinity, anisotropies from both layers, etc [29, 285, 286]. Specifically, in the hard/soft systems previously studied, SFO platelet/Co (chapter 5) and SFO thin film/Co (chapter 6), it has been found that both layers are magnetically uncoupled, although, for the latter, a concordance was observed in the easy axis magnetization between both layers attributed to structural coupling.

This chapter discusses the magnetic behaviour of a bilayer system consisting of a cobalt ferrite (CFO) thin film as the magnetically-hard material and an iron-cobalt (FeCo) alloy layer as soft material, through micromagnetic simulations [86]. These simulations were performed to support and understand results obtained in a CFO/FeCo bilayer experiment carried out previously.
The initial purpose of the experiment was to determine the thickness threshold of the FeCo layer, which separates the rigid and the spring/partial exchange coupling regimes [19, 35, 287]. However, a spring magnet behaviour was observed in the soft-material thickness much below such threshold. A complete coupling should thus appear. In other words, below the soft material critical thickness, the reversal magnetization should occur simultaneously for both layers. However, the soft phase switched reversibly at lower magnetic fields than the hard one. This partial exchange coupling was suggested as a consequence of the dominance of domain-wall propagation in the soft phase during the reversal process.

Therefore, considering the accepted spring magnet theory [30], different parameters in the micromagnetic simulations such as soft exchange stiffness, exchange coupling strength, or the saturation magnetization of the soft layer have been modified to determine the possible factors involved in the spring magnet response observed in the experimental bilayer system.

The results presented in this chapter have been published in:

- A. Quesada, G. Delgado, L. Pascual, A. M. Aragón, P. Marín, C. Granados-Miralles, M. Foerster, L. Aballe, J. E. Prieto, J. de la Figuera, J. F. Fernández, and P. Pri-

eto, "Exchange-spring behavior below the exchange length in hard-soft bilayers in multidomain configurations," Physical Review B, vol. 98, no. 21, p. 214435, 2018.

8.2 Experimental background

$CoFe_2O_4$ was selected due to its high chemical stability and large magnetocrystalline anisotropy. Iron-cobalt alloy was selected due to its high saturation magnetization. This system has been the subject of previous work in which a wide variety of magnetic behaviours have been reported (spring magnet, decoupling and antiferromagnetic coupling). The coupling can be tuned by a proper choice of growth conditions [288, 289]. Nonetheless, the critical thickness of the soft layer, which is one of the factors that govern magnetization reversal of the system, had not been researched in-depth. To this end, the present experiment was performed.

The CFO/FeCo bilayers were deposited on Si (001) substrates covered with a 6 nm TiN buffer layer by Ar^+ ion-beam sputtering [290]. Structural and compositional analysis was performed by TEM and RBS (figure 8.1). TEM characterization revealed the composition of the layers and the separation of them at the interface. The fast Fourier transform of the atomically resolved TEM image confirmed the spinel and cubic structure of the cobalt ferrite and FeCo films, respectively. Furthermore, an [101] FeCo/ [100] CFO epitaxial relationship between both phases was determined. The grown films showed a high degree of structural coherence except for some dislocations. The thicknesses for the different grown films were determined by Rutherford backscattering spectroscopy. The grown samples had hard layer thicknesses ranging from 76 to 81 nm, while the soft thickness ranged from 2 to 17.5 nm.

The magnetic behavior was determined through magnetization curves comparing the isolated cobalt ferrite thin film with the bilayer systems with soft layer thicknesses of 2 nm (FC2) and 4 nm (FC4), figure 8.2a. The squareness ratio in the CFO hysteresis loops was $Mr/Ms = 0.46$, indicating that the hard phase breaks into a multidomain patter. This is because the easy axis of magnetization of each grain in the film has a different preferential orientation, which generates a reduction in magnetization in remanence compared to when an external magnetic field is applied in one direction producing magnetization alignment in the film [13]. The most interesting point presented in that figure and the one that brings forward the novel result in this research is related to the magnetization curves with the soft layer. At low negative fields, a steep decrease in magnetization was observed, associated with the reversal of the soft phase. At higher fields, the gradual irreversible rotation in CFO occurred. The onset of soft layer reversal at low negative fields is defined as the nucleation field H_n, while the switching field H_{sw} corresponds to the irreversible magnetization reversal of the hard layer [293, 170]. Thus, both layers reverse the magnetization at different applied magnetic fields and in consequence, there is no rigid coupling in these systems. This behaviour of different reversal magnetizations for both layers ($H_n < H_{sw}$) was observed for all thicknesses studied in the investigation, figure 8.2b.

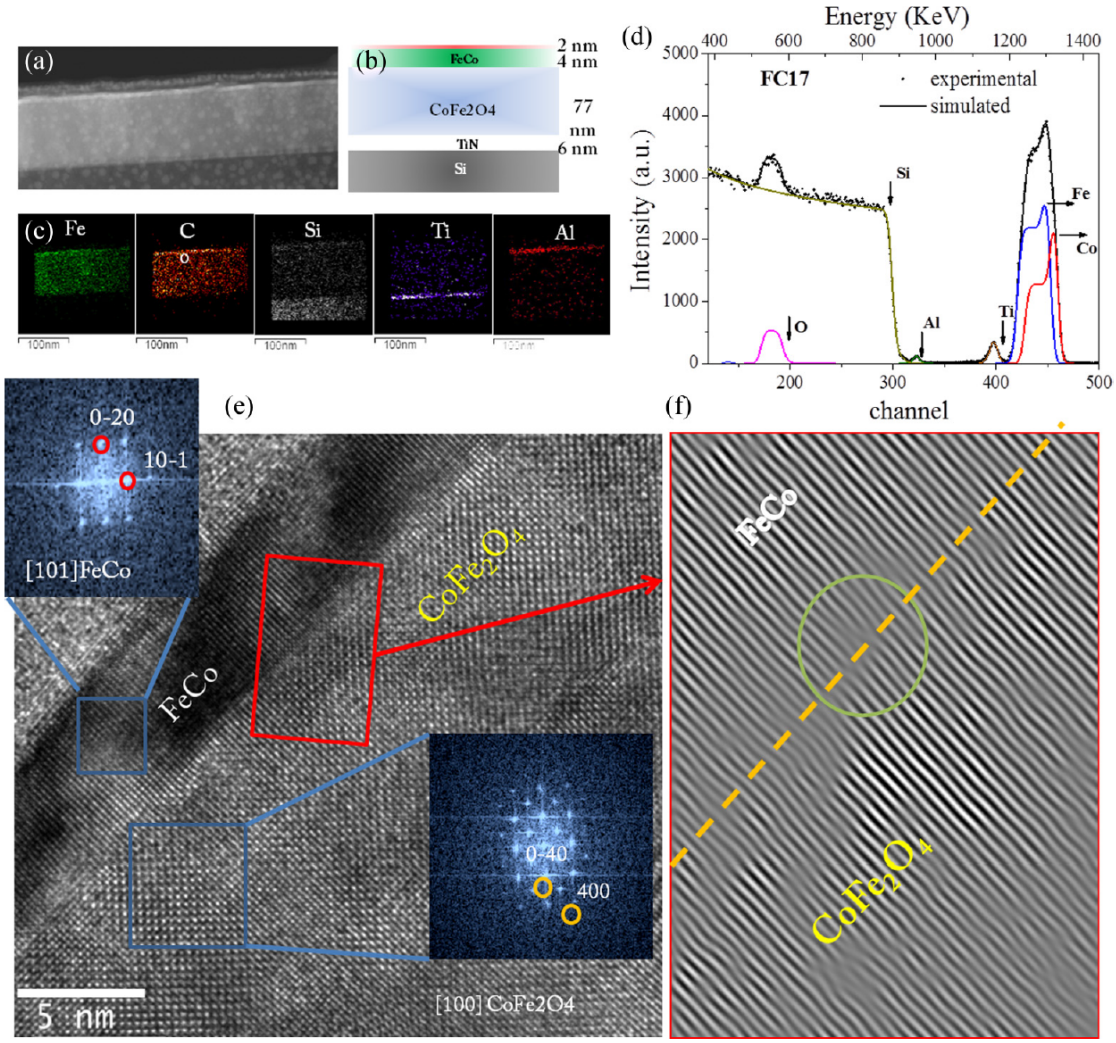

Figure 8.1: (a) Low resolution HAADF-STEM[291] image showing the multilayer arrangement sketched in (b). (c) Energy dispersive X-Ray spectroscopy (EDXS) maps for different elements present in the stack. (d) RBS data corresponding to a bilayer with soft FeCo thickness of 17 nm. A high resolution TEM image of the CFO/FeCo interface is shown in (e), with insets containing fast Fourier-transform patterns for each film. In (f), a filtered image using together the (10-1) in FeCo and (400) in CFO of the interface region (delimited in red) is presented. Figure extracted from publication [292].

In order to predict the nucleation field for the soft phase according to the spring magnet theory, the following relation was used:

$$H_n = \frac{\pi^2 A_s}{2 M_s t_s^2} \tag{8.1}$$

where A_s is the exchange stiffness, M_s is the saturation magnetization, and t_s is the thickness of the soft phase. Substituting in equation 8.1 with the bibliographic values $M_s(FeCo)$ = 1.85 x 10^6 A/m and the accepted stiffness value of A_S = 1.7 x 10^{-11} J/m [294], the theoretical curve was obtained for the different soft thicknesses (figure 8.2b). From this

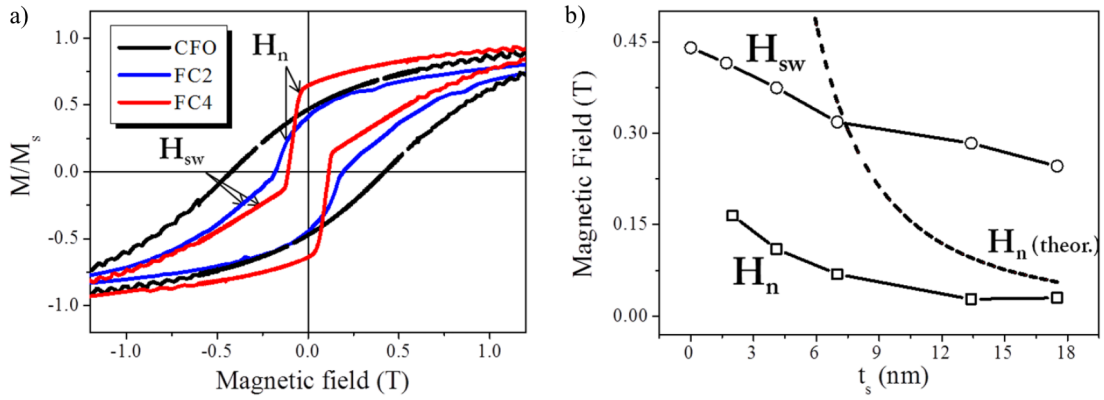

Figure 8.2: (a) VSM magnetization curves measured at room temperature of a reference CFO film for a 2-nm (FC2) and a 4-nm soft bilayer (FC4). (b) H_n and H_{sw} extracted from the magnetization curves as a function of soft thickness.

curve a critical soft thickness of approximately 8 nm was deduced (H_n=H_{sw}). This value was in agreement to the Bloch wall width δw of the hard phase, which has been predicted to be close to the critical soft thickness. δw for CFO is of the order of 8–10 nm [293]. This spring magnet theory was fulfilled in the study carried out by Lavorato et al. [293] for the $CoFe_2O_4/Fe_3O_4$ system. They observed rigid coupling in the system with thickness soft layer of 5 nm and a spring-magnet behavior with thicknesses of 15 and 25 nm.

In our experiments, following the theoretical predictions, the magnetic behaviour of the CFO/FeCo bilayer systems should have been rigidly coupled at the thicknesses under study, although experimentally, such behaviour was not observed. It is important to note that, although both layers did reverse independently, they were not wholly decoupled. Otherwise, the soft nucleation field would remain constant at any thickness. Recoil loops using a recoil field (applied magnetic field with values between H_n and H_{sw}) confirmed that spring behaviour, and MOKE measurements pointed out a robust degree of coupling, expected since the hard and soft easy axes aligned along Si[110].

Additionally, XMCD-PEEM images at the Fe L_3 absorption edge revealed magnetic domains between 100-500 nm and a domain wall of approximately δw = 17 nm. However, the lateral resolution of the instrument [74] is 15-20 nm, so δw could be smaller. The origin of the unexpected spring behaviour observed experimentally as a function of the first magnetization curves was discussed. For this purpose, an isolated cobalt ferrite film was compared with the CFO (76 nm)/FeCo (4 nm) system. For the former, gradual growth of magnetization associated with domain nucleation was revealed, while for the latter, a clear increase in magnetization at low fields, that rapidly magnetizes the soft layer, is observed. This is normally attributed to domain wall propagation (DWP) mechanisms [295, 296]. It is important to understand that the exchange-spring magnet models that have been developed so far only take into account domain nucleation and not DWP in their description [19, 35]. The coercivity field observed in these systems are often lower than predicted, which combined with the fact that DWP seems the dominating remagnetization mechanism in the soft layer suggests that it may be playing an important role in the overall demagnetization curve.

8.3 Micromagnetic simulations of $CoFe_2O_4$/FeCo system

Micromagnetic simulations have been carried out to support the experimental results. Different micromagnetic parameters have been changed in order to study the spring magnet response predicted by the theory: (i) the exchange stiffness of the soft layer *(A_s)*, (ii) exchange-coupling between the soft and the hard layer *(κ)* and (iii) saturation magnetization of the soft layer *(M_s)*.

The simulation cell size was set to 4 x 4 x 2 nm^3 for both layers and slabs with the in-plane size 800 x 800 nm^3 with several replicas were employed to mimic periodic boundary conditions avoiding isolated system behavior. The thicknesses of $CoFe_2O_4$ and FeCo layers have been chosen to be 76 nm and 4 nm, respectively, i.e. the same as the experimental bilayer with the thinnest soft layer that showed a spring magnet effect. The exchange stiffness and anisotropy values were taken from the literature [269, 294], while the saturation magnetization was obtained from experimental measurements of single-layer films of the soft and hard layers. Thus, the following starting point magnetic parameters were used in simulations for hard (H, i.e. $CoFe_2O_4$) and soft (S, i.e. FeCo) layers: exchange stiffness $A_H = 1.10 \times 10^{-11}$ J/m, $A_S = 1.7 \times 10^{-11}$ J/m, saturation magnetizations $M_H = 3.41 \times 10^5$ A/m and $M_S = 1.85 \times 10^6$ A/m, magnetocrystalline constants $K_H = 5.10 \times 10^5$ J/m^3 and $K_S = 0.472 \times 10^3$ J/m^3.

8.3.1 Exchange stiffness of soft layer

Figure 8.3 presents the simulated magnetization curves and their derivative for four different exchange stiffness values at an applied magnetic field of up to 2 T in [110] direction in these simulations. A single-domain initial configuration for both layers is defined. Moreover, taking into account that the experimental data indicate a good crystalline order of the interface, an interface exchange coupling of 75% has been assumed.

First, the hysteresis loop with an exchange stiffness value of $A_S = 1.7$ x 10^{-11} J/m for the soft layer, corresponds to the red curve in figure 8.3a. In this case, the hysteresis cycle shows a rigid coupled system, in agreement with the predictions of classic spring magnet theory [30, 294]. In fact, performing the derivate dM/dH from this curve, a soft layer reversal at low negative fields is not observed (see figure 8.3b same color pattern).
In order to force the spring magnet behaviour seen in the experiment, we have estimated the value of the required exchange stiffness according to the classic spring theory equation 8.1 using experimental parameters obtained (saturation magnetization, $M_S = 1.85 \times 10^6$ A/m, and nucleation field, 0.04 T). A value of $A_S = 3.1 \times 10^{-12}$ J/m was determined. For this soft material exchange stiffness, we observe in figure 8.3a the typical "jump" characteristic from the spring magnet regime. This feature is related to the reversal of the soft layer, which occurs at a lower magnetic field than for the hard layer. This can be better observed in the dM/dH plot where a clear maximum is appreciated (figure 8.3b).

Hysteresis cycles were calculated with exchange stiffness values intermediate between those two. In figure 8.3a, we see that for both $A_S = 8.5 \times 10^{-12}$ J/m and $A_S = 7 \times 10^{-12}$ J/m it is difficult to define whether there is a spring behaviour. However, looking at the derivatives, a slight maximum is observed for $A_S = 8.5 \times 10^{-12}$ J/m while for the other

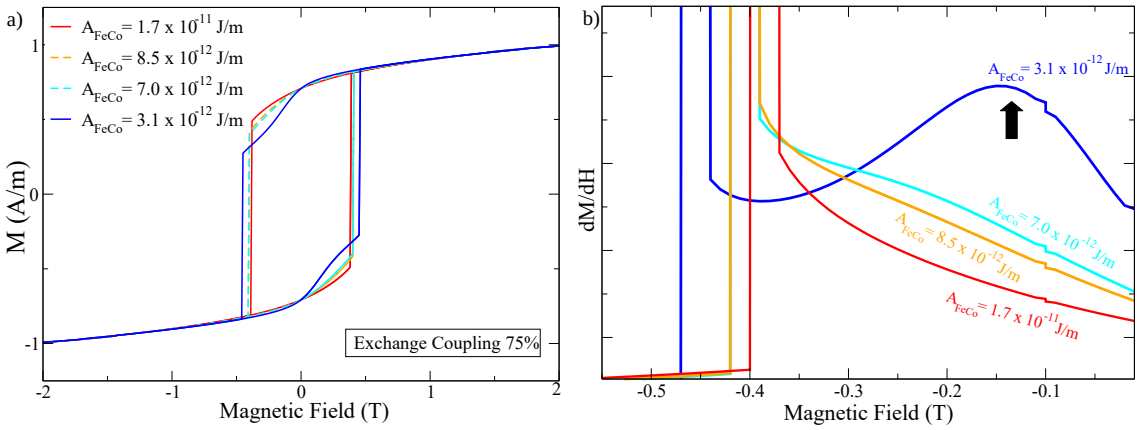

Figure 8.3: (a) Simulated dM/dH curve for four different exchange stiffness values for a 76-nm $CoFe_2O_4$/ 4-nm FeCo bilayer. (b) Simulated magnetization curves corresponding to the highest and lowest stiffness values. The arrow indicates the curve maximum which indicates the spring magnet behavior.

value, the maximum has practically disappeared (curves in colors cyan and orange from figure 8.3b, respectively). Therefore, from the micromagnetism simulations performed in this section, it is confirmed that the system behaves as a rigid/spring magnet above/below $A_S = 8 \times 10^{-12}$ J/m. We note, however, that such value of exchange stiffness is much too low compared with reported values for FeCo (typically 6x larger, $A_S = 1.7 \times 10^{-11}$ J/m) [294].

8.3.2 Interlayer exchange coupling

Another way to induce a partial decoupling of the two layers is by reducing the exchange coupling between the soft and hard layer by the κ parameter. κ is the factor that rescales the exchange coupling value between both layers, ranging from $\kappa = 1$ (perfect coupling) to $\kappa = 0$ (complete exchange decoupling). In figure 8.4, hysteresis loops of the $CoFe_2O_4$/FeCo bilayer at an applied magnetic field of up to 2 T in the [110] direction are plotted for two values κ (0.05 and 1) of the interlayer exchange coupling, keeping the other magnetic parameters constant at the values indicated at the beginning of the section. A single-domain initial configuration for both layers was defined in these simulations.

It was found that in order to observe the exchange-spring behaviour in the bilayers, the value of κ has to be as low as 0.05. This exchange coupling value is unrealistic since the experimental observations pointed out a coherent and sharp interface with a few separate misfit dislocations. Thus, as for the exchange stiffness parameter discussion, the magnetic spring behaviour can only be reproduced by forcing the material parameters to unrealistic values.

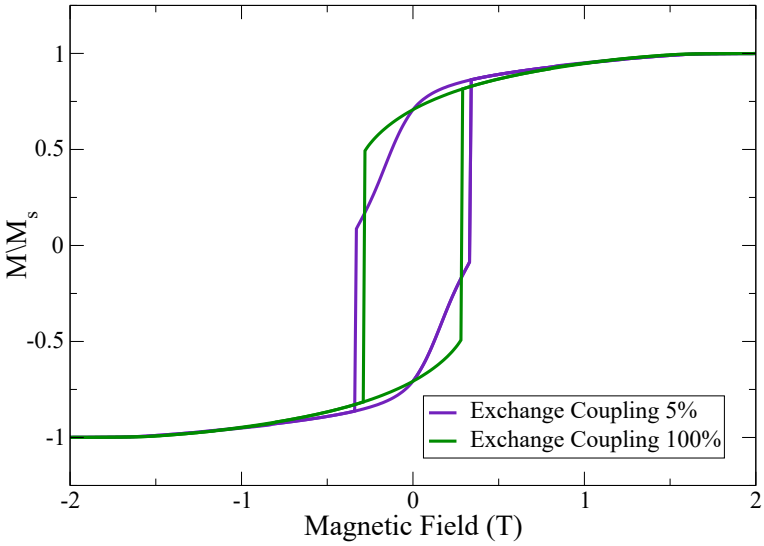

Figure 8.4: Simulated hysteresis loops of the $CoFe_2O_4$/FeCo bilayer for two different κ values (0.05 and 1.0)

8.3.3 Saturation magnetization of soft layer

As it has already been mentioned in the "experimental background" section, a study performed by Laborato et al. [293] used magnetite as the soft magnetic layer (Fe_3O_4) instead of FeCo. In such work, the spring magnet thickness limits of the classic theory were fulfilled. The main difference with our study comes from the fact that the saturation magnetization of magnetite is considerably lower than that of iron-cobalt alloy.

In this part, the influence of the saturation magnetization of the soft is studied, keeping the rest of the parameters constant (beginning of the section). For this, two micromagnetism simulations were performed using the magnetization value of magnetite ($M_s = 4.8 \times 10^6$ A/m) and the magnetizing value of the cobalt-iron alloy ($M_s = 1.85 \times 10^6$ A/m). For both, the exchange stiffness was set to $A_S = 3.1 \times 10^{-12}$. This is the value calculated to reproduce the spring magnet behavior in the CFO/FeCo bilayer system (see figure 8.3). Further, a single-domain initial configuration for both layers was defined in these simulations.

Figure 8.5 shows the magnetization curves of the $CoFe_2O_4$/FeCo bilayer at an applied magnetic field of up to 2 T in [110] direction for the two saturation magnetization values. Using the M_s for FeCo leads to the exchange-spring reversal, while the M_s of Fe_3O_4 yields a 'rigid' behavior. Although, the fact that CFO and Fe_3O_4 have very similar values makes it incredibly difficult to discern rigid from spring behavior only from magnetization curves. This observation proves the important influence of the M_s of the soft phase and hints at reasons for the discrepancy with Lavorato et al. results. In addition, it supports the idea that considering the exchange length of the hard phase as the main parameter determining critical thickness is an oversimplification.

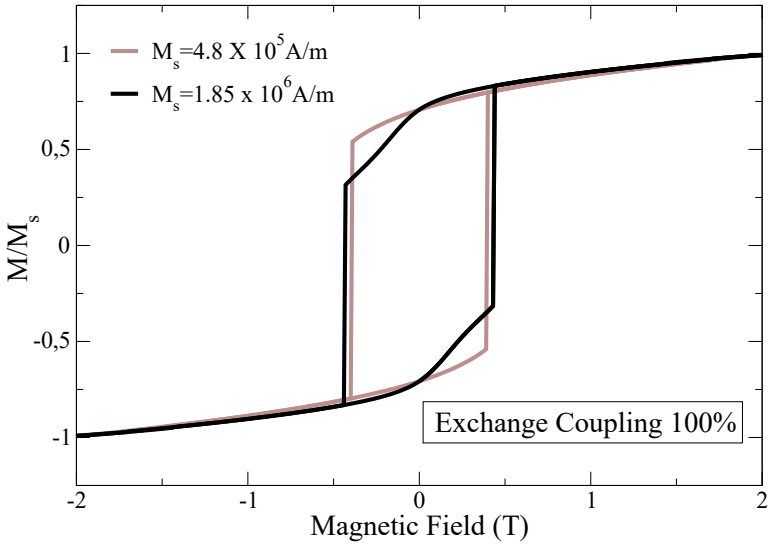

Figure 8.5: Simulated hysteresis loops of the $CoFe_2O_4$/FeCo bilayer for two different magnetization values of FeCo

8.3.4 Simulating multi- and single-domain configurations

In this section, we have attempted a slightly more realistic model of the hard layer. Instead of a monocrystalline hard layer, a multi-domain state was obtained by defining grains with an average in-plane size of 100 nm in the $CoFe_2O_4$ layer using the Voronoi tessellation. The exchange coupling between these grains was set to zero, i.e., the grains are exchange-decoupled from one another. It is worth noting that exchange-coupling does occur between these grains/domains in reality, with magnetic domain walls pinned at antiphase boundaries (APB)[1]. Both rotational processes within each domain/grain and depinning of magnetic domain walls from APB are expected to contribute to the magnetization process in the CFO layer alone. Thus, it is important to keep in mind that the micromagnetic model presented here still constitutes a simplification compared to the real experimental system.

A single continuous soft layer is covering the CFO grains. The exchange coupling set between the CFO multi-domain state from cobalt ferrite and iron-cobalt single domain state was $\kappa = 0.75$ to approach the experimental conditions. Further, the micromagnetic simulation was performed using the same parameters from both phases showed at the beginning except the soft exchange stiffness constant, which was set $A_S = 3.1 \times 10^{-12}$ J/m since spite of to be an unrealistic value, we want to simulate for the present study the spring magnet behavior observed in the experimental part. This is not reproduced with literature A_S value.

[1] APB separates two domains of the same ordered phase. It arises from symmetry breaking that occurs during ordering processes, which might begin at different locations in a disordered lattice. The antiphase boundary is formed when two such regions come into contact and there a mismatch in the composition across the interface [297].

Figure 8.6 presents the magnetization change of the bilayer system with an applied magnetic field of up to 3 T and depicts the bilayer magnetization state at different magnetic fields. At remanence (0 T) the soft layer is found coupled with the $CoFe_2O_4$ domains. When the applied magnetic field increases, the magnetization of the top of the FeCo layer differs from the bottom side, which is in contact with the hard $CoFe_2O_4$ multidomain state. At a magnetic field of 0.38 T the average magnetization of the soft layer changes direction to that of the applied field, showing domain walls (separation between the orange and yellow regions), and it is not until 1.5 T that the soft film is fully oriented. In contrast, the domain walls formed in the CFO disappear at around 2.2 T. Therefore, in this simulation, a propagation of the domain wall in the soft phase is observed, which is the factor that promotes the magnetization orientation in the bilayer.

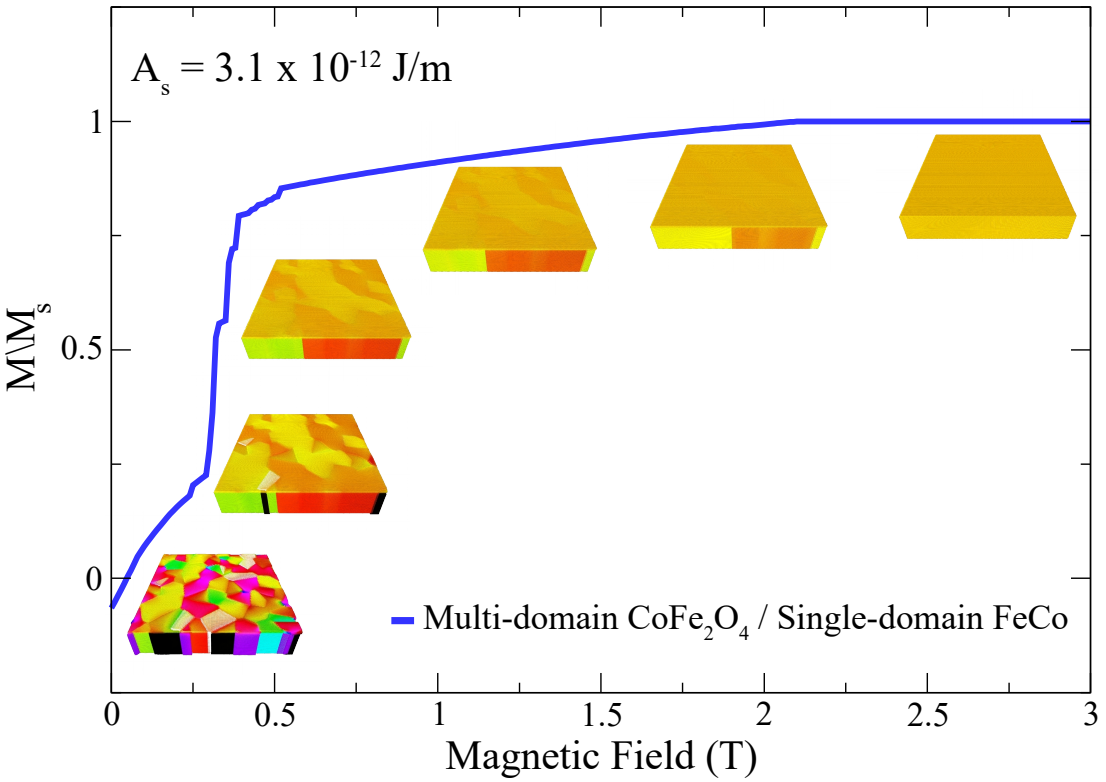

Figure 8.6: Simulated magnetization curve for the $CoFe_2O_4$/FeCo bilayer starting from a multidomain initial configuration. Inset shows magnetization states during the magnetization process.

8.4 Conclusions

Micromagnetic models that follow the accepted spring theory force us to use unrealistic stiffness and exchange coupling conditions in order to reproduce the experimental observations. In addition, saturation magnetization confirms that domain wall propagation plays an important role in the soft layer's demagnetization. Indeed, iron-cobalt layer saturation magnetization is an influencing factor in the bilayer magnetic behaviour, demonstrating that the hard phase exchange length is not the only parameter involved. The micromagnetic simulation using a multi-domain configuration of the hard layer and a value of exchange stiffness of $A_S = 3.1 \times 10^{-12}$ J/m, which is the value calculated from experiment results, reproduced the bilayer behaviour. Virgin magnetization curve and images from the bilayer magnetic state evolution showed a propagation of domains in the soft reflecting an increase of the magnetization at a field of 0.38 T. Reversal of the magnetically hard layer is produced at higher magnetic fields. Therefore, micromagnetic simulations confirmed the spring magnet-like behaviour due to domain wall propagation observed in the $CoFe_2O_4$/FeCo bilayer system.

9 General conclusions

In this thesis, the magnetic and structural properties of hard ferrites, strontium hexaferrite and cobalt ferrite have been investigated by different characterization techniques. These materials are of high interest due to their widespread use as permanent magnets, recording media and components in different electronic devices. The interaction of these ferrites with a magnetically soft layer has brought forward the understanding of the magnetic coupling regime experimented in this type of system as well as elucidated the interaction conditions needed to enable the improvement of magnetic properties, making these materials more competitive. The most important conclusions of this research are presented below.

1. **$SrFe_{12}O_{19}$ platelets**

   Strontium hexaferrite platelets grown by hydrothermal synthesis have been studied through microscopies, diffraction and spectroscopic techniques. These platelets showed a lateral size of microns and a thickness of tens of nanometers.

   The results pointed out an increase of the iron cations in tetrahedral sites with respect to the octahedral ones in the region near the platelet surface. This fact resulted in a lower net magnetic moment for the platelets than that strontium ferrite commercial powder since the iron in tetrahedral environments in the former presents spin moments aligned antiferromagnetically to the net magnetization.

   The platelets have displayed magnetic domains, which represented a magnetization perpendicular to the platelet plane. This is in good agreement with the c-axis direction determined due to the magnetization easy axis lies along it, which is also perpendicular to the platelet plane.

2. **SFO platelets with cobalt layer**

   With the aim to improve the SFO platelets magnetization, a layer of a magnetically soft material (cobalt) was deposited on top of them by MBE at room temperature.

   Specifically, a platelet with a single magnetic domain and its magnetic interaction with the cobalt overlayer was characterized by X-ray absorption techniques. These revealed a magnetization orientation in the sample plane for the soft layer and out-of-plane magnetization for the platelet. The lack of correlation between the magnetic domains of both phases indicated the absence of exchange coupling. Such non-correlation was interpreted as a consequence of the metallic layer shape anisotropy dominating over the external perpendicular field produced by the hexaferrite layer.

Micromagnetic simulations corroborated the experimental result and predicted that a low exchange-coupling strength between both layers should lead to an efficient alignment of the soft moments with the hard phase. This outcome gave rise to a new strategy of developing hard/soft systems since domain wall propagation is avoided.

3. SFO thin films and their interaction with cobalt layer

As previously observed for the platelet/metal system, coupling between the two phases to improve the hard/soft system magnetic properties is not easy to achieve. In this chapter, an attempt was made to promote the magnetostatic interaction between both layers by growing a strontium hexaferrite thin film with the magnetization direction within the plane to prevent the competition observed in the previous chapter and thus facilitate alignment with the magnetically soft layer.

$SrFe_{12}O_{19}$ films were grown by RF magnetron sputtering. The annealing step in air was required to obtain SFO. Indeed, the non-annealed SFO film presented a nanosized maghemite phase and likely a SrO amorphous oxide.

The net magnetization orientation for SFO thin films was adjusted in the sample plane, depositing at several sputtering powers with constant deposition times (and thus different thickness). These samples' characterization by spectroscopic and diffraction methods has demonstrated that the films are textured, and their c-axis orientation, and consequently their magnetization easy axis, changes with the sputtering power and the thickness. SFO films 360 nm thick grown at the highest power used (260 W) showed preferential in-plane magnetization.

On this thin film, the cobalt layer was grown by MBE to study the magnetic interaction with a soft magnetic layer. The bilayer analysis performed using XAS, and XMCD techniques showed the oxidation of some cobalt atoms in the interface with the SFO and the magnetic domains corresponding to each layer. The magnetization vector alignment was along the directions at 160° and 340° in the film plane for both layers. However, the magnetic domains in the two layers again were not correlated, implicating a lack of exchange-coupling between them. We suggested that the coincidence in the direction of the uniaxial easy axis is caused by structural coupling.

4. $CoFe_2O_4$ thin films

In this chapter, we have studied the properties of the cobalt ferrite ultrathin films (5 nm and 20 nm thick) grown by oxygen assisted molecular beam epitaxy on a Pt(111) single crystal with the particularity that the characterization was carried out *in-situ* under UHV conditions.

As-grown thin films presented a superparamagnetic/poorly crystalline state composed of a distribution of Fe^{3+} containing-aggregates of different sizes in the nanometer scale and a minor Fe^{2+} phase. The unexpected 1×1 LEED pattern for CFO suggested a $Fe_xCo_{1-x}O$ termination of the films. The thinner film presented higher magnetic ordering than the thicker sample, which was explained due to the lower deposition rate employed, allowing a cation distribution similar to canonical $CoFe_2O_4$.

Annealing in vacuum promoted an increase in particles size, resulting in the development of magnetic ordering at RT, although the annealing treatment has not entirely removed the superparamagnetic contribution. The iron in tetrahedral and octahedral sites ratios revealed cobalt ferrite formation after the annealing process achieving the thinner film a cation distribution close to that expected for a CFO inverse spinel after annealing in oxygen. Thus, the O-MBE process provided cobalt ferrite thin films using intermediate temperatures (up to 773 K), preventing the formation of different phases, island features, or dewetting phenomena.

5. CFO with iron-cobalt layer

An experimental system composed of cobalt ferrite (76 nm) and iron-cobalt layer (4 nm) layers showed a spring magnet behaviour in conditions where a rigid coupling was expected. So, the purpose of this section was to understand this interaction through micromagnetic simulations. These simulations reproduced such scenario using unrealistic values of exchange stiffness, magnetization saturation and exchange coupling. Considering that the simulations followed the accepted spring theory that does not include the domain wall propagation mechanism, the results evidenced the latter mechanism's importance in the hard/soft bilayer systems' spring magnet regime.

10 Conclusiones generales

En esta tesis se han investigado las propiedades magnéticas y estructurales de las ferritas duras, hexaferrita de estroncio y ferrita de cobalto, mediante diferentes técnicas de caracterización. Estos materiales son de gran interés debido a su amplio uso como imanes permanentes, soportes de grabación y componentes en diferentes dispositivos electrónicos. La interacción de estas ferritas con una capa magnéticamente blanda ha permitido avanzar en la comprensión del régimen de acoplamiento magnético experimentado en este tipo de sistemas, así como dilucidar las condiciones de interacción necesarias para permitir la mejora de las propiedades magnéticas, produciendo que estos materiales sean más competitivos. A continuación se presentan las conclusiones más importantes de esta investigación.

1. Plaquetas de $SrFe_{12}O_{19}$

Las plaquetas de hexaferrita de estroncio crecidas por síntesis hidrotermal se han estudiado mediante técnicas de microscopía, difracción y espectroscopia. Estas plaquetas mostraron un tamaño lateral de micras y un espesor de decenas de nanómetros.

Los resultados señalaron un aumento de los cationes de hierro en sitios tetraédricos con respecto a los sitios octaédricos en la región cercana a la superficie de la plaqueta. Este hecho dio lugar a un momento magnético neto menor para las plaquetas que el del polvo comercial de ferrita de estroncio, ya que el hierro en entornos tetraédricos en las primeras presenta momentos de espín alineados antiferromagnéticamente a la imanación neta.

Las plaquetas han exhibido dominios magnéticos que presentaban una imanación perpendicular al plano de la plaqueta. Esta evidencia está en concordancia con la dirección del eje c obtenida debido a que el eje fácil de imanación se encuentra a lo largo del mismo, siendo también perpendicular al plano de la plaqueta.

2. Plaquetas de SFO con una capa de cobalto

Con el objetivo de mejorar la imanación de las plaquetas de SFO, se depositó sobre ellas una capa de un material magnéticamente blando (cobalto) mediante epitaxia de haces moleculares a temperatura ambiente.

En concreto, se caracterizó una plaqueta con un único dominio magnético y su interacción magnética con la capa de cobalto mediante técnicas de absorción de rayos X. Éstas revelaron una orientación de la imanación en el plano de la muestra para la capa blanda y una imanación fuera del plano para la plaqueta. La falta de correlación entre los dominios magnéticos de ambas fases indicó la ausencia de acoplamiento de

intercambio. Dicha no correlación se interpretó como consecuencia a la superposición de la anisotropía de forma de la capa metálica sobre el campo perpendicular externo producido por la capa de hexaferrita.

Las simulaciones micromagnéticas corroboraron el resultado experimental y predijeron que una fuerza de acoplamiento de intercambio baja entre ambas capas debería conducir a una alineación eficiente de los momentos blandos con la fase dura. Este resultado impulsa una nueva estrategia de desarrollo de sistemas duros/blandos, ya que se evita la propagación de la pared de dominio.

3. Películas delgadas de SFO y su interacción con la capa de cobalto

Como se observó anteriormente para el sistema plaqueta/metal, el acoplamiento entre las dos fases para mejorar las propiedades magnéticas del sistema duro/blando no es fácil de conseguir. En este capítulo se ha intentado promover la interacción magnetostática entre ambas capas mediante el crecimiento de una lámina delgada de hexaferrita de estroncio con la dirección de imanación dentro del plano para evitar la competencia observada en el capítulo anterior y así facilitar el alineamiento con la capa magnéticamente blanda.

Las películas de $SrFe_{12}O_{19}$ se crecieron mediante pulverización catódica. El paso de calentamiento posterior en aire fue necesario para obtener SFO. De hecho, la película de SFO sin proceso térmico presentó una fase de maghemita de tamaño nanométrico junto probablemente un óxido amorfo de SrO.

La orientación de la imanación neta de las películas delgadas de SFO se ajustó en el plano de la muestra, depositando a varias potencias con tiempos de deposición constantes (y por lo tanto, con diferentes espesores). La caracterización de estas muestras mediante métodos espectroscópicos y de difracción ha demostrado que las películas están texturizadas, y que su orientación en el eje c, y en consecuencia su eje fácil de imanación, cambia con la potencia y el espesor. Las películas de SFO de 360 nm de espesor crecidas a la mayor potencia utilizada (260 W) mostraron una imanación preferente en el plano.

Sobre esta película delgada se hizo crecer la capa de cobalto por MBE para estudiar la interacción magnética con una capa magnética blanda. El análisis de la bicapa realizado mediante las técnicas XAS y XMCD mostró la oxidación de algunos átomos de cobalto en la interfaz con la lámina de SFO y los dominios magnéticos correspondientes a cada capa. La alineación del vector de imanación se produjo a lo largo de las direcciones a 160° y 340° en el plano de la película para ambas capas. Sin embargo, los dominios magnéticos de las dos capas de nuevo no estaban correlacionados, lo que implicó una falta de acoplamiento de intercambio entre ellos. Sugerimos que la coincidencia en la dirección del eje fácil uniaxial se debe principalmente a un acoplamiento estructural.

4. Películas delgadas de $CoFe_2O_4$

En este capítulo hemos estudiado las propiedades de las películas ultra-finas de ferrita de cobalto (de 5 nm y 20 nm de espesor) crecidas por epitaxia de haz molecular asistida por oxígeno sobre un monocristal de Pt(111) con la particularidad de que la caracterización se realizó *in-situ* en condiciones de UHV.

Las películas delgadas recién crecidas presentaron un estado superparamagnético/pobremente cristalino compuesto por una distribución de agregados de diferentes tamaños en la escala nanométrica formados por Fe^{3+} y una fase menor de Fe^{2+}. El inesperado patrón de LEED 1×1 para el CFO sugirió una terminación Fe_xCo_{1-x} de las películas. La película más delgada presentó un ordenamiento magnético mayor que la muestra más gruesa, lo que se discutió en base a la menor tasa de deposición empleada. Esta tasa permitió una distribución de cationes similar a la del $CoFe_2O_4$ canónico.

El calentamiento en vacío promovió un aumento del tamaño de las partículas, lo que dio lugar al desarrollo del ordenamiento magnético a temperatura ambiente. Sin embargo, este tratamiento no eliminó por completo la contribución superparamagnética. Las proporciones de hierro en sitios tetraédricos y octaédricos revelaron la formación de ferrita de cobalto tras el proceso térmico, logrando la película más fina una distribución de cationes cercana a la esperada para una espinela inversa de CFO tras el calentamiento en atmósfera de oxígeno. Por lo tanto, el proceso O-MBE proporcionó películas delgadas de ferrita de cobalto utilizando temperaturas intermedias (hasta 773 K), evitando la formación de diferentes fases, crecimiento en forma de islas o fenómenos de deshidratación.

5. CFO con capa de hierro-cobalto

Un sistema experimental compuesto por capas de ferrita de cobalto (76 nm) y de aleación hierro-cobalto (4 nm) mostró un comportamiento de imán tipo “muelle” en condiciones en las que se esperaba un acoplamiento tipo "rígido". Por ello, el objetivo de esta sección era comprender esta interacción mediante simulaciones micromagnéticas. Estas simulaciones reprodujeron dicho escenario utilizando valores poco realistas de rigidez de intercambio, imanación de saturación y acoplamiento de intercambio. Teniendo en cuenta que las simulaciones siguieron la teoría aceptada que no incluye el mecanismo de propagación de la pared de dominio, los resultados evidenciaron la importancia de este último mecanismo en el régimen de “muelles” magnéticos de los sistemas bicapa duros/blandos.

A List of acronyms and abbreviations

SFO Strontium Hexaferrite ($SrFe_{12}O_{19}$)

MBE Molecular Beam Epitaxy

XAS X-ray Absorption Spectroscopy

XMCD X-ray magnetic Circular Dichroism

PEEM Photoemission Electron Microscopy

CFO Cobalt Ferrite ($CoFe_2O_4$)

FeCo Iron-Cobalt alloy

RE Rare Earth

BH$_{Max}$ Energy Product

H$_c$ Coercive Field

B$_r$ Remanence Magnetization

LEEM Low Energy Electron Microscopy

PVD Physical Vapour Deposition

RF Radio Frequency

DC Direct Current

HV High Voltage

UHV Ultra High Vacuum

I$_{Fil}$ Filament Current

I$_{Emiss}$ Emission Current

O-MBE Oxygen Assisted-MBE

TEM Transmission Electron Microscopy

SAED Selected Area Electron Diffraction

TXM Transmission X-ray Microscopy

FZP Fresnel Zone Plate

XRD X-Ray Diffraction

XPS X-ray Photoelectron Spectroscopy

VSM Vibrating Sample magnetometer

RBS Rutherford Backscattering Spectrometry

AFM Atomic Force Microscopy

AES Auger Spectroscopy

LEED Low Energy Electron Diffraction

STM Scanning Tunneling Microscopy

f Recoilless Free Fraction

Γ Linewidth

$\mathbf{K}_B$ Boltzmann Constant

δ Isomer Shift

$\Delta\mathbf{E}_Q$ Quadrupole Splitting

ε Quadrupole Shift

EFG Electric Field Gradient

μ_B Bohr magneton

H Hyperfine Magnetic Field

CEMS Conversion Electron Spectroscopy

ILEEMS Integral Low Energy Electron Mössbauer Spectroscopy

TEY Total Electron Yield

IMFP Inelastic Mean Free Path

eV Electronvolt

$\mathbf{M}$ Magnetization

$\mu^{+/-}$ Positive or Negative Helicity Light

$\mathbf{m}_{orb}$ Orbital Magnetic Moment

$\mathbf{m}_{spin}$ Spin Magnetic Moment

$\mathbf{N}_h$ Number of holes

$\mathbf{T}_z$ Dipole operator

$\mathbf{M}_s$ Saturation Magnetization

$\mathbf{A}_s$ Exchange Stiffness Constant

$\mathbf{K}_u$ Uniaxial Magnetocrystalline Anisotropy Constant

$\mathbf{K}_c$ Cubic Magnetocrystalline Anisotropy Constant

κ Interlayer Exchange Coupling Strength

$\mathbf{H}_{eff}$ Effective Magnetic Field

Block S Spinel Block

Block R Rock-salt Block

$\mathbf{K}_c$ Cubic Magnetocrystalline Anisotropy Constant

$\mathbf{T}_c$ Curie Temperature

$\mathbf{T}_N$ Neil Temperature

Å Amgstron

$\mathbf{U}_{ij}$ Exchange Energy

$\mathbf{J}_{ij}$ Exchange Integral

$\mathbf{D}_c$ Critical diameter

σ_w **or** $\mathbf{D}_w$ Domain wall

a Lattice parameter

c Lattice parameter

P Pressure

RT Room Temperature

LT Low Temperature

Oh Octahedral site

Td Tetrahedral site

Bipy Bipyramidal site

DFT Density Functional Theory

PDOS Projected Density Of States

fcc Face Centered Cubic

hcp Hexagonal Close Packed

$\mathbf{E}_{Zeeman}$ Zeeman Energy

$\mathbf{L}_{ex}$ Exchange Length

RMS Root Mean Square Roughness

λ_s Magnetostriction Constant

$\mathbf{T}_B$ Blocking Temperature

$\mathbf{H}_{AVG}$ Average Field Distribution

DWP Domain Wall Propagation

$\mathbf{H}_n$ Nucleation Field

APB Antiphase Boundaries

t Thickness

B List of publications

1. G. D. Soria, K. Freindl, J. E. Prieto, A. Quesada, J. de la Figuera, N. Spiridis, J. Korecki, and J. F. Marco, "Growth and characterization of ultrathin cobalt ferrite films on Pt(111)", in preparation.

2. G. D. Soria, C. Granados-Miralles, A. Mandziak, P. Jenus, M. Saura-Múzquiz, M. Christensen, M. Foerster, L. Aballe, J. F. Fernández, J.d.l. Figuera, and A. Quesada, "Uncorrelated magnetic domains in decoupled $SrFe_{12}O_{19}$/Co hard/soft bilayers", Journal of Physics D: Applied Physics, vol. 54, no. 5, p. 054003, 2020.

3. A. Mandziak, G. D. Soria, J. E. Prieto, M. Foerster, J. d. l. Figuera, and L. Aballe, "Different spin axis orientation and large antiferromagnetic domains in Fe-doped NiO/Ru(0001) epitaxial films", Nanoscale, vol. 12, pp. 21225–21233, 2020.

4. G. D. Soria, J. F. Marco, A. Mandziak, S. Sánchez-Cortés, M. Sánchez-Arenillas, J. E. Prieto, J. Dávalos, M. Foerster, L. Aballe, J. López-Sánchez, J. C. Guzmán-Mínguez, C. Granados-Miralles, J. d. l. Figuera, and A. Quesada, "Influence of the growth conditions on the magnetism of $SrFe_{12}O_{19}$ thin films and the behavior of Co/$SrFe_{12}O_{19}$ bilayers", Journal of Physics D: Applied Physics, vol. 53, p. 344002, 2020.

5. S. Ruiz-Gómez, A. Mandziak, J. E. Prieto, M. Aristu, E. M. Trapero, G. D. Soria, A. Quesada, M. Foerster, L. Aballe, and J. de la Figuera, "A real-time XAS PEEM study of the growth of cobalt iron oxide on Ru(0001)", The Journal of Chemical Physics, vol. 152, p. 074704, 2020.

6. A. Mandziak, G. D. Soria, J. E. Prieto, P. Prieto, C. Granados-Miralles, A. Quesada, M. Foerster, L. Aballe, and J. de la Figuera, "Tuning the Néel temperature in an antiferromagnet: the case of $Ni_xCo_{1-x}O$ microstructures", Scientific Reports, vol. 9, p. 13584, 2019.

7. G. D. Soria, P. Jenus, J. F. Marco, A. Mandziak, M. Sanchez-Arenillas, F. Moutinho, J. E. Prieto, P. Prieto, J. Cerdá, C. Tejera-Centeno, S. Gallego, M. Foerster, L. Aballe, M. Valvidares, H. B. Vasili, E. Pereiro, A. Quesada, and J. de la Figuera, "Strontium hexaferrite platelets: a comprehensive soft X-ray absorption and Mössbauer spectroscopy study", Scientific Reports, vol. 9, no. 1, p. 11777, 2019.

8. A. Quesada, G. D. Soria, L. Pascual, A. M. Aragón, P. Marín, C. Granados-Miralles, M. Foerster, L. Aballe, J. E. Prieto, J. de la Figuera, J. F. Fernández, and P. Prieto, "Exchange-spring behavior below the exchange length in hard-soft bilayers in multidomain configurations", Physical Review B, vol. 98, no. 21, p. 214435, 2018.

9. A. Mandziak, J. de la Figuera, S. Ruiz-Gómez, G. D. Soria, L. Pérez, P. Prieto, A. Quesada, M. Foerster, and L. Aballe, “Structure and magnetism of ultrathin nickel-iron oxides grown on Ru(0001) by high-temperature oxygen-assisted molecular beam epitaxy", Scientific Reports, vol. 8, p. 17980, 2018.

10. G. D. Soria, J. R. Espinosa, J. Ramirez, C. Valeriani, C. Vega, and E. Sanz, “A simulation study of homogeneous ice nucleation in supercooled salty water", The Journal of Chemical Physics, vol. 148, p. 222811, 2018.

11. J. R. Espinosa, G. D. Soria, J. Ramirez, C. Valeriani, C. Vega, and E. Sanz, “Role of Salt, Pressure, and Water Activity on Homogeneous Ice Nucleation", The Journal of Physical Chemistry Letters, vol. 8, pp. 4486–4491, 2017.

Bibliography

[1] A. Basak, *Permanent-magnet DC linear motors*. Clarendon Press, 1996.

[2] O. Gutfleisch, M. A. Willard, E. Brück, C. H. Chen, S. G. Sankar, and J. P. Liu, "Magnetic materials and devices for the 21st century: stronger, lighter, and more energy efficient," *Advanced Materials*, vol. 23, no. 7, pp. 821–842, 2011.

[3] S. Sugimoto, "Current status and recent topics of rare-earth permanent magnets," *Journal of Physics D: Applied Physics*, vol. 44, no. 6, p. 064001, 2011.

[4] J. M. D. Coey, "Permanent magnetism," *Solid State Communications*, vol. 102, no. 2, pp. 101–105, 1997.

[5] J. Coey, "Permanent magnets: Plugging the gap," *Scripta Materialia*, vol. 67, no. 6, pp. 524–529, 2012.

[6] B. D. Cullity and C. D. Graham, "Hard magnetic materials," in *Introduction to Magnetic Materials*, pp. 477–504, 2008.

[7] K. H. J. Buschow and F. R. de Boer, "Permanent magnets," in *Physics of Magnetism and Magnetic Materials*, pp. 105–129, 2003.

[8] P. Jenus, A. Ucakar, S. Repse, C. Sangregorio, M. Petrecca, M. Albino, R. Cabassi, C. de Julian Fernandez, and B. Belec, "Magnetic performance of $SrFe_{12}O_{19}$-$Zn_{0.2}Fe_{2.8}O_4$ hybrid magnets prepared by Spark Plasma Sintering," *Journal of Physics D: Applied Physics*, 2021.

[9] O. Gutfleisch, "Controlling the properties of high energy density permanent magnetic materials by different processing routes," *Journal of Physics D: Applied Physics*, vol. 33, no. 17, pp. R157–R172, 2000.

[10] N. Haque, A. Hughes, S. Lim, and C. Vernon, "Rare earth elements: Overview of mining, mineralogy, uses, sustainability and environmental impact," *Resources*, vol. 3, no. 4, pp. 614–635, 2014.

[11] V. Balaram, "Rare earth elements: A review of applications, occurrence, exploration, analysis, recycling, and environmental impact," *Geoscience Frontiers*, vol. 10, no. 4, pp. 1285–1303, 2019.

[12] S. H. Ali, "Social and environmental impact of the rare earth industries," *Resources*, vol. 3, no. 1, pp. 123–134, 2014.

[13] J. Smit and H. Wijn, "Ferrites, Philips technical library," *Eindhoven, The Netherlands*, vol. 278, 1959.

[14] J. Went, G. Rathenau, G. E.W, and G. Van Oosterhout, "Ferroxdure, a class of new permanent magnet materials," *Philips Technical Review*, vol. 13, no. 7, p. 194–208, 1952.

[15] V. A. M. Brabers, "Chapter 3 Progress in spinel ferrite research," in *Handbook of Magnetic Materials*, vol. 8, pp. 189–324, 1995.

[16] J. L. Snoek, *New developments in ferromagnetic materials: with introductory chapters on the statics and the dynamics of ferromagnetism.* No. 19, Elsevier Publishing Company, 1947.

[17] A. Goldman, *Modern Ferrite Technology.* Springer, 2 ed., 2006.

[18] F. Kools, "Hard magnetic ferrites," in *Concise Encyclopedia of Advanced Ceramic Materials*, pp. 200–206, 1991.

[19] E. E. Fullerton, J. S. Jiang, M. Grimsditch, C. H. Sowers, and S. D. Bader, "Exchange-spring behavior in epitaxial hard/soft magnetic bilayers," *Physical Review B*, vol. 58, no. 18, pp. 12193–12200, 1998.

[20] G. E. Fish, "Soft magnetic materials," *Proceedings of the IEEE*, vol. 78, no. 6, pp. 947–972, 1990.

[21] L. H. Lewis and F. Jiménez-Villacorta, "Perspectives on Permanent Magnetic Materials for Energy Conversion and Power Generation," *Metallurgical and Materials Transactions A*, vol. 44, no. 1, pp. 2–20, 2013.

[22] A. Quesada, C. Granados-Miralles, A. López-Ortega, S. Erokhin, E. Lottini, J. Pedrosa, A. Bollero, A. M. Aragón, F. Rubio-Marcos, M. Stingaciu, G. Bertoni, C. d. J. Fernández, C. Sangregorio, J. F. Fernández, D. Berkov, and M. Christensen, "Energy product enhancement in imperfectly exchange-coupled nanocomposite magnets," *Advanced Electronic Materials*, vol. 2, no. 4, p. 1500365, 2016.

[23] G. C. Hadjipanayis, "Nanophase hard magnets," *Journal of Magnetism and Magnetic Materials*, vol. 200, no. 1, pp. 373–391, 1999.

[24] A. López-Ortega, M. Estrader, G. Salazar-Alvarez, A. G. Roca, and J. Nogués, "Applications of exchange coupled bi-magnetic hard/soft and soft/hard magnetic core/shell nanoparticles," *Physics Reports*, vol. 553, pp. 1–32, 2015.

[25] O. Masala, D. Hoffman, N. Sundaram, K. Page, T. Proffen, G. Lawes, and R. Seshadri, "Preparation of magnetic spinel ferrite core/shell nanoparticles: Soft ferrites on hard ferrites and vice versa," *Solid State Sciences*, vol. 8, no. 9, pp. 1015–1022, 2006.

[26] Y.-M. Kang, J.-B. Park, Y. J. Kang, and K. Ahn, "Magnetic properties of M-type Sr hexaferrite/Fe bilayers," *Thin Solid Films*, vol. 594, pp. 40–44, Nov. 2015.

[27] S. M. Parhofer, J. Wecker, C. Kuhrt, G. Gieres, and L. Schultz, "Remanence enhancement due to exchange coupling in multilayers of hard- and softmagnetic phases," *IEEE Transactions on Magnetics*, vol. 32, no. 5, pp. 4437–4439, 1996.

[28] C. d. J. Fernandez, C. Sangregorio, J. d. l. Figuera, B. Belec, D. Makovec, and A. Quesada, "Topical review: Progress and prospects of hard hexaferrites for permanent magnet applications," *Journal of Physics D: Applied Physics*, 2020.

[29] S. Sabet, A. Moradabadi, S. Gorji, M. Yi, Q. Gong, M. H. Fawey, E. Hildebrandt, D. Wang, H. Zhang, B.-X. Xu, C. Kübel, and L. Alff, "Impact of interface structure on magnetic exchange coupling in MnBi/Fe_xCo_{1-x} bilayers," *Physical Review B*, vol. 98, no. 17, p. 174440, 2018.

[30] E. E. Fullerton, J. S. Jiang, and S. D. Bader, "Hard/soft magnetic heterostructures: model exchange-spring magnets," *Journal of Magnetism and Magnetic Materials*, vol. 200, no. 1, pp. 392–404, 1999.

[31] G. Asti, M. Ghidini, R. Pellicelli, C. Pernechele, M. Solzi, F. Albertini, F. Casoli, S. Fabbrici, and L. Pareti, "Magnetic phase diagram and demagnetization processes in perpendicular exchange-spring multilayers," *Physical Review B*, vol. 73, no. 9, p. 094406, 2006.

[32] A. J. Zambano, H. Oguchi, I. Takeuchi, Y. Choi, J. S. Jiang, J. P. Liu, S. E. Lofland, D. Josell, and L. A. Bendersky, "Dependence of exchange coupling interaction on micromagnetic constants in hard/soft magnetic bilayer systems," *Physical Review B*, vol. 75, no. 14, p. 144429, 2007.

[33] J. S. Jiang, J. E. Pearson, Z. Y. Liu, B. Kabius, S. Trasobares, D. J. Miller, S. D. Bader, D. R. Lee, D. Haskel, G. Srajer, and J. P. Liu, "A new approach for improving exchange-spring magnets," *Journal of Applied Physics*, vol. 97, p. 10K311, May 2005.

[34] J. S. Jiang and S. D. Bader, "Magnetic reversal in thin film exchange-spring magnets," *Scripta Materialia*, vol. 47, no. 8, pp. 563–568, 2002.

[35] G. Asti, M. Solzi, M. Ghidini, and F. M. Neri, "Micromagnetic analysis of exchange-coupled hard-soft planar nanocomposites," *Physical Review B*, vol. 69, no. 17, p. 174401, 2004.

[36] D. M. Mattox, "Chapter 1 - Introduction," in *Handbook of Physical Vapor Deposition (PVD) Processing*, pp. 1–24, William Andrew Publishing, second edition ed., 2010.

[37] P. J. Kelly and R. D. Arnell, "Magnetron sputtering: a review of recent developments and applications," *Vacuum*, vol. 56, no. 3, pp. 159–172, 2000.

[38] S. Swann, "Magnetron sputtering," *Physics in Technology*, vol. 19, no. 2, pp. 67–75, 1988.

[39] K. V. Madhuri, "10 - Thermal protection coatings of metal oxide powders," in *Metal Oxide Powder Technologies*, Metal Oxides, pp. 209–231, Elsevier, 2020.

[40] D. A. Glocker, S. Shah, and W. Westwood, *Handbook of Thin Film Process Technology*. No. 1-2, Institute of Physics Publication, 1995.

[41] J. M. D. Coey, M. Venkatesan, and H. Xu, "Introduction to Magnetic Oxides," in *Functional Metal Oxides*, pp. 1–49, John Wiley & Sons, Ltd, 2013.

[42] B. R. Acharya, S. Prasad, N. Venkataramani, S. N. Shringi, and R. Krishnan, "The effect of deposition and annealing conditions on textured growth of sputter-deposited strontium ferrite films on different substrates," *Journal of Applied Physics*, vol. 79, no. 1, pp. 478–484, 1996.

[43] A. Y. Cho and J. R. Arthur, "Molecular beam epitaxy," *Progress in Solid State Chemistry*, vol. 10, pp. 157–191, 1975.

[44] M. A. Herman and H. Sitter, *Molecular Beam Epitaxy: Fundamentals and Current Status*. Springer Series in Materials Science, 2 ed., 1996.

[45] J. R. Arthur, "Molecular beam epitaxy," *Surface Science*, vol. 500, no. 1, pp. 189–217, 2002.

[46] B. Fultz and J. M. Howe, *Transmission electron microscopy and diffractometry of materials*. Springer Science & Business Media, 2012.

[47] F. Adams and C. Barbante, "Chapter 6 - X-Ray Imaging," in *Comprehensive Analytical Chemistry*, vol. 69 of *Chemical Imaging Analysis*, pp. 213–268, Elsevier, 2015.

[48] B. D. Cullity, *Elements of x-ray diffraction*. Addison-Wesley Publishing Company, Inc., 1978.

[49] J. F. Watts, "X-ray photoelectron spectroscopy," *Vacuum*, vol. 45, no. 6, pp. 653–671, 1994.

[50] B. D. Cullity and C. D. Graham, "Experimental methods," in *Introduction to Magnetic Materials*, pp. 23–86, John Wiley & Sons, Ltd, 2008.

[51] S. Foner, "Versatile and sensitive vibrating-sample magnetometer," *Review of Scientific Instruments*, vol. 30, no. 7, pp. 548–557, 1959.

[52] H. Lüth, *Surfaces and interfaces of solid materials*. Springer Study Edition, 3 ed., 1995.

[53] H. H. Telle, A. G. Ureña, and R. J. Donovan, *Laser chemistry: spectroscopy, dynamics and applications*. John Wiley & Sons, 2007.

[54] H. J. Butler, L. Ashton, B. Bird, G. Cinque, K. Curtis, J. Dorney, K. Esmonde-White, N. J. Fullwood, B. Gardner, P. L. Martin-Hirsch, M. J. Walsh, M. R. McAinsh,

N. Stone, and F. L. Martin, "Using Raman spectroscopy to characterize biological materials," *Nature Protocols*, vol. 11, no. 4, pp. 664–687, 2016.

[55] B. Voigtlaender, *Scanning probe microscopy: Atomic force microscopy and Scanning tunneling microscopy*. Nanoscience and technology, Springer-Verlag, 2015.

[56] V. D. Lyles, W. K. Serem, J.-J. Yu, and J. C. Garno, "Surface Characterization Using Atomic Force Microscopy (AFM) in Liquid Environments," in *Surface Science Techniques*, pp. 599–620, Springer, 2013.

[57] L. E. Davis, *Handbook of Auger electron spectroscopy: a reference book of standard data for identification and interpretation of Auger electron spectroscopy data*. Perkin-Emer Corp., 1979.

[58] J. B. Pendry, "Low-Energy Electron Diffraction," in *Interaction of Atoms and Molecules with Solid Surfaces*, Physics of Solids and Liquids, pp. 201–211, 1990.

[59] G. Binnig and H. Rohrer, "Scanning tunneling microscopy," *Surface Science*, vol. 126, no. 1, pp. 236–244, 1983.

[60] N. N. Greenwood and T. C. Gibb, *Mössbauer Spectroscopy*. Dordrecht: Springer Netherlands, 1971.

[61] W. Keune, "Application of Mössbauer spectroscopy in magnetism," *Hyperfine Interactions*, vol. 204, no. 1, pp. 13–45, 2012.

[62] G. J. Long, ed., *Mössbauer Spectroscopy Applied to Inorganic Chemistry*. Modern Inorganic Chemistry, Springer US, 1984.

[63] Y. Yoshida and G. Langouche, eds., *Mössbauer Spectroscopy: Tutorial Book*. Berlin Heidelberg: Springer-Verlag, 2013.

[64] R. L. Mössbauer, "Kernresonanzfluoreszenz von Gammastrahlung in Ir191," *Zeitschrift für Physik*, vol. 151, no. 2, pp. 124–143, 1958.

[65] J. R. Gancedo, M. Gracia, and J. F. Marco, "Practical aspects of Mössbauer spectroscopy instrumentation," *Hyperfine Interactions*, vol. 83, no. 1, pp. 71–78, 1994.

[66] F. Salvat and J. Parellada, "Theory of conversion electron Mössbauer spectroscopy (CEMS)," *Nuclear Instruments and Methods in Physics Research Section B: Beam Interactions with Materials and Atoms*, vol. 1, no. 1, pp. 70–84, 1984.

[67] J. R. Gancedo, M. Gracia, and J. F. Marco, "Cems methodology," *Hyperfine Interactions*, vol. 66, no. 1, pp. 83–93, 1991.

[68] J. F. Marco, J. R. Gancedo, M. Monti, and J. d. l. Figuera, "Mössbauer spectroscopy and surface analysis," in *Mössbauer Spectroscopy*, pp. 455–469, 2013.

[69] N. Spiridis, K. Freindl, J. Wojas, N. Kwiatek, E. Madej, D. Wilgocka-Ślęzak,

P. Dróżdż, T. Ślęzak, and J. Korecki, "Superstructures on epitaxial $Fe_3O_4(111)$ films: Biphase formation versus the degree of reduction," *Journal of Physical Chemistry C*, vol. 123, no. 7, pp. 4204–4216, 2019.

[70] F. d. Groot and A. Kotani, *Core Level Spectroscopy of Solids*. CRC Press, 2008.

[71] G. van der Laan and A. I. Figueroa, "X-ray magnetic circular dichroism—A versatile tool to study magnetism," *Coordination Chemistry Reviews*, vol. 277-278, pp. 95–129, 2014.

[72] C. C. Chusuei and D. W. Goodman, "X-Ray Photoelectron Spectroscopy," in *Encyclopedia of Physical Science and Technology (Third Edition)*, pp. 921–938, Academic Press, 2003.

[73] F. Jiménez-Villacorta, C. Prieto, Y. Huttel, N. D. Telling, and G. van der Laan, "X-ray magnetic circular dichroism study of the blocking process in nanostructured iron-iron oxide core-shell systems," *Physical Review B*, vol. 84, no. 17, p. 172404, 2011.

[74] L. Aballe, M. Foerster, E. Pellegrin, J. Nicolas, and S. Ferrer, "The alba spectroscopic leem-peem experimental station: layout and performance," *Journal of Synchrotron Radiation*, vol. 22, no. 3, pp. 745–752, 2015.

[75] J. Stöhr, "Exploring the microscopic origin of magnetic anisotropies with X-ray magnetic circular dichroism (XMCD) spectroscopy," *Journal of Magnetism and Magnetic Materials*, vol. 200, no. 1, pp. 470–497, 1999.

[76] T. Funk, A. Deb, S. J. George, H. Wang, and S. P. Cramer, "X-ray magnetic circular dichroism—a high energy probe of magnetic properties," *Coordination Chemistry Reviews*, vol. 249, no. 1, pp. 3–30, 2005.

[77] E. Bauer, *Surface Microscopy with Low Energy Electrons*. Springer, 2014.

[78] J. Stöhr and H. C. Siegmann, *Magnetism: From Fundamentals to Nanoscale Dynamics*. Springer Series in Solid-State Sciences, 2006.

[79] P. Fischer, "Magnetic Imaging with Polarized Soft X-rays," in *Magnetism and Synchrotron Radiation: Towards the Fourth Generation Light Sources*, Springer Proceedings in Physics, pp. 155–183, 2013.

[80] W. Kuch and C. M. Schneider, "Magnetic dichroism in valence band photoemission," *Reports on Progress in Physics*, vol. 64, no. 2, p. 147, 2001.

[81] A. Barla, J. Nicolás, D. Cocco, S. M. Valvidares, J. Herrero-Martín, P. Gargiani, J. Moldes, C. Ruget, E. Pellegrin, and S. Ferrer, "Design and performance of boreas, the beamline for resonant x-ray absorption and scattering experiments at the alba synchrotron light source," *Journal of Synchrotron Radiation*, vol. 23, no. 6, pp. 1507–1517, 2016.

[82] C. T. Chen, Y. U. Idzerda, H.-J. Lin, N. V. Smith, G. Meigs, E. Chaban, G. H. Ho, E. Pellegrin, and F. Sette, "Experimental Confirmation of the X-Ray Magnetic Circular Dichroism Sum Rules for Iron and Cobalt," *Physical Review Letters*, vol. 75, no. 1, pp. 152–155, 1995.

[83] S. Günther, B. Kaulich, L. Gregoratti, and M. Kiskinova, "Photoelectron microscopy and applications in surface and materials science," *Progress in Surface Science*, vol. 70, no. 4, pp. 187–260, 2002.

[84] T. Schmidt, S. Heun, J. Slezak, J. Diaz, K. C. Prince, G. Lilienkamp, and E. Bauer, "SPELEEM: Combining LEEM and Spectroscopic Imaging," *Surface Review and Letters*, vol. 05, no. 06, pp. 1287–1296, 1998.

[85] G. Bracco and B. Holst, eds., *Surface Science Techniques*. Springer Series in Surface Sciences, 2013.

[86] A. Vansteenkiste, J. Leliaert, M. Dvornik, M. Helsen, F. Garcia-Sanchez, and B. Van Waeyenberge, "The design and verification of MuMax3," *AIP Advances*, vol. 4, p. 107133, 2014.

[87] T. L. Gilbert, "A lagrangian formulation of the gyromagnetic equation of the magnetization field," *Physical Review D*, vol. 100, p. 1243, 1955.

[88] L. D. Buda-Prejbeanu, *Modelling of spintronic devices: from basic operation mechanisms toward optimization*. Habilitation à diriger des recherches, Communauté Université Grenoble Alpes, 2017.

[89] V. Adelsköld, "X-ray studies on magneto-plumbite, PbO. $6Fe_2O_3$, and other substances resembling "beta-alumina", Na_2O. $11Al_2O_3$," *Arkiv for Kemi Mineralogioch Geologi, Series A-12*, vol. 29, pp. 1–9, 1938.

[90] H. Kojima, "Chapter 5 Fundamental properties of hexagonal ferrites with magnetoplumbite structure," in *Handbook of Ferromagnetic Materials*, vol. 3, pp. 305–391, Elsevier, 1982.

[91] R. Pullar, *Hexagonal Ferrites: A Review of the Synthesis, Properties and Applications of Hexaferrite Ceramics*, vol. 57. 2012.

[92] J. Kreisel, H. Vincent, F. Tasset, M. Paté, and J. P. Ganne, "An investigation of the magnetic anisotropy change in $BaFe_{12-2x}Ti_xCo_xO_19$ single crystals," *Journal of Magnetism and Magnetic Materials*, vol. 224, no. 1, pp. 17–29, 2001.

[93] K. Momma and F. Izumi, "*VESTA 3* for three-dimensional visualization of crystal, volumetric and morphology data," *Journal of Applied Crystallography*, vol. 44, no. 6, pp. 1272–1276, 2011.

[94] W. Heisenberg, "Mehrkörperproblem und Resonanz in der Quantenmechanik," *Zeitschrift für Physik*, vol. 38, no. 6, pp. 411–426, 1926.

[95] P. A. M. Dirac and R. H. Fowler, "On the theory of quantum mechanics," *Proceedings of the Royal Society of London. Series A, Containing Papers of a Mathematical and Physical Character*, vol. 112, no. 762, pp. 661–677, 1926.

[96] E. Gorter, *Saturation magnetization and crystal chemistry of ferrimagnetic oxides*. PhD thesis, 1954.

[97] C. Tejera-Centeno, S. Gallego, and J. I. Cerdá, "An ab initio study of the magnetic properties of strontium hexaferrite," *Scientific Reports*, vol. 11, no. 1, p. 1964, 2021.

[98] A. Grill and F. Haberey, "Effect of diamagnetic substitutions in BaFe12O19 on the magnetic properties," *Applied physics*, vol. 3, no. 2, pp. 131–134, 1974.

[99] J. M. D. Coey, *Magnetism and Magnetic Materials*. Cambridge: Cambridge University Press, 2010.

[100] F. X. N. M. Kools, *Science and technology of ferrite magnets : modelling of coercivity and grain growth inhibition*. PhD thesis, 2003.

[101] G. Bertotti, "Chapter 5 - Exchange and Anisotropy," in *Hysteresis in Magnetism*, pp. 129–162, Academic Press, 1998.

[102] F. Kools and P. J. v. d. Valk, "Ferrites," in *Kirk-Othmer Encyclopedia of Chemical Technology*, 2004.

[103] F. Hellman in *Encyclopedia of Materials: Science and Technology*, pp. 4761–4767, Elsevier, 2001.

[104] E. F. Bertaut, A. Deschamps, R. Pauthenet, and S. Pickart, "Substitution dans les hexaferrites de l'ion Fe^{3+} par Al^{3+}, Ga^{3+}, Cr^{3+}," *Journal de Physique et le Radium*, vol. 20, no. 2-3, pp. 404–408, 1959.

[105] L. Jahn and H. G. Müller, "The Coercivity of Hard Ferrite Single Crystals," *physica status solidi (b)*, vol. 35, no. 2, pp. 723–730, 1969.

[106] C. Zener, "Classical Theory of the Temperature Dependence of Magnetic Anisotropy Energy," *Physical Review*, vol. 96, no. 5, pp. 1335–1337, 1954.

[107] G. Herzer, "Grain size dependence of coercivity and permeability in nanocrystalline ferromagnets," *IEEE Transactions on Magnetics*, vol. 26, no. 5, pp. 1397–1402, 1990.

[108] A. Verma, O. Pandey, and P. Sharma, "Strontium ferrite permanent magnet-An overview," *Indian Journal of Engineering Materials Sciences*, vol. 7, no. 5-6, 2000.

[109] M. Sugimoto, "The Past, Present, and Future of Ferrites," *Journal of the American Ceramic Society*, vol. 82, no. 2, pp. 269–280, 1999.

[110] D. Y. Chen, Y. Y. Meng, D. C. Zeng, Z. W. Liu, H. Y. Yu, and X. C. Zhong, "CTAB-

assisted low-temperature synthesis of $SrFe_{12}O_{19}$ ultrathin hexagonal platelets and its formation mechanism," *Materials Letters*, vol. 76, pp. 84–86, 2012.

[111] M. M. Hessien, M. M. Rashad, and K. El-Barawy, "Controlling the composition and magnetic properties of strontium hexaferrite synthesized by co-precipitation method," *Journal of Magnetism and Magnetic Materials*, vol. 320, no. 3, pp. 336–343, 2008.

[112] E. Kiani, A. S. H. Rozatian, and M. H. Yousefi, "Synthesis and characterization of $SrFe_{12}O_{19}$ nanoparticles produced by a low-temperature solid-state reaction method," *Journal of Materials Science: Materials in Electronics*, vol. 24, no. 7, pp. 2485–2492, 2013.

[113] D. Chen, Y. Meng, K. H. Gandha, D. Zeng, H. Yu, and J. Ping Liu, "Morphology control of hexagonal strontium ferrite micro/nano-crystals," *AIP Advances*, vol. 7, no. 5, p. 056214, 2017.

[114] A. Ghasemi and A. Morisako, "Structural and electromagnetic characteristics of substituted strontium hexaferrite nanoparticles," *Journal of Magnetism and Magnetic Materials*, vol. 320, no. 6, pp. 1167–1172, 2008.

[115] A. Z. Eikeland, M. Stingaciu, H. A. Mamakhel, M. Saura-Múzquiz, and M. Christensen, "Enhancement of magnetic properties through morphology control of $SrFe_{12}O_{19}$ nanocrystallites," *Scientific Reports*, pp. 1–9, 2018.

[116] S. Ketov, E. Lopatina, T. Bulatov, Y. Yagodkin, and V. Menushenkov, "Effect of milling in various media and annealing on the structure and magnetic properties of strontium hexaferrite powder," *Solid State Phenomena*, vol. 190, pp. 183–187, 2012.

[117] A. Baykal, M. S. Toprak, Z. Durmus, and H. Sozeri, "Hydrothermal synthesis of $SrFe_{12}O_{19}$ and its haracterization," *Journal of Superconductivity and Novel Magnetism*, vol. 25, no. 6, pp. 2081–2085, 2012.

[118] A. Xia, C. Zuo, L. Chen, C. Jin, and Y. Lv, "Hexagonal $SrFe_{12}O_{19}$ ferrites: Hydrothermal synthesis and their sintering properties," *Journal of Magnetism and Magnetic Materials*, vol. 332, pp. 186–191, 2013.

[119] T. Zhang, X. Peng, J. Li, Y. Yang, J. Xu, P. Wang, D. Jin, H. Jin, B. Hong, X. Wang, and H. Ge, "Platelet-like hexagonal $SrFe_{12}O_{19}$ particles: Hydrothermal synthesis and their orientation in a magnetic field," *Journal of Magnetism and Magnetic Materials*, vol. 412, pp. 102–106, 2016.

[120] E. Rezaie, A. Rezanezhad, L. S. Ghadimi, A. Hajalilou, and N. Arsalani, "Effect of calcination on structural and supercapacitance properties of hydrothermally synthesized plate-like $SrFe_{12}O_{19}$ hexaferrite nanoparticles," *Ceramics International*, vol. 44, no. 16, pp. 20285–20290, 2018.

[121] F. H. Gjørup, M. Saura-Múzquiz, J. V. Ahlburg, H. L. Andersen, and M. Chris-

tensen, "Coercivity enhancement of strontium hexaferrite nano-crystallites through morphology controlled annealing," *Materialia*, vol. 4, pp. 203–210, 2018.

[122] Y. Jing, L. Jia, Y. Zheng, and H. Zhang, "Hydrothermal synthesis and competitive growth of flake-like M-type strontium hexaferrite," *RSC Advances*, vol. 9, no. 57, pp. 33388–33394, 2019.

[123] S. Pramanik and P. Das, "Chapter 3 - metal-based nanomaterials and their polymer nanocomposites," in *Nanomaterials and Polymer Nanocomposites*, pp. 91–121, Elsevier, 2019.

[124] S. Cherevko and K. J. J. Mayrhofer, "On-line inductively coupled plasma spectrometry in electrochemistry: Basic principles and applications," in *Encyclopedia of Interfacial Chemistry*, pp. 326–335, Elsevier, 2018.

[125] K. Kimura, M. Ohgaki, K. Tanaka, H. Morikawa, and F. Marumo, "Study of the bipyramidal site in magnetoplumbite-like compounds, $SrM_{12}O_{19}$ (M = Al, Fe, Ga)," *Journal of Solid State Chemistry*, vol. 87, no. 1, pp. 186–194, 1990.

[126] J. Otón, E. Pereiro, A. J. Pérez-Berná, L. Millach, C. O. S. Sorzano, R. Marabini, and J. M. Carazo, "Characterization of transfer function, resolution and depth of field of a soft X-ray microscope applied to tomography enhancement by Wiener deconvolution," *Biomedical Optics Express*, vol. 7, no. 12, pp. 5092–5103, 2016.

[127] A. Sorrentino, J. Nicolás, R. Valcárcel, F. J. Chichón, M. Rosanes, J. Avila, A. Tkachuk, J. Irwin, S. Ferrer, and E. Pereiro, "MISTRAL: a transmission soft X-ray microscopy beamline for cryo nano-tomography of biological samples and magnetic domains imaging," *Journal of Synchrotron Radiation*, vol. 22, no. 4, pp. 1112–1117, 2015.

[128] P. Scherrer, "Bestimmung der Größe und der inneren Struktur von Kolloidteilchen mittels Röntgenstrahlen," *Nachrichten von der Gesellschaft der Wissenschaften zu Göttingen, Mathematisch-Physikalische Klasse*, vol. 1918, pp. 98–100, 1918.

[129] B. J. Evans, F. Grandjean, A. P. Lilot, R. H. Vogel, and A. Gérard, "^{57}Fe hyperfine interaction parameters and selected magnetic properties of high purity $MFe_{12}O_{19}$ (M=Sr, Ba)," *Journal of Magnetism and Magnetic Materials*, vol. 67, no. 1, pp. 123–129, 1987.

[130] M. Jean, V. Nachbaur, J. Bran, and J.-M. Le Breton, "Synthesis and characterization of $SrFe_{12}O_{19}$ powder obtained by hydrothermal process," *Journal of Alloys and Compounds*, vol. 496, no. 1-2, pp. 306–312, 2010.

[131] F. J. Berry, J. F. Marco, C. B. Ponton, and K. R. Whittle, "Preparation and characterization of rare earth-doped strontium hexaferrites $Sr_{1-x}M_xFe_{12}O_{19}$ (M=La, Eu)," *Journal of Materials Science Letters*, vol. 20, no. 5, pp. 431–434, 2001.

[132] G. Wiesinger, M. Müller, R. Grössinger, M. Pieper, A. Morel, F. Kools, P. Tenaud,

J. Le Breton, and J. Kreisel, "Substituted ferrites studied by nuclear methods," *Physica Status Solidi A*, vol. 189, no. 2, pp. 499–508, 2002.

[133] I. Chorkendorff and J. W. Niemantsverdriet, "Catalyst characterization," in *Concepts of Modern Catalysis and Kinetics*, pp. 129–166, John Wiley & Sons, Ltd, 2005.

[134] M. Baermann GmbH, "Commercial powder of strontium hexaferrite," 2018.

[135] Y. X. Lu, J. S. Claydon, Y. B. Xu, S. M. Thompson, K. Wilson, and G. van der Laan, "Epitaxial growth and magnetic properties of half-metallic Fe_3O_4 on GaAs(100)," *Physical Review B*, vol. 70, no. 23, p. 233304, 2004.

[136] R. A. D. Pattrick, G. V. d. Laan, C. M. B. Henderson, P. Kuiper, E. Dudzik, and D. J. Vaughan, "Cation site occupancy in spinel ferrites studied by x-ray magnetic circular dichroism developing a method for mineralogists," *European Journal of Mineralogy*, vol. 14, no. 6, pp. 1095–1102, 2002.

[137] E. Goering, "Large hidden orbital moments in magnetite," *Physica Status Solidi B*, vol. 248, no. 10, pp. 2345–2351, 2011.

[138] E. Pellegrain, M. Hagelstein, S. Doyle, H. O. Moser, J. Fuchs, D. Vollath, S. Schuppler, M. A. James, S. S. Saxena, L. Niesen, O. Rogojanu, G. A. Sawatzky, C. Ferrero, M. Borowski, O. Tjernberg, and N. B. Brookes, "Characterization of nanocrystalline γ-Fe_2O_3 with synchrotron radiation techniques," *Physica Status Solidi B*, vol. 215, no. 1, pp. 797–801, 1999.

[139] Y. Guyodo, P. Sainctavit, M.-A. Arrio, C. Carvallo, R. L. Penn, J. J. Erbs, B. S. Forsberg, G. Morin, F. Maillot, F. Lagroix, P. Bonville, F. Wilhelm, and A. Rogalev, "X-ray magnetic circular dichroïsm provides strong evidence for tetrahedral iron in ferrihydrite," *Geochemistry, Geophysics, Geosystems*, vol. 13, no. 6, 2012.

[140] Y. Prado, N. Daffé, A. Michel, T. Georgelin, N. Yaacoub, J.-M. Grenèche, F. Choueikani, E. Otero, P. Ohresser, M.-A. Arrio, C. Cartier-dit Moulin, P. Sainctavit, B. Fleury, V. Dupuis, L. Lisnard, and J. Fresnais, "Enhancing the magnetic anisotropy of maghemite nanoparticles via the surface coordination of molecular complexes," *Nature Communications*, vol. 6, p. 10139, 2015.

[141] M. W. Haverkort, "Spin and orbital degrees of freedom in transition metal oxides and oxide thin films studied by soft x-ray absorption spectroscopy," *Thesis University of Cologne Faculty of Mathematics and Natural Sciences Physics Department*, vol. PhD, p. 214, 2005.

[142] M. Retegan, "Crispy," 2018.

[143] X. Obradors, X. Solans, A. Collomb, D. Samaras, J. Rodriguez, M. Pernet, and M. Font-Altaba, "Crystal structure of strontium hexaferrite $SrFe_{12}O_{19}$," *Journal of Solid State Chemistry*, vol. 72, no. 2, pp. 218–224, 1988.

[144] J. E. Beevers, C. J. Love, V. K. Lazarov, S. A. Cavill, H. Izadkhah, C. Vittoria,

R. Fan, G. van der Laan, and S. S. Dhesi, "Enhanced magnetoelectric effect in m-type hexaferrites by Co substitution into trigonal bi-pyramidal sites," *Applied Physics Letters*, vol. 112, pp. 082401–1 – 082401–5, 2018.

[145] S. Brice-Profeta, M.-A. Arrio, E. Tronc, N. Menguy, I. Letard, C. Cartier dit Moulin, M. Noguès, C. Chanéac, J.-P. Jolivet, and P. Sainctavit, "Magnetic order in - nanoparticles: a XMCD study," *Journal of Magnetism and Magnetic Materials*, vol. 288, pp. 354–365, 2005.

[146] D. J. Huang, C. F. Chang, H.-T. Jeng, G. Y. Guo, H.-J. Lin, W. B. Wu, H. C. Ku, A. Fujimori, Y. Takahashi, and C. T. Chen, "Spin and orbital magnetic moments of Fe_3O_4," *Physical Review Letters*, vol. 93, no. 7, p. 077204, 2004.

[147] A. Pelissetto and E. Vicari, "Critical phenomena and renormalization-group theory," *Physics Reports*, vol. 368, no. 6, pp. 549–727, 2002.

[148] H. Kleinert, "Critical exponents from seven-loop strong-coupling theory in three dimensions," *Physical Review D*, vol. 60, pp. 085001(1)–085001(15), 1999.

[149] R. Wu and A. J. Freeman, "Limitation of the magnetic-circular-dichroism spin sum rule for transition metals and importance of the magnetic dipole term," *Physical Review Letters*, vol. 73, no. 14, pp. 1994–1997, 1994.

[150] C. Fang, F. Kools, M. R., G. de With, and R. de Groot, "Magnetic and electronic properties of strontium hexaferrite $SrFe_{12}O_{19}$ from first-principles calculations," *Journal of Physics: Condensed Matter*, vol. 15, no. 36, p. 6229–6237, 2003.

[151] M. Yu and D. R. Trinkle, "Accurate and efficient algorithm for Bader charge integration," *The Journal of Chemical Physics*, vol. 134, no. 6, p. 064111, 2011.

[152] Z. Y. Wu, S. Gota, F. Jollet, M. Pollak, M. Gautier-Soyer, and C. R. Natoli, "Characterization of iron oxides by x-ray absorption at the oxygen K edge using a full multiple-scattering approach," *Physical Review B*, vol. 55, no. 4, pp. 2570–2577, 1997.

[153] S. Giovannini, F. Boscherini, R. Carboni, L. Signorini, L. Pasquini, N. Mahne, A. Giglia, M. Pedio, S. Nannarone, M. Benfatto, and S. D. Longa, "Multiple Scattering Analysis of O K-Edge NEXAFS in Iron Oxides," *Physica Scripta*, p. 424, 2005.

[154] F. M. F. de Groot, M. Grioni, J. C. Fuggle, J. Ghijsen, G. A. Sawatzky, and H. Petersen, "Oxygen 1*s* x-ray-absorption edges of transition-metal oxides," *Physical Review B*, vol. 40, no. 8, pp. 5715–5723, 1989.

[155] C. M. Schneider and G. Schönhense, "Investigating surface magnetism by means of photoexcitation electron emission microscopy," *Reports on Progress in Physics*, vol. 65, pp. 1785–1839, 2002.

[156] S. Ruiz-Gomez, L. Perez, A. Mascaraque, A. Quesada, P. Prieto, I. Palacio, L. Martín-García, M. Foerster, L. Aballe, and J. de la Figuera, "Geometrically defined

spin structures in ultrathin Fe_3O_4 with bulk like magnetic properties," *Nanoscale*, vol. 10, pp. 5566–5573, 2018.

[157] A. Hubert and R. Schäfer, *Magnetic Domains: The Analysis of Magnetic Microstructures*. Springer Science & Business Media, 2008.

[158] E. Cespedes, G. Rodriguez-Rodriguez, C. Navio, and et al., "Inter-grain effects on the magnetism of M-type strontium ferrite," *Journal of Alloys and Compounds*, vol. 692, no. 692, pp. 280–287, 2017.

[159] G. Varvaro, F. Casoli, and F. Casoli, *Ultra-High-Density Magnetic Recording : Storage Materials and Media Designs*. Jenny Stanford Publishing, 2016.

[160] D. Makarov, J. Lee, C. Brombacher, C. Schubert, M. Fuger, D. Suess, J. Fidler, and M. Albrecht, "Perpendicular FePt-based exchange-coupled composite media," *Applied Physics Letters*, vol. 96, no. 6, p. 062501, 2010.

[161] H. Kronmüller and D. Goll, "Micromagnetic theory of the pinning of domain walls at phase boundaries," *Physica B: Condensed Matter*, vol. 319, no. 1, pp. 122–126, 2002.

[162] A. K. Patra, F. Fleischhauer, S. Oswald, L. Schultz, and V. Neu, "Coercivity mechanism in hard magnetic $SmCo_5/PrCo_5$ bilayers," *Journal of Physics D: Applied Physics*, vol. 47, no. 21, p. 215001, 2014.

[163] Z. B. Li, B. G. Shen, E. Niu, and J. R. Sun, "Nucleation of reversed domain and pinning effect on domain wall motion in nanocomposite magnets," *Applied Physics Letters*, vol. 103, no. 6, p. 062405, 2013.

[164] E. A. Owen and D. M. Jones, "Effect of grain size on the crystal structure of cobalt," *Proceedings of the Physical Society. Section B*, vol. 67, no. 6, pp. 456–466, 1954.

[165] V. A. de la Peña OShea, P. R. de la Piscina, N. Homs, G. Aromí, and J. L. G. Fierro, "Development of hexagonal closed-packed cobalt nanoparticles stable at high temperature," *Chemistry of Materials*, vol. 21, no. 23, pp. 5637–5643, 2009.

[166] V. Sechovský, "Magnetism in Solids: General Introduction," in *Encyclopedia of Materials: Science and Technology*, pp. 5018–5032, Elsevier, 2001.

[167] J. Espinosa, H. Shi, and D. Lederman, "In situ measurements of cobalt thin-film surface roughening upon annealing," *Journal of Applied Physics*, vol. 99, no. 2, p. 023516, 2006.

[168] P. Kruse, "Scanning Probe Microscopy: The lab on a tip," *Journal of Electron Spectroscopy and Related Phenomena*, vol. 135, no. 1, p. 83, 2004.

[169] N. Kaushik, P. Sharma, H. Kimura, A. Inoue, and A. Makino, "Exchange coupling in nanocomposite FePtB thin film magnets," *Journal of Applied Physics*, vol. 103, no. 7, p. 07E121, 2008.

[170] R. Skomski and J. M. D. Coey, "Giant energy product in nanostructured two-phase magnets," *Physical Review B*, vol. 48, no. 21, pp. 15812–15816, 1993.

[171] M. Saura-Múzquiz, C. Granados-Miralles, M. Stingaciu, E. D. Bøjesen, Q. Li, J. Song, M. Dong, E. Eikeland, and M. Christensen, "Improved performance of $SrFe_{12}O_{19}$ bulk magnets through bottom-up nanostructuring," *Nanoscale*, vol. 8, no. 5, pp. 2857–2866, 2016.

[172] M. Welke, J. Gräfe, R. K. Govind, V. H. Babu, M. Trautmann, K.-M. Schindler, and R. Denecke, "XMCD studies of thin Co films on BaTiO3," *Journal of Physics: Condensed Matter*, vol. 27, p. 326001, July 2015.

[173] T. J. Regan, H. Ohldag, C. Stamm, F. Nolting, J. Lüning, J. Stöhr, and R. L. White, "Chemical effects at metal/oxide interfaces studied by x-ray-absorption spectroscopy," *Physical Review B*, vol. 64, no. 21, p. 214422, 2001.

[174] B. Belec, G. Dražić, S. Gyergyek, B. Podmiljšak, T. Goršak, M. Komelj, J. Nogués, and D. Makovec, "Novel Ba-hexaferrite structural variations stabilized on the nanoscale as building blocks for epitaxial bi-magnetic hard/soft sandwiched maghemite/hexaferrite/maghemite nanoplatelets with out-of-plane easy axis and enhanced magnetization," *Nanoscale*, vol. 9, no. 44, pp. 17551–17560, 2017.

[175] D. Primc and D. Makovec, "Composite nanoplatelets combining soft-magnetic iron oxide with hard-magnetic barium hexaferrite," *Nanoscale*, vol. 7, no. 6, pp. 2688–2697, 2015.

[176] Y. Park, E. E. Fullerton, and S. D. Bader, "Growth-induced uniaxial in-plane magnetic anisotropy for ultrathin Fe deposited on MgO(001) by oblique-incidence molecular beam epitaxy," *Applied Physics Letters*, vol. 66, no. 16, pp. 2140–2142, 1995.

[177] B. D. Cullity and C. D. Graham, "Ferromagnetism," in *Introduction to Magnetic Materials*, pp. 115–149, John Wiley & Sons, Ltd, 2008.

[178] M. T. Johnson, P. J. H. Bloemen, F. J. A. d. Broeder, and J. J. d. Vries, "Magnetic anisotropy in metallic multilayers," *Reports on Progress in Physics*, vol. 59, no. 11, pp. 1409–1458, 1996.

[179] D. C. Jiles, *Introduction to Magnetism and Magnetic Materials, Second Edition*. CRC Press, June 1998.

[180] F. E. Luborsky, J. D. Livingston, and G. Y. Chin, "Chapter 29 - magnetic properties of metals and alloys," in *Physical Metallurgy (Fourth Edition)*, pp. 2501–2565, North-Holland, 1996.

[181] S. Sabet, A. Moradabadi, S. Gorji, M. Fawey, E. Hildebrandt, I. Radulov, D. Wang, H. Zhang, C. Kübel, and L. Alff, "Correlation of Interface Structure with Magnetic Exchange in a Hard/Soft Magnetic Model Nanostructure," *Physical Review Applied*, vol. 11, no. 5, p. 054078, 2019.

[182] F. Casoli, F. Albertini, L. Nasi, S. Fabbrici, R. Cabassi, F. Bolzoni, and C. Bocchi, "Strong coercivity reduction in perpendicular FePtFe bilayers due to hard/soft coupling," *Applied Physics Letters*, vol. 92, no. 14, p. 142506, 2008.

[183] J. Lee, B. Dymerska, J. Fidler, V. Alexandrakis, T. Speliotis, D. Niarchos, P. Pongratz, and D. Suess, "Fabrication and high-resolution electron microscopy study of FePt L10/A1 graded exchange spring media," *physica status solidi (a)*, vol. 210, no. 7, pp. 1305–1310, 2013.

[184] B. Dymerska, J. Lee, J. Fidler, and D. Suess, "Micromagnetic study of exchange spring media with a rough interface on an example of FePt films," *Journal of Physics D: Applied Physics*, vol. 45, no. 49, p. 495001, 2012.

[185] H. Yang, M. Liu, Y. Lin, and Y. Yang, "Simultaneous enhancements of remanence and $(BH)_{max}$ in $BaFe_{12}O_{19}/CoFe_2O_4$ nanocomposite powders," *Journal of Alloys and Compounds*, vol. 631, pp. 335–339, 2015.

[186] M. Khaleeq-ur Rahman, K. A. Bhatti, M. S. Rafique, A. Latif, and S. fou-uz Zia, "Deposition and characterization of strontium hexaferrite ($SrFe_{12}O_{19}$) by PLD technique," *Optics and Laser Technology*, vol. 47, pp. 361–365, 2013.

[187] J. Buršík, I. Drbohlav, Z. Frait, K. Knížek, R. Kužel, and K. Kouřil, "Oriented $SrFe_{12}O_{19}$ thin films prepared by chemical solution deposition," *Journal of Solid State Chemistry*, vol. 184, no. 11, pp. 3085–3094, 2011.

[188] K. Kato, R. Watanuki, and A. Ito, "High-speed epitaxial growth of M-type Strontium hexaferrite films on sapphire using metal–organic chemical vapor deposition and their magnetic property," *Materials Letters*, vol. 274, p. 128046, 2020.

[189] S. M. Masoudpanah and S. A. S. Ebrahimi, "Effect of citric acid content on the structural and magnetic properties of $SrFe_{12}O_{19}$ thin films," *Thin Solid Films*, vol. 520, no. 1, pp. 199–203, 2011.

[190] B. Ramamurthy Acharya, S. Prasad, N. Venkataramani, E. Ebarra, and T. Suzuki, "The magnetic properties and microstructure of strontium ferrite films with perpendicular and in-plane magnetic anisotropy," *IEEE Transactions on Magnetics*, vol. 33, no. 5, pp. 3640–3642, 1997.

[191] A. Morisako, M. Matsumoto, S. Takei, and T. Yamazaki, "Effect of substrate temperature on magnetic properties of strontium ferrite thin films," *IEEE Transactions on Magnetics*, vol. 33, no. 5, pp. 3100–3102, 1997.

[192] B. R. Acharya, R. Krishnan, S. Prasad, N. Venkataramani, A. Ajan, and S. N. Shringi, "Sputter deposited strontium ferrite films with c-axis oriented normal to the film plane," *Applied Physics Letters*, vol. 64, no. 12, pp. 1579–1581, 1994.

[193] T. L. Hylton, M. A. Parker, and J. K. Howard, "Preparation and magnetic properties of epitaxial barium ferrite thin films on sapphire with in-plane, uniaxial anisotropy," *Applied Physics Letters*, vol. 61, no. 7, pp. 867–869, 1992.

[194] T. S. Cho, S. J. Doh, J. H. Je, and D. Y. Noh, "Thickness dependence of the crystallization of ba-ferrite films," *Journal of Applied Physics*, vol. 86, no. 4, pp. 1958–1964, 1999.

[195] A. Kaewrawang, A. Ghasemi, X. Liu, and M. A., "Underlayer dependence of microtexture, microstructure and magnetic properties of c-axis oriented strontium ferrite thin films," *Thin Solid Films*, vol. 518, no. 23, p. 7059–7063, 2010.

[196] A. Morel, J. M. Le Breton, J. Kreisel, G. Wiesinger, F. Kools, and P. Tenaud, "Sublattice occupation in $Sr_{1x}La_xFe_{12x}Co_xO_{19}$ hexagonal ferrite analyzed by Mössbauer spectrometry and Raman spectroscopy," *Journal of Magnetism and Magnetic Materials*, vol. 242-245, pp. 1405–1407, 2002.

[197] J. Kreisel, G. Lucazeau, and H. Vincent, "Raman study of substituted barium ferrite single crystals, $BaFe_{122x}Me_xCo_xO_{19}$(Me=Ir, Ti)," *Journal of Raman Spectroscopy*, vol. 30, no. 2, pp. 115–120, 1999.

[198] G. P. Nethala, R. Tadi, G. R. Gajula, K. N. Chidambara Kumar, and V. Veeraiah, "Investigations on the structural, magnetic and mossbauer properties of cerium doped strontium ferrite," *Physica B: Condensed Matter*, vol. 550, pp. 136–144, Dec. 2018.

[199] J. Kreisel, G. Lucazeau, and H. Vincent, "Raman spectra and vibrational analysis of $BaFe_{12}O_{19}$ hexagonal ferrite," *Journal of Solid State Chemistry*, vol. 137, pp. 127–137, Apr. 1998.

[200] B. Ramamurthy Acharya, N. Venkatramani, S. Prasad, S. Shringi, R. Krishnan, M. Tessier, and Y. Dumond, "Preparation and magnetic properties of strontium ferrite thin films," *IEEE Transactions on Magnetics*, vol. 29, no. 6, pp. 3370–3372, 1993.

[201] Y. Hui, W. Cheng, G. Lin, and X. Miao, "Effect of heat treatments on the structural and magnetic properties of La-Co substituted strontium ferrite films," *Journal of Electronic Materials*, vol. 43, no. 9, pp. 3640–3645, 2014.

[202] J. E. Snyder, V. G. Harris, N. C. Koon, X. Sui, and M. H. Kryder, "Local anisotropic structure in amorphous Ba-Fe-O films and its role in determining magnetic anisotropy in crystallized Ba-hexaferrite films," *IEEE Transactions on Magnetics*, vol. 31, no. 6, pp. 3844–3846, 1995.

[203] J. E. Snyder, V. G. Harris, N. C. Koon, X. Sui, and M. H. Kryder, "Local structure of the amorphous precursor to Ba-Hexaferrite thin films: an anisotropic octahedral Fe-O glass network," *Physical Review Letters*, vol. 77, no. 16, pp. 3383–3386, 1996.

[204] J. E. Snyder, V. G. Harris, B. N. Das, N. C. Koon, X. Sui, and M. H. Kryder, "Determination of local order in the amorphous precursor to Ba-hexaferrite thin-film recording media," *Journal of Applied Physics*, vol. 79, no. 8, pp. 4890–4892, 1996.

[205] P. Batti, "Phase diagrams, structure, and magnetic behavior of hexagonal ferrites," *Ceramurgia*, vol. 6, no. 1, pp. 11–16, 1976.

[206] M. Mayer, "SIMNRA User's Guide," p. 67.

[207] M. Azim, S. Atiq, S. Riaz, and S. Naseem, "Indexing the structural parameters and investigating the magnetic properties of lanthanum doped strontium hexaferrites," *IOP Conference Series: Materials Science and Engineering*, vol. 60, p. 012045, 2014.

[208] M. Aliahmad and N. Nasiri Moghaddam, "Synthesis of maghemite (γ-Fe_2O_3) nanoparticles by thermal-decomposition of magnetite (Fe_3O_4) nanoparticles," *Materials Science-Poland*, vol. 31, no. 2, pp. 264–268, 2013.

[209] A. Ruíz-Baltazar, R. Esparza, G. Rosas, and R. Pérez, "Effect of the surfactant on the growth and oxidation of iron nanoparticles," *Journal of Nanomaterials*, 2015.

[210] Zulfiqar, M. U. Rahman, M. Usman, S. K. Hasanain, Zia-ur-Rahman, A. Ullah, and I. W. Kim, "Static magnetic properties of Maghemite nanoparticles," *Journal of the Korean Physical Society*, vol. 65, no. 11, pp. 1925–1929, 2014.

[211] W. Kim, C.-Y. Suh, S.-W. Cho, K.-M. Roh, H. Kwon, K. Song, and I.-J. Shon, "A new method for the identification and quantification of magnetite–maghemite mixture using conventional X-ray diffraction technique," *Talanta*, vol. 94, pp. 348–352, 2012.

[212] I. V. Chernyshova, M. F. H. Jr, and A. S. Madden, "Size-dependent structural transformations of hematite nanoparticles. 1. Phase transition," *Physical Chemistry Chemical Physics*, vol. 9, no. 14, pp. 1736–1750, 2007.

[213] M. Elansary, M. Belaiche, C. A. Ferdi, E. Iffer, and I. Bsoul, "New nanosized Gd–Ho–Sm doped M-type strontium hexaferrite for water treatment application: experimental and theoretical investigations," *RSC Advances*, vol. 10, no. 42, pp. 25239–25259, 2020.

[214] M. I. Dar and S. A. Shivashankar, "Single crystalline magnetite, maghemite, and hematite nanoparticles with rich coercivity," *RSC Advances*, vol. 4, no. 8, pp. 4105–4113, 2013.

[215] J. M. J. Santillán, D. Muñetón Arboleda, D. F. Coral, M. B. Fernández vanRaap, D. Muraca, D. C. Schinca, and L. B. Scaffardi, "Optical and magnetic properties of Fe nanoparticles fabricated by femtosecond laser ablation in organic and inorganic solvents," *ChemPhysChem*, vol. 18, no. 9, pp. 1192–1209, 2017.

[216] L. B. M. Lopez, J. D. Pasteris, and P. Biswas, "Sensitivity of micro-Raman spectrum to crystallite size of electrospray-deposited and post-annealed films of iron-oxide nanoparticle suspensions," *Applied Spectroscopy*, vol. 63, no. 6, pp. 627–635, 2009.

[217] F. Menil, "Systematic trends of the ^{57}Fe Mössbauer isomer shifts in (FeOn) and (FeFn) polyhedra. Evidence of a new correlation between the isomer shift and the inductive effect of the competing bond T-X ($\rightarrow$ Fe) (where X is O or F and T any

element with a formal positive charge)," *Journal of Physics and Chemistry of Solids*, vol. 46, no. 7, pp. 763–789, 1985.

[218] A. G. Roca, J. F. Marco, M. d. P. Morales, and C. J. Serna, "Effect of nature and particle size on properties of uniform magnetite and maghemite nanoparticles," *The Journal of Physical Chemistry C*, vol. 111, no. 50, pp. 18577–18584, 2007.

[219] X. Sui, M. Kryder, B. Wong, and D. Laughlin, "Microstructural origin of the perpendicular anisotropy in M-type barium hexaferrite thin films deposited by RF magnetron sputtering," *IEEE Transactions on Magnetics*, vol. 29, no. 6, pp. 3751–3753, 1993.

[220] A. Ajan, B. R. Acharya, S. Prasad, S. N. Shringi, and N. Venkataramani, "Conversion electron Mössbauer studies on strontium ferrite films with in-plane and perpendicular anisotropies," *Journal of Applied Physics*, vol. 83, no. 11, pp. 6879–6881, 1998.

[221] X. Sui and M. H. Kryder, "Magnetic easy axis randomly in-plane oriented barium hexaferrite thin film media," *Applied Physics Letters*, vol. 63, no. 11, pp. 1582–1584, 1993.

[222] Xiaoyu Sui, M. Kryder, Bunsen Y. Wong, and D. Laughlin, "Magnetic properties and microstructures of M-type barium hexaferrite thin films deposited by Rf magnetron sputtering," in *Digests of international magnetics conference*, IEEE, 1993.

[223] H. W. Kim, D. H. Kim, E. Lee, S. Seong, J.-S. Kang, D. H. Kim, B. W. Lee, Y. Ko, and J.-Y. Kim, "Soft X-ray absorption spectroscopy study of multiferroic Bi-substituted $Ba_{1-x}Bi_xTi_{0.9}Fe_{0.1}O_3$," *Journal of the Korean Physical Society*, vol. 69, no. 3, pp. 361–364, 2016.

[224] T. Hayakawa, M. Arakawa, K. Ando, Y. Kiyomura, T. Kawano, and A. Terasaki, "Charge-state analysis of small barium-oxide clusters by x-ray absorption spectroscopy," *Journal of Physics: Condensed Matter*, vol. 31, no. 13, p. 134003, 2019.

[225] J. Bansmann, "Surface magnetism of iron and cobalt on W (110) probed with polarized synchrotron radiation:," *Applied Physics A Materials Science an Processing*, vol. 72, no. 4, pp. 447–453, 2001.

[226] H. Pinkvos, H. Poppa, E. Bauer, and J. Hurst, "Spin-polarized low-energy electron microscopy study of the magnetic microstructure of ultra-thin epitaxial cobalt films on W(110)," *Ultramicroscopy*, vol. 47, no. 4, pp. 339–345, 1992.

[227] G. Sarau, *Spin Dependent Transport in Cobalt Nanocontacts*. Forschungszentrum Jülich, 2007.

[228] R. Valenzuela, "Novel applications of ferrites," *Physics Research International*, 2012.

[229] M. J. Carey, S. Maat, P. Rice, R. F. C. Farrow, R. F. Marks, A. Kellock, P. Nguyen, and B. A. Gurney, "Spin valves using insulating cobalt ferrite exchange-spring pinning layers," *Applied Physics Letters*, vol. 81, no. 6, pp. 1044–1046, 2002.

[230] P. Durga Prasad and J. Hemalatha, "Enhanced magnetic properties of highly crystalline cobalt ferrite fibers and their application as gas sensors," *Journal of Magnetism and Magnetic Materials*, vol. 484, pp. 225–233, 2019.

[231] P. Lavela and J. L. Tirado, "$CoFe_2O_4$ and $NiFe_2O_4$ synthesized by sol–gel procedures for their use as anode materials for Li ion batteries," *Journal of Power Sources*, vol. 172, no. 1, pp. 379–387, 2007.

[232] O. Caltun, I. Dumitru, M. Feder, N. Lupu, and H. Chiriac, "Substituted cobalt ferrites for sensors applications," *Journal of Magnetism and Magnetic Materials*, vol. 320, no. 20, pp. e869–e873, 2008.

[233] S. Amiri and H. Shokrollahi, "The role of cobalt ferrite magnetic nanoparticles in medical science," *Materials Science and Engineering: C*, vol. 33, no. 1, pp. 1–8, 2013.

[234] M. Khodaei, S. Ebrahimi, Y. Park, S. Choi, C. Kim, J. Son, and S. Baik, "(111)-oriented $Co_{0.8}Fe_{2.2}O_{4+\delta}$ thin film grown by pulsed laser deposition: Structural and magnetic properties," *Journal of Materials Science*, vol. 48, pp. 6960–6969, 2013.

[235] M. Khodaei, S. A. Seyyed Ebrahimi, Y. J. Park, S. H. Choi, C. Kim, J. Son, and S. Baik, "Thickness dependent magnetic properties of (111)-oriented $Co_{0.8}Fe_{2.2}O_4$ thin film grown by pulsed laser deposition," *Thin Solid Films*, vol. 571, 2014.

[236] D. S. Mathew and R.-S. Juang, "An overview of the structure and magnetism of spinel ferrite nanoparticles and their synthesis in microemulsions," *Chemical Engineering Journal*, vol. 129, no. 1, pp. 51–65, 2007.

[237] Y. Suzuki, "Epitaxial Spinel Ferrite Thin Films," *Annual Review of Materials Research*, vol. 31, no. 1, pp. 265–289, 2001.

[238] L. J. Cote, A. S. Teja, A. P. Wilkinson, and Z. J. Zhang, "Continuous hydrothermal synthesis of $CoFe_2O_4$ nanoparticles," *Fluid Phase Equilibria*, vol. 210, no. 2, pp. 307–317, 2003.

[239] G. Hu, J. H. Choi, C. B. Eom, V. G. Harris, and Y. Suzuki, "Structural tuning of the magnetic behavior in spinel-structure ferrite thin films," *Physical Review B*, vol. 62, no. 2, pp. R779–R782, 2000.

[240] J. G. dos S. Duque, M. A. Macêdo, N. O. Moreno, J. L. Lopez, and H. D. Pfanes, "Magnetic and structural properties of $CoFe_2O_4$ thin films synthesized via a sol–gel process," *Journal of Magnetism and Magnetic Materials*, vol. 226-230, pp. 1424–1425, 2001.

[241] J.-G. Lee, J. Y. Park, Y.-J. Oh, and C. S. Kim, "Magnetic properties of $CoFe_2O_4$ thin films prepared by a sol-gel method," *Journal of Applied Physics*, vol. 84, no. 5, pp. 2801–2804, 1998.

[242] S. N. Okuno, S. Hashimoto, and K. Inomata, "Preferred crystal orientation of cobalt

ferrite thin films induced by ion bombardment during deposition," *Journal of Applied Physics*, vol. 71, no. 12, pp. 5926–5929, 1992.

[243] P. Prieto, J. F. Marco, J. E. Prieto, S. Ruiz-Gomez, L. Perez, R. P. del Real, M. Vázquez, and J. de la Figuera, "Epitaxial integration of $CoFe_2O_4$ thin films on Si (001) surfaces using TiN buffer layers," *Applied Surface Science*, vol. 436, pp. 1067–1074, 2018.

[244] M. Foerster, M. Iliev, N. Dix, X. Martí, M. Barchuk, F. Sánchez, and J. Fontcuberta, "The poisson ratio in $CoFe_2O_4$ spinel thin films," *Advanced Functional Materials*, vol. 22, no. 20, pp. 4344–4351, 2012.

[245] M. Oujja, L. Martín-García, E. Rebollar, A. Quesada, M. A. García, J. F. Fernández, J. F. Marco, J. de la Figuera, and M. Castillejo, "Effect of wavelength, deposition temperature and substrate type on cobalt ferrite thin films grown by pulsed laser deposition," *Applied Surface Science*, vol. 452, pp. 19–31, 2018.

[246] M. Sánchez-Arenillas, M. Oujja, F. Moutinho, J. de la Figuera, M. V. Cañamares, A. Quesada, M. Castillejo, and J. F. Marco, "Bulk and surface characterisation of micrometer-thick cobalt ferrite films grown by IR PLD," *Applied Surface Science*, vol. 470, pp. 917–922, 2019.

[247] J.-G. Lee, K. P. Chae, and J. C. Sur, "Surface morphology and magnetic properties of $CoFe_2O_4$ thin films grown by a RF magnetron sputtering method," *Journal of Magnetism and Magnetic Materials*, vol. 267, no. 2, pp. 161–167, 2003.

[248] F. Rigato, J. Geshev, V. Skumryev, and J. Fontcuberta, "The magnetization of epitaxial nanometric $CoFe_2O_4(001)$ layers," *Journal of Applied Physics*, vol. 106, no. 11, p. 113924, 2009.

[249] L. Horng, G. Chern, M. C. Chen, P. C. Kang, and D. S. Lee, "Magnetic anisotropic properties in Fe_3O_4 and $CoFe_2O_4$ ferrite epitaxy thin films," *Journal of Magnetism and Magnetic Materials*, vol. 270, no. 3, pp. 389–396, 2004.

[250] A. V. Ramos, J.-B. Moussy, M.-J. Guittet, M. Gautier-Soyer, C. Gatel, P. Bayle-Guillemaud, B. Warot-Fonrose, and E. Snoeck, "Influence of a metallic or oxide top layer in epitaxial magnetic bilayers containing $CoFe_2O_4(111)$ tunnel barriers," *Physical Review B*, vol. 75, no. 22, p. 224421, 2007.

[251] L. Martín-García, A. Quesada, C. Munuera, J. F. Fernández, M. García-Hernández, M. Foerster, L. Aballe, and J. de la Figuera, "Atomically flat ultrathin cobalt ferrite islands," *Advanced Materials*, vol. 27, no. 39, pp. 5955–5960, 2015.

[252] S. Ruiz-Gómez, A. Mandziak, J. E. Prieto, M. Aristu, E. M. Trapero, G. D. Soria, A. Quesada, M. Foerster, L. Aballe, and J. de la Figuera, "A real-time XAS PEEM study of the growth of cobalt iron oxide on Ru(0001)," *The Journal of Chemical Physics*, vol. 152, no. 7, p. 074704, 2020.

[253] M. De Santis, A. Bailly, I. Coates, S. Grenier, O. Heckmann, K. Hricovini, Y. Joly,

V. Langlais, A. Y. Ramos, C. Richter, X. Torrelles, S. Garaudée, O. Geaymond, and O. Ulrich, "Epitaxial growth and structure of cobalt ferrite thin films with large inversion parameter on Ag(001)," *Acta Crystallographica B*, vol. 75, no. 1, 2019.

[254] R. Gargallo-Caballero, L. Martín-García, A. Quesada, C. Granados-Miralles, M. Foerster, L. Aballe, R. Bliem, G. S. Parkinson, P. Blaha, J. F. Marco, and J. d. l. Figuera, "Co on Fe_3O_4(001): Towards precise control of surface properties," *Journal of Chemical Physics*, vol. 144, no. 9, p. 094704, 2016.

[255] J. Rodewald, J. Thien, T. Pohlmann, M. Hoppe, F. Timmer, F. Bertram, K. Kuepper, and J. Wollschläger, "Formation of ultrathin cobalt ferrite films by interdiffusion of Fe_3O_4/CoO bilayers," *Physical Review B*, vol. 100, no. 15, p. 155418, 2019.

[256] J. Thien, J. Bahlmann, A. Alexander, M. Hoppe, T. Pohlmann, K. Ruwisch, C. Meyer, F. Bertram, K. Küpper, and J. Wollschläger, "Effects of post-deposition annealing on epitaxial CoO/Fe_3O_4 bilayers on $SrTiO_3$(001) and formation of thin high-quality cobalt ferrite-like films," *Journal of Physical Chemistry C*, vol. 124, no. 43, pp. 23895–23904, 2020.

[257] M. Takahashi and M. E. Fine, "Magnetic behavior of quenched and aged $CoFe_2O_4$-Co_3O_4 alloys," *Journal of Applied Physics*, vol. 43, no. 10, pp. 4205–4216, 1972.

[258] J. A. Moyer, C. A. F. Vaz, D. P. Kumah, D. A. Arena, and V. E. Henrich, "Enhanced magnetic moment in ultrathin Fe-doped $CoFe_2O_4$ films," *Physical Review B*, vol. 86, no. 17, p. 174404, 2012.

[259] S. Krupička and P. Novák, "Chapter 4 Oxide spinels," in *Handbook of Ferromagnetic Materials*, vol. 3, pp. 189–304, Elsevier, 1982.

[260] F. Eskandari, S. B. Porter, M. Venkatesan, P. Kameli, K. Rode, and J. M. D. Coey, "Magnetization and anisotropy of cobalt ferrite thin films," *Physical Review Materials*, vol. 1, no. 7, p. 074413, 2017.

[261] J. W. D. Martens, W. L. Peeters, H. M. van Noort, and M. Erman, "Optical, magneto-optical and mössbauer spectroscopy on Co^{3+} substituted cobalt ferrite $Co^{2+}Fe_{2-x}Co_{3+x}O_4(0 \leq x \leq 2)$," *Journal of Physics and Chemistry of Solids*, vol. 46, no. 4, pp. 411–416, 1985.

[262] P. de Bakker, R. Vandenberghe, and E. De Grave, "Hyperfine interactions and site population in the spinel compounds $Ca_xCo_{1-x}Fe_2O_4$," *Hyperfine Interactions*, vol. 94, no. 1, pp. 2023–2027, 1994.

[263] H. Le Trong, L. Presmanes, E. De Grave, A. Barnabé, C. Bonningue, and P. Tailhades, "Mössbauer characterisations and magnetic properties of iron cobaltites $Co_xFe_{3x}O_4$ ($1 \leq x \leq 2.46$) before and after spinodal decomposition," *Journal of Magnetism and Magnetic Materials*, vol. 334, pp. 66–73, 2013.

[264] J. de la Figuera, A. Quesada, L. Martín-García, M. Sanz, M. Oujja, M. Castillejo, A. Mascaraque, A. T. N'Diaye, M. Foerster, L. Aballe, and J. F. Marco, "Mössbauer

and magnetic properties of coherently mixed magnetite-cobalt ferrite grown by infrared pulsed-laser deposition," *Croatica Chemica Acta*, vol. 88, no. 4, pp. 453–460, 2015.

[265] S. Gallego and C. Tejera, "Private communication regarding a future publication,"

[266] C. M. Srivastava, G. Srinivasan, and N. G. Nanadikar, "Exchange constants in spinel ferrites," *Physical Review B*, vol. 19, no. 1, pp. 499–508, 1979.

[267] S. A. Chambers, R. F. C. Farrow, S. Maat, M. F. Toney, L. Folks, J. G. Catalano, T. P. Trainor, and G. E. Brown, "Molecular beam epitaxial growth and properties of $CoFe_2O_4$ on MgO(001)," *Journal of Magnetism and Magnetic Materials*, vol. 246, no. 1, pp. 124–139, 2002.

[268] J. A. Moyer, C. A. F. Vaz, D. A. Arena, D. Kumah, E. Negusse, and V. E. Henrich, "Magnetic structure of Fe-doped $CoFe_2O_4$ probed by x-ray magnetic spectroscopies," *Physical Review B*, vol. 84, no. 5, p. 054447, 2011.

[269] M. Getzlaff, *Fundamentals of Magnetism*. Springer-Verlag, 2008.

[270] A. Hubin and H. Terryn, "Chapter 6 X-ray photoelectron and Auger electron spectroscopy," in *Comprehensive Analytical Chemistry*, vol. 42 of *Non-Destructive Microanalysis of Cultural Heritage Materials*, pp. 277–312, Elsevier, 2004.

[271] C. J. Powell, "Practical guide for inelastic mean free paths, effective attenuation lengths, mean escape depths, and information depths in x-ray photoelectron spectroscopy," *Journal of Vacuum Science and Technology A*, vol. 38, no. 2, p. 023209, 2020.

[272] R. K. Mishra and G. Thomas, "Surface energy of spinel," *Journal of Applied Physics*, vol. 48, no. 11, pp. 4576–4580, 1977.

[273] W. Weiss and W. Ranke, "Surface chemistry and catalysis on well-defined epitaxial iron-oxide layers," *Progress in Surface Science*, vol. 70, no. 1-3, pp. 1–151, 2002.

[274] G. S. Parkinson, "Iron oxide surfaces," *Surface Science Reports*, vol. 71, no. 1, pp. 272–365, 2016.

[275] N. Spiridis, D. Wilgocka-Ślęzak, K. Freindl, B. Figarska, T. Giela, E. Młyńczak, B. Strzelczyk, M. Zając, and J. Korecki, "Growth and electronic and magnetic structure of iron oxide films on Pt(111)," *Physical Review B*, vol. 85, no. 7, p. 075436, 2012.

[276] W. J. Schuele, S. Shtrikman, and D. Treves, "Observation of Superparamagnetism by the Mössbauer Effect," *Journal of Applied Physics*, vol. 36, no. 3, pp. 1010–1011, 1965.

[277] Y. I. Kim, D. Kim, and C. S. Lee, "Synthesis and characterization of $CoFe_2O_4$

magnetic nanoparticles prepared by temperature-controlled coprecipitation method," *Physica B: Condensed Matter*, vol. 337, no. 1, pp. 42–51, 2003.

[278] J. López, W. P. Serrano, and H. Pfannes, "Magnetic properties of crystalline cobalt ferrite films," *Revista Colombiana de Física*, vol. 38, pp. 1074–1077, 2006.

[279] H. Yanagihara, K. Uwabo, M. Minagawa, E. Kita, and N. Hirota, "Perpendicular magnetic anisotropy in $CoFe_2O_4$(001) films epitaxially grown on MgO(001)," *Journal of Applied Physics*, vol. 109, no. 7, p. 07C122, 2011.

[280] R. Brand, "NORMOS Mössbauer fitting program user's guide," pp. 1–123, 1995.

[281] J. de la Figuera, A. Quesada, L. Martín-García, M. Sanz, M. Oujja, E. Rebollar, M. Castillejo, P. Prieto, Muñoz-Martín, L. Aballe, and J. F. Marco, "Self-organized single crystal mixed magnetite/cobalt ferrite films grown by infrared pulsed-laser deposition," *Applied Surface Science*, vol. 359, pp. 480–485, 2015.

[282] R. E. Vandenberghe and E. D. Grave, "Mössbauer effect studies of oxidic spinels," in *Mössbauer Spectroscopy Applied to Inorganic Chemistry*, no. 3 in Modern Inorganic Chemistry, pp. 59–182, 1989.

[283] J. Korecki, B. Handke, N. Spiridis, T. Ślęzak, I. Flis-Kabulska, and J. Haber, "Size effects in epitaxial films of magnetite," *Thin Solid Films*, vol. 412, no. 1, pp. 14–23, 2002.

[284] F. C. Voogt, T. T. M. Palstra, L. Niesen, O. C. Rogojanu, M. A. James, and T. Hibma, "Superparamagnetic behavior of structural domains in epitaxial ultrathin magnetite films," *Physical Review B*, vol. 57, no. 14, pp. R8107–R8110, 1998.

[285] T. R. Gao, L. Fang, S. Fackler, S. Maruyama, X. H. Zhang, L. L. Wang, T. Rana, P. Manchanda, A. Kashyap, K. Janicka, A. L. Wysocki, A. T. N'Diaye, E. Arenholz, J. A. Borchers, B. J. Kirby, B. B. Maranville, K. W. Sun, M. J. Kramer, V. P. Antropov, D. D. Johnson, R. Skomski, J. Cui, and I. Takeuchi, "Large energy product enhancement in perpendicularly coupled MnBi/CoFe magnetic bilayers," *Physical Review B*, vol. 94, no. 6, p. 060411, 2016.

[286] R. Skomski, P. Manchanda, P. Kumar, B. Balamurugan, A. Kashyap, and D. J. Sellmyer, "Predicting the future of permanent-magnet materials," *IEEE Transactions on Magnetics*, vol. 49, no. 7, pp. 3215–3220, 2013.

[287] E. Goto, N. Hayashi, T. Miyashita, and K. Nakagawa, "Magnetization and switching characteristics of composite thin magnetic films," *Journal of Applied Physics*, vol. 36, no. 9, pp. 2951–2958, 1965.

[288] N. Viart, R. S. Hassan, C. Mény, P. Panissod, C. Ulhaq-Bouillet, J. L. Loison, G. Versini, F. Huber, and G. Pourroy, "Diversity of the magnetic coupling behaviors in the $CoFe_2/CoFe_2O_4$ system," *Applied Physics Letters*, vol. 86, no. 19, p. 192514, 2005.

[289] R. S. Hassan, C. Mény, N. Viart, C. Ulhaq, G. Versini, J. L. Loison, and G. Pourroy, "Tuning the coercive field of $CoFe_2$ in hard/soft $CoFe_2O_4/CoFe_2$ bilayers," *New Journal of Physics*, vol. 9, no. 10, pp. 364–364, 2007.

[290] B. P. Kafle, "Chapter 6 - Introduction to nanomaterials and application of UV–Visible spectroscopy for their characterization," in *Chemical Analysis and Material Characterization by Spectrophotometry*, pp. 147–198, 2020.

[291] M. T. Otten, "High-Angle annular dark-field imaging on a tem/stem system," *Journal of Electron Microscopy Technique*, vol. 17, no. 2, pp. 221–230, 1991.

[292] A. Quesada, G. Delgado, L. Pascual, A. M. Aragón, P. Marín, C. Granados-Miralles, M. Foerster, L. Aballe, J. E. Prieto, J. de la Figuera, J. F. Fernández, and P. Prieto, "Exchange-spring behavior below the exchange length in hard-soft bilayers in multidomain configurations," *Physical Review B*, vol. 98, no. 21, p. 214435, 2018.

[293] G. Lavorato, E. Winkler, B. Rivas-Murias, and F. Rivadulla, "Thickness dependence of exchange coupling in epitaxial $Fe_3O_4/CoFe_2O_4$ soft/hard magnetic bilayers," *Physical Review B*, vol. 94, no. 5, p. 054405, 2016.

[294] N. L. Guo, G. P. Zhao, H. W. Zhang, X. L. Zhou, and Y. Deng, "Magnetic reversal processes and critical thickness in FePt/α-Fe/FePt trilayers," *Journal of Magnetism and Magnetic Materials*, vol. 323, no. 23, pp. 3049–3053, 2011.

[295] F. Wang, X. Xu, Y. Liang, J. Zhang, and H. Wu, "FeAu/FePt exchange-spring media fabricated by magnetron sputtering and postannealing," *Applied Physics Letters*, vol. 95, no. 2, p. 022516, 2009.

[296] K. Mibu, T. Nagahama, and T. Shinjo, "Reversible magnetization process and magnetoresistance of soft-magnetic (NiFe) /hard-magnetic (CoSm) bilayers," *Journal of Magnetism and Magnetic Materials*, vol. 163, no. 1, pp. 75–79, 1996.

[297] J. M. Howe, "14 - Structure, Composition and Energy of Solid–Solid Interfaces," in *Physical Metallurgy (Fifth Edition)*, pp. 1317–1451, 2014.